MAX PLANCK INSTITUTE FOR CHEMISTRY

JOHANNES GUTENBERG UNIVERSITÄT MAINZ

Size Dependent Hygroscopicity of Aerosol Nanoparticles

Dissertation

zur Erlangung des Grades

„Doktor der Naturwissenschaften“

im Promotionsfach Chemie

am Fachbereich Chemie, Pharmazie, Pharmazie, Geographie und Geowissenschaften

der Johannes Gutenberg-Universität Mainz

Ting Lei

geb. in Baoji, V, R China

Mainz, 2020

Declaration

I hereby declare that I wrote the dissertation without any unauthorized external assistance. I used only sources acknowledged in the work. All textual passages which are appropriated verbatim or paraphrased from published and unpublished texts as well as all information obtained from oral sources are duly indicated and listed in accordance with bibliographical rules. In carrying out this research, I complied with the rules of standard scientific practice as formulated in the statutes of Johannes Gutenberg-University Mainz to insure standard scientific practice.

Mainz, Ting Lei

Abstract

The hygroscopicity of aerosol nanoparticles and related physical-chemical properties are crucial for atmospheric multiphase processes, physical chemistry, and materials science. One of the main problems of current research on aerosol hygroscopicity is that the most studies due to technical challenges lack measurements in the sub-10 nm size range, which is highly relevant for research on new particle formation and its initial growth. The goal of this thesis is to solve the technical problems and use the advanced nano-hygroscopicity tandem differential mobility analyzer (nano-HTDMA) to investigate the size dependent hygroscopicity of aerosol nanoparticles with diameters down to 6 nm.

(1) In the first part of this thesis, the detailed information on the design of a nano-HTDMA system is presented. To enable high accuracy and precision in hygroscopicity measurements of aerosol nanoparticles, especially in the sub-10 nm size range, systematic and comprehensive calibration criteria of the nano-HTDMA have been developed and applied, including the calibration of nanoparticle sizing, sheath and aerosol flow rates, DMA voltage, relative humidity (RH) sensor, and temperature (T) sensor. After calibration, the nano-HTDMA system has been shown to have an accurate sizing and a small sizing offset between nano-DMAs (< 1.4 %) for aerosol nanoparticles with diameters down to 6 nm. Moreover, to maintain the RH-uniformities that prevent the pre-deliquescence and non-prompt phase transition of nanoparticles within nano-DMA2, the RH of sheath flow is kept as same as that of aerosol flow at inlet of nano-DMA2. Since temperature and RH are closely linked, the nano-DMA2 with its humidification system is placed in a well-insulated air-conditioned chamber, which maintains a constant temperature. Using the nano-HTDMA apparatus, we measure the hygroscopic behavior of aerosol nanoparticles of two inorganic substances (i.e., ammonium sulfate and sodium sulfate). We find a weak size dependence of deliquescence and efflorescence relative humidity (DRH and ERH, respectively) of ammonium sulfate nanoparticles but a strong size dependence of DRH and ERH of sodium sulfate nanoparticles down to 6 nm in size.

(2) The second part of this thesis is about hygroscopic properties of organic nanoparticles with diameters down to 6 nm (i.e., levoglucosan and D-glucose) measured by a nano-HTDMA system. Levoglucosan is a biomass burning tracer compound and can contribute substantially (16.6–30.9% by mass) to the total

organics in $PM_{2.5}$. D-glucose, a hydrolysis product of cellulose and levoglucosan, is one of the major pyrolysis products of wood. Due to the partial evaporation of levoglucosan with diameters smaller than 20 nm in the nano-HTDMA system, we investigate the hygroscopicity of levoglucosan nanoparticles in the size range from 20 to 100 nm. A weak size dependence of hygroscopic growth factor is observed for levoglucosan and D-glucose nanoparticles with diameters down to 20 nm, while a strong size dependence of the hygroscopic growth factor is found for D-glucose nanoparticles with diameters from 6 to 20 nm. We further compare measurements for levoglucosan and glucose nanoparticles with modelling results of the Extended Aerosol Inorganics Model (E-AIM) and the ideal solution theory, respectively. The ideal solution theory well describes the hygroscopic growth factors of levoglucosan and D-glucose nanoparticles with diameters larger than 15 nm, while the E-AIM model prediction well describes measured growth factors of sub-15 nm D-glucose nanoparticles.

(3) The goal of the third part of this work is to investigate the hygroscopicity of organic surrogate compounds from biomass burning and their interaction with inorganic ammonium sulfate aerosols using an HTDMA. The organic surrogate compounds represent a selection of some of the most abundant pyrolysis products of biomass burning. We find that levoglucosan and humic acid aerosol nanoparticles release water gradually in the range from 90 % down to 5% RH. However, 4-Hydroxybenzoic acid aerosol nanoparticles remain in the solid state and exhibit a small shrink in size in the whole dehumidification process. Predicted growth factors using the Aerosol Inorganic-Organic Mixtures Functional groups Activity Coefficients (AIOMFAC) model, the E-AIM, and a fitted hygroscopicity function are in general consistent with measured hygroscopic growth factors of levoglucosan, respectively. However, the use of the AIOMFAC and the E-AIM models without consideration of crystalline organic phases is not appropriate to describe the hygroscopicity of 4-hydroxybenzoic acid. Furthermore, we observe several effects of these organic components on the hygroscopicity behavior of mixtures containing ammonium sulfate in relation to the different mass fractions of organic compounds: (i) A shift of ERH of ammonium sulfate to the higher RH due to the presence of 25 wt % levoglucosan in the mixture. (ii) There is a phase transition at 25% RH for mixtures containing 50 wt % of 4-hydroxybenzoic acid compared to the ERH (i.e.,

35 %) for organic-free AS nanoparticles, and a liquid-to-solid phase transition of 4-hydroxybenzoic acid in the mixed particles during dehydration process. (iii) The presence of humic acid components shows no significant effects on the efflorescence of AS in mixed aerosol nanoparticles. In addition, consideration of a solid-liquid phase transition of AS in both the AIOMFAC and the E-AIM models leads to a general agreement between models and measurements, as well as ERH of AS in the mixed system. The measured diameter growth factors of aerosol nanoparticles containing humic acid and ammonium sulfate are well predicted by Zdanovskii-Stokes-Robinson (ZSR) relation. Lastly, the mixtures containing organic surrogates (i.e., levoglucosan, 4-hydroxybenzoic acid, and humic acid) and ammonium sulfate with increasing organics mass fractions is used to mimic, in a simplified manner, ambient conditions in the Amazon Basin during the wet and dry season. The measured hygroscopicity parameters (κ_{dry} and κ_{wet}) show relatively good agreement with field data in the dry and wet seasonal period in the Amazon Basin, respectively. This suggests that laboratory-generated mixtures of organic surrogate compounds with ammonium sulfate can be used to represent the chemical composition of ambient aerosols from the Amazon Basin for the purpose of RH-dependent hygroscopicity studies.

Zusammenfassung

Die Hygroskopizität von Aerosol-Nanopartikeln und die damit in Zusammenhang stehenden physikalisch-chemischen Eigenschaften sind für die multiphasenchemischen Prozesse der Erdatmosphäre, die physikalische Chemie und die Materialwissenschaften von entscheidender Bedeutung. Ein Hauptproblem der aktuellen Forschung zur Aerosol-Hygroskopizität ist der technisch bedingte Mangel an Messdaten im Größenbereich von unter 10 nm, die sowohl für die Partikelbildung als auch deren initiales Wachstums sehr wichtig sind. Das Ziel der vorliegenden Arbeit ist es diese technischen Probleme durch den Einsatz eines weiterentwickelten (Nano) Hygroscopicity Tandem Differential Mobility Analyzers (Nano-HTDMA) zu lösen, um die größenabhängige Hygroskopizität von Aerosol-Nanopartikeln mit kleinsten Durchmessern von bis zu 6 nm zu untersuchen.

(1) Im ersten Teil dieser Arbeit wird eine detaillierte Beschreibung des Aufbaus des Nano-HTDMA-Systems vorgestellt. Um die notwendige hohe Präzision bei hygroskopischen Messungen von Aerosol-Nanopartikeln zu ermöglichen, insbesondere im Größenbereich unter 10 nm, wurden umfassende systematische Kalibrierungskriterien für den Nano-HTDMA erstellt und angewandt, einschließlich der Kalibrierung von Nanopartikelgrößen, Mantelluftstrom- und Aerosolstrom-Durchflussraten, DMA-Spannung, und der relativen Feuchte (RH) und Temperatur (T) Sensoren. Nach der Kalibrierung konnte gezeigt werden, dass das Nano-HTDMA-System für Aerosol-Nanopartikel mit kleinsten Durchmessern bis zu 6 nm eine präzise Größenbestimmung mit kleinem Offset (< 1.4 %) zwischen beiden Nano-DMAs aufweist. Zur Aufrechterhaltung der RH-Uniformitäten, die eine vorzeitige Deliqueszenz (Verflüssigung) und einen verzögerten Phasenübergang der Nanopartikel im Nano-DMA2 verhindern, wird außerdem die relative Luftfeuchte des Mantel-Luftstroms mit dem des Aerosol-Luftstroms am Einlass des Nano-DMA2 abgeglichen. Da die Temperatur und die relative Luftfeuchtigkeit eng miteinander verbunden sind, ist der Nano-DMA2 mit seinem Befeuchtungssystem in einer gut isolierten und klimatisierten Kammer platziert, die eine konstante Temperatur aufrechterhält. Mit der Nano-HTDMA-Apparatur wurde das hygroskopische Verhalten von Aerosol-Nanopartikeln zweier anorganischer Substanzen (Ammoniumsulfat und Natriumsulfat) untersucht. Wir haben eine schwache Größenabhängigkeit der relativen Deliqueszenz- und Effloreszenzfeuchten (DRH

bzw. ERH) der Ammoniumsulfat-Nanopartikel beobachtet, aber eine starke Größenabhängigkeit von DRH und ERH der Natriumsulfat-Nanopartikel bis zu einer kleinsten Größe von 6 nm.

(2) Der zweite Teil dieser Arbeit beschäftigt sich mit den hygroskopischen Eigenschaften von organischen Nanopartikeln mit kleinsten Durchmessern bis zu 6 nm (d.h. Levoglucosan und D-Glucose), die mit einem Nano-HTDMA-System untersucht wurden. Levoglucosan ist ein Indikator für Biomasseverbrennung, der einen erheblichen Anteil (16,6–30,9 Massenprozent) der organischen Substanz im $PM_{2,5}$ ausmachen kann. D-Glucose, ein Hydrolyseprodukt aus Zellulose und Levoglucosan, ist eines der wichtigsten Pyrolyseprodukte von Holz. Aufgrund des teilweisen Verdampfens von Levoglucosan mit Durchmessern kleiner als 20 nm im Nano-HTDMA-System, untersuchen wir die Hygroskopizität von Levoglucosan-Nanopartikeln im Größenbereich zwischen 20 bis 100 nm. Für Levoglucosan- und D-Glucose-Nanopartikel mit kleinsten Durchmessern von bis zu 20 nm wird eine schwache Größenabhängigkeit des hygroskopischen Wachstumsfaktors beobachtet, während für D-Glucose-Nanopartikel mit Durchmessern von 6 bis 20 nm eine starke Größenabhängigkeit des hygroskopischen Wachstumsfaktors gefunden wird. Außerdem vergleichen wir die Messungen der Levoglucosan- und Glucose-Nanopartikel mit Modellierungsergebnissen des Extend Aerosol Inorganics Model (E-AIM) bzw. mit der Theorie der idealen Lösung. Die Theorie der idealen Lösung beschreibt die hygroskopischen Wachstumsfaktoren von Levoglucosan- und D-Glukose-Nanopartikeln mit Durchmessern von über 15 nm gut, während die Prognose des E-AIM Modells die gemessenen Wachstumsfaktoren von D-Glukose-Nanopartikeln unter 15 nm gut beschreibt.

(3) Ziel des dritten Teils dieser Arbeit ist die Untersuchung der Hygroskopizität von organischen Surrogat-Verbindungen aus der Biomasseverbrennung und deren Wechselwirkungen mit anorganischen Ammoniumsulfat-Aerosolen mittels Nano-HTDMA. Die organischen Surrogat-Verbindungen stellen eine Auswahl einiger der häufigsten Pyrolyseprodukte der Biomasseverbrennung dar. Wir konnten feststellen, dass Levoglucosan und Huminsäure Aerosol Nanopartikel im gesamten Luftfeuchtebereich von 90 % bis zu 5 % RH graduell Wasser abgeben. Demgegenüber bleiben Aerosol Nanopartikel der 4-Hydroxybenzoesäure im festen Zustand, und weisen während des gesamten Entfeuchtungsprozesses nur eine geringe

Größenschrumpfung auf. Die unter Verwendung des AIOMFAC-Modells (Aerosol Inorganic-Organic Mixtures Functional groups Activity Coefficients), des E-AIM und einer angepassten Hygroskopizitäts-Funktion vorhergesagten Wachstumsfaktoren stimmen im Allgemeinen mit den gemessenen hygroskopischen Wachstumsfaktoren von Levoglucosan überein. Die Verwendung des AIOMFAC- und des E-AIM-Modells ohne Berücksichtigung kristalliner organischer Phasen ist jedoch nicht geeignet, um die Hygroskopizität von 4-Hydroxybenzoesäure zu beschreiben. Darüber hinaus konnten wir verschiedene Auswirkungen dieser organischen Komponenten auf das Hygroskopizitätsverhalten von Gemischen mit Ammoniumsulfat beobachten, abhängig von den Massenanteilen der organischen Verbindungen: (i) Eine Verschiebung der ERH von Ammoniumsulfat zu einer höheren RH bei Anwesenheit von 25 Gew.-% Levoglucosan in der Mischung. (ii) Das Vorhandensein einer Huminsäure-Komponente zeigt keinen signifikanten Einfluss auf die Effloreszenz von AS in gemischten Aerosol-Nanopartikeln. Darüber hinaus führt die Berücksichtigung des Übergangs von fester zu flüssiger Phase von AS sowohl im AIOMFAC- als auch im E-AIM-Modell zu einer guten Übereinstimmung zwischen Modellen und Beobachtungen, wie auch der ERH der AS im gemischten System. Die gemessenen Wachstumsfaktoren der Aerosol-Nanopartikel die Huminsäure und Ammoniumsulfat enthalten wurden durch die Zdanovskii-Stokes-Robinson Relation (ZSR) Beziehung gut vorhergesagt. Schließlich werden Gemische, die organische Surrogate (d.h. Levoglucosan, 4-Hydroxybenzoesäure und Huminsäure) und Ammoniumsulfat mit zunehmenden organischen Massenanteilen enthalten, verwendet um auf vereinfachte Weise die Umgebungsbedingungen des Amazonasbeckens währen der Regen- und der Trockenzeit zu simulieren. Die gemessenen Hygroskopizitätsparameter (κ_{wet} und κ_{dry}) zeigen eine relativ gute Übereinstimmung mit den Felddaten. Dies weist darauf hin, dass im Labor erzeugte Gemische von organischen Surrogat-Verbindungen mit Ammoniumsulfat verwendet werden können, um die chemische Zusammensetzung von atmosphärischen Aerosolen des Amazonasbeckens zum Zweck von RH-abhängigen Hygroskopizitätsstudien darzustelle.

Contents

1. Introduction

1.1 Hygroscopicity of aerosol nanoparticles and its significance in the atmosphere

In the atmospheric aerosol research, hygroscopicity is defined as the ability of aerosol nanoparticles to uptake/release water. The ability of water uptake/release by aerosol nanoparticles mainly depends on relative humidity (RH), temperature, chemical composition, and size. When relative humidity (RH) increases over the crystalline aerosol particles (e.g., ammonium sulfate, sodium chloride), they spontaneously absorb gas-phase water to form aqueous droplets. This process is called deliquescence. Efflorescence is the reverse process of deliquescence. Aqueous aerosol nanodroplets continuously shrink with decreasing RH and finally crystallize with the accompanying evaporation of all remaining water to the gas-phase at a certain RH value. Deliquescence relative humidity (DRH) and efflorescence relative humidity (ERH) are not equal for aerosol nanoparticles due to a hysteresis effect in which nanoparticles at a given RH may be crystalline or aqueous depending on RH history (Martin 2000; Cheng et al., 2015). Note that not all of the pure aerosol nanoparticles exhibit the solid-liquid phase transition in both deliquescence (from low RH to high RH) and efflorescence (from high RH to low RH) mode (Martin, 2000; Cheng et al., 2015; Jing et al. 2016; Biskos et al., 2006a, b, 2007). Instead, some inorganic and organic aerosol nanoparticles (e.g., sodium nitrate, levoglucosan, glucose) absorb or release water gradually as RH increases or decreases. Size dependence of hygroscopicity (e.g., growth factor and phase transition) of nanoparticles was observed in the previous studies (Biskos et al., 2006a, b, 2007). For example, the DRH&ERH, hygroscopic growth factor of 6-nm sodium chloride, for example, differ considerably from large particles.

Hygroscopicity of aerosol nanoparticles has essential implications in the atmosphere. Firstly, hygroscopicity is one of the most important physicochemical properties, which directly determines the size and the physical state of aerosol nanoparticles (Köhler, 1936; Tang, 1996; Martin, 2000). Secondly, the water uptake by aerosol particles affects their optical properties and consequently their impacts on visibility and direct radiative forcing (Cheng et al., 2008, 2009; Burgos et al., 2019). Also, the hygroscopic properties of aerosols determine which a fraction of aerosol particles can effectively act as cloud condensation nuclei (CCN) and thus contribute to the aerosol indirect effect (Pilinis et al., 1995; McFiggans et al., 2006; Wiedensohler et al., 2009). Lastly, the amount of water in the particles under a given condition may control heterogeneous and

multiphase reactions of aerosol particles (Bertram and Thornton, 2009; Rubasinghege and Grassian, 2013; Shiraiwa et al., 2011; Cheng et al., 2016).

1.2 The thermodynamic models for predicting hygroscopicity of aerosol particles

The current thermodynamic models mostly depend on concentration-dependent thermodynamic properties (e.g., water activity, liquid-vapor surface tension). These thermodynamic data are available by either measuring the micrometer-sized particles, bulk solution (Fredenslund et al., 1975; Hansen et al., 1991; Tang and Munkelwitz, 1994; Tang, 1996; Pruppacher et al., 1997; Kreidenweis et al., 2005; Seinfeld and Pandis, 2006), or applying Differential Köhler Analysis (DKA) approach to the measurement results of hygroscopic growth factor of nanoparticles in the different sizes (Cheng et al., 2015). Therefore, using the thermodynamic properties is to predict the hygroscopic growth factor of nanoparticles against relative humidity based on the Köhler equation (1-1) (Köhler, 1936).

$$\frac{RH}{100} = \frac{p_w}{p_w^o} = s_w = a_w exp\left(\frac{4\sigma_{lv}v_w}{RTD_{RH}}\right) = a_w exp\left(\frac{4\sigma_{lv}v_w}{RTD_o g_f}\right) \quad (1\text{-}1)$$

where p_w is the partial pressure of water, p_w^o is the saturation vapor pressure of water. s_w is water saturation ratio. a_w, σ_{lv}, and v_w are the water activity, liquid-vapor surface tension of the solution, the partial molar volume of water in solution, respectively. R is the ideal gas constant and T is the droplet temperature. The hygroscopic growth factor (g_f) is defined by $g_f = D_{RH}/D_o$, where D_{RH} and D_o are particle diameter at a defined RH and a dry RH ($RH < 10\%$), respectively.

(1) Extended Aerosol Inorganics (E-AIM) Model

E-AIM is a thermodynamic equilibrium model for modeling the water activity, liquid-vapor surface tension, and density of aqueous solution containing inorganic and organic components (http://www.aim.env.uea.ac.uk/aim/model3/model3a.php). The universal quasi-chemical functional group activity (UNIFAC) (Fredenslund et al., 1975; Hansen et al., 1991) can be used within the E-AIM model to predict the thermodynamic properties in the aqueous solutions of multifunctional organic compounds (Clegg et al., 2001).

In this thesis, we apply the E-AIM model (modeling water activity, surface tension) to stimulate the hygroscopic growth factor as a function of RH based on Eq. (1-1) and Eq. (1-2) in the equilibrium state of aerosol system.

$$g_f = \left(\frac{\rho_s}{x_s\rho_{sol}}\right)^{\frac{1}{3}} \quad (1\text{-}2)$$

Here, ρ_s and ρ_{sol} are the density of solute and solution, respectively. x_s is the mass fraction of solute.

(2) Ideal Solution Theory

The ideal solution theory assumes that the water activity of an ideal solution containing a non-volatile, non-electrolyte component is equal to the mole fraction of water (i.e., activity coefficient of unity) (Mochida and Kawamura, 2004; Lei et al., 2014; 2018). Also, for an ideal solution, liquid-vapor surface tension of aqueous solution is that of pure water at *T*. The partial molar volume of pure water in the solution is equal to the molar volume of pure water. Thus, the ideal solution theory is used to predict the hygroscopic growth factor of pure organics using the following Eq. (1-3), which defined as a function of molar ratio (x_j), molar mass (M_j), and mass density (ρ_j) of components.

$$GF = \left[\frac{\sum_j \left(x_j M_j \frac{1}{\rho_j}\right)}{\sum_{j,j\neq w}\left(x_j M_j \frac{1}{\rho_j}\right)}\right]^{\frac{1}{3}} \quad (1\text{-}3)$$

(3) Zdanovskii-Stokes-Robinson (ZSR) relation

For the inorganic-organic mixtures, the assumption of the ZSR mixing rule is that the partial volumes of individual components/phases are additive, the *GF* of a mixture, GF_{mix}(RH), can be estimated from the GF_{j} of the pure components *j* and their respective volume fractions, ε_{j}, in the mixture (Malm and Kreidenweis, 1997):

$$GF_{mix} = \left[\sum_j \varepsilon_j \left(GF_j\right)^3\right]^{\frac{1}{3}} \quad (1\text{-}4)$$

(4) Aerosol Inorganic-Organic Mixtures Functional group Activity Coefficients (AIOMFAC) Model

The AIOMFAC model proposed by Zuend et al. (2008, 2011) is a thermodynamic group-contribution model designed to calculate water activity covering inorganic, organic, and organic-inorganic interactions in aqueous solutions over a wide concentration range (http://www.aiomfac.caltech.edu/).

$$GF = \left(\frac{\frac{1}{1-w_w}\sum j \frac{w_j}{\rho_j}}{\left(\sum s \frac{w_s}{\rho_s}\right)_{dry}}\right)^{\frac{1}{3}} \quad (1\text{-}5)$$

Here, the predicted hygroscopic growth factor is the function of mass fraction (w_j), water fraction (w_w), liquid density (ρ_j) of components (j), mass fraction (w_s), and solid

density ρ_s of non-water components (*s*). Note that liquid-vapor surface tension is often assumed to be constant (frequently the value of pure water at *T* is used).

(5) Differential Köhler Analysis (DKA)

The expressions proposed by Cheng et al. (2015), theoretical based on Köhler equation (Köhler, 1936), is determined water activity and liquid-vapor surface tension by measuring hygroscopic growth factors of aerosol nanoparticles in different sizes.

$$a_w = \frac{s_{w1}^{\left(\frac{D_{s1}}{D_{s1}-D_{s2}}\right)}}{s_{w2}^{\left(\frac{D_{s2}}{D_{s1}-D_{s2}}\right)}} \tag{1-6}$$

$$\sigma_{lv} = \left(\frac{A}{D_{s1}} - \frac{A}{D_{s2}}\right)^{-1} (lns_{w1} - lns_{w2}) \tag{1-7}$$

Where s_{w1} and s_{w2} are measured at the same g_f but at different initial dry diameter (D_{s1}, D_{s2}), respectively. Using the DKA method can predict the hygroscopic growth factor combining Eq. (1-1) and Eq. (1-2). Cheng et al. (2015) presented parameterization models for the DKA-derived water activity and the liquid-vapor surface tension of aqueous solution of nanodroplets of ammonium sulfate and sodium chloride, respectively. These parameterizations are functions of solute concentration. In addition, we list the parameterizations of water activity and liquid-vapor surface tension of ammonium sulfate solution widely used in the communities. According to different measurements of micrometer-sized particles, bulk solution, and nanoparticles with different sizes, the validated range of these parameterization models varies as shown in Table 1-1. Also, Figure 1-1 shows that literature data of water activity and liquid-vapor surface tension are compared with water activity and liquid-vapor surface tension parameterization models. It shows that data of water activity and liquid-vapor surface tension derived from measurements of the micrometer-sized particles or bulk solution of ammonium sulfate are limited ffrom bulk solution to highly supersaturated solution. By application the DKA method to the measured results of hygroscopic growth factor of ammonium sulfate with diameters from 6 to 60 nm, water activity and liquid-vapor surface tension with molality is up to b ~ 160 mol kg^1, which extend to the highly supersaturated concentration range. Also, the DKA-derived data are consistent with the previous data of water activity derived from micrometer-sized particle or bulk solution measurements. These parameterization models (e.g., AIM, TM, KD, SP, PK) for water activity and liquid-vapor surface tension available from the previous studies are in good agreement with measured data from bulk solutions to the saturated

concentration but deviated from DKA-derived data of water activity and liquid-vapor surface tension in the highly supersaturated concentration range. Therefore, the discrepancies between measurements and previous model predictions ((e.g., AIM, TM, KD, SP, PK) of the hygroscopic behavior of nanoparticles are due to a lack of thermodynamic parameters in the highly supersaturated concentration range. The application of parameterization models of DKA-derived data of water activity and liquid-vapor surface tension closes the gap between measurements and model predictions (Cheng et al., 2015).

Table 1-1.Thermodynamic parameterizations in the concentration range

Parameter (reference)	Parametrization model	Solute concentration range
DKA a_w (Cheng et al., 2015)	$a_w = \frac{46.29 + 26.42x + 12.51x\text{^}2}{80.77 + 103.6x + 55.09x^2 + x\text{^}3}$ $x = \frac{b - 13.02}{17.15}$	$0 < x_s < 0.96$
KD a_w (Kreidenweis et al., 2005)	$g_f = \left(1 + (2.42848 - 3.85261a_w + 1.88159a_w^2)\frac{a_w}{1 - a_w}\right)$	$0 < x_s < 0.3$
TM a_w (Tang and Munkelwitz, 1994; Tang, 1996)	$a_w = 1 + \sum_q A_q(100x_s)^q$ $A_1 = -2.175 \times 10^{-3};\ A_2 = 3.113 \times 10^{-5};$ $A_3 = -2.336 \times 10^{-6}; A_4 = 1.412 \times 10^{-8};$	$0 < x_s < 0.78$
DKA σ_{lv} (Cheng et al., 2015)	$\sigma_{lv} = 0.072 + \sum C_i x_s^i$ $C_1 = 0.04070;\ C_2 = -0.4627;$ $C_3 = 3.799;\ C_4 = -14.46;$ $C_5 = 27.80; C_6 = -24.63; C_7 = 8.016$	$0 < x_s < 0.96$
SP σ_{lv} (Seinfeld and Pandis, 2006)	$\sigma_{lv} = \sigma_w + 2.17 \times 10^{-3}C_s$ $\sigma_w = 0.0761 - 1.55 \times 10^{-4}(T - 273.15)$	$0 < x_s < 0.78$
PK σ_{lv} (Pruppacher et al., 1997)	$\sigma_{lv} = 0.072 + \frac{2.34 \times 10^{-2}x_s}{1 - x_s}$	$0 < x_s < 0.78$

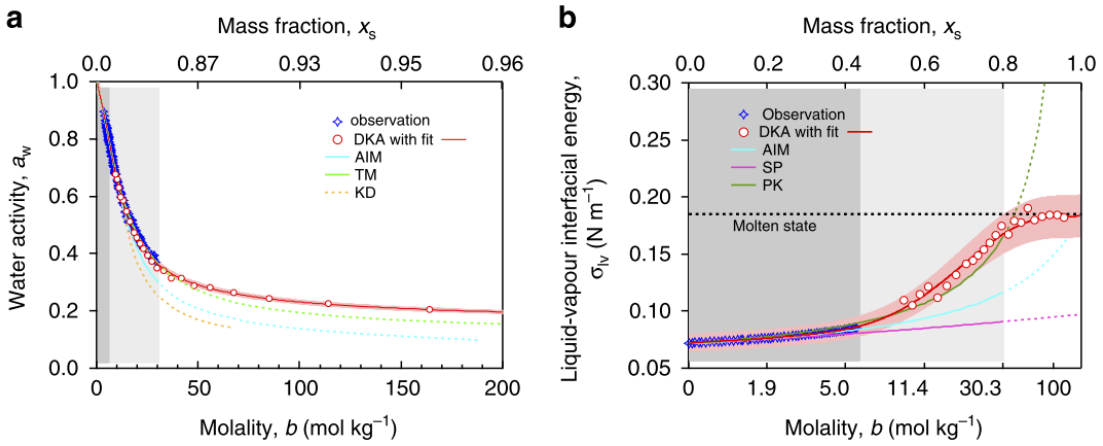

Figure 1-1: Concentration-dependent thermodynamic properties of ammonium sulphate solution. (a, b) Water activity (a_w, on a mole fraction basis) and liquid-vapor interfacial energy (σ_{lv}) are plotted against solute molality (b) and mass fraction (x_s). The DKA-derived a_w and σ_{lv} (red open circles) are compared with observations (blue stars), AIM (Aerosol Inorganic Model, blue line), and other parameterizations for a_w (TM=Tang-Munkelwitz, green line; KD=Kreidenweis, orange line) and σ_{lv} (PK=Pruppacher-Klett, dark green line; SP=Seinfeld-Pandis, purple line) and the best fit of DKA results (red lines). Dashed lines indicate extrapolation beyond validated concentration range. Red shaded areas indicate the uncertainties in the DKA retrieval, estimated by Monte Carlo analyses. The dark and light grey shaded areas mark the sub-saturated and saturated concentration with respect to bulk solution and supersaturated concentration before efflorescence of supermicrometre droplets, respectively. The white area marks the highly supersaturated concentration where the a_w data are not available in the literature. Permission with Cheng et al. (2015).

1.3 Techniques for investigating the hygroscopicity of aerosol particles

Table 1-2 shows specific techniques commonly used in laboratory over the past ten years for measuring the hygroscopic properties of aerosol particles under subsaturation conditions (i.e., RH < 100 %) in different sizes. These techniques can be mainly applicable to measure particle size (D_p): (i) $D_p > 1$ μm; (ii) 10 nm < $D_p < 1$ μm; and (iii) $D_p < 10$ nm.

The early laboratories for hygroscopicty measurements focus on the deposited micrometer-sized particles with increasing RH with spectroscopy (Dong et al., 2009; Zhao et al., 2013). Accordingly, experimental techniques are developed to characterize their physical state, morphology, phase transition (solid-liquid, liquid-liquid phase separation), mixing state, and chemical composition of aerosol articles. For example, optical microscopy is widely used to investigate solid-liquid and liquid-liquid phase separation of aerosol particles during the humidity cycle. Scanning electron microscopy (SEM) and transmission electron microscopy (TEM) are used to quantitatively measure the physical properties of aerosol particles with diameter from micron down to nanoscale. The use of Fourier transform infrared spectrometer (FT-IR) (Zhao et al., 2016) and Raman spectroscopy (Dong et al., 2009) is to measure the hygroscopic growth of aerosol particles on the molecular level by vibrational spectroscopy (i.e., Raman and infrared spectroscopy). Subsequently, techniques are developed for capturing and levitating a single charged micrometer particle in an electrodynamic balance (EDB) and observing changes in particle mass as the environmental RH (Chan and Chan, 2003; Chan et al., 2008). However, the more recent development of optical tweezers (3D trapping, in which axial and lateral forces are much greater than gravitational forces, enables high accuracy and precision in size measurements (Reid et al., 2011; Rickards et al., 2013). Also, the atomic force microscopy (AFM) (Estillore et al., 2017) is employed to directly measure the three-dimension morphology, phase transition, and height of particles with diameter down to 10 nm. Different from the single particle measured by the optical tweezers and the AFM, the hygroscopicity tandem differential mobility analyzer (HTDMA) systems are frequently used to measure the sub-micro assembly of particles at a given RH, then further calculate the particle diameter growth factor (Rader and McMurry, 1986; Mikhailov et al., 2004, 2008, 2009, 2020; Cheng et al., 2008, 2009; Eichler et al., 2008; Stock et al., 2011; Let et al., 2014, 2018; Hong et al., 2014, 2015). In the sub-20 nm size range, however,

HTDMA setup is difficult or even impossible to maintain the sizing accuracy and a small sizing offset between two DMAs, especially in the sub-10 nm range. Therefore, the development of a nano-HTDMA apparatus enables the high accuracy and precision of hygroscopicity measurements of sub-20 nm aerosol nanoparticles.

Using these techniques, most of the early lab studies focused on the hygroscopic behavior of the known-composition aerosol particles, including deliquescence, efflorescence of pure components, and the effect of organics on the deliquescence and efflorescence of these inorganic components in the mixtures.

Table 1-2. Techniques for investigating the hygroscopic behavior of aerosol particles

Techniques (reference)	Size range	Brief introduction
Optical microscopy (Tang et al., 2019)	≥10 um	Particles deposited on the glass slide were monitored using a microscope, and particle images were recorded using a charge-coupled device camera with adjusting the RH.
Fourier transform infrared spectrometer (FT-IR) Raman spectroscopy (Dong et al., 2009; Zhao et al., 2013)	≥10 um	Characterizing the molecular vibrations and their shift of a single particle deposited on the substrate by water absorption or release when RH increases or decreases.
Electrodynamic balance (EDB) (Chan and Chan, 2003; Chan et al., 2008)	≥10 um	Levitating a single charged particle by a combination of alternating and direct current (AC and DC) electric fields. When increasing or decreasing RH, the mass of a particle undergoing condensation/evaporation is proportional to the DC balancing change. The mass change of solute in a particle is determined by the ratio of DC balancing voltage to that in the dry condition.
Optical tweezers (AOT) (Reid et al., 2011; Rickards et al., 2013)	≥400 nm	The continuous laser light beams are used to create a single beam gradient force optical trap to capture a single charged particle of aerosol flow through a trapping chamber.
Atomic force microscopy (AFM) (Estillore et al., 2017)	≥10 nm	Particles are deposited in a controlling-humidity chamber and their height and phase image can be measured by a molecule force probe.
Scanning electron microscopy (SEM) and transmission electron microscopy (TEM) (Tang et al., 2019)	≥10 nm	Producing morphology, mixing state images of particles in the vacuum condition by scanning the surface with a focused beam of electrons.
Hygroscopicity tandem differential mobility analyzer (HTDMA) (Rader and McMurry, 1986; Mikhailov et al., 2004, 2008, 2009, 2020; Cheng et al., 2008, 2009; Eichler et al., 2008; Stock et al., 2011; Let et al., 2014, 2018; Hong et al., 2014, 2015)	20 nm-1 μm	Measuring the diameter of aerosol particles at different RHs and further obtaining the hygroscopic growth factor of aerosol particles with dimeter above 20 nm, (i.e., the hygroscopic growth factor is defined as the ratio of diameter after humidification to that in the dry condition)
Nano-hygroscopicity tandem differential mobility analyzer (nano-HTDMA) (Biskos et al., 2006a, b, 2007)	3 nm-20 nm	Under high accuracy and stability measurement condition, the change in diameter of aerosol particles is measured at different RHs, especially in the sub-10 nm sizing range.

1.4 Research objectives and questions to be solved

(1) As discussed above, knowledge of hygroscopicity of sub-10 nm aerosol nanoparticles is very little (Hämeri et al., 2000, 2001; Biskos et al., 2006a, b, 2007; Wang et al., 2015; Giamarelou et al., 2018). For example, Biskos et al. (2006a, b, 2007) studied the hygroscopicity of ammonium sulfate and sodium chloride nanoparticles with diameters down to 6 nm using a hygroscopic tandem nano-differential mobility analyzer. In addition, Wang et al. (2015) designed a nano-cloud concentration nuclei counter for measuring size-resolved hygroscopicity and inferring chemical composition of nanoparticles smaller than 10 nm. As we notice, excluding the apparatus designed by Wang et al. (2015), the other studies aforementioned were all focused on using an HTDMA system. However, current knowledge of the hygroscopicity of nanoparticles is restricted by the limitations of HTDMA techniques. (1) An accurate sizing and a small sizing offset between two DMAs. To obtain the accurate growth factor of nanoparticles, the particle sizing and sizing offset between two DMAs should be within ±2-3% (Massling et al., 2011; Zhang et al., 2016), which is however very difficult to maintain for the sub-10 nm size range. Furthermore, a large sizing offset may lead to significant error in the measured hygroscopic growth factor based on error propagation (Mochida and Kawamura, 2004). The particle sizing crucially depends on the sheath flow rates and DMA voltages in the HTDMA system. Uncertainties in sheath flow rates and DMA voltages will increase as size decreases, which directly influences the sizing accuracy and further results in a big sizing offset between two DMAs. For example, calibration of the DMA voltage with low accuracy of ± 1% can lead to ~5.4% of the sizing offset between two DMAs for 8-nm ammonium sulfate nanoparticles. (2) Highly stable measurement conditions in the whole HTDMA system are vital to maintain a small perturbation with regard to temperature, RH, and pressure for investigating the hygroscopic behavior of nanoparticles. E.g., a 0.8 K fluctuation of the experimental temperature can result in a 4% difference in RH (0-90 %) during the measurements. Due to the RH/temperature non-uniformities within DMA2 system, the pre-deliquescence and non-prompt phase transition of aerosol nanoparticles (e.g., ammonium sulfate, sodium sulfate) were observed by previous studies (Hämeri et al., 2000, 2001; Gysel et al., 2002; Gao et al., 2006; Duplissy et al., 2009; Mikhailov et al., 2009, 2020; Wu et al., 2011). The results of DRH and ERH of ammonium sulfate nanoparticles show non-uniformities in the previous studies. For example, as shown in

Figure 1-2, the DRH of 50-nm ammonium sulfate is at 78% RH, which smaller than other previous studies (DRH=80 %) (Biskos et al., 2006b; Hämeri et al., 2000). Also, the non-prompt phase transition of ammonium sulfate occurs for 8-nm ammonium sulfate (Hämeri et al., 2000).

Therefore, in the first objective of thesis, we present the design of a nano-HTDMA setup that can measure the accurate phase transition and hygroscopic growth factor of aerosol nanoparticles with diameters less than 10 nm. Also, we discuss in detail how to maintain the accurate sizing, the small sizing offset of two nano-DMAs, and the highly stable measurement conditions. Finally, we apply the nano-HTDMA system to study the size dependence of hygroscopicity of aerosol nanoparticles of two specific inorganic compounds (e.g., ammonium sulfate and sodium sulfate) for sizes down to 6 nm.

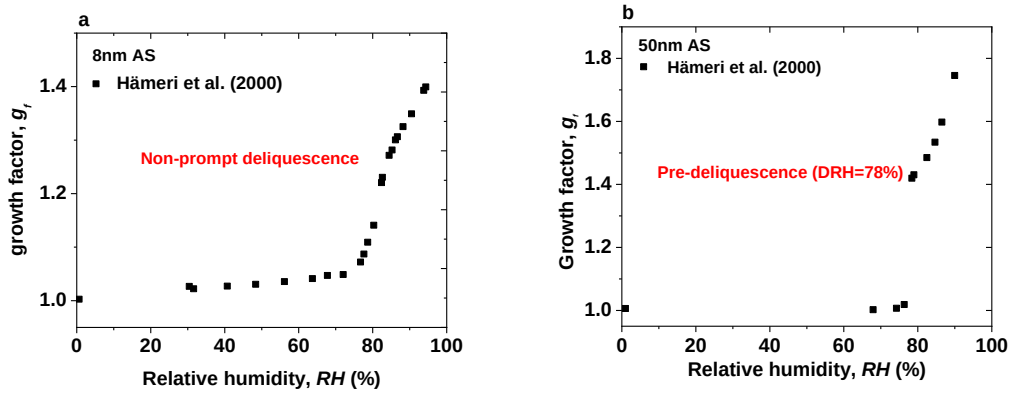

Figure 1-2: (a) The non-prompt deliquescence of 8-nm ammonium sulfate (AS); **(b)** the pre-deliquescence of 50-nm ammonium sulfate. The hygroscopic results of ammonium sulfate (black square: deliquescence mode) are from Hämeri et al. (2000).

(2) Investigation of hygroscopicity of sub-10 nm organic aerosol nanoparticles is still lacking in the literature. The previous studies have been focused on investigating hygroscopicity of organic aerosol particles in accumulation modes and super-micron size ranges (Chan et al., 2005; Peng et al., 2010). Biomass burning is one of the most important sources of anthropogenic atmospheric organic aerosols. Particles in biomass burning smoke enriched with hygroscopic organics account for up to 99% of water soluble organic carbon (Psichoudaki and Pandis, 2013). These hygroscopic aerosols nanoparticles determine which fraction of aerosol nanoparticles can efficiently act as cloud condensation nuclei (CCN) and form the cloud droplets. Levoglucosan is both biomass burning tracer compound and the most abundant compositions in wood burning aerosols, D-glucose is major pyrolysis products of wood. They show the significant hygroscopic behavior in the biomass burning (Mochida and Kawamura, 2004). Thus, to study their interaction with water is essential to improve the understanding of biomass burning aerosol formation, transportation, and climate. However, due to the Kelvin effect, some small organic aerosol nanoparticles are more likely to evaporate in the HTDMA system. Also, there are very few thermodynamic data in the highly supersaturated concentration for organics nanodroplets (Clegg et al., 1998; Bhandari and Bareyre, 2003; Chan et al., 2005; Koehler et al., 2006; Peng et al., 2010) such as levoglucosan and D-glucose. This may lead to the discrepancy between measurement results and thermodynamic model prediction.

Therefore, in the second objective of thesis, we investigate the size dependent hygroscopicity of levoglucosan and glucose nanoparticles in size down to 6 nm using a nano-HTDMA. In addition we use the Extended Aerosol Inorganic Model (E-AIM) (Clegg et al., 2001; Clegg and Seinfeld, 2006; available online: http://www.aim.env.ac.uk/aim/aim.php) and the ideal solution theory to predict the hygroscopic growth of levoglucosan and glucose aerosol nanoparticles with diameters down to 6 nm.

(3) Most of the water-soluble organics in the biomass burning have been found to be internally mixed with ubiquitous inorganic compounds (e.g., ammonium sulfate and sodium chloride) (Saxena et al., 1995; Shi et al., 2012; Lei et al., 2014, 2018). Hygroscopicity measurements of real biomass burning aerosol particles is limited due to the complex chemical organic compositions observed in the Amazon and other regions (Artaxo et al., 2002; Decesari et al., 2006; Rissler et al., 2006). One way is to

identify a set of model substances that may be representative in reproducing the hygroscopic behavior of water-soluble organic fraction of the real aerosol particles (Rissler et al., 2010; Wu et al., 2011; Zamora et al., 2011). Levoglucosan, 4-hydroxybenzoic acid, and humic acid have been represented as common water-soluble compound classes from biomass burning (Lei et al., 2014, 2018), which is a selection of some of the most abundant pyrolysis products of biomass burning (Mochida and Kawamura, 2004; Lei et al., 2014, 2018). There are few studies, however, to systematically investigate their interactions with water molecules and further their effect on the efflorescence of inorganic components in the mixtures. Also, current thermodynamic models such as the E-AIM, the ZSR, and the AIOMFAC models are commonly used for predicting the hygroscopic growth of organic/inorganic mixtures (Zuend et al., 2008, 2011; Peng et al., 2010; Lie et al., 2014, 2018). However, providing accurate thermodynamic model predictions of the hygroscopic growth behavior of mixed organic-inorganic systems remains a challenging problem. Firstly, these thermodynamic models have different assumptions for hygroscopic growth factors of mixtures. For example, the ZSR relation assumes that water uptake of each of the components of mixed organic-inorganic particles can be treated independently at a given RH. Secondly, at a different RH, especially at moderate and low RH levels, particles become highly supersaturated in concentration. This may lead to a step-like or gradual crystallization, which mainly depends on the organic/inorganic mass ratio and the chemical nature of the mixture constituents. This range of measurement-model comparisons is highly difficult to reach consistency.

Therefore, in the third objective of thesis, we investigate hygroscopic growth factors of organic surrogate compounds representing biomass burning and mixed organic–inorganic aerosol particles in the dehumidification process. Also, the use of the ZSR mixing rule, the E-AIM model, and the AIOMFAC model to predict the measured hygroscopicity behavior of mixed aerosol particles, respectively. Afterwards, the difference between model predictions and measurements would be explained in details.

2. Nano-hygroscopicity tandem differential mobility analyzer (nano-HTDMA) for investigating hygroscopic properties of sub-10 nm aerosol nanoparticles

This work has been published as Lei et al. (2020):

Lei, T., Ma, N., Hong, J., Tuch, T., Wang, X., Wang, Z., Pöhlker, M., Ge, M., Wang, W., Mikhailov, E., Hoffmann, T., Pöschl, U., Su, H., Wiedensohler, A., and Cheng, Y.: Nano-hygroscopicity tandem differential mobility analyzer (nano-HTDMA) for investigating hygroscopic properties of sub-10 nm aerosol nanoparticles, Atmospheric Measurement Techniques, 13, 5551–5567, 2020

I am the first-author of this work and my contribution to this work includes modifying and advancing the basic hygroscopicity tandem differential mobility analyzer (HTDMA) system into the nano-HTDMA for measuring the hygroscopic properties of aerosol nanoparticles in the sub-10 nm size range, performing the experiments, analyzing all the data, making all the figures and tables, and writing the manuscript together with Dr. Cheng and Dr. Su.

The following text, figures, and tables quoted (within "") from page 17 to page 63 are exactly the same as published on Lei et al. (2020) which is cited on page 16.

"**Abstract.** Interactions between water and nanoparticles are relevant for atmospheric multiphase processes, physical chemistry, and materials science. Current knowledge of the hygroscopic and related physicochemical properties of nanoparticles, however, is restricted by the limitations of the available measurement techniques. Here, we present the design and performance of a nano-hygroscopicity tandem differential mobility analyzer (nano-HTDMA) apparatus that enables high accuracy and precision in hygroscopic growth measurements of aerosol nanoparticles with diameters less than 10 nm. Detailed methods of calibration and validation are provided. Besides maintaining accurate and stable sheath and aerosol flow rates (±1%), high accuracy of differential mobility analyzer (DMA) voltage (±0.1%) in the range of ~0-50 V is crucial for achieving accurate sizing and small sizing offsets between the two DMAs (<1.4%). To maintain a stable relative humidity (RH), the humidification system and the second DMA are placed in a well-insulated and air conditioner housing (±0.1K). We also tested and discussed different ways of preventing predeliquescence in the second DMA. Our measurement results for ammonium sulfate nanoparticles are in good agreement with Biskos et al. (2006b), with no significant size effect on the deliquescence and efflorescence relative humidity (DRH and ERH, respectively) at diameters down to 6 nm. For sodium sulfate nanoparticles, however, we find a pronounced size dependence of DRH and ERH between 20 and 6 nm nanoparticles.

1 Introduction

The climatic effects of aerosol nanoparticles have attracted increasing interest in recent years (Wang et al., 2016; Andreae et al., 2018; Fan et al., 2018). Interactions between water and nanoparticles are relevant for atmospheric multiphase processes, physical chemistry, and materials science (Zheng et al., 2015; Cheng et al., 2015, 2016). Aerosol nanoparticles in the atmosphere mostly originate from new particle formation, and a fraction of these nanoparticles could potentially grow into sizes that enables them to efficiently act as cloud condensation nuclei and, thus, to change the contributions of aerosol nanoparticles to climate forcing (Lihavainen 2003; Wiedensohler et al., 2009; Sihto et al., 2011; Kirkby et al., 2011; Keskinen et al., 2013; Dunne et al., 2016; Kim et al., 2016). These processes strongly depend on the chemical composition and

physicochemical properties of these nanoparticles (Köhler, 1936; Su et al., 2010; Wang et al., 2015; Cheng et al., 2015). One of the most important physicochemical properties of nanoparticles is their hygroscopic behavior, which describes their ability to take up water, and it can differ significantly from that of larger particles (Hämeri et al., 2000, 2001; Gao et al., 2006; Biskos et al., 2006a, b, 2007; Cheng et al., 2015).

To understand and predict the hygroscopic properties of nanoparticles, current thermodynamic models mostly rely on the concentration-dependent thermodynamic properties (such as water activity and interfacial energy) derived from the measurements of large aerosol particles or even bulk samples (Tang and Munkelwitz, 1994; Tang 1996; Pruppacher and Klett, 1997; Clegg et al., 1998). They are thus difficult or impossible to apply to describe the hygroscopic behavior of sub-10 nm nanoparticles, which can often be supersaturated in concentration compared to bulk solutions (Cheng et al., 2015). Furthermore, the nanosize effect on these properties may also need to be considered (Cheng et al., 2015). The lack of such data hinders the understanding and accurate simulation of the interaction of water vapor and atmospheric nanoparticles. In addition, by knowing the hygroscopicity of newly formed nanoparticles, one can infer the involving chemical species (e.g., organic ratio) in particle formation and initial growth (Wang et al., 2010), which is otherwise difficult and highly challenging to measure directly (Wang et al., 2010; Ehn et al., 2014). Hence, measuring the hygroscopicity of nanoparticles is essential for improving our understanding of aerosol formation, transformation, and their climate effects.

Different techniques have been employed to characterize the hygroscopic properties of aerosol particles in different sizes (Fig. S1; Tang et al., 2019), such as the Fourier transform infrared spectrometer (FTIR; Zhao et al., 2006), Raman spectroscopy (Dong et al, 2009), electrodynamic balance (EDB; Chan and Chan, 2003, 2005; Chan et al., 2008), optical tweezers (Reid et al., 2011; Rickards et al., 2013), a hygroscopicity tandem differential mobility analyzer (HTDMA; e.g., Rader and McMurry, 1986; Mikhailov et al., 2004; 2008; 2009; Biskos et al., 2006a, b, 2007; Cheng et al., 2008, 2009; Eichler et al., 2008; Stock et al., 2011; Hong et al., 2014, 2015; Lei et al., 2014; 2018; Mikhailov and Vlasenko, 2020), and atomic force microscopy (AFM; Estillore et al., 2017). Using these techniques, most of the early laboratory studies focused on the hygroscopic behavior of particles in the accumulation modes and super-micron size range, including deliquescence, efflorescence of pure components and the effect of

organics on the change or suppression of the deliquescence and efflorescence of these inorganic components in mixtures.

For nanoparticles with diameters down to sub-10 nm, there are, however, only very few studies that have attempted to investigate their interactions with water molecules; these studies mainly utilized the setup with humidified tandem differential mobility analyzers (DMAs) (Hämeri et al., 2000, 2001; Sakurai et al., 2005; Biskos et al., 2006a, b, 2007; Giamarelou et al., 2018). In Table S1, we summarized the measured DRH and ERH of ammonium sulfate nanoparticles in the size range from 6 to 100 nm, using HTDMAs. In the studies, the results of the observed DRH and ERH and prompt or nonprompt phase transitions of ammonium sulfate nanoparticles, however, do not show universal agreement. The technical challenges in HTDMA measurements, especially in the sub-10 nm size range, mainly relate to the: (1) accurate sizing and small sizing offset of the two DMAs and (2) highly stable measurement conditions in the whole system. A large sizing offset between the two DMAs may lead to significant errors in the measured growth factor based on error propagation (Mochida and Kawamura, 2004). Massling et al. (2011) and Zhang et al. (2016) suggested that to achieve good hygroscopic growth factor of nanoparticles, the sizing offset of the two DMAs should be within ±2-3%, which is, however, very difficult to maintain for the sub-10 nm size range. To accurately measure phase transition (e.g., DRH and ERH), a highly stable measurement condition is essential, especially for maintaining a small temperature perturbation in the humidification system and inside the second DMA to prevent predeliquescence. For example, a 0.8 K fluctuation in the experimental temperature during the measurement can result in a 4% difference in RH (0-90%) inside the humidified DMA (Hämeri et al., 2000), leading to an inaccurate determination of the phase transition. Another problem is the prompt versus nonprompt phase transition. Although the effects of impurities on the phase transition of aerosol nanoparticles (Biskos et al., 2006a; Russell and Ming, 2002) may be one possible reason for the previously observed nonprompt phase transitions (e.g., Hämeri et al., 2000), the apparent nonprompt phase transition of aerosol nanoparticles has been thought to be mainly due to the inhomogeneity of relative humidity (RH) and temperature in the humidified DMA during measurements (Biskos et al., 2006b; Bezantakos et al., 2016). Moreover, the hygroscopic measurements are, in general, difficult for nanoparticles with diameters below 20 nm due to high diffusion losses of nanoparticles (Seinfeld and Pandis, 2006).

In this study, we present the design of a nano-HTDMA setup that enables high accuracy and precision in the hygroscopic growth measurements of aerosol nanoparticles with diameters less than 10 nm. Detailed methods of calibration and validation are provided. We discuss in detail how to maintain the good performance of the system by minimizing uncertainties associated with the stability and accuracy of RH, temperature, voltage for nanoparticle classification, and sheath and aerosol flows in the DMA systems. We then apply the nano-HTDMA system to study the size dependence of the deliquescence and the efflorescence of aerosol nanoparticles of two specific inorganic compounds (e.g., ammonium sulfate and sodium sulfate) for sizes down to 6 nm.

2. Methods

2.1 Nano-HTDMA system

We designed a nano-HTDMA system to measure the aerosol nanoparticle hygroscopic growth factor (g_f), especially aiming for accurate measurements of the phase transition and hygroscopic growth factor for nanoparticles in the sub-10 nm size range. Here, g_f is defined as the ratio of the mobility diameters of nanoparticles after humidification ($D_m(RH)$) to those in the dry condition (D_m(< 10% RH); see SI. S1. Eq. (S1)). As presented in Fig. 1, the nano-HTDMA is comprised of three main components, including two nano-differential mobility analyzers (nano-DMA; TROPOS; model no. Vienna-type short DMA; Birmili et al., 1997), an ultrafine condensation particle counter (CPC, TSI; model no. 3776), and a humidification system. Table 1 shows the technical specification, where the DMA system, humidification system, and temperature system of the three HTDMAs setup are compared to the systems of Biskos et al. (2006b), Hämeri et al. (2000), and this study.

In our setup (Fig. 1), the first nano-DMA (nano-DMA1) is used to produce quasi-monodisperse nanoparticles at a desired dry diameter. The flow rate of the closed-loop sheath flow in the nano-DMA1 is maintained at 10 l min^{-1}. The ratio of sheath flow to aerosol flow is 10:1.5. The sheath flow is dried in parallel to RH below 10% by two custom-built Nafion dryers (TROPOS; model no. ND.070). The quasi-monodisperse nanoparticles produced by nano-DMA1 then enter the humidification system, which can be set to deliquescence mode (from low RH to high RH for measuring deliquescence) or efflorescence mode (from high RH to low RH for measuring efflorescence). In the deliquescence mode, dry nanoparticles are humidified by a Nafion

humidifier (NH-1, TROPOS; model no. ND.070; length 60 cm) to a target RH. In the efflorescence mode, nanoparticles are first exposed to a high RH condition (~97% RH) in a Nafion humidifier (NH-2, Perma Pure; Model no. MH-110; length 30 cm) and then dried to a target RH through NH-1. The humid flow in the outer tube of NH-1 is a mixture of high-humidity air produced with a custom-built Gore-Tex humidifier and heater (GTHH; TROPOS; inner radius 1.5 cm and length 30 cm) and dry air in variable proportions. To have precise control of the aerosol RH, the flow rates of the humid and dry air are adjusted with a proportional-integral-derivative (PID) system, including two mass flow controllers (MFC; MKS; model no. MF1) and an RH sensor (Vaisala; model no. HMT330) downstream of NH-1.

The residence time is ~5.4 s in the NH-1 for both the deliquescence and the efflorescence modes. Many groups have reported that the residence time of a few seconds is sufficient for reaching equilibrium to measure the hygroscopic growth or shrink of inorganic salt particles, e.g., ammonium sulfate and chloride sodium (Chan and Chan, 2005; Duplissy et al., 2009; Lei et al., 2014, 2018; Giamarelou et al., 2018). More specifically, Kerminen (1997) estimated the time for reaching the water equilibrium to be between 8 x 10^{-6} s and 0.005 s for 100 nm nanoparticles at 90% RH at 25°C, with accommodation coefficients from 0.001 to 1, respectively. In our study, we measured the inorganic aerosol nanoparticles with diameters from ~100 nm down to 6 nm, thus, the equilibrium time should be even shorter as the nanoparticle size decreases (Table. S2). In NH-2, the residence time is ~0.07 s for the deliquescence of inorganic aerosol nanoparticles at very high RH conditions (~97% RH), which is much longer than the time estimated for the phase transition by Duplissy et al. (2009; of the order of a few milliseconds) and Raoux et al. (2007; of the order of a few nanoseconds). In addition, we have tested a longer NH-2 (Perma Pure; model no. MH-110; length 121 cm) in the efflorescence mode, and no significant difference in measured growth factors is found, indicating that the residence time in NH-1 and NH-2 should be sufficient.

The number size distribution of the humidified nanoparticles is measured with a combination of the second nano-DMA (nano-DMA2) and the ultrafine CPC. Similar to Biskos et al. (2016b), a multiple Nafion humidifier (NH-3; Perma Pure; model no. PD-100) is used in our nano-HTDMA system to rapidly adjust the RH of the sheath flow of nano-DMA2. The sheath flow is fed into the outer tube of the NH-3 to minimize its pressure drop. The RH of humid flow in the inner tube of NH-3 is controlled with a

similar PID system to that of NH-1. An RH sensor (Vaisala; model no. HMT330) downstream of NH-3 is used to provide feedback to the PID system. In our nano-HTDMA system, a dew point mirror (DPM; Edgetech; model no. DPM-99) is placed in the excess flow line to measure the RH and temperature of the excess flow of the nano-DMA2. During the operation, the difference between sheath flow RH and aerosol flow RH was maintained within ±1% (see more details in Section 2.2).

The sheath flow is maintained at the set flow rate with a PID-controlled recirculation blower (RB; Ametek; series Minispiral). Prior to every size scan, the sheath flow rate of the nano-DMA2 is adjusted by the PID system according to the measurement of a mass flow meter (MFM; TSI; series 4000) in the sheath flow line. In order to minimize the pressure drop along the recirculating sheath flow loop, a low flow resistance MFM and hydrophobic filter (HF; Whatman; model no. 6702-3600) are used. A heat exchanger (HE; Ebm-papst; model no. 4414FM) is installed downstream of the RB to minimize the temperature perturbation in the sheath flow by the heat generated in the RB.

As mentioned before, temperature nonuniformity is the main contributor to the fluctuation of RH within humidified DMA. A temperature difference within nano-DMA2 is unavoidable mainly due to temperature difference between the inner electrode and the rest of nano-DMA2 parts and/or the temperature difference between aerosol and sheath flow (Duplissy et al., 2009; Bezantakos et al., 2016). As shown in Fig. 1, in order to investigate and monitor the temperature difference within nano-DMA2 during measurements, a temperature sensor (Thermo Electron; model no. Pt100) is placed at the inlet of the sheath flow, and the temperature of sheath excess flow is monitored by the DPM. Note that a DPM should be installed as close as possible to the nano-DMA2 in the excess flow to better represent the conditions inside the nano-DMA2, such as temperature and RH (Wiedensohler et al., 2012). In addition, the temperature of the aerosol flow is monitored at the inlet of the aerosol flow of nano-DMA2.

Moreover, to maintain a stable environment that is required for the growth factor measurements, a nano-DMA2, with its sheath flow humidification system, is placed in a well-insulated housing chamber (marked with yellow dashed lines in Fig. 1). An air conditioner (Telemeter Electronic GmbH; model no. TEK-1004-RR-24-IP55) is installed inside the housing to maintain a constant temperature (292.15±0.1 K), which is set to be ~1 K lower than the constant laboratory temperature (293 K) in order to

achieve high RH (~90%) inside nano-DMA2.

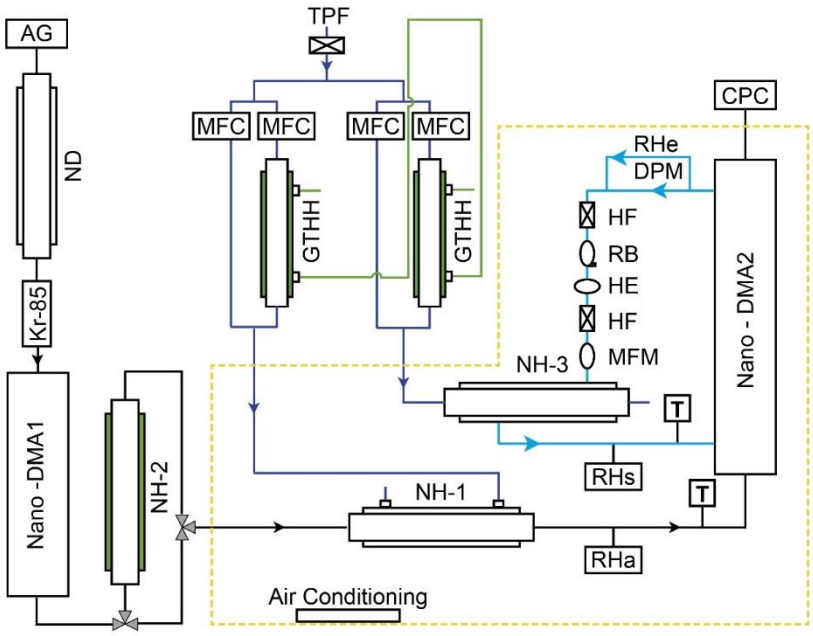

Figure 1. Experimental setup of the nano-HTDMA. Note: AG - aerosol generator (aerosol atomizer or electrospray); ND - Nafion dryer; Kr-85 - Krypton source aerosol neutralizer; Nano-DMA - nano differential mobility analyzer; TPF - total particle filter; HF - hydrophobic filter; MFC: mass flow controller; MFM - mass flow meter; RB - recirculation blower; DPM - dew point mirror; GTHH - Gore-Tex humidifier and heater; NH - Nafion humidifier; HE - heat exchanger; CPC - condensation particle counter; black line - aerosol line; blue line - sheath line; royal blue line - humidified air; green line – Milli-Q water (resistivity of 18.2 MΩ cm at 298.15 K). RH_a and RH_s (measured by RH sensors) represent the relative humidity (RH) of aerosol and sheath flow in the inlet of nano-DMA2, respectively. RH_e (measured by dew point) represents the RH of excess air. *T* represents the temperature of aerosol and sheath flow in the inlet of nano-DMA2, respectively.

2.2 Calibration of nano-HTDMA

The purpose of this study is to design and build a nano-HTDMA system that is able to measure the hygroscopic properties of nanoparticles, especially in the sub-10 nm size range. A small perturbation in the measurement conditions may lead to large biases in the results. Hence, in order to provide high-quality hygroscopicity measurements of nanoparticles, systematic calibration of the nano-HTDMA should be conducted regularly to ensure the accuracy and stability of the measurement conditions. Table 1 lists the possible sources of uncertainty which could affect the performance of the HTDMAs. In our setup, nanoparticle sizing, aerosol/sheath flow rates, the high voltage

(HV) applied to nano-DMAs, RH sensors, and temperature sensors are calibrated and verified independently.

Note that in the following, for calibration and/or checking of different parameters, the criteria and/or standards that the nano-HTDMA system has to meet are listed mainly according to the suggestions from Duplissy et al., (2009) and Wiedensohler et al. (2012), which are not specifically provided for accurately measuring the size or hygroscopic growth of sub-10 nm nanoparticles. Compared with these criteria, for measuring the hygroscopic growth of sub-10 nm nanoparticles, we have achieved a better condition for our nano-HTDMA system after comprehensive calibrations, as described in the following (for more details about the performance of our system see section 3).

Table 1. Accuracy, precision and sources of uncertainty associated with HTDMA measurements.

	Biskos et al. (2006b)	Hämeri et al. (2000)	Nano-HTDMA (this study)
DMA System			
Type of DMA1 & DMA2	TSI nano-DMAs	Hauke-type DMAs	Vienna-type short DMAs
Accuracy of aerosol flow in DMA2	±1% (0.3-1.5 l min^{-1})	-	±1% (1.5 l min^{-1})
Accuracy of sheath flow in DMA2	±1% (5-15 l min^{-1})	-	±1% (10 l min^{-1})
Accuracy of DMA voltage	±0.1% (0-500V)	-	±0.1% (0-350V)
Sizing accuracy of DMA2 using PSL	3%	-	0.4% (100-nm PSL)
Sizing agreement between DMAs using ammonium sulfate	3.1% (10 nm) [a]	±1% [b]	0.6% (100 nm) [c] 0.5% (60 nm) [c] 1.4% (20 nm) [c] 0.9% (10 nm) [c] -0.2% (8 nm) [c] 1.4% (6 nm) [c]
Precision of particle sizing	<2%	-	<2% (6-200 nm) [d]
Humidification System			
Type of RH sensor	RH sensors (Omega; model no. HX93AV)	Dew point mirror (GE) RH sensors (Vaisala Humitter; model no. 50Y)	Dew point mirror (Edge) RH sensors (Vaisala; model no. HMT 330)
Accuracy of RH sensors	±2.5% RH	±3% RH [e]	±1% (RH sensor)

(0-90% RH)			
Position of the probe in the system	Inlet of DMA2 (RH_a sensor [f]; RH_s sensor [g])	Inlet of DMA2 (RH_a sensor) and excess air (RH_s sensor; dew point mirror)	Inlet of DMA2 (RH_a sensor, RH_s sensor) and excess air (dew point mirror)
RH setting	RH_a=RH_s	$RH_s \geq RH_a$+3%	RH_a=RH_s
Temperature Control System			
Temperature control type	Thermally isolated environment (humidification+DMA2)[h]	Thermally isolated environment (DMA2)	Box *T* regulated (humidification+DMA2)
Difference in T between inlet and outlet of DMA2	-	-	<0.2°C

Note: the "-" shows figures not reported. [a] According to the scans of the second DMA for the hygroscopic growth of 10 nm ammonium sulfate and the growth factors at different RHs provided by Biskos et al. (2006b), we retrieved an average sizing offset of Biskos et al. (2006b) system to be ~3.1% at 10 nm (see Sect, S1). [b] Size range not given. [c] See Table S2 in supporting information. [d] Value calculated according to the relative standard derivation. [e] From Vaisala Humitter model 50Y manual. [f] RH_a: the RH of aerosol flow. [g] RH_s: the RH of sheath flow. [h] Bezantakos et al. (2016).

2.2.1 Sizing accuracy

For particle diameters higher than 100 nm, the verification of sizing accuracy of DMAs can be accomplished by using certified particles of known sizes such as polystyrene latex (PSL) spheres (Hennig et al., 2005; Mulholland et al., 2006; Duplissy et al., 2009; Wiedensohler et al., 2012, 2018). The particle sizing of nano-DMA2 is checked with PSL by switching off the sheath flow and the HV supply of nano-DMA1, which actually in this case does not function as a DMA, but rather a stainless-steel tube. Sizing agreement between measured diameters and nominal diameters of PSL particles above 100 nm should be within ±3% (Wiedensohler et al., 2012). After confirming the accurate sizing of nano-DMA2, the sizing accuracy of nano-DMA1 can be, in turn, checked by the nano-DMA2 with a full scan of a certain size of PSL spheres selected by the nano-DMA1. Note that it is important to check not only the sizing accuracy of both DMAs but also the sizing agreement between the nano-DMA1 and nano-DMA2. To achieve good hygroscopicity measurements of nanoparticles, the sizing offset of the two DMAs should be within ±2-3% (Massling et al., 2011; Zhang et al., 2016).

For nanoparticles with diameters smaller than 100 nm, the sizing accuracy is, however, difficult to check by using PSL nanoparticles. This is mainly because the size of the residual material in the solution also peaks around 20 – 30 nm (Fig. S2a), resulting in an asymmetric number size distribution of generated PSL nanoparticles (Fig. S2b; Wiedensohler et al., 2012). PSL nanoparticles with diameters below 20 nm are not commercially available (https://www.thermofisher.com/order/catalog/product/3020A, last access: 1 April 2020), making verifications in this size range even more impossible. The sizing accuracy of nanoparticles is critically determined by sheath flow rates and HV applied to the nano-DMAs. However, unlike for the 100 nm nanoparticles, a ±2-3% sizing offset between the two DMAs would be very difficult to maintain for nanoparticles with diameters smaller than 20 nm. Thus, accurate calibrations of the sheath flow rates and HV are crucial for constraining the uncertainty associated with sizing of nanoparticles below 100 nm. The calibrations for aerosol/sheath flow, DMA voltage, and sensors will be described in detail Sect. 2.2.2-2.2.5.

2.2.2 Aerosol and sheath flow

The sizing accuracy of a DMA directly depends on the accuracy of aerosol and sheath flow rates. The aerosol flow rate at the inlet of the nano-DMA1 is checked by using a bubble flow meter (Gilian; model Gilibrator-2). Wiedensohler et al. (2012)

recommended that the measured aerosol flow rate should not deviate by more than 5 % from the set flow rate during the measurements; otherwise, one should check the flow rate of CPC or check if there is a leak in the system. Details about leak checking can be found in Birmili et al. (2016).

To calibrate the sheath flow, a verified MFM (TSI; series 4000) is placed in the recirculating sheath flow closed loop upstream of the MFM. By applying a series of sheath flow rates, a calibration curve (flow rate vs. MFM analog output) can be obtained according to the reading of the reference MFM. A maximum deviation of 2% from the sheath flow rate value of the reference MFM is recommended by Wiedensohler et al. (2012), which can keep the sizing accuracy of 200 nm PSL particles within ±2%.

2.2.3 DMA voltage

The sizing of nano-DMAs is very sensitive to the accuracy and precision of the voltages applied, especially when measuring nanoparticles in the sub-10 nm diameter range. A verified reference voltage meter, with voltage up to 1000 V (Prema; model no. 5000 DMM; accuracy 0.005%) is used to calibrate the HV supply of the nano-DMAs (0-350 V). By setting a series of analog voltage values, the HV applied to nano-DMA can be calibrated according to the values shown in the reference voltage meter. For our nano-DMAs, sub-10 nm particle sizes correspond to voltage below 50 V. Thence, voltage calibration should be performed with a higher resolution (smaller voltage interval) from 0 to 50 V (shown in the inset of Fig. 2).

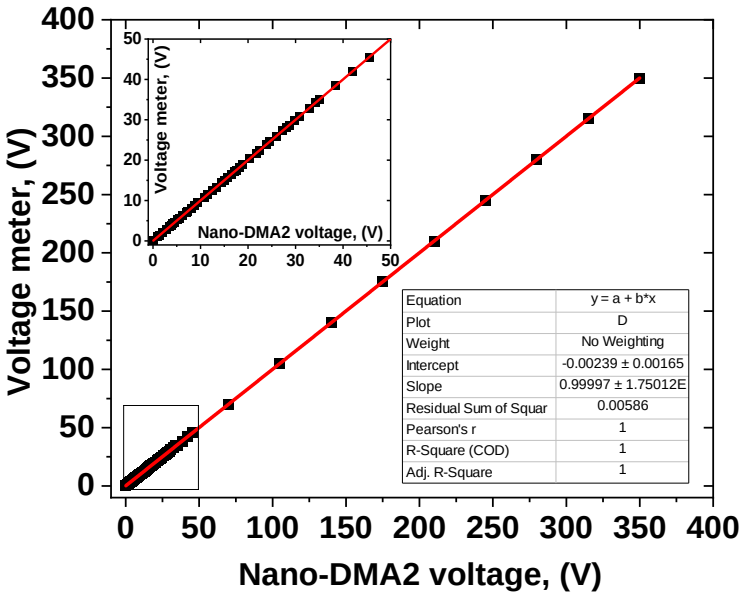

Figure 2. An example of voltage calibration of the nano-DMA2.

2.2.4 RH sensor

One typical method for calibrating RH sensors in a HTDMA system is measuring the hygroscopic growth factors of ammonium sulfate (Hennig et al., 2005), although the effects of shape factors, restructuring, and impurities in the solutions may hamper a reliable RH calibration with this method (Duplissy et al., 2009). Moreover, this indirect RH sensor calibration through the measurement of the hygroscopic growth factors of ammonium sulfate (usually with nanoparticle diameters around or above 100 nm) only calibrates the RH values higher than the ERH of the pure salt. Calibration of RHs below the ERH of ammonium sulfate is important for the phase transition measurements. Most importantly, we are investigating the hygroscopic growth factors of ammonium sulfate nanoparticles. Hence, using ammonium sulfate nanoparticles to calibrate RH sensors in our system becomes invalid.

Therefore, we alternatively calibrate the RH sensors by using a DPM (Edgetech; model no. MIRRPR-99), which has been recommended in several previous studies (Hennig et al., 2005; Duplissy et al., 2009; Biskos et al., 2006a, b, 2007). In the calibration, the DPM and RH sensors should be kept in the well-insulated chamber with constant laboratory conditions (e.g., flow rates, temperature, and pressure). By running the DPM and all the other RH sensors in parallel at various RHs (5% to 90%), a calibration curve of the RHs measured by the DPM against the analog voltages of RH sensor can be obtained.

2.2.5 Temperature sensor

Since all our temperature sensors and the highly accurate DPM (Edgetech; model no. MIRROR-99) are installed in the aforementioned well-insulated chamber, and the chamber temperature is maintained with an air conditioner at about 292.15±0.1 K, we calibrate the temperature sensors and correct their systematic shift by comparing the record of the temperature sensors and the DPM by keeping them in parallel inside the chamber over a 12-hour time period.

2.3 Particle generation

The experiments shown in this study were conducted using laboratory-generated ammonium sulfate and sodium sulfate nanoparticles. Nanoparticles with diameters of 6, 8, and 10 nm were generated by an electrospray (AG; TSI; model no. 3480) with 1, 5, and 20 mM aqueous solution of ammonium sulfate and sodium sulfate (Sigma-Aldrich; 99.99%), respectively. The generated particles were then diluted and dried to

RH below 2% by mixing them with dry and filtered N_2 (1 l min^{-1}) and CO_2 (0.1 l min^{-1}). The dried polydisperse aerosol nanoparticles were subsequently neutralized by a Po-210 neutralizer. To avoid blocking the 25-μm capillary of the electrospray with a high-concentration solution, we used an atomizer (AG; TSI; model no. 3076) to generate nanoparticles with diameters of 60-100 nm and 20 nm, with a 0.05 and 0.001 wt % solution of ammonium sulfate and sodium sulfate (Sigma-Aldrich; 99.99%), respectively. Also, 100-nm PSL nanoparticles were atomized from a PSL solution by mixing three drops of 100-nm PSL with 300 mL distilled and deionized Milli-Q water. The generated nanoparticles were subsequently dried to RH below 10 % with a custom-built Nafion dryer (ND; TROPOS; model no. ND.070) and then neutralized by a Kr^{85} neutralizer.

The solutions used in our measurements were prepared with distilled and deionized Milli-Q water (resistivity of 18.2 MΩ cm at 298.15 K). Note that, for 100-60 nm and 20 nm, the solution concentration was adjusted so that the sizes selected by the nano-DMA1 were always larger than the peak diameter of the number size distribution of the generated nanoparticles to minimize the influence of the multiple charged nanoparticles in the hygroscopicity measurements. The influence of multiple charges on sub-10 nm particles is expected to be very small; we, however, still used different concentrations so that the sizes selected by the nano-DMA1 were always around the peak of the number size distribution of the nanoparticles generated by the electrospray (Fig. S3). This was to ensure that we could have as many particles as possible to compensate the strong loss of very small particles in the whole humidification system.

3 Results and discussion

3.1 Performance of the nano-HTDMA

3.1.1 Sizing accuracy

In this section, we show the performance of our nano-HTDMA after a full calibration, including accuracy and stability of the aerosol and sheath flow rates, the voltage applied to the nano-DMAs, and nanoparticle sizing accuracy. In our study, the sheath/aerosol flow rates and nano-DMA voltage supply have been calibrated every day and every 2 weeks, respectively. The deviations of the measured aerosol/sheath flow rates from the set-point values are less than ±1%, which is lower than the maximum variation of 2% recommended by Wiedensohler et al. (2012).

The voltage applied to the nano-DMAs (up to 350 V) is kept within ±0.1% around the set value shown in the voltage meter. As shown in Fig. 3a, when testing with 100-nm PSL nanoparticles, the average peak diameter of scans from the nano-DMA2 is 100.4 nm, which matches well with the mean diameter of PSL nanoparticles (100±3 nm, Thermo Fisher Scientific Inc.). Afterwards, when using nano-DMA1 to select 100 nm PSL, the scanned size distribution by nano-DMA2 has a peak diameter at 100.3 nm (Fig. 3b), indicating a good sizing accuracy of the nano-DMA1 too. As discussed in Sec. 2.2.1, it is difficult to verify the sizing accuracy of sub-100 nm aerosol nanoparticles using PSL nanoparticles. Duplissy et al. (2009) and Wiedensohler et al. (2012) suggested estimating the sizing accuracy of sub-100 nm nanoparticles through the DMA transfer function. The theoretical DMA transfer function (see SI. S2. Eq. (S2-S4)) was proposed by Knutson and Whitby (1975) and they noted that sizing is crucially dependent on flow rates and HV applied to the DMA. In our study, the flow accuracy calibrated by the mass flow meter (TSI series 4000) is within ±2%. The variation in voltage applied to the nano-DMAs (0-12500 V, 0-350 V) around the set value was measured with voltage power supply (HCE 0-12500; HCE 0-350; Fug Electronic) and is summarized in Table S5. According to the error propagation formula (see SI. S2. Eq. (S5)) (Taylor and Taylor, 1997), the calculated uncertainty in the sizing of 6-100 nm nanoparticles increases as size decreases (Table S5). The estimated sizing accuracy is slightly smaller than the sizing offset of the two nano-DMAs, but in principle they are still consistent with each other. This suggests that uncertainties in slip correction, DMA dimensions (inner and outer radius and length), temperature, pressure, and viscosity of air may also affect the sizing accuracy (see SI. S2. Eq. (S4); Kinney et al., 1991). Besides, Wiedensohler et al. (2012) also suggested that particle losses and the size- and material-dependent CPC counting efficiency can affect the size accuracy of DMAs.

After calibration, on average a <1.4% sizing offset between the two nano-DMAs can be achieved for ammonium sulfate nanoparticles with dry diameters of 100 nm, 60 nm, and 20 nm (Fig. 3c, Fig.5, S4, and S5; Table S3), which is much better than the 2-3% criteria recommended by Massling et al. (2011) and Zhang et al. (2016). For sub-10 nm ammonium sulfate nanoparticles, our system has an average sizing offset of <0.9% for 10 and 8 nm particles and ~1.4% for 6 nm particles, respectively (Fig. 3d, 5, and S6; Table S3). As discussed above, uncertainties in the sheath flow rates and nano-DMA voltages will increase as size decreases, which results in a larger sizing offset of

6-nm nanoparticles compared with other sizes. Note that we also tested the calibration of the DMA voltage with a voltage meter with lower accuracy of ±1%, and the DMA voltages can only be kept within ±1% around the set value. In this way, we found a much larger sizing offset for the sub-10 nm particles, i.e., 5.4% and 6.0% for 8 and 6 nm ammonium sulfate nanoparticles, respectively. These results show that maintaining an accurate sheath/aerosol flow (with ±1% around the set value) together with a careful voltage calibration (with ±0.1% around the set value, especially in low-voltage range, i.e., <50 V for our system) is the key for accurate sizing of sub-10 nm nanoparticles.

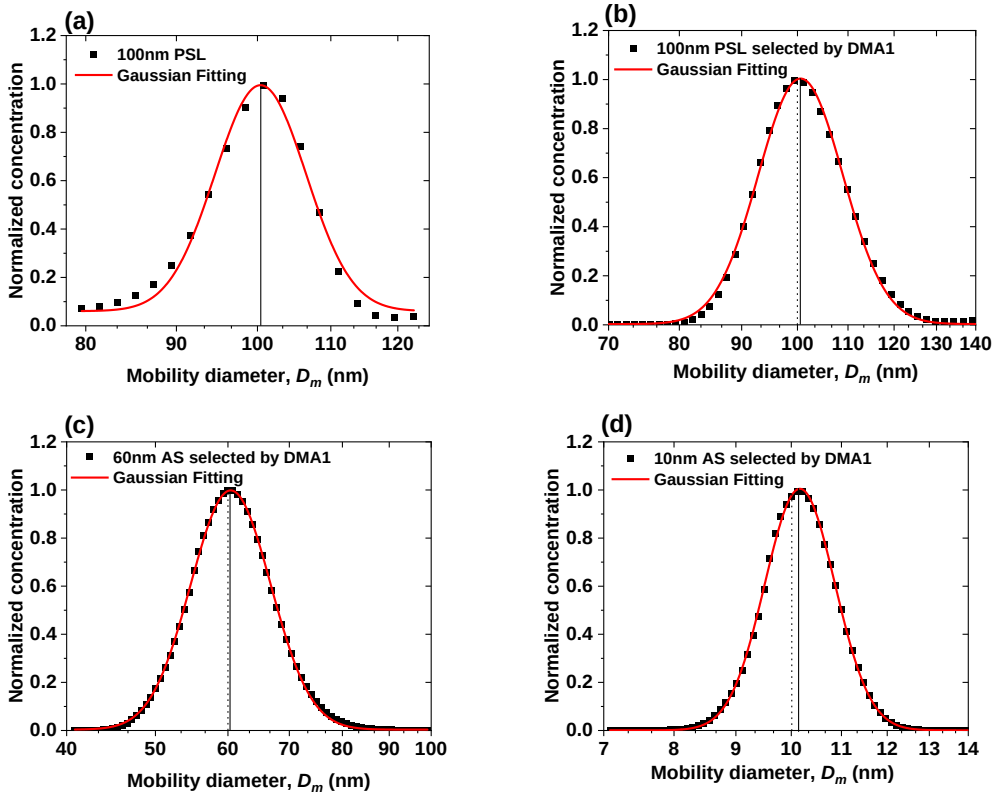

Figure 3. Sizing accuracy and sizing offset of nano-DMAs after calibration. **(a)** Normalized number size distribution scanned by the nano-DMA2 for 100-nm PSL nanoparticles (black solid square). Normalized number size distributions scanned by the nano-DMA2 for 100-nm PSL nanoparticles **(b)** and 60-nm **(c)** and 10-nm **(d)** ammonium sulfate (AS) selected by the nano-DMA1 at RH below 5% at 298 K (black solid square). The dotted lines mark the diameters of the monodispersed nanoparticles selected by the nano-DMA1, i.e., 100 nm in **(b)**, 60 nm in **(c),** and 10 nm in **(d)**. The black solid lines mark the peak diameters from the Gaussian fits (red curve).

3.1.2 Preventing predeliquescence in the deliquescence measurement mode

Predeliquescence of dry nanoparticles in the deliquescence measurement mode is an important issue that needs to be resolved in order to obtain accurate DRH (Biskos et al., 2006b; Duplissy et al., 2009; Bezantakos et al., 2016; Hämeri et al., 2000). Since temperature and RH are closely linked and accurate monitoring of these two quantities in the system is critical for nano-HTDMA measurements, we calibrated all RH and *T* sensors regularly (every 2 weeks in this study). To prevent predeliquescence and to optimize the system, we have conducted three tests using ammonium sulfate nanoparticles with a dry diameter of 100 nm. In the first test, we regulated the RH of the excess flow (RH_e) and made it equal to that of the aerosol flow at the inlet of nano-DMA2 (RH_a), i.e., $RH_e=RH_a$, as done by previous HTDMA measurements (e.g., Villani et al., 2008). As shown in Fig. 4a, the measured growth factors of 100-nm ammonium sulfate are in good agreement with predictions of the Extended Aerosol Inorganics Model (E-AIM; Clegg et al., 1998) at RH above 80 %. However, the ammonium sulfate nanoparticles deliquesce at 75 % RH, which is significantly lower than the expected DRH (80%; Tang and Munkelwitz (1994)). Since our RH sensors were all well calibrated, and the uncertainty of RH measurement is ±1%, it is reasonable to hypothesize that the RH upstream of nano-DMA2 has already reached the deliquescence RH of ammonium sulfate nanoparticles. When these aerosol nanoparticles move downstream of the nano-DMA2, the RH decreases back to 75 %, which dehydrates the deliquesced ammonium sulfate nanoparticles. To avoid the predeliquescence, Hämeri et al. (2001) have suggested setting RH_a to be 3-5% lower than RH_e. In the second test, we configured and regulated the system following this suggestion, i.e., $RH_e \geq RH_a+3\%$. In this case, the ammonium sulfate nanoparticles still deliquesce at 79 % RH (Fig. 4b), even if RH_a is 6 % lower than RH_e.

Previous studies (Biskos et al., 2006b; Bezantakos et al., 2016) have shown that RH nonuniformities within the nano-DMA2 can result in inaccurate measurements of the phase transition and hygroscopic growth of aerosol nanoparticles. One reason for RH nonuniformities within nano-DMA2 is that the sheath flow RH is different from the aerosol flow RH at the inlet of the DMA (Hämeri et al., 2000, 2001). Another important reason is the existence of the temperature gradient within nano-DMA2 (Bezantakos et al., 2016). Hence, in the third test, we moved the RH sensor from the excess flow downstream of the nano-DMA2 to the sheath flow upstream of the nano-DMA2 and

then regulated RH of sheath flow (RH_s) to be the same as RH_a (shown in Fig. 1); i.e., RH_s=RH_a, as done by Kreidenweis et al. (2005), Biskos et al. (2006a, b), and Massling et al. (2011). Note that, to minimize the temperature gradient within the nano-DMA2 in our system so that nanoparticles can undergo almost the same RH conditions, the nano-DMA2 with its sheath flow humidification system has been placed in a well-insulated air-conditioned chamber. The air temperature inside the chamber can be maintained at an almost constant level (292.15±0.1 K). In addition, a heat exchanger was installed downstream of the recirculation blower to minimize the temperature perturbation in the sheath flow by the heat generated in the RB. Unlike previously reported by Bezantakos et al. (2016), who said that the RH at the outlet was higher than at the inlet of the sheath air, we monitored the sheath flow temperature at the inlet of nano-DMA2 so that it was slightly lower (less than ~0.2 K) than that at the outlet (i.e., the RH_s at the inlet of nano-DMA2 is slightly higher (~ 1%) than the RH of the excess air at the outlet), while the temperature of the sheath flow was equal to that of the aerosol flow at the inlet of nano-DMA2 during the measurements. A small temperature difference in nano-DMA2 is more likely due to the heat transfer between the inner electrode and air which flows around it by convection/conduction (Bezantakos et al., 2016). The plausible reason for this could be that when charged nanoparticles (similar to the electric current) hit the inner electrode, the inner electrode has some resistive heating from the electric current that flows. Such a temperature difference/gradient within DMA was observed in previous studies (Biskos et al., 2007; Villani et al., 2008; Duplissy et al., 2009; Bezantakos et al., 2016; Giamarelou et al., 2018). For example, a ±0.5 °C temperature difference within DMA was observed by Giamarelou et al. (2018) during the measurements. Except for the possibly slightly higher temperature of the inner electrode than the surrounding air, the temperature gradient in DMA2 may also be caused by environmental disturbances or temperature differences between other parts of DMA and between sheath flow and aerosol flow. In this study, we calculate the change in heat (Q) of a nano-DMA2 system at a constant pressure, which is estimated to be ~0.08 W ($Q = mdTC_{p,k}$) by considering the density and heating capacity of air and aerosol and sheath air flow rate (ρ=1.2041 kg/m^3; C_p= 1.859 kJ/kg°C; Atkins et al., 2006). Although this temperature perturbation (less than ~0.2 K between the sheath flow at the inlet and the excess flow at the outlet of the nano-DMA2) is larger than the ideal condition of less than 0.1 K that Duplissy et al. (2009) and Wiedensohler et al.

(2012) suggested, our experimental results show that a prompt phase transition can still be achieved. In this case, the measured DRH of ammonium sulfate nanoparticles is almost at 80 % (Fig. 4c and 4d).

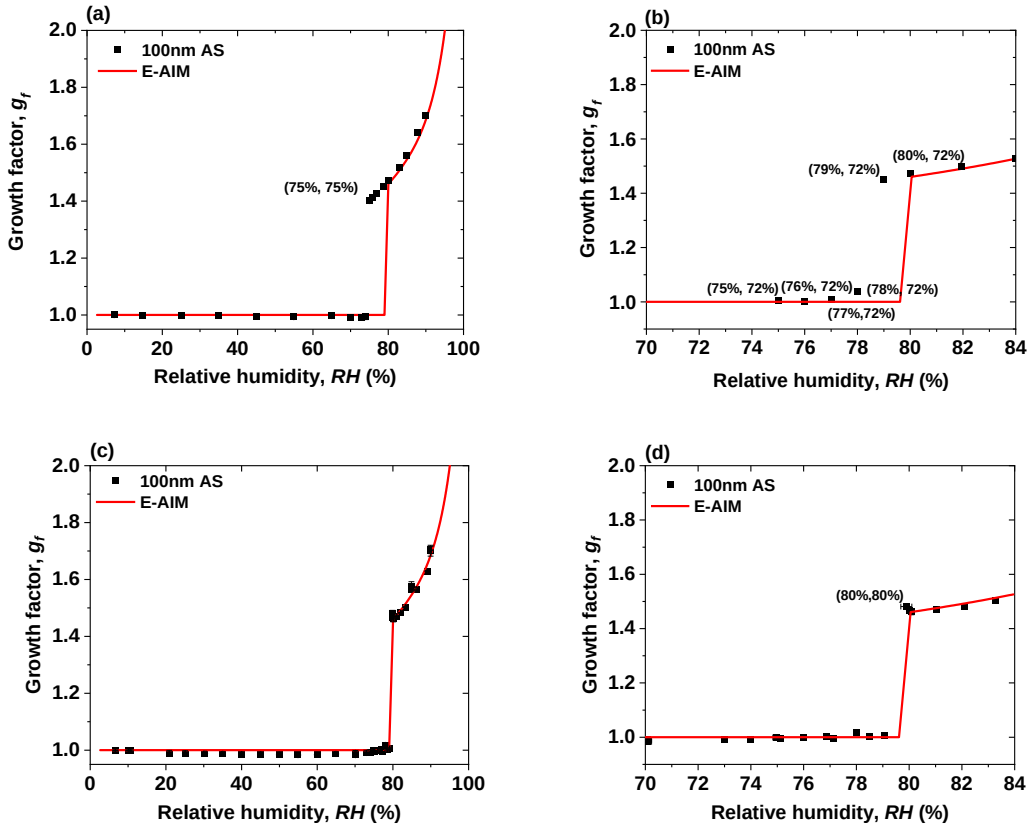

Figure 4. Mobility diameter hygroscopic growth factors (g_f) of 100-nm ammonium sulfate (AS) nanoparticles at 298 K measured in deliquescence mode. In comparison, the E-AIM model predicted growth factors of ammonium sulfate nanoparticles at 100 nm. **(a) RH_e=RH_a** (75%, 75%) represents the RH_e and RH_a; **(b) RH_e≥RH_a+3%** (75%, 72%) represents the RH_e,and RH_a; and **(c) RH_s = RH_a.** (**d)** The enlarged view of the RH range of 70% to 84% in Fig. 4c. The (80%, 80%) points represent the RH_s, and RH_a. RH_s and RH_e are the RH of sheath flow in the inlet of nano-DMA2 and in the excess air line, respectively. RH_a is the RH of aerosol flow in the inlet of nano-DMA2.

3.1.3 Prompt phase transition of ammonium sulfate

Figure 5 and 6 show the normalized particle number size distributions measured by the nano-DMA2 in the respective deliquescence and efflorescence measurement modes for ammonium sulfate nanoparticles with dry mobility diameters of 20 nm, 10 nm, and 6 nm (see Fig. S4 for 100 nm; see Fig. S5 for 60 nm; see Fig. S6 for 8 nm). In the deliquescence measurement mode (Fig. 5, Fig. S4a, and Fig. S5a), we observed a

similar double-mode phenomenon to that reported by Mikhailov et al. (2004) and Biskos et al. (2006b, 2007). For example, at 20 nm there are two distinct intersecting modes of particle size distributions determined by the nano-DMA2 in the RH range from 79% to 83% RH (around the DRH of ammonium sulfate). Biskos et al. (2006b, 2007) attributed these two modes to the coexistence of solid and liquid phase nanoparticles at RH close to the DRH of ammonium sulfate. This is due to the slight inhomogeneity of RH in the second nano-DMA, i.e., some nanoparticles have already undergone deliquescence (liquid state) and some have not (solid). This is evident through a double-mode log-normal fitting (red and blue modes in Fig. 5). Until RH ~82 %, the peak diameter of the red mode at 82 % RH is similar to that at 11 % RH, indicating that these nanoparticles are still in a solid state. At 82% RH, a population of ammonium sulfate nanoparticles starts to deliquesce and exists in a distinct mode with significantly larger peak diameter (blue mode), although the majority of the nanoparticles remain solid (red mode). As RH further increases, the peak diameter of the normalized number size distribution of the blue mode increases, indicating the continuous growth of the nanoparticles after deliquescence. However, in our case, the double-mode phenomenon was not observed for 8 and 6 nm ammonium sulfate nanoparticles (Fig. 5 and Fig. S6a). To have a better estimation of DRH when the double modes occurred, the peak diameter of the mode with the larger number of nanoparticles was chosen for growth factor calculation (Biskos et al., 2006b, 2007). For example, for 20 nm ammonium sulfate nanoparticles, the peak diameters of the normalized number size distribution of the red and blue modes are used to calculate the growth factor at RH between 79 % to 83 %, respectively.

For the efflorescence measurement mode, we adopted the approach of Biskos et al. (2006b) and used the geometric standard deviation of the number size distribution (e.g., sigma-σ) to quantify the diversity in the sizes of the nanoparticles. As shown in Fig. 6, Fig. S4b, Fig. S5b, and Fig. S6b, a broadening of the normalized number size distributions measured with nano-DMA2 was only observed for 20-nm ammonium sulfate nanoparticles in the RH range from 33 % to 30 %. There, at RH higher than 33 % or lower than 30 %, σ stays stable at 1.072. However, clear increases in σ (1.078-1.087) were observed for RH between 33 % and 30 %. The normalized number size distributions in the RH range from 33 % to 30 % can be further resolved by double-mode fit with a fixed σ of 1.072 (the red and the blue mode in Fig. 6 for 20 nm). The

ammonium sulfate nanoparticles in the red mode at RH between 33 % and 30 % are in the solid state because the peak diameter of red mode is similar to that at 11 % RH. However, within this RH range, the peak diameter of the blue mode is significantly larger, indicating that these nanoparticles are still in the liquid state. Further decreasing RH (lower than 30 %) leads to only one mode being observed and the peak diameter of the normalized number size distribution is almost unchanged as RH decreases (red mode in Fig. 6 for 20 nm), which means that the nanoparticles have all been in the solid state. Similar to the deliquescence measurement shown above and in Fig. 5, the coexistence of solid and aqueous phase nanoparticles at RH 30-33 % is also very likely to stem from the slightly heterogeneous RH in nano-DMA2 (Biskos et al., 2006b). To have a better estimation of ERH when the broadening phenomenon exists, the peak diameter of the mode with the larger number of nanoparticles was used for the growth factor calculation. After such data processing in both the deliquescence and efflorescence modes, we obtained prompt deliquescence and efflorescence of 6 to 100 nm ammonium sulfate nanoparticles (more details in Sect 3.1.4).

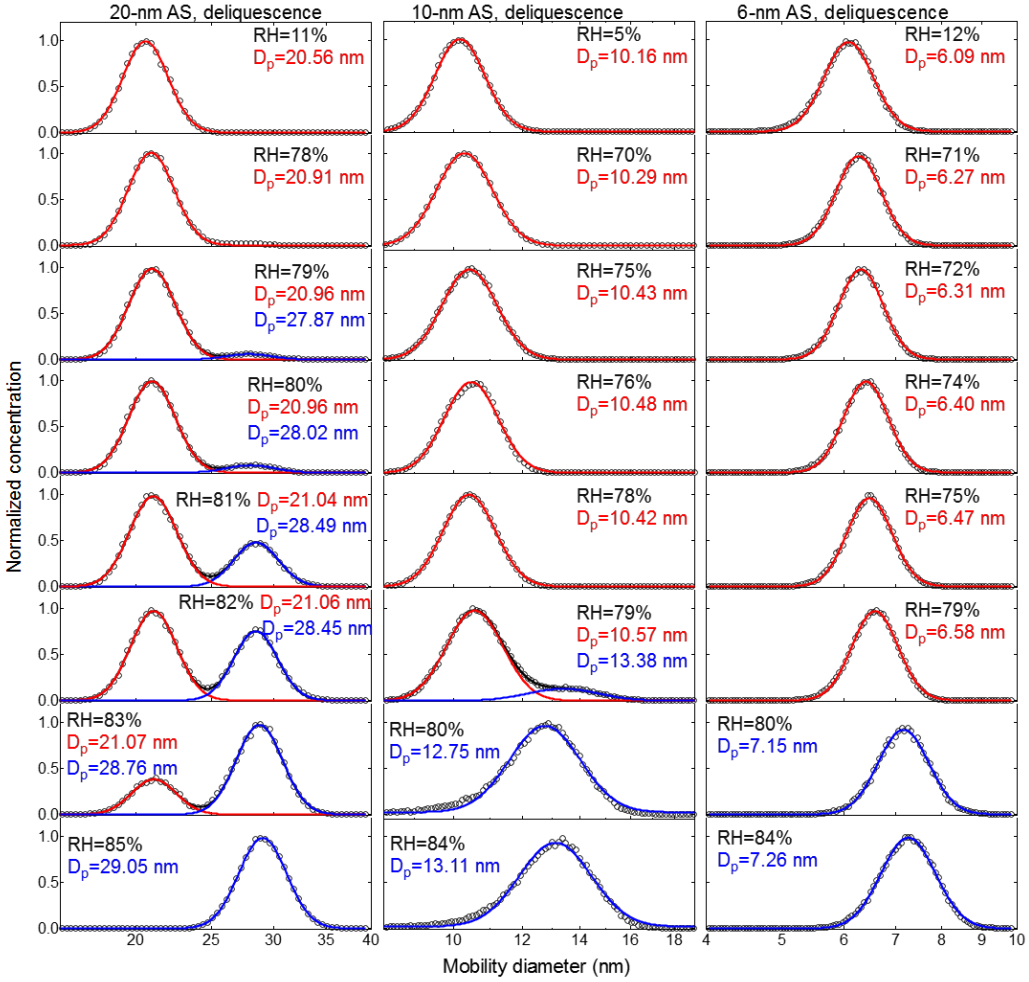

Figure 5. Deliquescence-mode measurements of ammonium sulfate (AS) aerosol nanoparticles with dry mobility diameter from 20-6nm. The measured (black circles) and fitted (solid lines) normalized size distribution are shown for increasing RH. The red and blue lines represent the aerosol nanoparticles in the solid and liquid state, respectively. The RH history in each measurement is 5% → X%, where X is the RH value given in each panel.

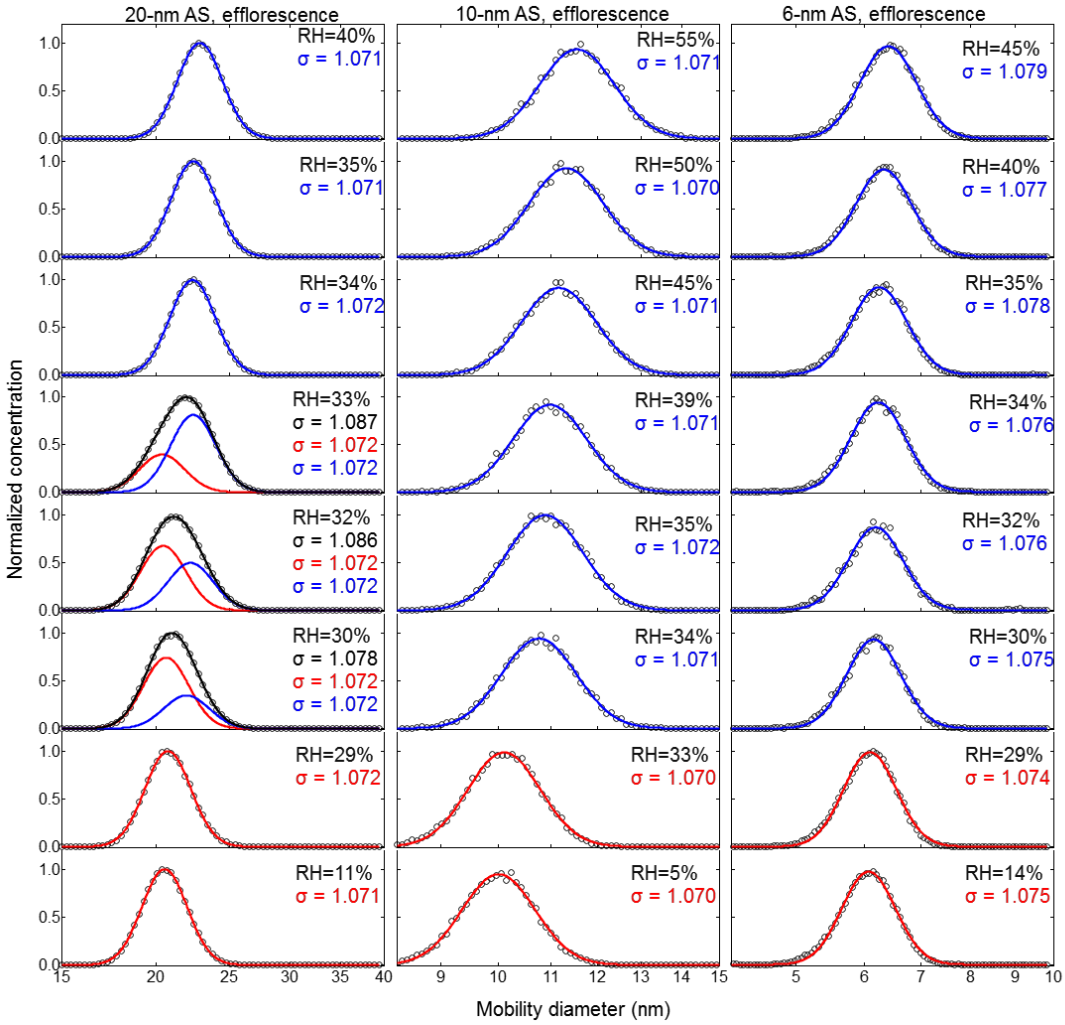

Figure 6. Efflorescence-mode measurements of ammonium sulfate (AS) aerosol nanoparticles with a dry mobility diameter from 20-6nm. The measured (black circles) and fitted (solid lines) normalized size distribution are shown for increasing RH. The red and blue lines represent the aerosol nanoparticles in the solid and liquid state, respectively. The RH history in each measurement is 5%→97%→X%, where X is the RH value given in each panel.

3.1.4 Size-dependent hygroscopicity of ammonium sulfate nanoparticles

Figure 7 shows the humidogram of ammonium sulfate nanoparticles measured by our nano-HTDMA system in the size (dry diameter) range of 6-100 nm. The detailed

comparison between our results and those of Biskos et al. (2006b) during both deliquescence and efflorescence measurements is presented in Fig. 8a and b (also Fig. S7). In general, our results are in good agreement with the measurement results of Biskos et al (2006) and the theoretical prediction by Cheng et al. (2015). First, there is a strong size dependence in the hygroscopic growth factor of ammonium sulfate nanoparticles, and smaller ammonium sulfate nanoparticles exhibit a lower growth factor at a certain RH. For example, the difference in the growth factor between 6 and 100 nm nanoparticles is up to 0.28 at 80 % RH (Fig. S8a). Second, there is, however, no significant size dependence in both DRH and ERH (Fig. S8b). For nanoparticles of different sizes (6-100 nm), the DRH and ERH of ammonium sulfate varies slightly from ~80 % to 83 % and ~30 % to 34 %, respectively. This variation in the DRH and ERH with respect to the size is much smaller for ammonium sulfate nanoparticles than for sodium chloride (Biskos et al. 2006a, 2007).

Although our results in general agree well with Biskos et al. (2006b), the growth factors of 10, 8, and 6 nm ammonium sulfate nanoparticles that we measured at high RH (i.e., > ~70 %) are slightly lower (~0.02 in growth factor) than those in Biskos et al. (2006b) in both deliquescence and efflorescence processes (Fig. 8b and Fig. S7). We calculated the uncertainties in the growth factor of 10-nm ammonium sulfate from 80 % to 90 % RH for our system and the Biskos et al. (2006b) system with the following: $\sqrt{\left(\left(g_f \frac{\sqrt{2}\varepsilon_{Dp}}{D_p}\right)^2 + \left(\varepsilon_{RH} \frac{dg_f}{dRH}\right)^2, \right)}$ (Mochida and Kawamura, (2004)). Here, ε_{Dp}, ε_{RH}, and g_f are the uncertainty of the particle mobility diameter, the uncertainty of relative humidity, and the growth factor with respect to RH, respectively. The average sizing offsets of our system, and the system of Biskos et al. (2006b) for 10 nm ammonium sulfate are taken here as $\frac{\varepsilon_{Dp}}{D_p}$ (see Table 1). As shown in the inset of Fig. 8b, the discrepancies between the two systems are still within the measurement uncertainty.

In addition, compared to Biskos et al. (2006b), our results show a similar restructuring in the deliquescence mode at RH between about 20 % and 75 % for 100 and 60 nm ammonium sulfate nanoparticles (Fig 8c). However, different to Biskos et al. (2006b), we do not find restructuring for smaller ammonium sulfate nanoparticles (20, 10, 8, and 6 nm) at RH below the deliquescence point (Fig. 8c and Fig. 8d). There seems to be continuous water adsorption, and the adsorbed water layers (Romakkaniemi et al.,

2001) become significantly thicker when RH is closer to the DRH (i.e, RH > 70 %). For example, a slight increase in the hygroscopic growth factor of 6-nm ammonium sulfate nanoparticles is observed in the RH range from 65 % to 79 % RH before deliquescence. This is attributed to water adsorption on the surfaces of these nanoparticles. It seems that smaller nanoparticles have a stronger tendency to adsorb water when approaching the DRH than the larger ones. A similar phenomenon was also observed by Hämeri et al. (2000, 2001), Romakkaniemi et al. (2001), Biskos et al. (2006a, b, 2007), and Giamarelou et al. (2018). The reason for such enhanced adsorption at smaller sizes still needs to be investigated. Note that the ammonium sulfate hygroscopic data from Biskos et al. (2006b) shown here are all generated by an electrospray, but in our experiments, only the ammonium sulfate nanoparticles with diameters smaller than 20 nm (i.e., 10, 8, and 6 nm) were generated by an electrospray, while the larger nanoparticles (i.e., 20, 60, and 100 nm) were generated by an atomizer. Different from the generation conditions of for 6-10 nm ammonium sulfate nanoparticles in Biskos et al. (2006b), in our study, in order to minimize the multiple charged nanoparticles, three different concentrations were used so that the size selected by the nano-DMA1 (i.e., 6, 8, and 10 nm) was always slightly larger than peak of the number size distribution of the nanoparticles generated by the electrospray. This also helps us to have as many as nanoparticles as possible to compensate for the strong nanoparticle losses in the nano-HTDMA system. In addition, we used both an electrospray and an atomizer to generate 20-nm ammonium sulfate, and we compared their hygroscopic growth factors prior to deliquescence. Figure S12a shows a ~ 0.1 higher growth factor of 20 nm ammonium sulfate generated by the electrospray than when using the atomizer in the RH range from 55 % to 82 %, which is similar to the difference in the hygroscopic growth factor of 20 nm NaCl aerosol nanoparticles when using the different generation methods, shown in Fig S12b in Biskos et al. (2006a). Besides different generation conditions, the morphology of the dried ammonium sulfate particles may also differ slightly between our study and Biskos et al. (2006) because of the different dying rate, as the drying flow rates and RH of the dried ammonium sulfate in the two HTDMA systems are different too. This means the different generation methods and drying conditions may influence the surface structure of the nanoparticles and, thus, their interaction with the adsorbed water layers (Iskandar et al., 2003; Wang et al., 2019).

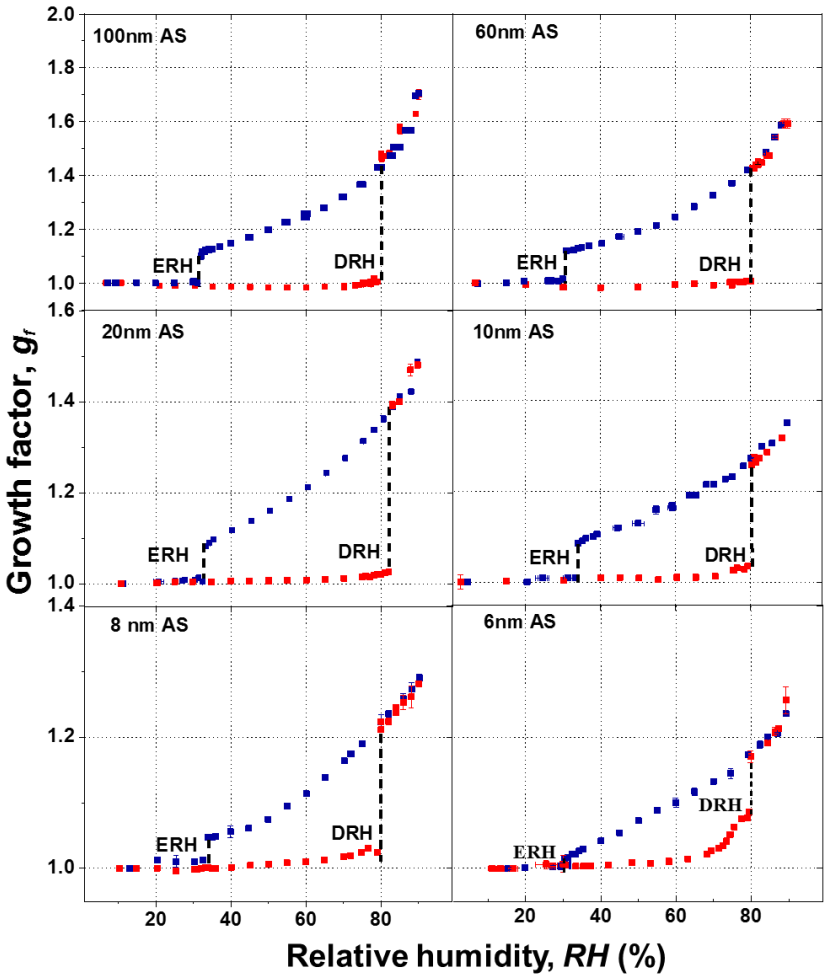

Figure 7. Mobility diameter hygroscopic growth factors (g_f) of ammonium sulfate (AS) aerosol nanoparticles with dry mobility diameter from 6 to 100 nm in the deliquescence mode (red square and error bar) and the efflorescence mode (royal blue square and error bar). Deliquescence and efflorescence relative humidity (DRH and ERH; black dashed line) of ammonium sulfate (AS) nanoparticles with dry mobility diameter from 6 to 100 nm.

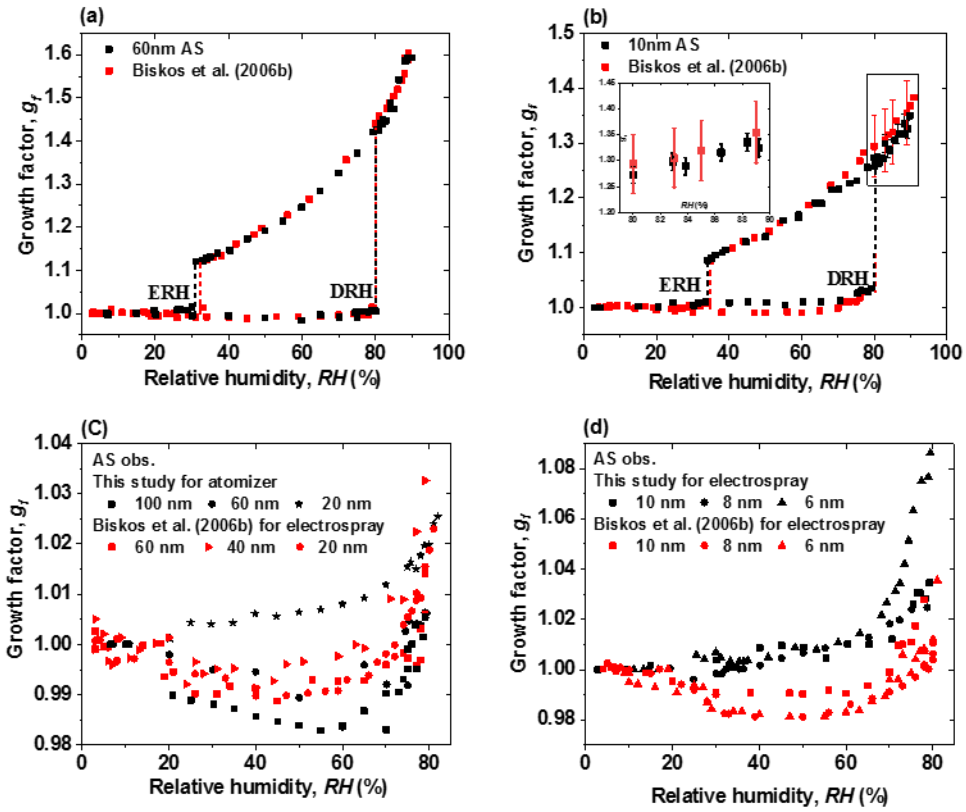

Figure 8. **(a-b)** Mobility diameter hygroscopic growth factors (g_f, black squares), deliquescence and efflorescence relative humidity (DRH and ERH; black dashed lines) of ammonium sulfate (AS) nanoparticles with a dry diameter of 60 and 10 nm, respectively. Red squares and red dashed lines show the respective results from Biskos et al. (2006b), respectively. Black and red uncertainties of growth factors at certain RH are calculated by the following: $\sqrt{\left(\left(g_f \frac{\sqrt{2}\varepsilon_{Dp}}{D_p}\right)^2 + \left(\varepsilon_{RH} \frac{dg_f}{dRH}\right)^2\right)}$, where ε_{Dp}, ε_{RH}, and g_f are the uncertainty of particle mobility diameter, the uncertainty of relative humidity, and the growth factor with respect to RH, respectively (Mochida and Kawamura 2004). **(c-d)** Comparison of growth factors of ammonium sulfate (AS) nanoparticles with a dry diameter range from 6 to 100 nm, with Biskos et al. (2006b) prior to deliquescence of ammonium sulfate nanoparticles.

3.2 Size-dependent hygroscopicity of sodium sulfate nanoparticles

As it is a common constituent of atmospheric aerosol particles (Tang and Munkelwitz, 1993, 1994; Tang 1996; Tang et al., 2007), the hygroscopicity of sodium sulfate with diameters above 20 nm particles has been investigated by a few groups (Tang et al., 2007; Xu and Schweiger, 1999; Hu et al., 2010). However, its hygroscopic behavior in the sub-10 nm size range has not been investigated yet. In this study, we applied our nano-HTDMA system to measure the hygroscopic growth factors, DRH, and ERH of

sodium sulfate nanoparticles with a dry size from 20 nm down to 6 nm.

Figure 9 shows the measured size-resolved hygroscopic growth factors of sodium sulfate nanoparticles. Different from the observations by Tang et al. (1995) using an electrodynamic balance (EDB), we observed a prompt deliquescence and efflorescence for both 20-nm and 6-nm sodium sulfate nanoparticles. Two intersecting modes in the measured number size distribution of the humidified sodium sulfate nanoparticles are observed at RH close to the DRH (Fig. S9 and S10 in the Supplementary Information) and at ERH, suggesting an external mixture of aqueous and solid nanoparticles. As shown in Sect. 3.1.3, a similar phenomenon is also observed for ammonium sulfate, which could be attributed to the slight RH heterogeneities in nano-DMA2; this makes only part of the nanoparticles deliquesce at RH close to the DRH, while the others remain in the solid state.

Together with the hygroscopic growth of 14-16 μm and 200-20 nm sodium sulfate measured previously by Tang et al. (1995) and Hu et al. (2010), we show a strong size dependence in hygroscopic growth factors of sodium sulfate nanoparticles (Fig. S11d). For example, at RH=84%, the hygroscopic growth factor of 6 nm sodium sulfate is only ~ 1.3 (in efflorescence mode), while the respective growth factors are about 1.5 and 1.8 for 20 nm and 14-16 μm particles. As shown in Fig. 9, E-AIM already agrees well with the hygroscopic growth of micrometer particles (14-16 μm) without shape correction (DeCarlo et al., 2004), i.e., shape factor (χ) of 1.0. However, to explain observation, a shape factor of ~1.16 and 1.26 would be needed for 20 nm and 6 nm sodium sulfate nanoparticles, respectively.

There is no significant change in DRH between 14-16 μm (~84 %) and 20 nm (~84 %) sodium sulfate particles (Fig. 9). This is consistent with Hu et al. (2010) where no change in DRH, from 200 nm down to 20 nm (~82 %; see Table 1 from Hu et al. (2010)), was observed. However, a significant increase in DRH occurred when further decreasing particle diameters to 6 nm (DRH = ~90 %). The size dependence of ERH is stronger than that of DRH, as there is already a clear increase in ERH from micrometer 14-16 μm (~57 %) to 20 nm (~62 %) sodium sulfate particles. When further reducing the particle diameters to 6 nm, an almost 6% increase in DRH can be found, compared to the micrometer 14-16 μm particles (i.e., ERH increases from 57 % to 82 %, respectively). Different from ammonium sulfate, for which DRH and ERH show no significant size dependence, there is a strong size dependence in the DRH and ERH of

sodium sulfate according to our observations down to 6 nm. The difference in the size dependence of DRH and ERH between sodium chloride and ammonium sulfate has been theoretically studied and explained by Cheng et al. (2015). The main reason is the different concentration dependence of the solute activities and the different solid-liquid surface tension (e.g., the same change in solute molality leads to a larger change in the solute activity of sodium chloride than that of ammonium sulfate). The phase transition concentration (deliquescence and crystallization concentration) of ammonium sulfate is thus more sensitive to the size change compared to that of sodium chloride, leading to the almost unchanged DRH and ERH of ammonium sulfate nanoparticles (Cheng et al., 2015). For the size dependence of the phase transition of sodium sulfate, the strong size effect on DRH and ERH is similar to that of sodium chloride but different from to that of ammonium sulfate in the size range from 6 to 20 nm, suggesting that the nonideality of the solution property is close to that of sodium chloride but weaker than that of ammonium sulfate. As different hydrates of sodium sulfate may exist during the deliquescence and efflorescence processes (Xu and Schweiger, 1999), explaining the underlying mechanism of the size-dependent hygroscopicity of sodium sulfate particles can be challenging.

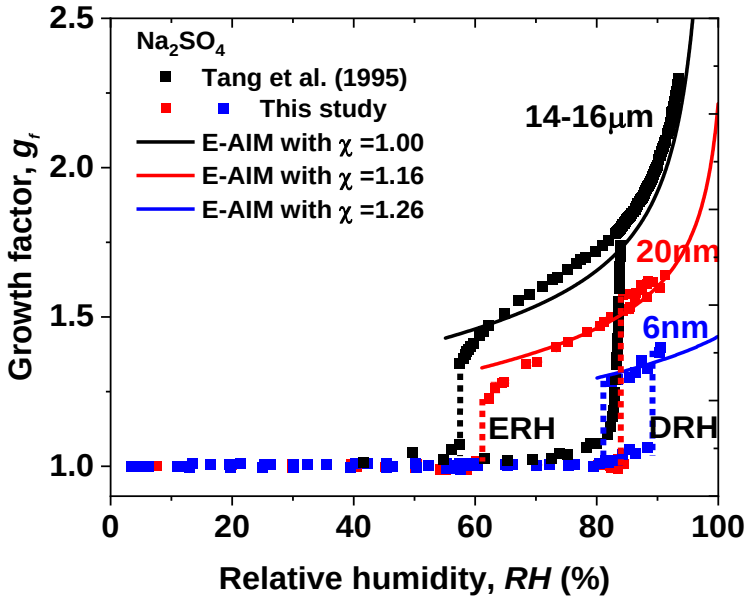

Figure 9. Mobility diameter hygroscopic growth factors (g_f) and deliquescence and efflorescence relative humidity (DRH and ERH; red and blue dashed lines) of sodium sulfate nanoparticles with a dry diameter of 20 nm (red squares) and 6 nm (blue squares), respectively. Black squares and black dashed lines show the respective results from Tang et al. (1995) with electrodynamic balance (EDB), respectively. In this study, the black, red, and blue curves show the E-AIM predictions, including the Kelvin effect and shape factors (χ).

Supplementary Information

Table S1: Deliquescence and efflorescence relative humidity of ammonium sulfate below 100 nm reported by difference studies in temperature ranging from 290-300K

Deliquescence relative humidity (DRH)	Efflorescence relative humidity (ERH)	Technique (initial particle size)	Reference
80-86%* (8 nm) 80-85%* (10 nm) 80-90%* (15 nm) 78-80%* (30 nm) 76-79%* (50 nm)		HTDMA (8.10,15,30,50 nm)	Hämeri et al. (2000) (cf. Figure 2a, 2b, 2c, 2d, and 2e)
76-80%*	65%*	HTDMA (100 nm)	Gysel et al. (2002) (cf. Figure 2)
82% (6 nm) 81% (8 nm) 80% (10 nm) 82% (20 nm) 80% (40 nm) 80% (60 nm)	34% (6 nm) 33% (8 nm) 35% (10 nm) 35% (20 nm) 36% (40 nm) 33% (6 nm)	HTDMA (6,8,10,20,40,60 nm)	Biskos et al. (2006b)
-	27-31%* (43.7 nm) 21-30.7%* (47 nm)	HTDMA (43.7,47 nm)	Gao et al. (2006) (cf. Figure 5)

78-81%*	-	HTDMA (100 nm)	Duplissy et al. (2009) (cf. Figure 4)
77-78%*	-	HTDMA (100 nm)	Duplissy et al. (2009) (cf. Figure 4)
78-80%*	29-34%*	HTDMA (100 nm)	Mikhailov et al. (2009) (cf. Fig4)
77-78%	-	HTDMA (100 nm)	Wu et al. (2011)

-: Not reported

*: Data retrieved from figures in the references

80-86%: Non-prompt deliquescence of 8-nm ammonium sulfate from 80% to 86% RH

27-31%: Non-prompt efflorescence of 43.7-nm ammonium sulfate from 31% to 27% RH

82%: Prompt deliquescence of 6-nm ammonium sulfate at 82% RH

Table S2. Residence time (s) for the water equilibrium for particles with diameter ranging from 6 to 100 nm particles at RH=90% at 25°C

χ	1	0.1	0.01	0.001
100nm	6.26×10^{-6}	3.55×10^{-5}	3.12×10^{-4}	0.00310
60nm	6.04×10^{-6}	3.34×10^{-5}	3.07×10^{-4}	0.00300
20nm	6.03×10^{-7}	5.17×10^{-6}	5.08×10^{-5}	5.07×10^{-4}
10nm	1.88×10^{-7}	1.74×10^{-6}	1.73×10^{-5}	1.72×10^{-4}
8nm	3.10×10^{-8}	1.93×10^{-7}	1.82×10^{-6}	1.81×10^{-5}
6nm	1.48×10^{-8}	1.08×10^{-7}	1.04×10^{-6}	1.03×10^{-5}

Table S3. Average sizing offset between nano-DMAs in the nano-HTDMA system at RH below 10%

	Average sizing offset (nm)[a]	Size agreement between nano-DMA1 and nano-DMA2[b]
100-nm $(NH_4)_2SO_4$	0.619	0.619%
60-nm $(NH_4)_2SO_4$	0.299	0.498%
20-nm $(NH_4)_2SO_4$_	0.278	1.39%
10-nm $(NH_4)_2SO_4$	0.0896	0.897%
8-nm $(NH_4)_2SO_4$	-0.0160	-0.200%
6-nm $(NH_4)_2SO_4$_	0.0840	1.40%

[a] Calculation from $(\overline{D}_{measured\ by\ nano-DMA2} - D_{selected\ by\ nano-DMA1})$

[b] Calculation from $[(\overline{D}_{measured\ by\ nano-DMA2} - D_{selected\ by\ nano-DMA1})/\ D_{selected\ by\ nano-DMA1}] \times 100\%$

Table S4. The values of D_m, g_f, and D_m (< 5% RH) of 10-nm ammonium sulfate of Biskos et al. (2006b) system in the different RHs.

Relative humidity	D_m	g_f	D_m (<5 % RH)
25%	10.4	0.991	10.5
76%	10.4	1.02	10.2
78%	10.5	1.03	10.3
80%	13.3	1.29	10.3
44%	11.6	1.12	10.3
35%	11.2	1.08	10.4
34%	10.6	1.01	10.5
32%	10.2	1.00	10.2
31%	10.2	1.00	10.2
30%	10.4	1.00	10.4
29%	10.3	1.00	10.3
24%	10.3	0.997	10.3

Table S5. Uncertainties of nano-DMA voltage (V) and sheath flow rates (Q_{sh}), and calculated size uncertainty.

Size (nm)	Uncertainties in V and Q_{sh}	Uncertainty (Sizing accuracy)
100	2.65×10^3±0.0259 V, 10±0.0200 L min^{-1}	0.200%
60	1.06×10^3±0.0269 V, 10±0.0200 L min^{-1}	0.200%
20	1.31×10^2±0.0152 V, 10±0.0200 L min^{-1}	0.200%
10	3.37×10^1±0.0244 V, 10±0.0200 L min^{-1}	0.213%
8	2.16×10^1±0.0373 V, 10±0.0200 L min^{-1}	0.264%
6	1.22×10^1±0.0692 V, 10±0.0200 L min^{-1}	0.601%

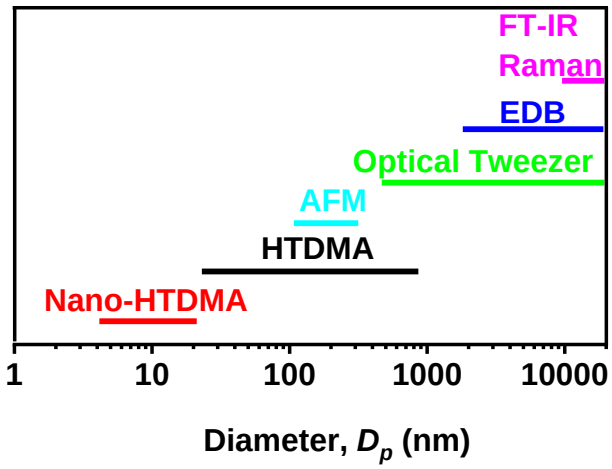

Figure S1. Methods for measuring hygroscopicity of atmospheric aerosol particles in different size (D_p).

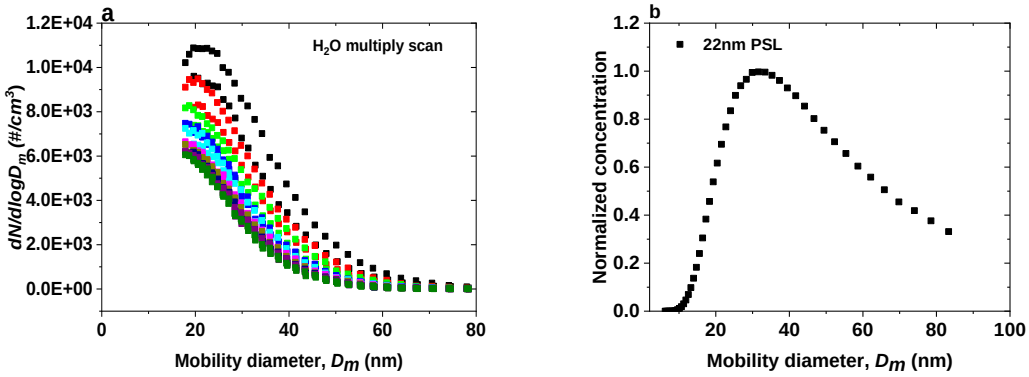

Figure S2. (a) Number concentration scanned for water nanoparticles by the nano-DMA2 at RH below 5 % at 298 K. **(b)** Normalized number size distribution scanned for 22-nm PSL nanoparticles by nano-DMA2 after calibration.

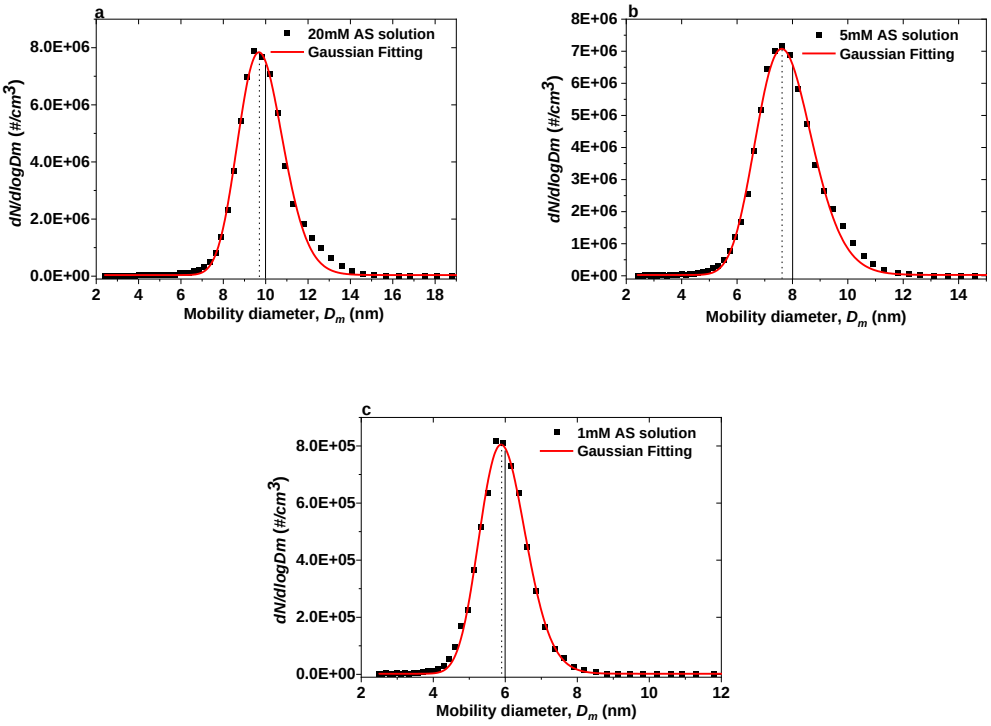

Figure S3. Number size distribution of ammonium sulfate (AS) nanoparticles (black solid square) generated by the electrospray. **(a)** 20mM, **(b)** 5mM, and **(c)** 1mM AS solution. The dotted line marks peak diameter from the Gaussian fits for the scan (red curve). The black solid lines mark the diameters of the monodispersed nanoparticles selected by the nano-DMA1.

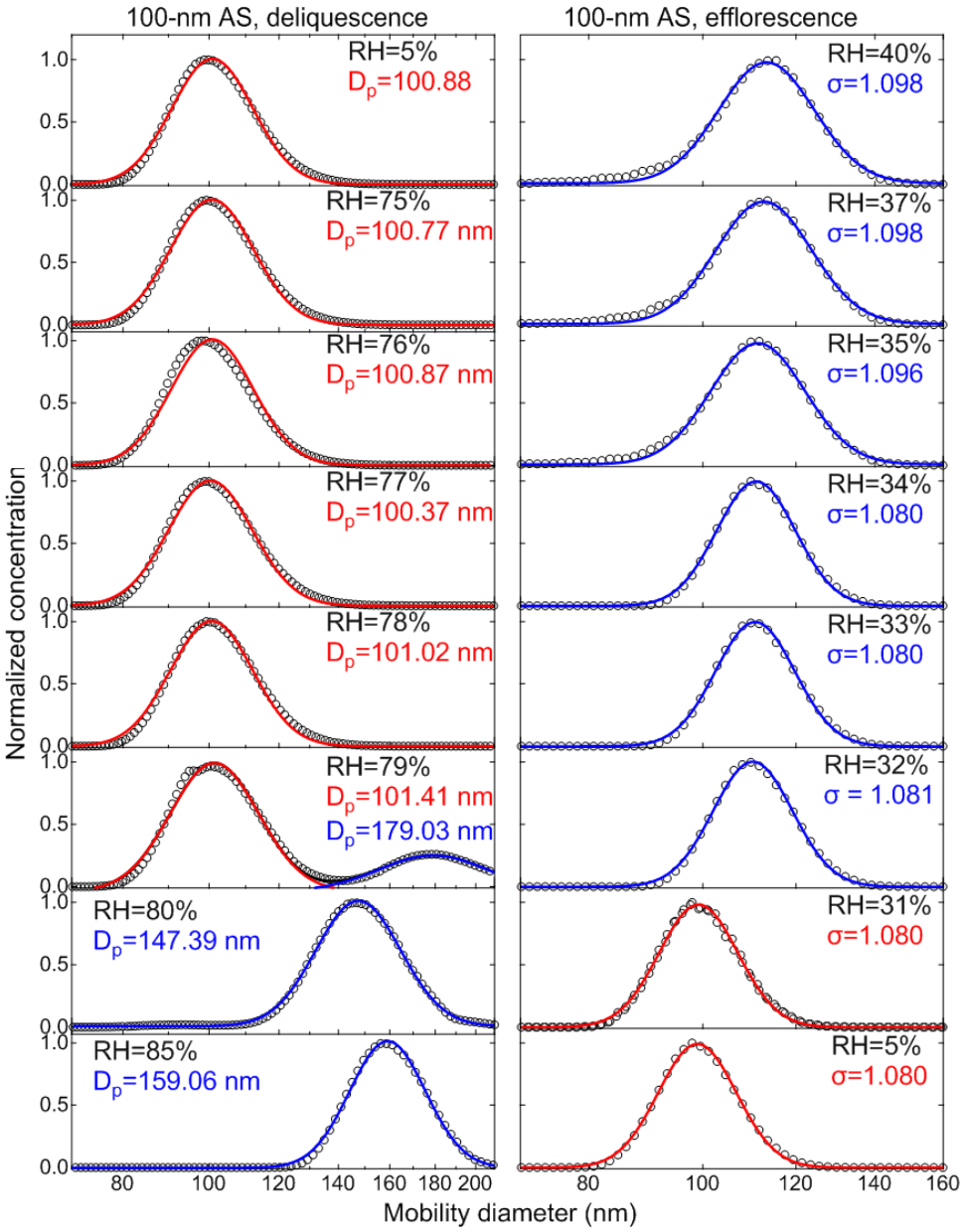

Figure S4. Deliquescence-mode **(a)** and efflorescence-mode **(b)** of 100-nm ammonium sulfate (AS) aerosol nanoparticles. The measured (black square) and fitted (solid lines) normalized size distribution are shown for increasing RH (5%→X%, where X is the RH value given in each panel) and decreasing RH (5%→97%→X%, where X is the RH value given in each panel), respectively. The red and blue lines represent the aerosol nanoparticles in the solid and liquid state, respectively.

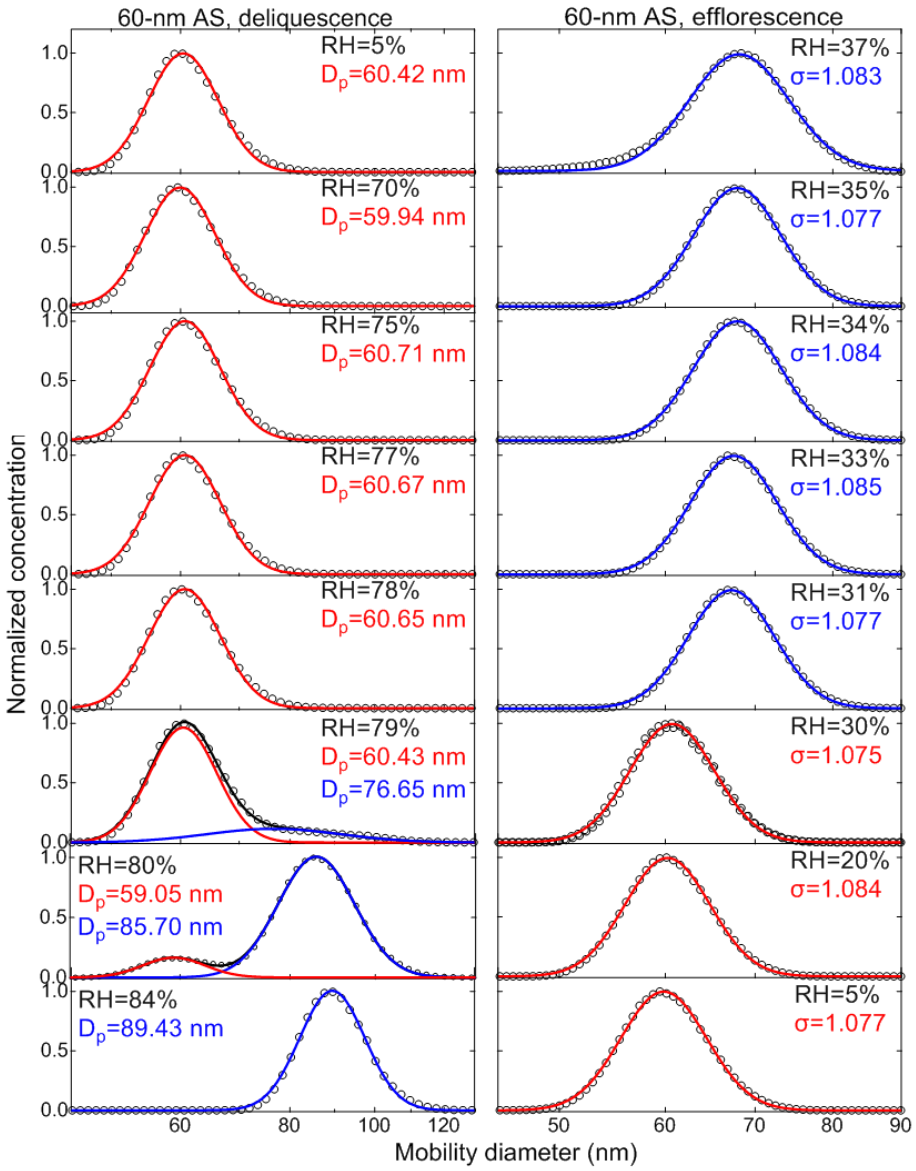

Figure S5. Deliquescence-mode **(a)** and efflorescence-mode **(b)** of 60-nm ammonium sulfate (AS) aerosol nanoparticles. The measured (black square) and fitted (solid lines) normalized size distribution are shown for increasing RH (5%→X%, where X is the RH value given in each panel) and decreasing RH (5%→97%→X%, where X is the RH value given in each panel), respectively. The red and blue lines represent the aerosol nanoparticles in the solid and liquid state, respectively.

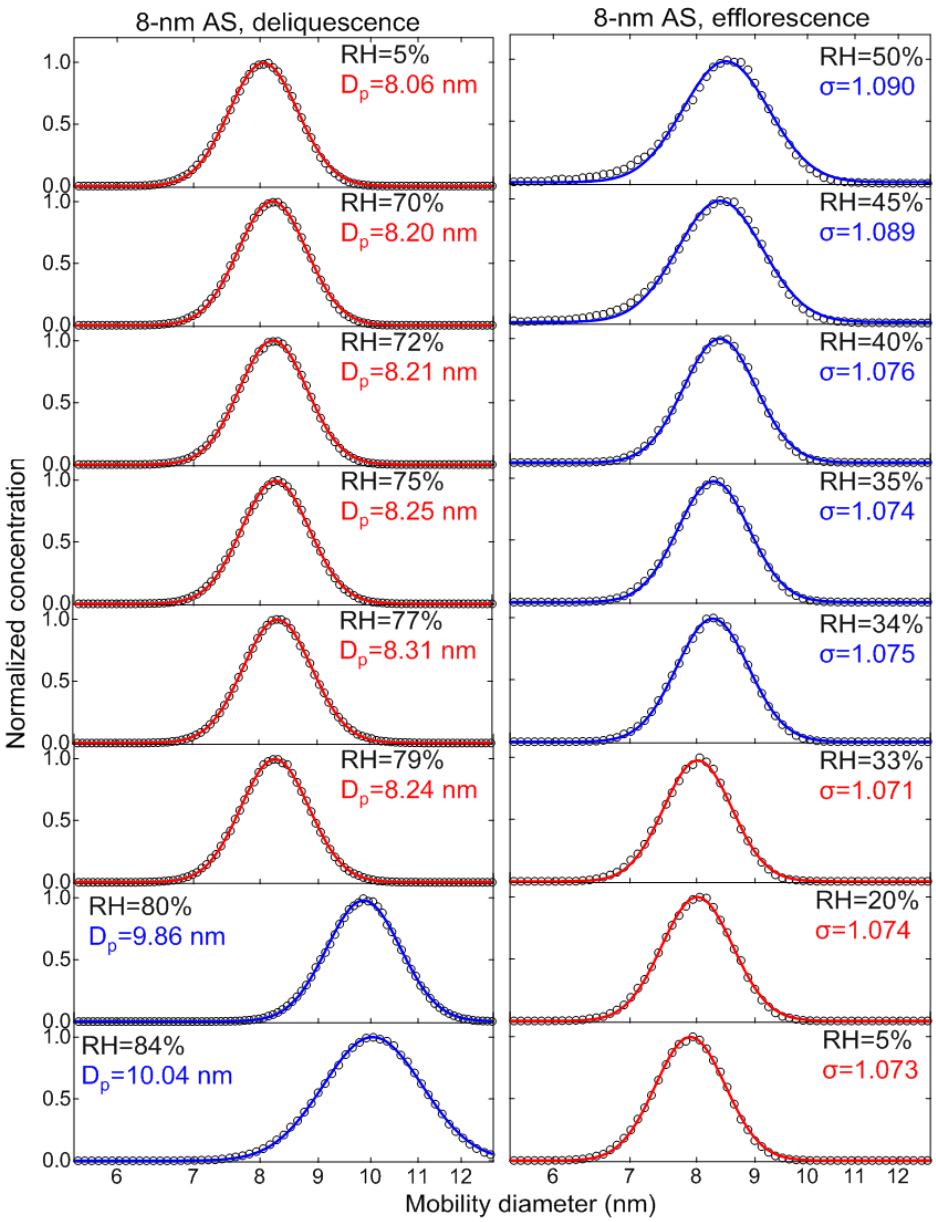

Figure S6. Deliquescence-mode **(a)** and efflorescence-mode **(b)** of 8-nm ammonium sulfate (AS) aerosol nanoparticles. The measured (black square) and fitted (solid lines, single-mode log-normal fit) normalized size distribution are shown for increasing RH (5%→X%, where X is the RH value given in each panel) and decreasing RH (5%→97%→X%, where X is the RH value given in each panel), respectively. The red and blue lines represent the aerosol nanoparticles in the solid and liquid state, respectively.

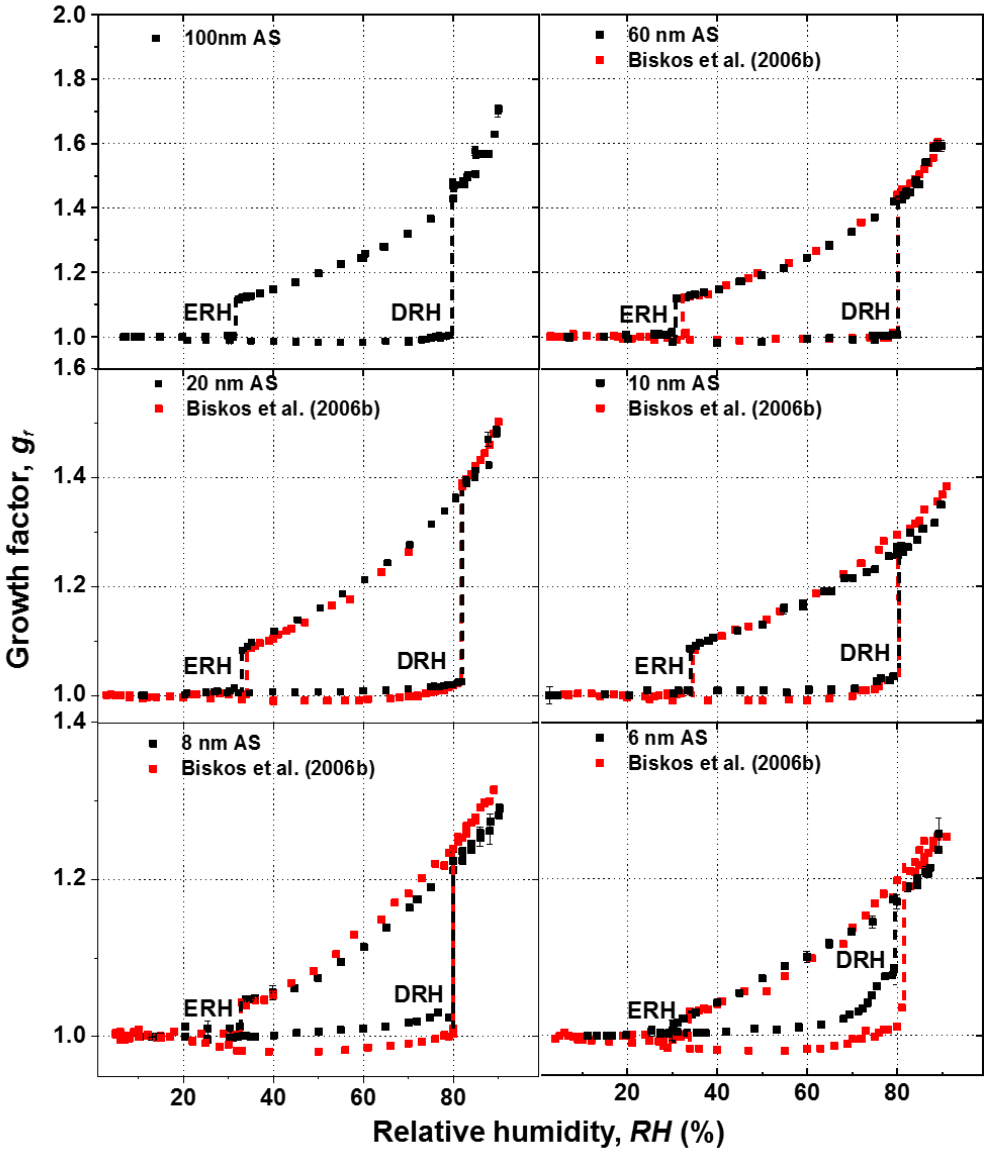

Figure S7. Mobility-diameter hygroscopic growth factors (g_r, black squares), deliquescence and efflorescence relative humidity (DRH&ERH, black dashed lines) of ammonium sulfate (AS) nanoparticles with dry diameter from 6 to 100 nm, respectively. Red squares and dashed lines show the respective results from Biskos et al. (2006b).

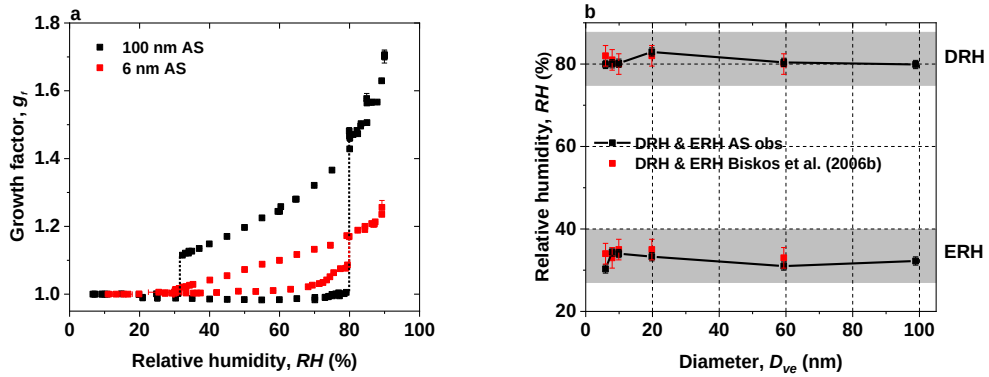

Figure S8. (a) Comparison of mobility-diameter hygroscopic growth factors (g_f) of 100-nm (black square) with 6-nm (red square) ammonium sulfate (AS) nanoparticles. **(b)** Dependence of deliquescence and efflorescence relative humidity (DRH&ERH) of ammonium sulfate (AS) on dry volume equivalent diameter (D_{ve}). The measured DRH and ERH of ammonium sulfate within RH uncertainty (black line + black square) compared with data from Biskos et al. (2006b) (red square) in the volume equivalent diameter with shape factor (χ=1.02) range from 5 to 100 nm.

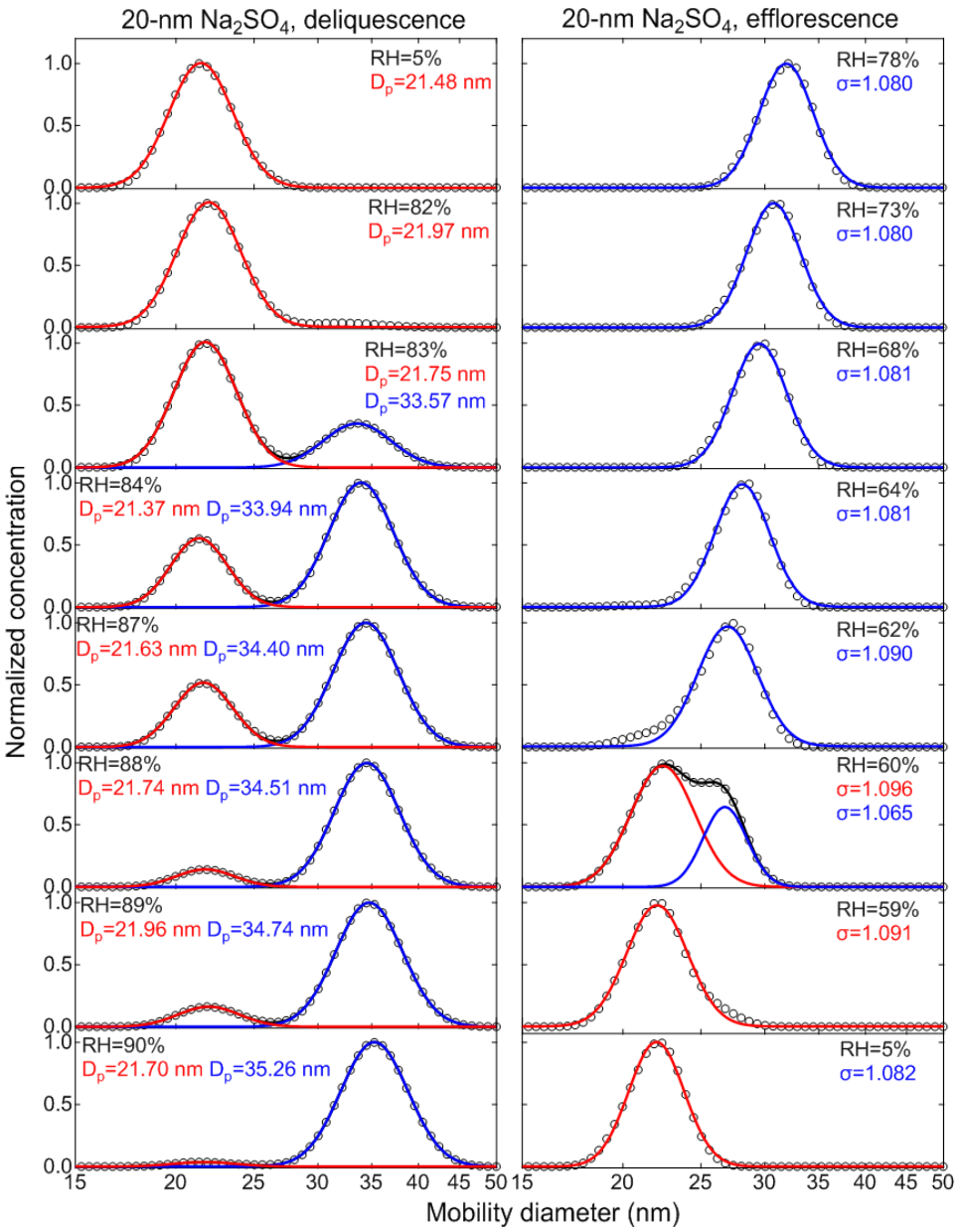

Figure S9. Deliquescence-mode **(a)** and efflorescence-mode **(b)** of 20-nm sodium sulfate aerosol nanoparticles. The measured (black square) and fitted (solid lines) normalized size distribution are shown for increasing RH (5%→X%, where X is the RH value given in each panel) and decreasing RH (5%→97%→X%, where X is the RH value given in each panel), respectively. Red/blue solid line is fitted by a single-mode log-normal fit. Red, blue, and black lines are fitted by a double-mode log-normal fit. The red and blue lines represent the aerosol nanoparticles in the solid and liquid state, respectively. The voltage applied to the nano-DMAs (0-12500 V) is kept within ±1% around the set value shown in the voltage meter.

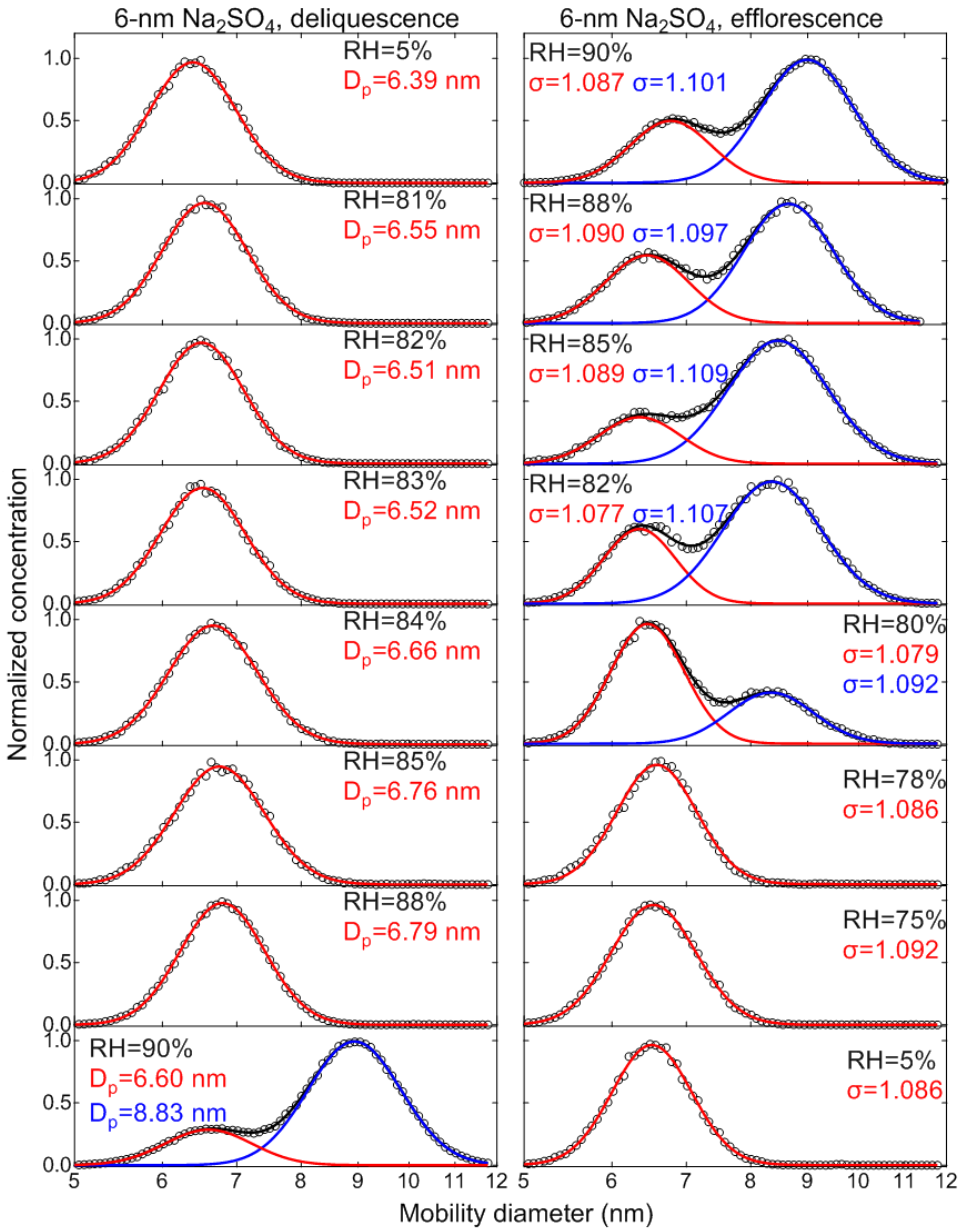

Figure S10. Deliquescence-mode **(a)** and efflorescence-mode **(b)** of 6-nm sodium sulfate aerosol nanoparticles. The measured (black square) and fitted (solid lines) normalized size distribution are shown for increasing RH (5%→X%, where X is the RH value given in each panel) and decreasing RH (5%→97%→X%, where X is the RH value given in each panel), respectively. Red/blue solid line is fitted by a single-mode log-normal fit. Red, blue, and black lines are fitted by a double-mode log-normal fit. The red and blue lines represent the aerosol nanoparticles in the solid and liquid state, respectively. The voltage applied to the nano-DMAs (0-350 V) is kept within ±1% around the set value shown in the voltage meter.

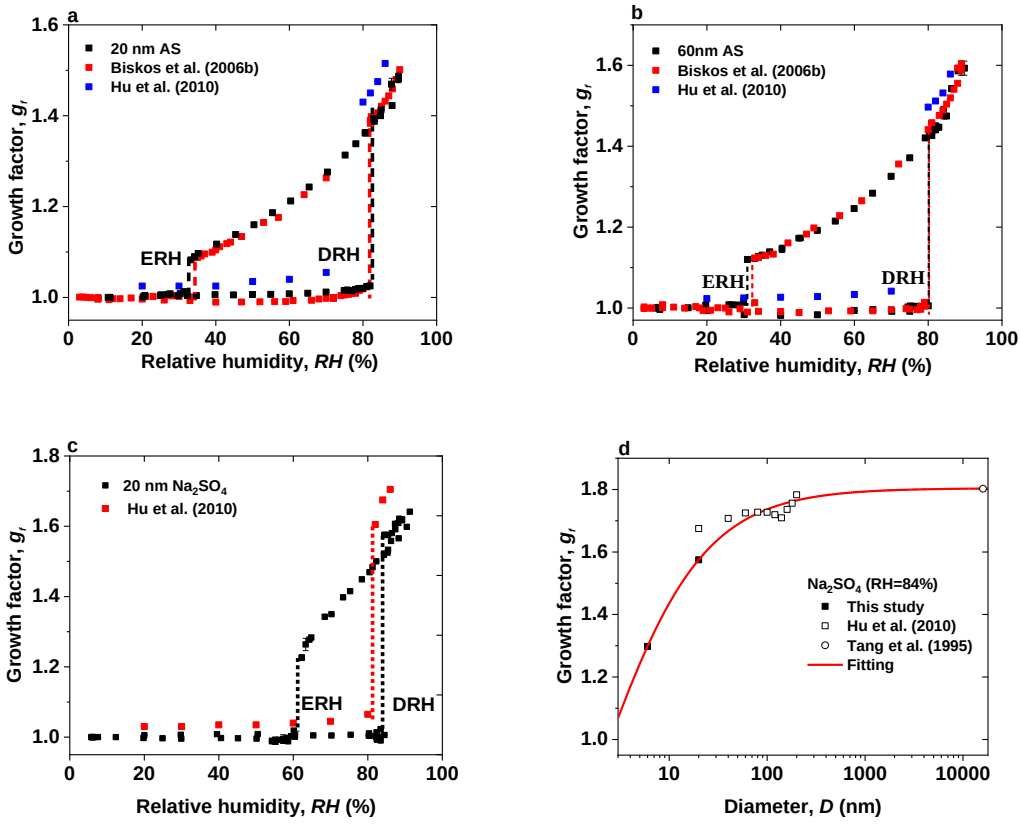

Figure S11. (a) Comparison of mobility-diameter hygroscopic growth factors (g_f) of 20-nm **(a)** and 60-nm **(b)** ammonium sulfate (AS) nanoparticles with Biskos et al. (2006b) and Hu et al. (2010). (black squares: in this study; red square: Biskos et al. (2006b); blue square: Hu et al. (2010)). **(c)** Comparison of mobility-diameter hygroscopic growth factors of 20-nm Na_2SO_4 nanoparticles with Hu et al. (2010). (black squares: in this study; red square: Hu et al. (2010)). **(d)** Mobility-diameter hygroscopic growth factors of Na_2SO_4 nanoparticles with diameter from 6 nm to 14~16 um at 84% RH (black solid squares: in this study; black open square: Hu et al. (2010); black open cycle: Tang et al. (1995)). A fitting equation ($g_f = \frac{1.804}{1+(0.5267*D)^{-0.8194}}$) based on this study at 6-nm, 20-nm Na_2SO_4, and 14~16 um data from Tang et al. (1995).

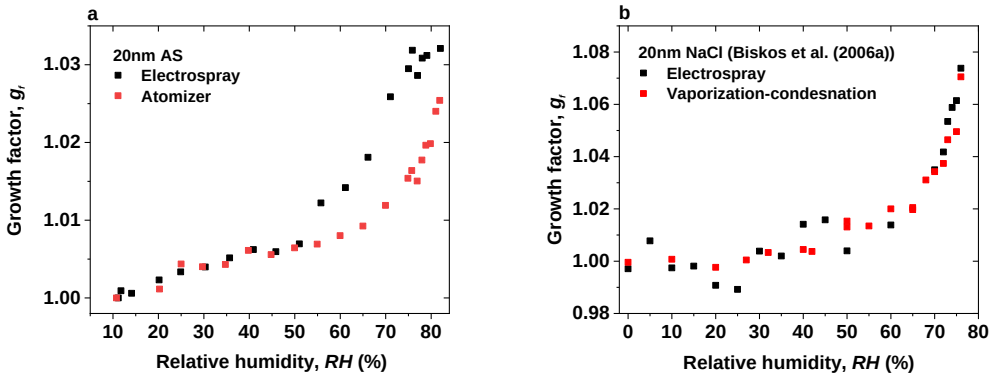

Figure S12. Hygroscopic growth factors of 20-nm **(a)** ammonium sulfate (AS) nanoparticles from our study and **(b)** sodium chloride (NaCl) nanoparticles from Biskos et al. (2006a) using the different generation methods prior to deliquescence of ammonium sulfate.

S1. Calculation of average sizing offset of 10-nm AS

The mobility growth factor (g_f) is given by:

$$g_f = \frac{D_m(RH)}{D_m(<10\ \%\ RH)} \quad \text{(S1)}$$

g_f was from the data of Biskos et al. (2006b) in the different RHs (see the SI. Fig.5). D_m was retrieved the data of Biskos et al. (2006b) in the different RHs (see the SI. Fig.2) as follows:

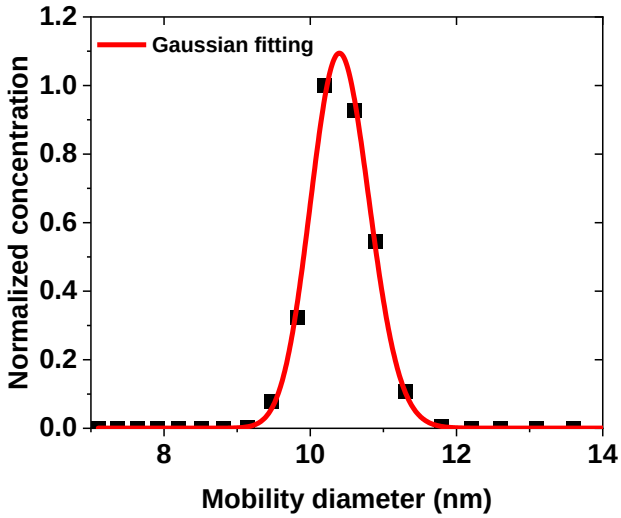

Figure S13. Measured (black square) and fitted (red solid line) normalized number size distributions are show for ammonium sulfate aerosol particles at 25% RH. The black square symbols show the data of Biskos et al. (2006b) (see the S1. Fig. 2).

Therefore, the initial dry mobility diameter (D_m (< 5% RH)) was obtained using Eq. (S1) based on values of g_f and D_m in the different RHs (see SI. S1. Table S4). We further calculated the average sizing offset of 10-nm ammonium sulfate of Biskos et al. (2006b) system based on the values of D_m (< 5% RH). The average sizing offset of 10-nm was ~3.25%.

S2. Calculation of sizing accuracy of sub-100 nanoparticles

Knutson and Whitby (1975) proposed the following theoretical differential mobility analyzer (DMA) transfer function and showed that sizing is crucially depend on sheath flow rates and high voltage (HV) applied to the DMA.

$$z_p^* = \frac{Q_{sh} ln\frac{r_2}{r_1}}{2\pi LV} \quad \text{(S2)}$$

$$z_p^* = \frac{neC_c}{3\pi\mu d_p^*} \quad \text{(S3)}$$

$$d_p^* = \frac{2VLneC_c}{3\mu Q_{sh} ln\frac{r_2}{r_1}} \quad \text{(S4)}$$

where z_p^* is the central electrical mobility, Q_{sh} is the sheath flow rate, V is the applied voltage, L is the length of the classification region within the DMA, and r_1 and r_2 are the inner and outer radii of the DMA annulus, respectively. n is the number of elementary charges of particles. e is the elementary charges. C_c is the slip correction. μ is the flow viscosity. d_p^* is the mean particle mobility diameter.

According to Eq. (S4) above, we use the following error propagation formula ((Taylor and Taylor, 1997) to calculate the uncertainties in sizing of nanoparticles. In our study, the flow accuracy of mass flow meter (TSI series 4000) is within ±2%. The deviation of voltage applied to the nano-DMAs (0-12500 V, 0-350 V) varies around the set value when test with voltage power supply (HCE 0-12500, HCE 0-350, Fug Electronic) shown in Table S5. Thence, the uncertainties in sizing of nanoparticles are obtained based on the following Eq. (S5) as shown in Table S5.

$$\frac{\delta d}{d} = \sqrt{\left(\frac{\delta V}{V}\right)^2 + \left(\frac{\delta Q_{sh}}{Q_{sh}}\right)^2} \quad \text{(S5)"}$$

3. Size dependent hygroscopicity of levoglucosan and D-glucose aerosol nanoparticles

This work is to be submitted as Lei et al. (2021):

Lei, T., Ma, N., Tuch, T., Hoffmann, T., Pöschl, U., Su, H., Wiedensohler, A., and Cheng, Y.: Size dependent hygroscopicity of levoglucosan and D-glucose aerosol nanoparticles, Atmospheric Chemistry and Physics, to be submitted, 2021

I am the first-author of this work and my contribution to this work includes performing the experiments using a nano-HTDMA for measuring the hygroscopic properties of levoglucosan and D-glucose aerosol nanoparticles with diameter down to 6 nm, analyzing all the data, making all the figures and tables, and writing the manuscript together with Dr. Cheng and Dr. Su.

The following text, figures, and tables quoted (within "") from page 65 to page 85 are exactly the same as the manuscript which is cited on page 64.

"**Abstract:** The interaction between water vapor and aerosol nanoparticles is of great significance in the atmospheric processes. However, current knowledge of hygroscopicity of sub-10 nm organic is scarcely available for literature. In this study, we investigate the hygroscopic properties of organics in size down to 6 nm (e.g., levoglucosan, D-glucose) using a nano-hygroscopic tandem differential mobility analyzer (nano-HTDMA). A reduction in diameter of sub-20 nm levoglucosan is observed during the measurements, which is explained by levoglucosan nanoparticle evaporation into gas phase, indicting high volatility of sub-20 nm levoglucosan aerosol nanoparticles. Thus, the hygroscopic growth factors of levoglucosan nanoparticles with diameters above 20 nm have been investigated. A weak size dependence of hygroscopic growth factor is observed for levoglucosan and D-glucose nanoparticles with diameters down to 20 nm. However, there is a clear size-dependent hygroscopic growth factor of D-glucose nanoparticles down to 6 nm in size. We further compare our measurements for levoglucosan and D-glucose nanoparticles with modelling results from the Extended Aerosol Inorganics Model (E-AIM) model and the ideal solution theory, respectively. The ideal solution theory agreed well with measured hygroscopic growth factors of levoglucosan and D-glucose nanoparticles with diameters higher than 15 nm, while the E-AIM model prediction describes well with results of sub-15 nm D-glucose nanoparticles.

1 Introduction

Atmospheric nanoparticles influence the radiative forcing of the earth's atmosphere (Chylek and Coakley, 1974; Charlson et al., 1992; Andreae and Gelencsér, 2006; Cheng et al., 2012). Atmospheric aerosol nanoparticles have a significant organic fraction (Zhang et al., 2004; Bzdek et al., 2011; Kulmala et al., 2013). Organics play an important role in new particle formation, subsequent growth, CCN, and thus in affecting visibility degradation, radiative forcing and climate (Dusek et al., 2010; Zhang et al., 2012; Kulmala et al., 2013). For example, it is found that an increase in mass fraction of organics during periods of new particle formation in the fields, suggesting organics involved in the growth of new particles to larger sizes and thus affecting CCN activity during new particle formation events (Dusek et al., 2010; Zhang et al., 2010; Bzdek et al., 2011; Kulmala et al., 2013). Both the size of nanoparticles and their ability to act as

CCN are directly related to its hygroscopicity that describes their ability to uptake/release water (Köhler, 1936; Kreidenweis et al., 2005; Su et al., 2010; Cheng et al., 2015; Wang et al., 2015). Therefore, the hygroscopicity of organic aerosol nanoparticles is fundamental in determining the role of aerosols in the radiative balance of the earth.

Levoglucosan aerosol nanoparticles have attracted increasing interest in recent years (Simoneit et al., 1999; Mochida and Kawamura, 2004; Mikhailov et al., 2009; Lei et al., 2014, 2018; Elias et al., 2010; Bhattarai et al., 2019) due to relative stability and high emission factors, which are considered as ideal tracer for characterization and quantitation the biomass burning (Fraser and Lakshmanan, 2000). Also, levoglucosan can contribute substantially (16.6–30.9% by mass) to the total organics in $PM_{2.5}$. D-glucose, a hydrolysis product of cellulose and levoglucosan, is one of the major pyrolysis products of wood ((Mochida and Kawamura, 2004). Levoglucosan and D-glucose substances may be representative in reproducing the hygroscopic behavior of the real biomass burning aerosol particles (Bhandari and Bareyre. 2003; Mochida and Kawamura, 2004; Chan et al., 2005; Koehler et al., 2006; Peng et al., 2010). Most previous lab studies have been focused on investigation of the hygroscopic behavior of 100-nm levoglucosan and 100-nm D-glucose aerosol nanoparticles, which mainly utilized the humidified tandem differential mobility analyzers (DMAs) (Mikhailov et al., 2004; Mochida and Kawamura. 2004; Koehler et al., 2006; Lei et al., 2014; 2018).

Early studies show that the solubility of ammonium sulfate and sodium sulfate exhibits a strong size dependence (Cheng et al., 2015). However, it is not clear how the size effect is going to influence the hygroscopic growth of organics, especially with no deliquescence relative humidity (DRH) and efflorescence relative humidity (ERH). There is the different size effect on the hygroscopicity (g_f, DRH, ERH) between inorganic nanoparticles and large particles (Hämeri et al., 2000, 2001; Biskos et al., 2006a, b, 2007; Lei et al., 2020). One of size dependence of the hygroscopicity of nanoparticles is the decrease in hygroscopic diameter growth factor with decreasing size of nanoparticles in the whole relative humidity (RH) range. Another one is the size dependence of DRH and ERH of nanoparticles. For example, in the previous studies, the hygroscopic growth factors of either ammonium sulfate, sodium sulfate, or sodium chloride nanoparticles decrease substantially with decreasing size down to 6 nm (Biskos et al., 2006a, b, 2007, Lei et al., 2020). Also, Biskos et al. (2006b) observed no

significant difference in the DRH and the ERH between ammonium sulfate nanoparticles with dry diameters of 6 and 60 nm (Let et al., 2020), while a pronounced difference of the DRH is up to 10 % RH between sodium chloride nanoparticles with dry diameters of 6 and 60 nm (Biskos et al., 2006a). However, there are only very few lab studies on investigating size dependence of hygroscopicity (g_f, DRH, ERH) of organic aerosol nanoparticles (Wang et al., 2017). Besides technique limitation, another reason is the high diffusion of sub-100 nm organics nanoparticles, especially in the sub-20 size range, which results in the high nanoparticle losses in the HTDMA system (Seinfeld and Pandis, 2006).

For inorganic aerosols, the lack of thermodynamic properties (e.g., water activity, surface tension) for the highly supersaturated aqueous solution nanodroplets (Tang and Munkelwitz, 1994; Tang 1996; Pruppacher and Klett, 1997; Clegg et al., 1998) are limiting predictability of aerosol hygroscopic behavior of sub-100 nm aerosol nanoparticles (Cheng et al., 2015). Also, there are very few thermodynamic data in the highly supersaturated concentration for organics solution (Bhandari and Bareyre. 2003; Chan et al., 2005; Koehler et al., 2006; Peng et al., 2010) such as levoglucosan and D-glucose, which results in disagreement between model predictions and measured results. By measuring hygroscopic growth factor of particles of different sizes, we may be able to retrieve these thermodynamic data using a differential Köhler analyses (DKA) method (Cheng et al., 2015). This will further help us to understand the aerosol formation, transportation, and their interactions between water molecules.

In this study, we investigate the hygroscopic growth factors of levoglucosan and D-glucose nanoparticles in size down to 6 nm using a nano-hygroscopic tandem differential mobility analyzer (nano-HTDMA), respectively. Moreover, we compared our measurement data with that from the Extended Aerosol Inorganic Model (E-AIM) (Clegg et al., 2001; Clegg and Seinfeld, 2006; available online: http://www.aim.env.ac.uk/aim/aim.php) and the ideal solution theory, respectively.

2 Methodology

2.1 Experimental

2.1.1 Nanoparticle generation

An electrospray is employed to generate the levoglucosan and D-glucose aerosol nanoparticles of 6, 8, 10, and 15 nm using 2, 3, 5, and 10 mM aqueous solution with

50% volume fraction of a 20 mM ammonium acetate buffer solution (Chen et al., 2005; Wang et al., 2015), respectively. The generated nanoparticles are diluted by mixing with dry and filtered N_2 (1 l min^{-1}) and CO_2 (0.1 l min^{-1}), bringing aerosol nanoparticles to a dry RH state (≤ 2 % RH). Subsequently, aerosol nanoparticles pass through a Po^{210} neutralizer to reach the equilibrium charge distribution (Wiedensohler 1986). In order to avoid blocking the 25-μm capillary tube in the electrospray with high solution concentration, the aerosol nanoparticles with diameters of 20-100 nm are generated by an atomizer with 0.01 wt % organic solution (e.g., levoglucosan and D-glucose). The chemical substances and their physical properties are characterized in Table S1. These solutions are prepared with distilled and de-ionized million-Q water (resistivity of 18.2 MΩ cm at 298.15 K). In addition, the solution concentrations are adjusted so that the sizes selected by the nano-DMA1 are always slightly larger than the peak diameter of the number size distribution of the generated nanoparticles to minimize the influence of the multiple charged nanoparticles in hygroscopicity measurements.

2.1.2 Nano-HTDMA setup

Figure 1 shows a schematic of the nano-HTDMA system for investigating the hygroscopic behavior of aerosol nanoparticles. The detailed description, calibration, and validation of nano-HTDMA setup have been reported in previous paper (Lei et al., 2020). In brief, the polydisperse aerosol nanoparticles pass through a silica gel diffusion dryer and a Nafion gas dryer (TROPOS; model no. ND.070), bring the aerosol nanoparticles to be dry state at RH below 10 %. The dry aerosol nanoparticles are charged by Kr^{85} bipolar charger and then enter the first nano-differential mobility analyzer (nano-DMA1; TROPOS; model no. Vienna-type short DMA)), where a monodisperse distribution of nanoparticles with the desired dry diameter is selected. The monodispersed nanoparticles subsequently are exposed to the different RH conditions, which can be set to deliquescence mode (from low RH to high RH for measuring deliquescence) or efflorescence mode (from the high RH to low RH for measuring efflorescence). In the deliquescence mode, the dry aerosol nanoparticles are gradually humidified to a target RH through a Nafion humidifier (NH-1; TROPOS; model no. ND.070, length 60 cm). In the efflorescence mode, after deliquescence of aerosol nanoparticles in a Nafion humidifier (NH-2; Perma Pure; model no. MH-110, length 30 cm), the deliquesced aerosol nanoparticles are stepwise dried to a target RH in NH-1. The number size distribution of the humidified nanoparticles is then measured

by a nano-differential mobility analyzer (nano-DMA2) at a target RH through a Nafion humidifier (NH-3; Perma Pure; model no. PD-100) coupled with an ultrafine condensation particle counter (CPC; TSI; model no. 3776). To have the uniform RH within the nano-DMA2 for the sizing accuracy, the difference between the sheath flow RH (RH_s) and the aerosol flow RH (RH_a) upstream of the nano-DMA2 is kept <1 %. Most importantly, the temperature difference between inlet and outlet of the nano-DMA2 is maintained below 0.2 °C. In addition, the residence time between the humidifier and the nano-DMA2 (~5.4 s) and deliquescence time for aerosol nanoparticles (~0.07 s) are sufficient for water-soluble aerosol nanoparticles to equilibrate with water vapor at a given RH and to occur solid-liquid phase transition (Kerminen 1997; Duplissy et al., 2005; Raoux et al., 2007).

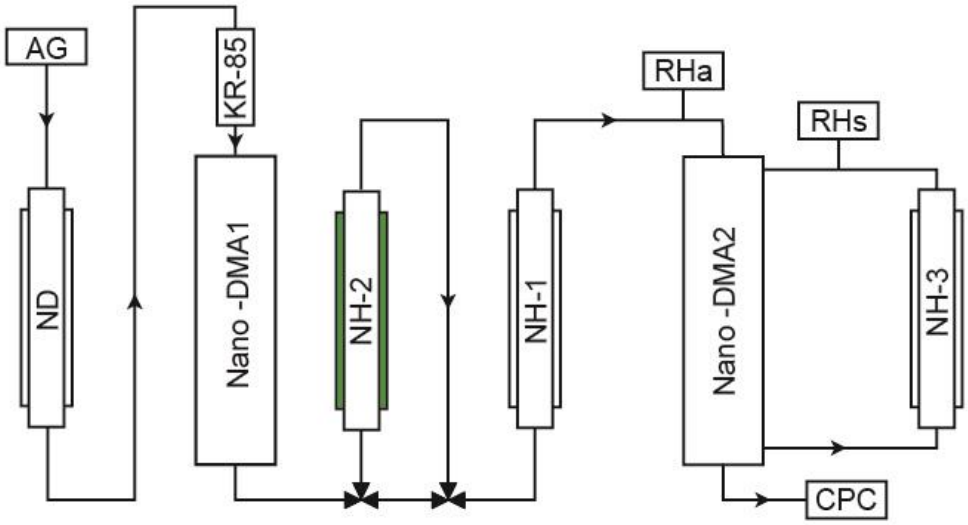

Figure 1. Experimental setup of the nano-HTDMA. Here, AG: aerosol generator (aerosol atomizer or electrospray); ND: nafion dryer; Kr-85: Krypton source aerosol neutralizer; Nano-DMA: nano differential mobility analyzer; NH: nafion humidifier; CPC: condensation particle counter; Black line: aerosol line; RH_a and RH_s (measured by RH sensors) represent the RH of aerosol and sheath flow in the inlet of nano-DMA2, respectively.

2.2 Theory and modeling methods

2.2.1 Köhler model

The equilibrium water saturation ratio (s) over a spherical droplet is equal to the fractional ambient relative humidity ($\frac{RH}{100}$) (Köhler 1936), is given by the following expression:

$$\frac{RH}{100} = s = a_w exp\left(\frac{4\sigma_{sol} v_w}{RTG_f D_s}\right) \quad (1)$$

where a_w is the water activity of the solution droplet, σ_{sol} is the liquid-vapor interfacial energy of solution droplet (also called liquid-vapor surface tension), v_w is the partial molar volume of water, R is the universal gas constant, T is the temperature, G_f is the diameter growth factor of aerosol particles, and D_s is the dry diameter of spherical aerosol particles. a_w, σ_{sol}, and v_w are all as a function of composition of solution droplet at a given temperature. These parameters within Köhler model are described in details in the following section. Note that, in this study, using the Köhler model is to calculate growth factor as a function of RH and then compared with measured growth factor of aerosol nanoparticles with diameter down to 6 nm.

Partial molar volume of water v_w can be expressed as a function of solution density as follows

$$v_w = \frac{M_w}{\rho_{sol}}(1 + \frac{dln\rho_{sol}}{dlnx_s}) \quad (2)$$

Here M_w is the molar mass of water, ρ_{sol} is the solution density, and x_s is the solute mass fraction (Kreidenweis et al., 2005).

The diameter growth factor G_f of spherical particles is defined by the following expression

$$G_f = (\frac{\rho_s}{x_s \rho_{sol}})^{\frac{1}{3}} \quad (3)$$

ρ_s and ρ_{sol} are the density of solute and solution, respectively, and x_s is the solute mass fraction.

2.2.2 Ideal solution growth factor

The ideal solution theory has been described in Mochida and Kawamura (2004) and Lei et al. (2014), assuming that the water activity a_w of the solution containing non-volatile and non-electrolyte solute component is equal to the molar ratio of water in the solution. Also, for an ideal solution, the partial molar volume of pure water in the solution is equal to the molar volume of pure water. Since the hygroscopic diameter growth factor measurements are on volume basis using nano-HTDMA system, the expression of Gf as a function of molar ratio (x_j), molar mass (M_j), and mass density (ρ_j) of components j as follows:

$$GF = \left[\frac{\sum_j \left(x_j M_j \frac{1}{\rho_j}\right)}{\sum_{j,j\neq w}\left(x_j M_j \frac{1}{\rho_j}\right)}\right]^{\frac{1}{3}} \quad (4)$$

Thus, in the case of an ideal solution, applying ideal solution theory to Köhler equation (Eq. (1)) is more applicable in dilution solution without phase transition of solute components.

2.2.3 Growth factor prediction by E-AIM model

Extended Aerosol Inorganic Model (E-AIM) (http://www.aim.env.uea.ac.uk/aim/model3/model3a.php) is a thermodynamic equilibrium model used for calculating phase partitioning (gas/liquid/solid). Most importantly, the E-AIM mode is able to model thermodynamic properties (e.g, water activity, liquid-vapor interfacial energy, and solution density) in the highly supersaturated concentration solution (Dutcher et al., 2013). Also, the standard universal quasi-chemical functional group activity coefficients (UNIFAC) within AIM can be used to predict a_w, σ_{sol}, and ρ_{sol} of organic aqueous solution (Fredenslund et al., 1975; Hansen et al., 1991). Note that in the following, The E-AIM calculations based on standard UNIFAC group contribution method are to predict hygroscopic growth factors of organic aerosol particles. (i.e., E-AIM model (standard UNIFAC) growth curves as a function of RH are based on Eq. (1) and Eq. (3).).

3 Results and discussion

3.1 Size dependent hygroscopicity of levoglucosan

Figure 2 shows the humidogram of 100-nm levoglucosan nanoparticles measured by the nano-HTDMA system. Levoglucosan nanoparticles absorb water continuously from 5 % to 90 % RH. Also, they stepwise release water as RH decreases down to 5 %. For example, the hygroscopic growth factors of levoglucosan nanoparticles at 80 % RH, 90 % RH are 1.15, 1.30, respectively in the deliquescence mode, which is similar to that of levoglucosan nanoparticles in the efflorescence mode (shown in Fig. S1). A good agreement in the hygroscopic growth factors of levoglucosan nanoparticles between deliquescence and efflorescence mode suggests growing and shrinking of particles are in equilibrium with water vapor surrounding moisture conditions. However, no prompt phase transition of levoglucosan nanoparticles is observed in both deliquescence and efflorescence mode. The possible reason is that levoglucosan

nanoparticles could be supersaturated condition even at RH below 5%. i.e., the nanoparticles at RH below 5% could consist of a minor fraction of water in the levoglucosan nanoparticles. A similar non-prompt phase transition of levoglucosan nanoparticles was observed in the previous studies (Mochida and Kawamura, 2004; Chan et al., 2005; Svenningsson et al., 2006; Mikhailov et al., 2008). Compared to the previous studies, in general, our results are in good agreement with measurement results of previous data, but there is a difference in the hygroscopic growth factor of levoglucosan nanoparticles between Mikhailov et al. (2008) and this study. The reason is that Mikhailov et al. (2008) used minimum mobility diameter measured in the hydration&dehydration mode instead of the initial dry mobility diameter measured in the hydration or dehydration mode to calculate the hygroscopic growth factor of levoglucosan nanoparticles, which could lead to the higher hygroscopic growth factors of levoglucosan nanoparticles than that of this study.

Figure 3 shows measured size-resolved hygroscopic growth factors of levoglucosan nanoparticles against RH. Firstly, we observed a good agreement of hygroscopic growth factors of levoglucosan with diameters from 20 to 100 nm in both deliquescence and efflorescence mode (shown in Fig. S1). For example, the measured growth factors of 100-nm levoglucosan nanoparticles are 1.18 and 1.26 at 80% and 88%, respectively, which are similar to measurement results of 60-nm and 20-nm levoglucosan nanoparticles. Secondly, there is a weak size dependence of hygroscopic growth factors of levoglucosan nanoparticles with diameters down to 20 nm. E.g., a difference in hygroscopic growth factor between 100 and 20-nm levoglucosan nanoparticles is ~0.02 at 88 % RH. Also, the use of E-AIM model and ideal solution theory is to predict our measurement results as shown in Fig. 3a and 3b, respectively. E-AIM (standard UNIFAC) model is applied to estimate the hygroscopic growth of organic aerosol nanoparticles according to UNIFAC group contribution method. Ideal solution theory is used to characterize water absorption of the diluted aqueous solution nanodroplets. Due to Kelvin effect, these model predictions are expected to present a size dependence of growth factors of nanoparticles in size from 100 down to 20 nm. For example, as shown in Fig. 3a, thermodynamic equilibrium model (E-AIM) shows a weak size dependence of the growth factors of levoglucosan nanoparticles with diameter 100, 60, and 20 nm at low RH but a strong size dependence of growth factors at RH above 70 %. The calculated growth factors of nanoparticles down to 20 nm in size are disagreed with

measured growth factors of levoglucosan nanoparticles, which is consistent with previous studies (Mochida and Kawamura, 2004; Lei et al., 2014, 2018). Mochida and Kawamura explained the possible reason for this discrepancy. The E-AIM (standard UNIFAC) calculations are optimized for organic compounds with lesser fraction of polar functional groups (Fredenslund et al., 1975; Hansen et al., 1991), but levoglucosan contains three OH groups in series. Thus, thermodynamic properties (e.g., water activity, liquid-vapor surface tension) are more likely to be invalid for levoglucosan system. However, a good agreement of growth factors of levoglucosan with diameter 100, 60, and 20 nm is observed between measurements and predictions by ideal solution theory in Fig. 3b. This suggested that these levoglucosan nanoparticles with diameter higher than 20 nm are ideal and diluted in the solution concentration. For sub-20 nm levoglucosan nanoparticle in the nano-HTDMA system, the measurements have been discussed below.

Figure 4a-b shows the measured peak diameter of normalized size distribution scanned by the nano-DMA2, which is smaller than diameter of levoglucosan nanoparticles selected by nano-DMA1. For 15-nm and 10-nm levoglucosan nanoparticles, obviously, a decrease in diameter is observed during measurements. As shown in Fig. 4a-b, the reduced sizes correspond to a decrease of 22% to 50% of the selected diameter of 15-nm and 10-nm levoglucosan nanoparticles, respectively. A similar phenomenon has been observed in the previous study (Mochida and Kawamura, 2004; Riipinen et al., 2006; Wex et al., 2007). For example, Wex et al. (2007) observed a reduction of a decrease of 6% to 10% of the dry diameter of succinic acid, for the DMA diameters of 200 nm and 250 nm, respectively, which partially is explained by succinic acid molecules evaporation to gas phase. Also, a shape factor and non-ideal of behavior of succinic acid in the concentrated concentration are more likely to lead to this decrease in particle diameter. In this study, it is recommended to estimate the ratio of gas-phase concentration to the total concentration of the generated levoglucosan particles in the different sizes. Firstly, the calculated gas-phase concentration of levoglucosan is based on the Kelvin equation and ideal gas equation as shown in Fig. 4c and Sect. S1. Fig. 4c shows that the saturation ratio of pure levoglucosan nanoparticles as droplet diameter increases from 0 to 100 nm. The inset is an enlarged view (black open square) of the saturation ratio of pure levoglucosan nanoparticles with diameters below 20 nm. The Kelvin effect on levoglucosan nanoparticles is weak at droplet diameters above 20 nm,

but a dramatically enhanced saturation ratio of levoglucosan particles with diameter decreasing is observed in the inset of Fig. 4c. Secondly, the total concentration of levoglucosan particles is estimated by Eq. (S2). Thus, the results of the ratio have been shown in Table 1 for levoglucosan nanoparticles in the diameter range from 10 to 100 nm. The calculated ratio of gas-phase concentration to the total concentration is consistent with measurements. E.g., the nanoparticle evaporation increases as levoglucosan size decreases from 100 to 10 nm, especially in the sub-20 nm size range, suggesting the high volatility of sub-20 nm levoglucosan during the measurements.

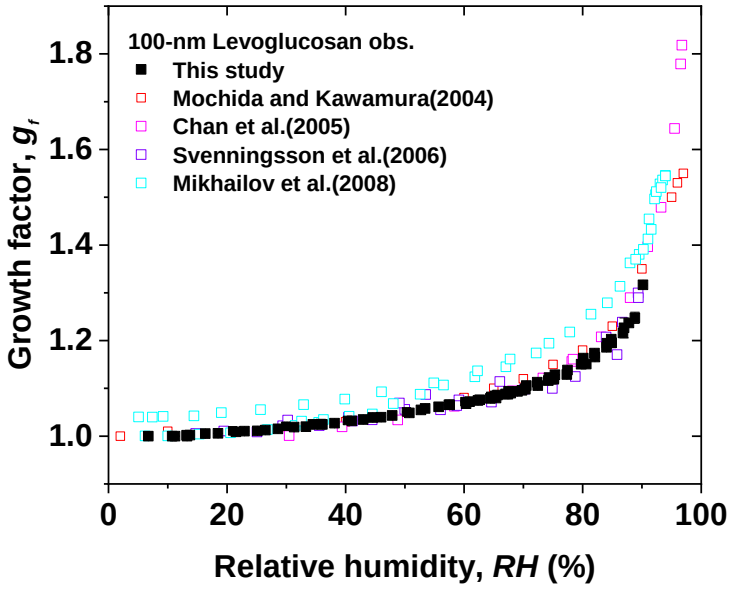

Figure 2. Hygroscopic diameter growth factor (G_f) of levoglucosan particles with dry diameter of 100 nm (black solid square). The measured data compared with observations from references (red open square: Mochida and Kawmura (2004); magenta open square: Chan et al. (2005); violet open square: Svenningsson et al. (2006); cyan open square: Mikhailov et al. (2008)).

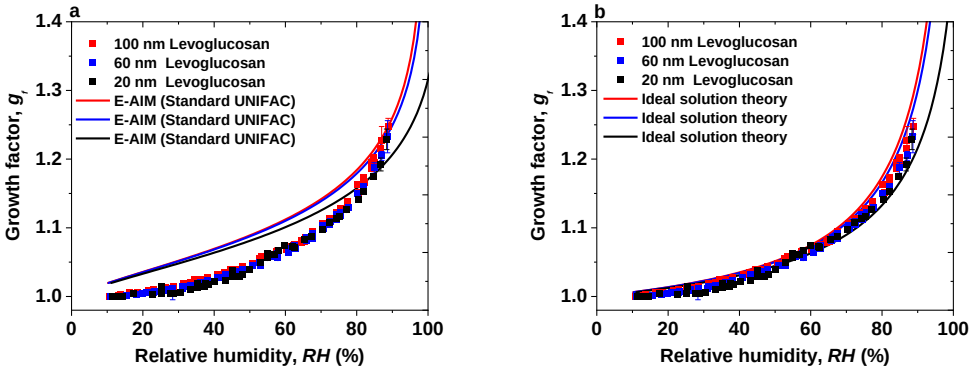

Figure 3. Hygroscopic diameter growth factor (G_f) of levoglucosan particles with dry diameter of 100 nm (red square), 60 nm (blue square), and 20nm (green square). Köhler model curves are based on different thermodynamic data sets: **(a)** AIM (Standard UNIFAC) (red, blue, green line), **(b)** ideal solution theory (red, blue, green line).

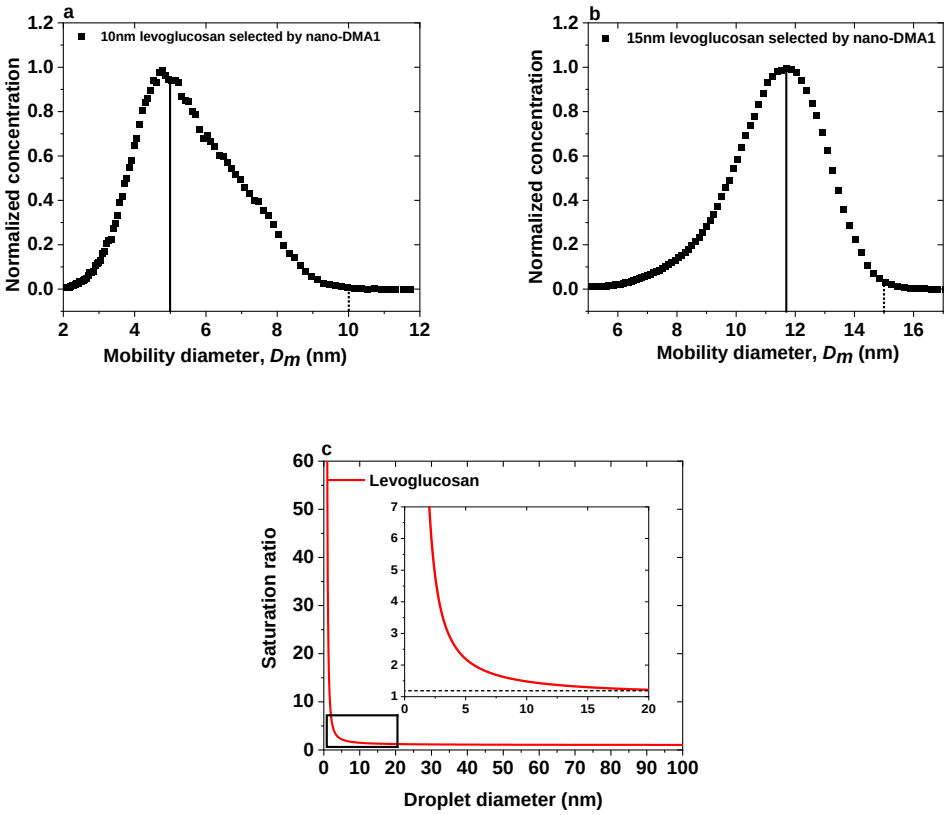

Figure 4. The normalized size distributions scanned by nano-DMA2 for: **(a)** 10 nm and **(b)** 15-nm levoglucosan at 10% at 298K. The dotted lines mark the diameters of the monodispersed nanoparticles selected by the nano-DMA1. The back solid lines mark the peak diameters from the normalized size distributions scanned by the nano-DMA2. **(c)** Saturation ratio of levoglucosan particles against droplet diameter according to the Kelvin equation ($P_A = P_A^0 exp\left(\frac{2\sigma M}{RT\rho_l R_p}\right)$, P_A and P_A^0 are vapor pressure, equilibrium vapor pressure, respectively. σ, M, ρ_l, and R_p mean surface tension, molecular weight of the substance, liquid-phase density, and a droplet of radius, respectively. The diameter range 0-20 nm for the saturation ratio of levoglucosan particles is shown as an inset. The value of surface tension of pure levoglucosan is 0.0227104 [J m^{-2}].

Table 1. Calculation of the ratio of gas-phase concentration to the total concentration for levoglucosan nanoparticles in the different sizes.

Levoglucosan diameter (nm)	The ratio of gas-phase concentration to the total concentration [a]
100	0.000811
60	0.000833097
20	0.001265617
15	0.177992638
10	0.328220471

[a] See S1

3.2 Size dependent hygroscopicity of D-glucose

Figure 5 shows the measured hygroscopic growth factors of 100-nm D-glucose nanoparticles as a function of RH. No significant difference in hygroscopic curve of 100-nm D-glucose nanoparticles is found between deliquescence and efflorescence measurement mode (Fig. S2). For example, the measured growth factors of D-glucose nanoparticles at 80 % RH, 85 % RH, 90 % RH are 1.17, 1.21, 1.30 in the deliquescence mode, respectively, in good agreement with results in the efflorescence mode (shown in Fig. S2). Also, measured hygroscopic growth factors of 100-nm D-glucose are consistent with results from previous studies in the RH range from 5% to 90% (Mochida and Kawamura. 2004; Suda and Petters, 2013; Estillore et al., 2017; Mikhailov and Vlasenko, 2020). No prompt phase transitions are observed during both deliquescence and efflorescence measurement modes. However, the bulk DRH of the D-glucose solution is ~89% to 90% at 298K (Mochida and Kawamura, 2004). The difference in hygroscopic behavior of D-glucose between 100-nm nanoparticles and bulk solution is due to morphology effect as earlier discussed in Mikhailov et al. (2009), Estillore et al. (2017), and Lei et al. (2018). For example, Estillore et al. (2017) observed a slightly amorphous structure of D-glucose particles under ambient conditions using atomic force microscopy (AFM) and D-glucose particle growth through gradual water uptake where the solid-liquid phase transition is non-discrete. Thus, a continuous growth/shrink of diameter both deliquescence and efflorescence modes is explained by the lack of crystallization of D-glucose nanoparticles upon drying to low RH and the presence of a metastable supersaturated aqueous D-glucose droplets at RH below 10%. Figure 6 shows the size dependence of measured hygroscopic growth factors of D-

glucose nanoparticles in the size range from 6 to 100 nm, with difference in growth factor up to 0.14 between 100-nm and 6-nm nanoparticles at 90 % RH (Fig. S2). A weak size dependence on the hygroscopic growth factors of particles is observed in the size range from 20 to 100 nm, which is similar to observation for levoglucosan nanoparticles with diameter down to 20 nm. However, there is a strong size dependent growth factor of D-glucose nanoparticles with diameter from 6 to 20 nm, indicating size dependence more pronounced as size deceases down to 6 nm in size. For example, measured growth factors of 20-6 nm D-glucose nanoparticles are ~1.21 and 1.13 at 85%, respectively. There is no evident difference in hygroscopic growth factors of D-glucose nanoparticles at RH below 70 % in size range from 6 to 100 nm, indicating the diameter change of D-glucose nanoparticles at low RH could be minor.

Figure 7 shows the measured hygroscopic growth factors of D-glucose nanoparticles with diameters of 6 nm and 100 nm compared with the model and the theory including Kelvin effects, respectively. E-AIM (standard UNIFAC) model is used to estimate the hygroscopic growth factor of organic aerosol nanoparticles according to UNIFAC group contribution method. Ideal solution theory is applied to describe water uptake of the diluted aqueous solution nanodroplets. The measured growth factors of 100-nm D-glucose nanoparticles are lower than predicted growth factors from E-AIM model, especially at RH below 87% shown in Fig. 7a and Fig. S3. A discrepancy exists between observations and E-AIM model predictions of D-glucose with diameter higher than 15 nm. One of possible reasons is inaccurate thermodynamic parameters applied to Eq. 1 in the diluted concentration range (e.g., water activity, liquid-vapor surface tension, the density of the aqueous nanoparticles). Another possible reason is that, as we discussed in Sect. 3.1, D-glucose contains five OH groups in series, which is disagreed with E-AIM (standard UINFAC) assumption. However, different from prediction for D-glucose nanoparticles in size down 15 nm, there is a general agreement between measured growth factors and E-AIM predictions for D-glucose nanoparticles with diameter smaller than 15 nm. Using ideal solution theory is to predict the hygroscopic curve of D-glucose nanoparticles with diameters of 6-100 nm shown in Fig. 7b and Fig. S3. There is a good agreement between measured growth factors of D-glucose with diameter higher than 15 nm and ideal theory calculations. This suggests that these physical parameters used in the ideal solution theory are accurate to predict the hygroscopic curve of nanoparticles (e.g., 60, 100 nm) and thus D-glucose nanoparticles

are ideal and diluted in solution concentration. However, an underestimation of growth factors of sub-15 nm D-glucose nanoparticles has been shown in Fig. 7b and Fig. S3 by ideal solution theory prediction. The possible reason is the unfavorable assumption of ideal solution theory, the sub-15 nm D-glucose nanodroplets can become more highly supersaturated when compared to the dilution solution.

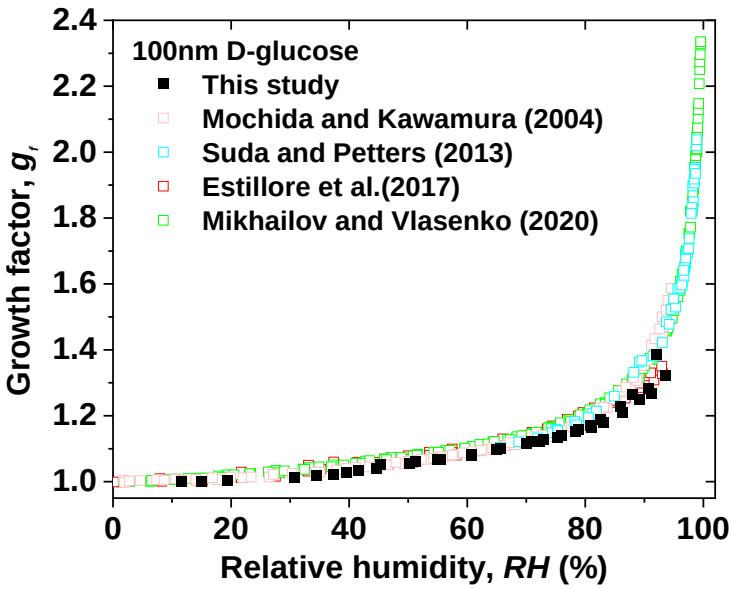

Figure 5. Hygroscopic diameter growth factor (G_f) of D-glucose particles with dry diameter of 100 nm (black solid square). The measured data compared with observations from references. (pink open square: Mochida and Kawmura (2004); red open square: Estillore et al., (2017); violet open square: Suda and Petters, (20017); green open square: Mikhailov and Vlasenko, 2020).

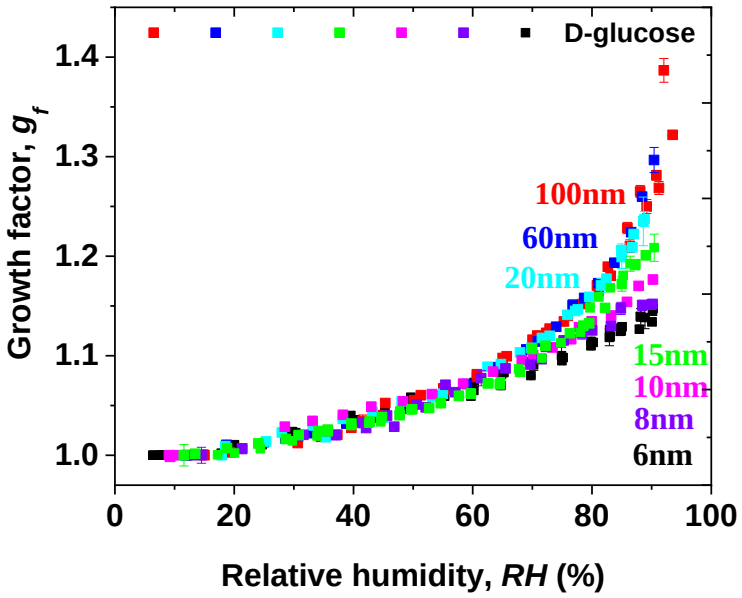

Figure 6. Hygroscopic diameter growth factor (G_f) of D-glucose nanoparticles with dry diameter of 100 nm (red square), 60 nm (blue square), 20 nm (cyan square), 15 nm (green square), 10 nm (pink square), 8 nm (royal square), and 6 nm (black square).

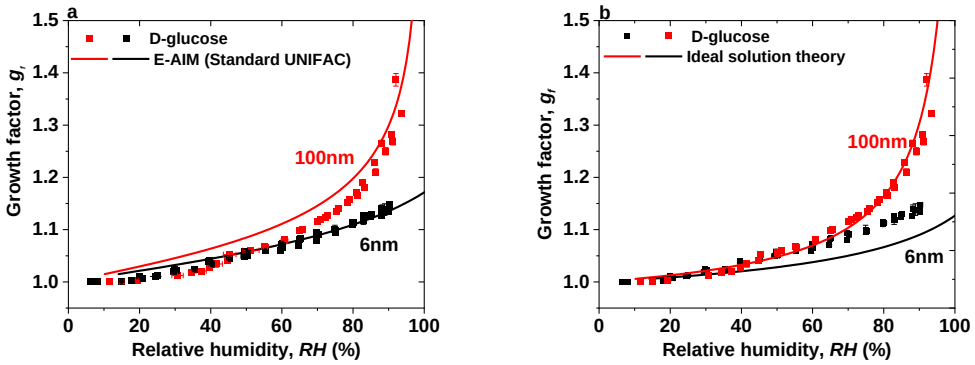

Figure 7. Hygroscopic diameter growth factor (G_f) of D-glucose nanoparticles with dry diameter of 100 nm (red square) and 6 nm (black square). Köhler model curves are based on different thermodynamic data sets: **(a)** AIM (Standard UNIFAC, red, black line) and **(b)** ideal solution theory (red, black line).

Supplementary Information

Table

Table S1. Substances and their physical properties used in this work.

Chemical compound	Chemical formula	Molar mass [$gmol^{-1}$]	Density [$g\ cm^{-3}$]	Solubility $mol\ kg^{-1}$	Solution surface tension [$J\ m^{-2}$]	Manufacture
Levoglucosan	$C_6H_{10}O_5$	162.141	1.69	-	0.073[b]	Sigma-Aldrich, 99.99%
D-glucose	$C_6H_{12}O_6$	180.16	1.562	5.69[a]	0.072	Sigma-Aldrich, 99.99%

[a] Ruegg and Blanc (1981)
[b] Tuckermann and Cammenga (2004)

Figure

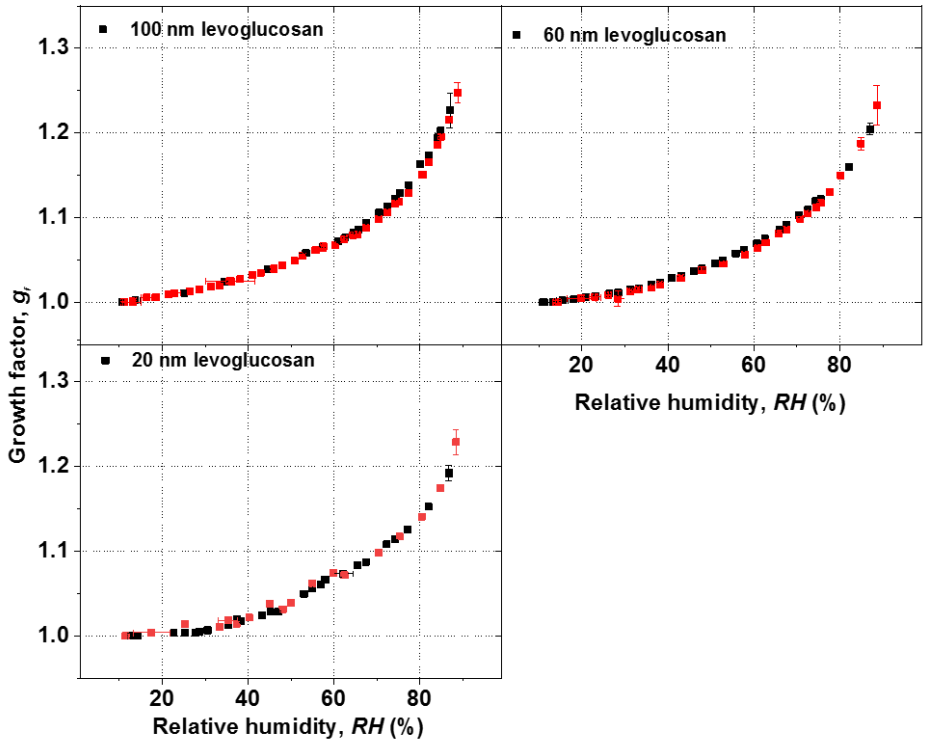

Figure S1. Mobility-diameter hygroscopic growth factors (g_f) of levoglucosan aerosol nanoparticles with dry mobility diameter from 20 to 100 nm in the deliquescence mode (black square and error bar) and the efflorescence mode (red square and error bar).

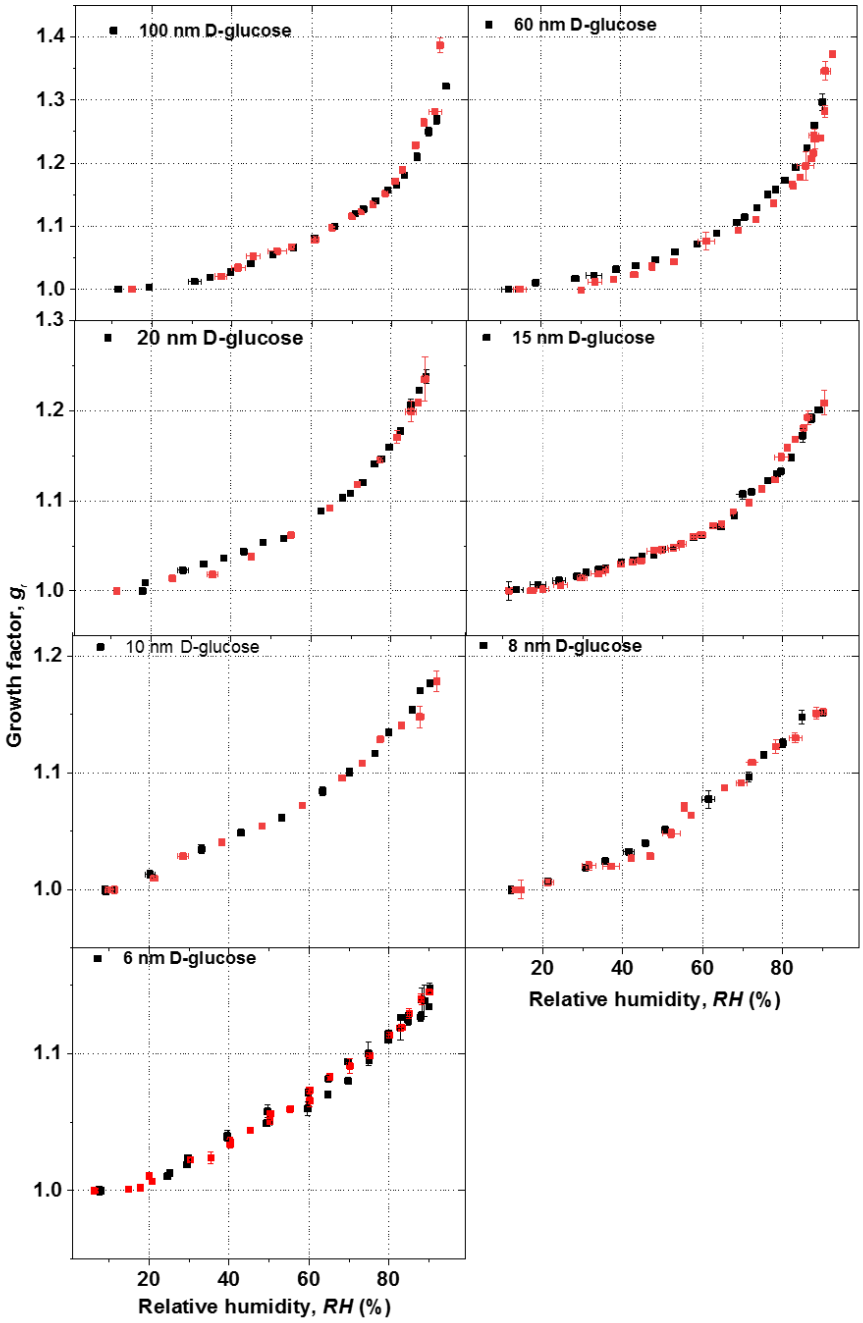

Figure S2. Mobility-diameter hygroscopic growth factors (g_f) of D-glucose aerosol nanoparticles with dry mobility diameter from 6 to 100 nm in the deliquescence mode (black square and error bar) and the efflorescence mode (red square and error bar).

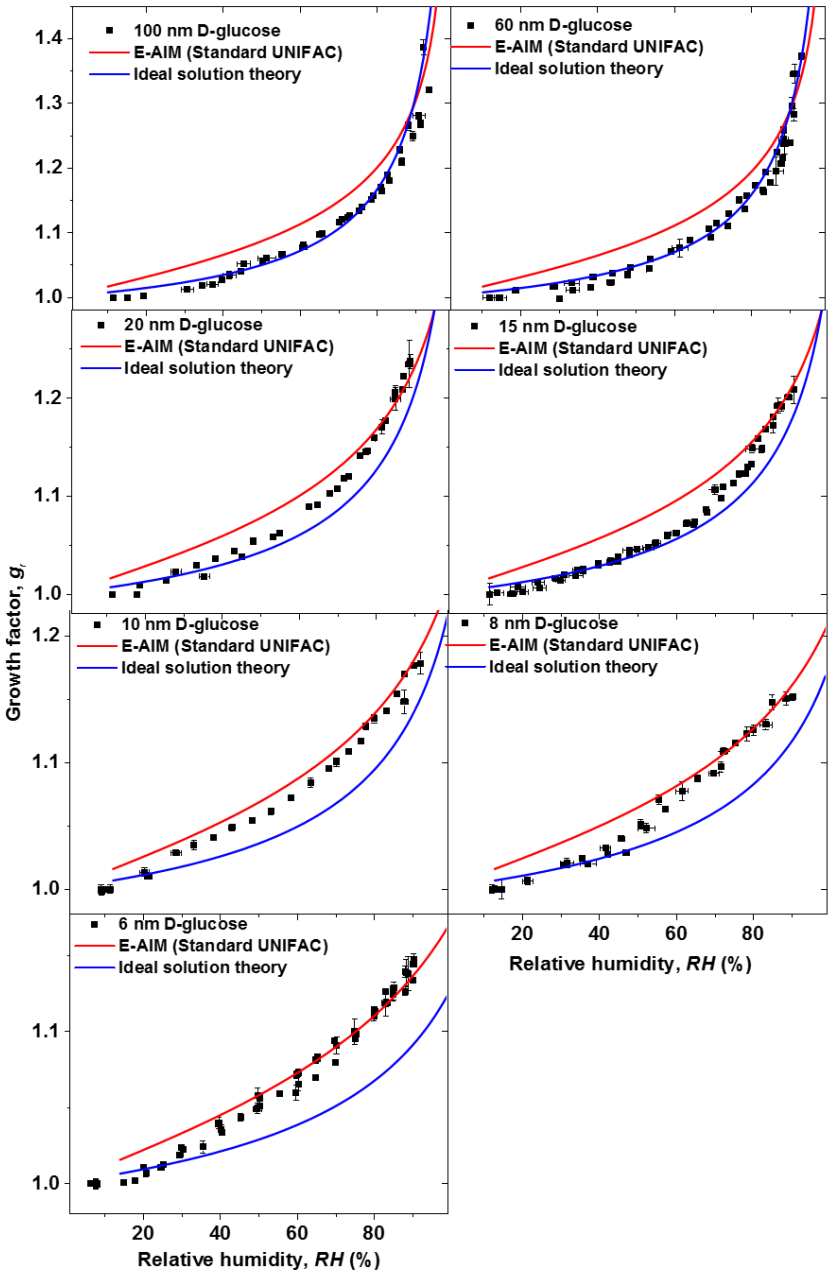

Figure S3. Mobility-diameter hygroscopic growth factors (g_f, balck squares) of D-glucose aerosol nanoparticles with dry mobility diameter from 100 down to 6nm. In comparison, E-AIM (Standard UNIFAC) (red line) and Ideal solution theory (blue line) predict growth factors of D-glucose aerosol nanoparticles.

S1. Calculation of ratio of gas-phase concentration to the total concentration

S1.1 Calculation of gas-phase concentration (g cm^{-3})

$$m_{gas} = \frac{PVM}{RT} \quad \text{(S1)}$$

This equation (Eq. (S1) establish a relationship between mass in gas phase (m_{gas}) and pressure (*P*), volume (*V*), mole mass (*M*), the ideal gas constant (*R*), and temperature. Here, Vapor pressure *(P*) is equal to saturated ratio of levoglucosan vapor (see Fig. 4c) multiplied saturated levoglucosan vapor pressure at 293.15 K.

S1.2 Calculation of total concentration of generated particles (g cm^{-3})

$$m_{total} = \frac{dN}{dlogD_p} \times dlogD_p \times \frac{\pi}{6} D_p^3 \times \rho \quad \text{(S2)}$$

where dN is particle concentration, D_p is the particle diameter, and ρ is the density of particles.

S1.3 ratio of the gas-phase concentration to the total concentration of generated particles

$$Ratio = \frac{m_{gas}}{m_{total}} \quad \text{(S3)"}$$

4. Hygroscopicity of organic surrogate compounds from biomass burning and their effect on the efflorescence of ammonium sulfate in mixed aerosol particles

This work has been published as Lei et al. (2018):

Lei, T., Zuend, A., Cheng, Y. F., Su, H., Wang, W. G., and Ge, M. F.: Hygroscopicity of organic surrogate compounds from biomass burning and their effect on the efflorescence of ammonium sulfate in mixed aerosol particles, Atmospheric Chemistry and Physics, 18, 1045–1064, 2018.

I am the first-author of this work and my contribution to this work includes assembling the hygroscopicity tandem differential mobility analyzer (HTDMA) system for investigating the hygroscopic properties of aerosol nanoparticles, performing the experiments, analyzing all the data, making all the figures and tables, and writing the manuscript.

The following text, figures, and table quoted (within "") from page 87 to page 115 are exactly the same as published on Lei et al. (2018) which is cited on page 86.

"**Abstract:** Hygroscopic growth factors of organic surrogate compounds representing biomass burning and mixed organic-inorganic aerosol particles exhibit variability during dehydration experiments depending on their chemical composition, which we observed using a hygroscopicity tandem differential mobility analyzer (HTDMA). We observed that levoglucosan and humic acid aerosol particles release water upon dehumidification in the range from 90 – 5 % relative humidity (RH). However, 4-Hydroxybenzoic acid aerosol particles remain in the solid state upon dehumidification and exhibit a small shrinking in size at higher RH compared to the dry size. For example, the measured growth factor of 4-hyroxybenzoic acid aerosol particles is ~0.96 at 90 % RH. The measurements were accompanied by RH-dependent thermodynamic equilibrium calculations using the Aerosol Inorganic-Organic Mixtures Functional groups Activity Coefficients (AIOMFAC) model and Extended Aerosol Inorganic Model (E-AIM), the Zdanovskii-Stokes-Robinson (ZSR) relation, and a fitted hygroscopicity expression. We observed several effects of organic components on the hygroscopicity behavior of mixtures containing ammonium sulfate (AS) in relation to the different mass fractions of organic compounds: (1) a shift of efflorescence relative humidity (ERH) of ammonium sulfate to higher RH due to the presence of 25 wt % levoglucosan in the mixture. (2) There is a distinct efflorescence transition at 25 % RH for mixtures consisting of 25 wt % of 4-hydroxybenzoic acid compared to the ERH at 35 % for organic-free AS particles. (3) There is indication for a liquid-to-solid phase transition of 4-hydroxybenzoic acid in the mixed particles during dehydration. (4) A humic acid component shows no significant effect on the efflorescence of AS in mixed aerosol particles. In addition, consideration of a composition-dependent degree of dissolution of crystallization AS (solid-liquid equilibrium) in the AIOMFAC and E-AIM models leads to a relatively good agreement between models and observed growth factors, as well as ERH of AS in the mixed system. The use of the ZSR relation leads to good agreement with measured diameter growth factors of aerosol particles containing humic acid and ammonium sulfate. Lastly, two distinct mixtures of organic surrogate compounds, including levoglucosan, 4-hydroxybenzoic acid, and humic acid were used to represent the average water-soluble organic carbon (WSOC) fractions observed during the wet and dry seasons in the central Amazon Basin. A comparison

of the organic fraction's hygroscopicity parameter for the simple mixtures, e.g. $\kappa \approx 0.12$ to 0.15 for the wet-season mixture in the 90 % to 40 % RH range, shows good agreement with field data for the wet season in Amazon (WSOC $\kappa \approx 0.14 \pm 0.06$ at 90 % RH). This suggests that laboratory-generated mixtures containing organic surrogate compounds and ammonium sulfate can be used to mimic, in a simplified manner, the chemical composition of ambient aerosols from the Amazon for the purpose of RH-dependent hygroscopicity studies.

1 Introduction

It is well established that biomass burning, as an important source of atmospheric aerosol particles, has a wide range of climate effects that can be classified into direct radiative effects through light-absorbing carbon aerosol particles and indirect effects by impact on cloud condensation nuclei (CCN) and cloud microphysics (Andreae and Gelencsér, 2006; Moosmüller et al., 2009; Hecobian et al., 2010; Rizzo et al., 2011; Rose et al., 2011; Cheng et al., 2012; Engelhart et al., 2012; Lack et al., 2012; Jacobson, 2014; Liu et al., 2014; Saleh et al., 2013, 2014). Atmospheric light-absorbing particles that arise from biomass burning play an important role as a driver of global warming (Favez et al., 2009; Hegg et al., 2010; Lack et al., 2012; Laborde et al., 2013; Srinivas and Sarin, 2013). According to the IPCC report (Boucher and David, 2013), the climate forcing of black carbon aerosol particles may rival that of methane, with a present-day global warming effect of up to 0.3–0.4 °C (Wang et al., 2014). Also, certain types of aerosol particles emitted by biomass burning, when immersed into cloud droplets, absorb solar radiation and facilitate water evaporation and cloud dispersion, which indicates an additional indirect aerosol effect that counteracts the cooling effect of cloud droplets nucleated by aerosols (Powelson et al., 2014). Therefore, a better understanding of the influence of aerosol particles from biomass burning on cloud formation, precipitation, and Earth's radiative budget is required to comprehend biomass burning aerosol properties and behavior.

The understanding of aerosol-cloud-climate impact of a vast range of biomass burning derived organic compounds, however, is rather limited due to the complexity of biomass burning emissions, gas- and aerosol-phase processing and the restricted availability of field measurements (Pratt et al., 2011; Lei et al., 2014; Paglione et al., 2014; Srinivas and Sarin, 2014; Zhong and Jang, 2014; Arnold et al., 2015; Lawson et

al., 2015; Gilman et al., 2015). Moreover, biomass burning particles are often mixtures of water-soluble organic carbon, black carbon, varying amounts of inorganic components, and water insoluble inclusions, such as mineral dust or poorly soluble organics (Väkevä et al., 2002; Sadezky et al., 2005; Saarnio et al., 2010). An appreciable amount of organic compounds affect the physicochemical properties of aerosols, such as hygroscopicity, liquid-solid and liquid-liquid phase transitions, and chemical reactivity in liquid phases and/or on particle surfaces (Shiraiwa et al., 2013). For example, equilibrium between the variable environmental water vapor mixing ratio and aerosol particles may lead to substantial changes in particle size, and chemical composition, all of which can influence light absorption and scattering (Seinfeld and Pandis, 2006; Zhang et al., 2016). Transitions between solid and liquid (aqueous) phases that are dependent on relative humidity (RH) are also important in determining optical properties (Martin et al., 2013; Wang et al., 2010; Kim et al., 2016; Wu et al., Denjean et al., 2015; 2016; Hodas et al., 2015; Atkinson et al., 2015). Studies have shown that water-soluble organic matter from biomass burning (approximately 70 % of total organic matter) can significantly suppress, enhance or have no effect on the deliquescence (e.g. the RH at which deliquescence occurs at a certain temperature, the DRH) and efflorescence processes (e.g. the efflorescence RH, ERH) of present inorganic electrolytes. The effect depends predominantly on the type of organics, mass fraction of organics relative to inorganic, and particle size (Zawadowicz et al., 2015; Hodas et al., 2015; Gupta et al., 2015). Whole particles, individual phases within particles, or specific chemical compounds can undergo a range of phase transitions including crystallization-efflorescence, dissolution-deliquescence, and liquid-liquid phase separation as the RH varies in the atmosphere. A number of laboratory studies have focused on liquid-liquid phase separations within particles consisting of inorganic and organics fractions (Svenningsson et al., 2006; Carrico et al., 2008; Dusek et al., 2011; Hodas et al., 2015). For example, studies about liquid-liquid separation occurring in mixed organic-inorganic aerosols were performed by Song et al. (2012, 2013) and You et al. (2013) using Raman and optical microscopy, establishing that liquid-liquid phase separation occurs typically in mixed organics + ammonium sulfate particles with an average elemental oxygen-to-carbon (O:C) ratio of the organic fraction of less than 0.6 and in some cases for $0.6 < O:C < 0.8$. You et al. (2013) further found that for a O:C ratio between 0.5 and 0.8, the occurrence of liquid-liquid phase separation at

moderate to high RH depends on the types of inorganic salts present (i.e., the effective strength of the salting-out effect), e.g., $(NH_4)_2SO_4 \geq NH_4HSO_4 \geq NaCl \geq NH_4NO_3$. Recently, the effect of a potential size-dependent morphology and dependence of the phase separation mechanism on the organic/inorganic mass ratio in mixed aerosol was studied for mixtures of poly(ethylene glycol)-400 + ammonium sulfate using cryogenic-transmission electron microscopy (Altaf et al., 2016). Therefore, many independent studies suggest that the occurrence of solid-liquid and/or liquid-liquid phase separations, as well as related (temperature-dependent) RH levels of phase transitions (DRH, ERH, and onset of RH of liquid-liquid phase separation, SRH), depend on the relative amounts of organic and inorganic aerosols components and their non-ideal mixing behavior.

The expected physical state and morphology of aerosol particles containing mixtures of a wide range of organic and inorganic salts and acids can, in principle, be predicted by a selection of specialized thermodynamic equilibrium models. Such models include the Extended Aerosol Inorganic Model (E-AIM) (Clegg and Seinfeld, 1998, 2006; available online: http://www.aim.env.uea.ac.uk/aim/aim.php), the Aerosol Diameter Dependent Equilibrium Model (ADDEM) (Topping et al., 2004), the universal quasichemical functional group activity coefficients (UNIFAC) model (Fredenslund et al.,1975; Hansen et al., 1991), and the Aerosol Inorganic-Organic Mixtures Functional croups Activity Coefficients (AIOMFAC) model (Zuend et al., 2008, 2011, 2012). These models have all been used to predict atmospheric aerosol thermodynamic equilibrium for a variety of inorganic and organic systems, yet not all of them can be used to compute nonideal mixing in organic-inorganic systems. AIOMFAC has been used to predict the distribution of components in multiple phases in a range of mixed organic-inorganic systems and demonstrated its broad applicability in predicting liquid-liquid phase separation in such mixtures (Zuend et al., 2010; Song et al., 2012; Zuend and Seinfeld, 2012; Shiraiwa et al., 2013; Renbaum-Woff et al., 2016; Rastak et al., 2017).

Several previous experimental studies using the hygroscopicity tandem differential mobility analyzer (HTDMA) technique (e.g. Zardini et al., 2008; Lei et al.2014) show that the deliquescence of inorganic compounds is affected by the presence of organic components, which manifests itself in a shift in the DRH of a salt compared to the corresponding organic-free system. For instance, a clear shift of AS DRH was observed

in the case of the levoglucosan + ammonium sulfate system (Lei et al., 2014). Here we focus on investigating the morphology, hygroscopicity and phase transitions of relevant organic compounds found in biomass burning aerosol during the dehydration-dehumidification process. Moreover, we study how the presence of organic compounds affects the water loss behavior of mixed organic-inorganic aerosols with AS in the supersaturated state as well as after efflorescence of AS. In addition, we compare the measured hygroscopicity behavior of mixed aerosol particles with predictions from the Zdanovskii–Stokes–Robinson (ZSR) mixing rule, the E-AIM model, and the AIOMFAC model.

2 Methods

2.1 Aerosol system

The three organic compounds levoglucosan, 4-hydroxybenzoic acid, and humic acid were used as surrogates for the rich-class of water-soluble organic components in biomass burning aerosols. The influence of the distinct chemical structure of these compounds was studied with regard to the water uptake and evaporation of the pure organic compounds as well as for mixed particles containing organic and AS. Furthermore, a comparison with field data from the Amazon was preformed to quantify the ability of mixtures of these three organic compounds to mimic the hygroscopic behavior of complex ambient organic particles originating from biomass burning emissions. Here we focus on the characterization of hygroscopic growth factors (HGFs) as well as solid-liquid and liquid-liquid phase transitions during the dehumidification conditions. The chemical substances and their physical properties are characterized in Table 1. All of the experimental solutions were prepared by dissolving in Milli-Q water (resistivity $\geq$ 18.2 MΩ) and the experiments were conducted at room temperature (~298 K). The chemical compositions of biomass burning model mixtures are introduced in Table 2.

2.2 Instrument design

Figure 1 shows a schematic of the HTDMA instrument; more detailed information about this instrument's setup, calibration and evaluation is described elsewhere (Lei et al., 2014; Jing et al., 2015, 2017; Liu et al., 2016). Briefly, Poly-dispersed sub-micrometer aerosol particles are generated by atomizing (MSP 1500, MSP) a 0.05 weight % aqueous solution consisting of different mass fractions of inorganic, and

organic components, assuming that the composition of the aerosol particles formed is initially the same as that of the solution used in the atomizer. Aerosol particles from an atomizer are routed though homemade silica diffusion dryers and then pass through a Nafion gas dryer (Perma Pure Inc., USA). After aerosol particles were dried to below 5 % RH (RH set point 1, RH1), they are directed to the impactor; those aerosols with diameter less than 1 μm are allowed to pass it and subsequently pass through a ^{85}Kr electric charger to reach a near-Boltzmann distribution of charges (Liu et al., 1985). After charging, the aerosol particles enter the first differential mobility analyzer (DMA1) at a sheath flow to aerosol flow ratio of 4:0.3. The sheath flow is circulated by the diaphragm pump in the first loop DMA1 system, and its RH is kept constant at below 5 % RH. The resulting monodisperse particle population, selected within uncertainty by the DMA1, is then exposed to high RH conditions during which the aerosol flow is humidified to 98 % RH by mixing water through a Nafion membrane humidifier at 30 °C. After passing through a saturator (Perma Pure Inc., USA), the aerosols are dried to a target RH level (RH2) through a series of two single-Nafion tubes (Perma Pure Inc., USA) with RH2 set to a value in the range of 90 to 5 % RH. Here, a pulse width modulator circuit is used to regulate the sheath flow on the basis of a proportional integral derivative system. When the second Nafion membranes allow for regulating the sheath flow to a desired RH and for controlled flow into the sample stream until the RH2 setting value is equal to the excess RH of sheath flow value (RH3), the mobility diameter of the dehumidified of aerosols at target RH are measured with the second DMA (DMA2, a scanning DMA) coupled with a condensation particle counter (Model 1500, MSP). In addition, the residence time between the humidifier and DMA2 is around 5 s, which is estimated to be sufficient for aerosols to grow or shrink to equilibrium size at a certain RH set point. Also, due to recirculation of the sheath flow and the pre-humidification of the aerosol flow, the sheath flow and aerosol sample flow are enabled to rapidly reach the same RH.

Table 1. Substances and their physical properties used in this work.

Chemical compound	Chemical formula	Molar Mass [g mol^{-1}]	Density in solid or liquid state [g cm^{-3}]	Solubility ($g/100cm^3H_2O$)	Solution surface Tension [J m^{-2}]	Manufacturer
Ammonium sulfate	$(NH_4)_2SO_4$	132.140	1.770[a] (solid), 1.550[a] (liquid)	74.400 (at 20°C)	0.072 (0.001-10mg/mL)	Alfa Aesar, 99.95%
Levoglucosan	$C_6H_{10}O_5$	126.100	1.618[b] (solid) 1.512[b] (liquid)		0.073[c] (0.01-10mg/mL)	Aldrich, 99%
4-Hydroxybenzoic acid	$C_7H_6O_3$	138.100	1.460 (solid) 1.372[d] (liquid)	0.675 (at 25°C)	0.070[e] (>10mg/mL)	Alfa Aesar, 99.99%
Humic acid		NA	0.800[f] (solid)	NA	0.073[g]	Aldrich, 99%

[a]Clegg and Wexler, (2011); [b]Lienhard et al, (2012); [c]Tuckermann and Cammenga (2004) at 293K; [d]Jedelsky et al, (2000); [e]Kiss et al, (2005); [f]Yates III and Wandruszka, (1999); [g]Mikhavilov et al. (2008).

Table 2. The chemical composition of biomass-burning model mixtures studied given as mass percentages (wt %).

Mixture name	Levoglucosan	4-Hydroxybenzoic acid	Humic acid	Ammonium sulfate
Mix-bio-dry	87.2%	9.2%	1.5%	2.1%
Mix-bio-wet	68.0%	26.0%	3.0%	3.0%

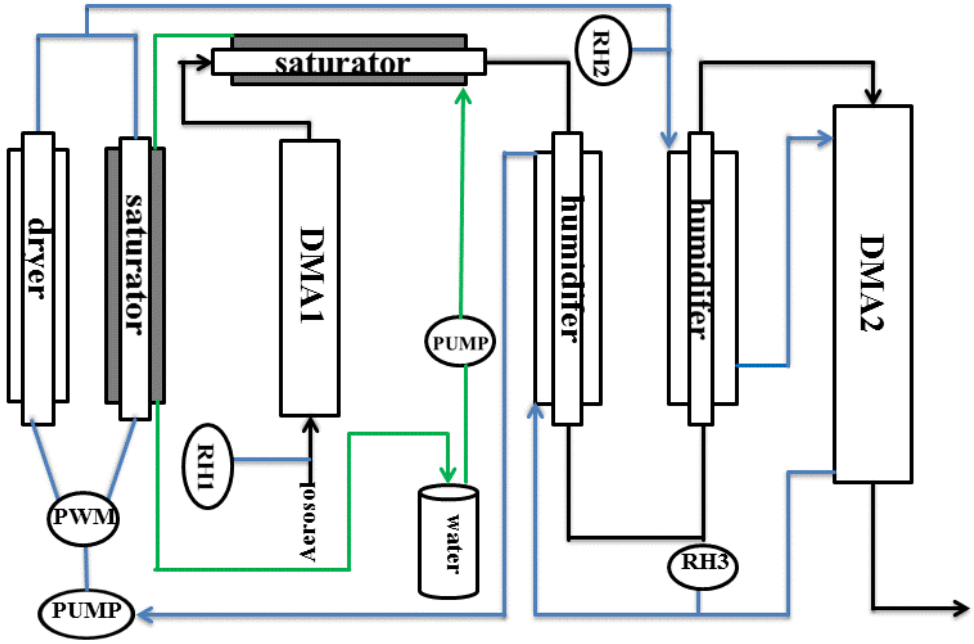

Figure 1. Schematic of the hygroscopicity tandem different mobility analyzer (HTDMA) system. The sheath flow, aerosol flow, and water flow have been represented by the blue, black, green line, respectively. PWM: Pulse Width Modulator circuit.

2.3 Theory and modeling methods

Models were applied to explore the extent to which measured (HGFs), particle phase states, and phase compositions under sub-saturation conditions can be predicted by thermodynamic equilibrium models. For the AS-containing systems studies, the current thermodynamic equilibrium predictions account for a crystalline AS phase with solid-liquid equilibria prior to the complete deliquescence of AS under hydration conditions. Similarly, the crystallization point followed by a solid-liquid equilibrium (SLE) of AS needs to be considered to predict the effect of organic components in the mixed particles on the shift/suppression of AS efflorescence during aerosol dehumidification, i.e. referring to processes occurring along the dehydration branch of a HTDMA humidification-dehumidification cycle. The calculation of the ERH of AS in an organic-inorganic solution is thermodynamically related to the solubility limit, but it is

not strictly deterministic (unlike the DRH) due to the stochastic nature of nucleation-and-growth of a crystal embryo. The molality of pure AS at saturation in an aqueous solution is known, e.g. measured by Apelblat (1993) at 298.15 K as $m_{AS}^{(sat)}$ = 5.790 mol kg^{-1}, while measurements are most often not available for the solubility limit of AS in aqueous inorganic-organic systems. However, crystalline AS in equilibrium with an aqueous mixture demonstrates a specific molal ion activity product (IAP) in that solution at a given temperature and atmospheric pressure. For example, in the case of a ternary liquid mixture of levoglucosan + AS + water in SLE with a crystalline AS phase at a certain temperature T, a constant molal ion activity product $\mathrm{IAP_{AS}} = \mathrm{IAP_{AS}^{(sat)}}(T)$ is established (necessary SLE condition). In this case the liquid mixture is a so-called saturated solution with respect to AS. While the molar amount of AS in a saturated solution depends on the other mixture constituents, the value of $\mathrm{IAP_{AS}^{(sat)}}(T)$ is a function of temperature only, since it is derived from the fixed chemical composition and associated chemical potential of the crystalline phase. A reference value for $\mathrm{IAP_{AS}^{(sat)}}(T)$ can therefore be calculated with the AIOMFAC model from an experimentally determined solubility limit of AS in a known mixtures, such as the molality of AS at the point of saturation in the binary aqueous system (water + AS). The RH at which full dissolution of a solid phase upon humidification is just reached, the DRH, is directly related to the conditions at which a saturated solution becomes subsaturated upon addition of water. Here the degree of saturation with AS can be determined unambiguously by the computed value of $\mathrm{IAP_{AS}}$ as a function of mixture composition and temperature. Making use of these thermodynamic relationships, the AIOMFAC-based equilibrium model is used to calculate the DRH and ERH of AS in the multicomponent system, as outlined below. Detailed information on the modeling of solid-liquid equilibria and the IAP-based prediction of ERH is given in Zuend et al. (2011) and Hodas et al. (2016). Briefly, the ERH is determined based on the following equations:

$$\mathrm{IAP_{AS}} = \left[a_{NH_4^+}^{(m)}\right]^2 \left[a_{SO_4^{2-}}^{(m)}\right]^1 \quad (1)$$

$$\mathrm{IAP_{AS}^{[crit]}} = c_{\mathrm{AS}} \times \mathrm{IAP_{AS}^{(sat)}} \quad (2)$$

Here $a_{NH_4^+}^{(m)}$ and $a_{SO_4^{2-}}^{(m)}$ are the molal activities of the ammonium and sulfate ions in solution (Zuend et al., 2010). Molality basis is indicated by superscript "(m)" (which is

not a mathematical exponent). $IAP_{AS}^{(sat)}$ denotes the molal ion activity product of AS at salt saturation computed by the thermodynamic equilibrium model for any aqueous AS system at a certain temperature (here 298.15 K). The calculated molal IAP at saturation of the corresponding binary salt solution is taken as the (known) reference value. The RH at which this $IAP_{AS}^{[sat]}$ value is just reached in certain bulk solution at equilibrium with its environment (in contrast to $IAP_{AS} < IAP_{AS}^{(sat)}$ at higher RH), is the (bulk) DRH of AS. Similarly, the ERH is determined at the point of crystallization by a critical IAP value denoted as $IAP_{AS}^{[crit]}$ (Hodas et al., 2016), the value of $IAP_{AS}^{[crit]} > IAP_{AS}^{[sat]}$ expresses the need for reaching a critical IAP threshold (critical level of AS super-saturation) for highly likely nucleation-and-growth of a new crystalline AS phase. The multiplication factor c_{AS} is used as a constant coefficient relating the IAP at AS saturation to the one expected at the point of crystallization in aqueous mixed particles. From the comparison of laboratory measurement of ERH for aqueous AS solution to the AIOMFAC-predicted IAP_{AS} at that RH, the value of $c_{AS} \approx 30$ was determined; this value is in particular applicable to submicron-sized AS droplets (Zardini et al., 2008; Ciobannu et al., 2010).

An analogous approach is used for the ERH predictions with the E-AIM model, however, since E-AIM provides activity coefficients and activities on mole fraction basis, denoted here by superscript "(*x*)" (rather than molality basis), the value of $c_{AS}^{(x)}$ need to be determined separately for that model. Expressing Eq. (1) by mole-fraction-based activities of NH_4^+ and SO_4^{2-} and comparison to the $IAP_{AS}^{(sat,x)}$ and $IAP_{AS}^{(crit,x)}$ computed by E-AIM for AS at the experimental solubility limit and ERH in aqueous AS solutions, a value of $c_{AS}^{(x)} \approx 40$ was determined for the calculation with E-AIM.

As discussed by Lei et al. (2014), predicting of HGFs with E-AIM includes a sophisticated composition-dependent solution density model, which considers the non-ideality effects on apparent molar volumes used for the calculation of the solution density in mixed organic-inorganic systems (Clegg and Wexler, 2011a, b). The AIOMFAC-based model applies a simpler solution density treatment by assuming that the partial molar volumes of solution species are independent of non-ideal interactions, i.e. the mixed solution density is calculated based on linear additivity of pure component solid or liquid volume contributions to obtain the HGF at a given RH. Differences in the density models are expected to lead to relatively small differences,

typically on the order of the HTDMA measurement error or less (e.g. Fig. 2a), in the application to HGF predictions, as demonstrated by Lei et al. (2014) for the case of diameter vs. mass-based HGF of AS droplets. Both models include sophisticated sets of equations to compute activity coefficients of all solution components in a thermodynamically consistent manner.

2.4 *κ*-Köhler theory and computation of the hygroscopicity parameter *κ*

The hygroscopicity parameter, *κ*, is commonly used to characterize the relative hygroscopicities of individual aerosol particles, known mixtures or complicated atmospheric aerosols (Petters and Kreidenweis, 2007), and to model the composition-dependence of the solution water activity. The saturation ratio, *S*, in the traditional Köhler equation (Eq. 3), over an aqueous droplet is calculated from

$$S = a_w \left(\frac{4\sigma_s M_w}{RT\rho_w D_{wet}}\right) \quad (3)$$

Where a_w is the mole-fraction-based water activity in solution, M_w and ρ_w are the molar mass of water and the density of pure water in the liquid state at temperature T, respectively. D_{wet}, the "wet" particle diameter at a given RH, is defined by $D_{wet} = HGF \times D_0$. D_0 denotes the diameter at dry conditions at RH below 5 %. The solution surface tension is denoted by σ_s. In the "*κ*-Köhler theory", the bulk solution water activity is described by a single parameter *κ*, with the hygroscopic parameter of the overall mixture related to Eq. (3) by

$$\kappa_{HGF} = 1 - HGF^3 + \frac{HGF^3 - 1}{S} \exp\left[\frac{4\sigma M_w}{RT\rho_w D_{wet}}\right] \quad (4)$$

This expression describes effective values of κ_{HGF} as a function of droplet diameter and HGF at a certain saturation ratio. In turn, known (measured) solution κ_{HGF}values or component-specific κ_i values can be used to parameterize or predict the HGF curve of a mixture (Petters and Kreidenweis, 2007).

2.5 GF data fit

As described by Dick et al. (2001), the relationship between measured hygroscopic growth factors and water activity can alternatively be parameterized by the following expression:

$$HGF = \left[1 + (c_1 + c_2 \times a_w + c_3 \times a_w^2)\frac{a_w}{1 - a_w}\right]^{\frac{1}{3}} \quad (5)$$

By substitution of Eq. (3) for a_w in Eq. (5) and a fit to the measured HGF the three adjustable coefficients c_1, c_2, c_3 of Eq. (5) were determined. The coefficient values are given in Table 3 for the different organic compounds considered.

2.6 GF prediction by ZSR

The ZSR mixing rule is widely used to approximate the water uptake of mixed systems by assuming additivity of the water uptake of each individual component in the mixed particles at a given RH (e.g., Malm and Kreidenweis, 1997). HGF_{mix} is based on the HGF_j of pure components j and their corresponding volume fraction, ε_j in the mixed particles.

$$HGF_{mix} = \left[\sum_j \varepsilon_j \left(HGF_j\right)^3\right]^{\frac{1}{3}} \quad (6)$$

Table 3. Coefficients (c_1, c_2, c_3) of the fitted growth factor parameterization (Eq. 5) as follows:

Chemical compounds	c_1	c_2	c_3
Levoglucosan	0.12868746	0.36582023	-0.39840382
4-Hydroxybenzoic acid	-1.389967×10^{-1}	2.325586×10^{-1}	-9.891943×10^{-2}
Humic acid	-1.618304×10^{-2}	2.202483×10^{-1}	2.005134×10^{-2}

3 Results and discussion

3.1 GF of single compounds systems

Figure 2a shows the measured diameter growth factors of AS particles as a function of RH for both humidification and dehumidification conditions. The measured ERH of 100 nm AS particles is approximately 35 % RH at 298.15 K. The models predicted GF and predicted solid-liquid phase transition of AS are in relatively good agreement with the experimental data and, in particular, the efflorescence (crystallization) of AS is captured by the AIOMFAC and E-AIM models. The good model-measurement agreement for the ERH is of course expected, since the aqueous AS system serves as the reference system for determining the value pairs of $IAP_{AS}^{(sat)}$ and c_{AS} on molality and mole fraction basis for use with AIOMFAC and E-AIM, respectively (section 2.3). An ERH of 31 % to 40 % RH was reported by other groups for a range of particle sizes and experimental techniques (Zardini et al., 2008; Ciobanu et al., 2010). There are several factors that contributed to the variability of reported ERH values, such as particles size, temperature, solution impurities and the stochastic nature of the homogeneous or heterogeneous nucleation of a crystalline phase near ERH (Ciobanu et al., 2010).

In Fig. 2b, upon dehydration, no efflorescence of the levoglucosan aerosol particles is

observed even at RH below 10 %. The agreement of the HGF between the hydration and dehydration processes demonstrates that these particles equilibrate with the surrounding water vapor under these moisture conditions. For example, the measured diameter growth factors of levoglucosan particles at 80, 60, and 30 % RH are 1.19, 1.09, and 1.03, respectively, which are similar to results obtained for the hydration process of such particles. Levoglucosan has a DRH of ~80 to 83 % (for a bulk system) at 293 to 298 K (Mochida and Kawamura, 2004; Zamora et al., 2011). The similarity of diameter growth factors both under hydration and dehydration conditions even below the DRH of levoglucosan is explained by the lack of crystallization of levoglucosan upon drying to low RH and the presence of a metastable supersaturated aqueous levoglucosan solution in both the hydration and dehydration modes for experiments initiated with liquid solution droplets (Mochida and Kawamura, 2004; Chan et al., 2005; Svenningsson et al., 2006). A possible reason for a persistent metastable supersaturated solution states is that levoglucosan particles remain liquid (possibly a viscous liquid state) upon drying to below 5 % RH, which was also observed previously with a reported ERH < 4 % RH (Mochida and Kawamura, 2004; Chan et al., 2005). Also, the measured diameter growth factors of levoglucosan particles are in good agreement with these estimated from the standard UNIFAC model within the E-AIM model and the AIOMFAC model, within experimental uncertainty. The UNIFAC models within E-AIM and AIOMFAC are based on the original model expressions by Fredenslund et al. (1975) and both include the extensive parameter set by Hansen et al. (1991) as well as revised parameters for certain group interactions of water with carboxyl and hydroxyl groups by Peng et al. (2001). Of relevance for levoglucosan and other sugar-like compounds, the AIOMFAC model also contains certain revised group parameters for hydroxyl groups and special alkyl groups for their interactions with water, introduced by Marcolli and Peter (2005) for polyols, as further detailed in Zuend et al. (2011). However, the molecular structure of levoglucosan with several polar functional groups in close vicinity may account for a small deviation between models and measured HGFs at RH below 70 %, because intramolecular interactions are not fully considered by these models.

The measured diameter growth factors of 4-hydroxybenzoic acid particles shown in Fig. 2c demonstrate untypical increase in diameter of 4-hydroxybenzoic acid particles during dehumidification from 90 to 10 % RH, which is consistent with previous

diameter growth factor for a few solid particles (Mochida and Kawamura, 2004). The organic particles measured are likely always in the effloresced, i.e. crystalline state apparently even at high RH. The apparent increase in diameter during dehumidification may be explained by particle shape restructuring, since the (poly)crystalline particles are likely non-spherical at dry conditions, but may become more sphere-like in shape when exposed to higher RH (Mikhailov et al., 2004). Also, no ERH of 4-hydroxybenzoic acid in the dehydration mode was observed during the experiments; the likely reason is that the highest RH reached in the humidifier was approximately 98 %, which may be below the ERH of 4-hydroxybenzoic acid, reported as above 98 % RH in another study (Mochida and Kawamura, 2004). As discussed previously by Lei et al. (2014), our HTDMA experiments are carried out such that RH = 98 % is reached initially before dehumidification to a series of RH values at set point RH2 (90-5 % RH), the crystallization of the organic, however, could occur at above 90 % RH. In addition, deviations between measurements and model prediction are obvious in Fig. 2c. The observations surpass by far the expected error in model performance, which is typically less than 0.05 in HGF units for RH < 85 %, as indicated also by an intercomparison of the AIOMFAC and E-AIM predictions in Fig. 2c and much- improved model-measurement agreement for the case of mixed 4-hydroxybenzoic acid + AS particles shown in Fig. 4 (discussed in Section 3. 2. 2). However, note that the validity of the shown model predictions in Fig. 2c depends on whether the assumption of a liquid solution droplet is plausible. Therefore, it is no surprise that the model-predicted curves deviate from the experimental hygroscopic behavior of 4-hydroxybenzoic acid particles. Morphology effects, such as the restructuring of non-spherical polycrystalline particles over a certain RH range or liquid-liquid phase-separated particles of nonspherical shapes, have been discussed by several groups (Sjogren et al., 2007; Reid et al., 2011; Lei et al., 2014). In the case of hygroscopic growth and deliquescence under hydration conditions for 4-hydroxybenzoic acid particles and mixtures of 4-hydroxybenzoic acid with ammonium sulfate. An offset between measurement and model predictions was observed both in the RH range below the deliquescence of the particles and above it, i.e. above 80 % RH, (Lei et al., 2014). It is suggested that deviations are primarily caused by a change in solid-state particle morphology during hydration, leading to a restructuring of the polycrystalline particle shape towards more compact, near-spherical shape as the RH approaches the particle deliquescence point.

This would explain rather uncommon HGF values of less than 1.0 at elevated RH also shown in Fig. 2c. Similar behavior was found for experimental growth factors of mixtures containing adipic acid and AS and systematic deviations between the associated ZSR predictions and observations by Sjogren et al. (2007). Thus, while experimental data hint to the possible influence of non-spherical particles and their humidity-induced restructuring as a source of uncertainty, model predictions of HGF, such as those with the AIOMFAC model, assume by default a spherical particle shape even for solid phases and/or in cases in which liquid-liquid phase separation (LLPS) is present.

The measured HGF curves of humic acid aerosol particles during dehumidification and humidification measurements do not agree very well within experimental uncertainty, in particular above 70 % RH. For instance, the growth factor of humic acid aerosol particles at 80 % RH is 1.2 according to the dehumidification measurement, which is higher than hygroscopic growth factor of humic acid particles in the humidification mode at the same RH. Humic acid aerosol particles shrink continuously due to loss of water content in the range from 90 to 10 % RH. For example, a stepwise change in the water absorption and desorption behavior within different RH range was observed in the case of Nordic Aquatic Fulvic Acid (NAFA) and Suwannee River Fulvic Acid (SRFA) by Chan and Chan (2005). These hygroscopic behaviors suggest that humic acid particles and structurally similar compounds remain some water down to the low RH levels achieved in the instruments (imperfect drying during particle residence in the instrument). In addition, the experimental growth factor of humic acid aerosol particles during dehumidification can be represented well by fitting Eq. (5) to the measurements. The determined fit parameters are listed in Table 3. The humic acid sample used (Aldrich, 99%) are a mixture of different polycarboxylic acids of undefined chemical structure. However, specific information on the chemical structure and mixture composition is necessary for corresponding model predictions with AIOMFAC and E-AIM. Therefore, no such model calculations are shown in Fig. 2d.

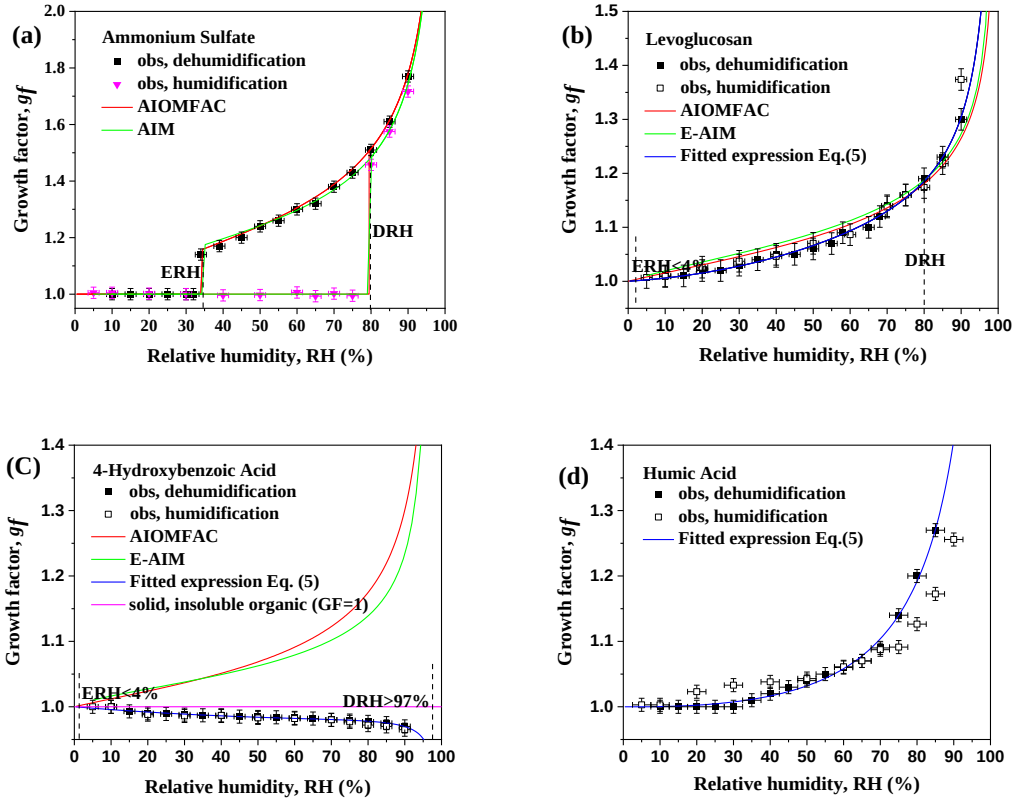

Figure 2. Hygroscopic growth, deliquescence and efflorescence of aerosol particles. Hygroscopic growth factors of (**a**) ammonium sulfate (AS), (**b**) levoglucosan, (**c**) 4-hydroxybenzoic acid, and (**d**) humic acid aerosol particles with dry diameter of 100 nm (open, black square). In this study, the green curves show E-AIM predictions, and the red curves the AIOMFAC predictions, and the blue lines the fitted expression (Eq. 5).

3.2 GF of mixtures of organic surrogate compounds + ammonium sulfate

Biomass burning aerosol particles are likely mixtures of a diversity of inorganic constituents and organic compounds in the atmosphere. For example, particles may consist of a combination of ammonium sulfate mixed with low- and semi-volatile organics from biomass burning emissions (Lee et al., 2003; Zhang et al., 2007; Pratt and Prather, 2010). Different water solubilities, and hygroscopic behavior of distinct organic compounds may affect the hygroscopic growth factors of mixtures of partially or fully dissolved inorganic and organic components. For example, Bodsworth et al. (2010) studied the effect of different mass fractions of citric acid on the efflorescence properties of mixed citric acid-ammonium sulfate particles at lower temperature and concluded that adding citric acid decreases the ERH of ammonium sulfate in the mixed aerosol particles. These hygroscopic behaviors of mixed aerosol particles, including phase transition in the range from moderate to low RH, are the focus of attention in this study.

3.2.1 Mixed system: levoglucosan + ammonium sulfate

Figure 3 shows measured growth factors of mixed aerosol particles containing levoglucosan + ammonium sulfate with different dry-state organic-to-inorganic mass ratios (1:3, 1:1, 3:1) in the RH range from 90 to 10 %. There is a reduction in the diameter growth factor of aerosol particles containing levoglucosan and AS with increasing levoglucosan mass fraction, as expected from a ZSR-like additivity concept of hygroscopicity. When the concentration of levoglucosan is low (25 wt %), a clear efflorescence signature of AS found, within the ERH shifting to a higher RH (40-45 %) in comparison to the ERH of pure AS occurring at 33-35 % RH (Fig.3a). A similar phenomenon has been found for the certain mixtures of NaCl and Nordic Aquatic Fulvic Acid (NAFA), in which the crystallization of NaCl shifted to higher RH by mixing with NAFA at a mass ratio of 1:1 (Chan and Chan. 2003). With increasing mass fraction of levoglucosan (i.e., 50 and 75 wt %), the mixtures release water gradually and no crystallization of AS was observed. Although a small step in the growth factor curve might have occurred (indicative of the crystallization of AS), it cannot be detected with sufficient certainty by our measurement setup. The rather high viscosity of solutions containing levoglucosan is expected to increase considerably toward RH (Marshall et al., 2016). This increase in viscosity might impede the crystallization of AS in the mixed systems on the time scale of the experiment. Mass transfer limitation effects on the deliquescence or efflorescence process of crystalline organic particles and the water uptake or evaporation have been investigated in several experimental studies (Peng et al., 2001; Choi and Chan, 2002; Chan and Chan, 2005; Sjogren et al., 2007; Zardini et al., 2008; Ciobanu et al., 2010; Smith et al., 2012; Mikhailov et al., 2013; Hodas et al., 2015). Mass transfer limitations may impact the outcome of experiments significantly if the characteristic time scales for equilibration is similar to or larger than the residence time of particles in the experimental setup. In this study, the total residence time of the aerosol sample during the equilibration phase before entering the DMA2 is about 8 s. In order to improve the probability that the particles reach equilibrium with the target RH during this residence time, the monodisperse aerosol selected by DMA1 is first humidified to 98 % RH. The aerosol particles are then exposed to a lower target RH by a two-step process using double Nafion tubes. Kerminen (1997) estimated the necessary residence time for achievement of water equilibrium of aqueous droplets to be between 0.005 and 0.1 s (water uptake coefficient

α_w = 0.001, 25°C) for 100 nm and 500 nm particles, respectively. Therefore, the typical residence time of a few seconds in the humidification or dehumidification section in a HTDMA measurement is assumed to be sufficient for most equilibrium hygroscopicity measurements (Brooks et al., 2004; Mikhailov et al., 2004). Moreover, our HGF results for the three pure organic components are in good agreement with respective data by Mochida and Kawamura, (2004), Brooks et al., (2004) and Chan and Chan (2005) conducted with different techniques and/or residence times. However, there are cases where water equilibration could be impeded substantially in the presence of highly viscous or glassy particles at low RH, e.g. for ternary sucrose + NaCl + water particles of > 6 μm in diameter studied by Bones et al. (2012), who report an equilibration time scale > 1000 s for such particles. Note that, aside from viscosity, there is an important size-dependence of the particles on the equilibration time scale (e.g. Koop et al. 2011). For aqueous 100 nm particles used in HTDMA experiments at room temperature, Bones et al. (2012) indicate that the equilibration time scale for water is likely only of concern for RH < 10 % in such an instrument. We therefore conclude that the residence time of 8 s is very likely sufficient to allow for equilibrium HGF measurements in dehydration mode, at least down to 10 % RH (when starting with aqueous solution droplets).

Mass transfer effects in hygroscopicity measurements of aerosol particles during hydration conditions have been encountered previously, particularly when a solid-liquid phase transition (deliquescence) is involved (Peng et al., 2001; Chan and Chan, 2005). For example, Peng et al. (2001) observed in electrodynamic balance (EDB) experiments under conditions of very slow humidification that glutaric acid aerosol particles showed a deliquescence phase transition in the RH range from 83 to 85 % over the course of several hours. This is a much longer time span than that of ~ 40 min for the deliquescence of other super-micron sized dicarboxylic acid particles (e.g., malonic acid) in EDB experiments. This observation indicates that the solid-liquid phase transition of glutaric acid particles may likely be mass transfer limited during the hydration process. In this context, it is possible that the deliquescence of initially solid, pure 4-hydroxybenzoic acid particles at RH > 97 % is further impeded by slow dissolution, which could have led to the absence of deliquesced particles (Fig. 2c) on experimental timescale.

In addition, the measured diameter growth factors of mixtures of levoglucosan and AS are compared to calculations of hygroscopic growth by the E-AIM and AIOMFAC

models. The E-AIM prediction is in relatively good agreement with results from the HTDMA measurement but typically overestimates the water content of particles consisting of organic-AS mixtures at the RH range close to the ERH of AS. The liquid-solid phase transition of ammonium sulfate in the mixed particles is considered in the E-AIM assumptions as described in Section 2.3. There is a more distinct shift of ERH of AS with higher mass fractions of levoglucosan. In the case of the AIOMFAC and E-AIM model predictions, it is assumed that the diameter growth factor contribution from AS is zero below the predicted ERH, i,e. there the growth factor deviation from 1.0 is solely due to the organic water uptake. The model prediction shows a slight deviation from the measurements, which may be in part due to (i) model uncertainty in the correct description of the hygroscopicity of levoglucosan, (ii) due to incomplete representation of AS + levoglucosan interactions in aqueous solutions and (iii) in part due to measurement error. Also, in the case of mixtures consisting of AS and levoglucosan with organic-to-inorganic dry mass ratio of 3:1 (75 wt % levoglucosan of dry particle composition), the underestimation of the growth factor by the AIOMFAC model at RH < 35 % in comparison to the measurements is explained in part by the model prediction of AS efflorescence (which seems to be absent in the measurements). However, with decreasing AS mass fraction, the hygroscopic behavior of levoglucosan dominates the diameter growth factors of the mixtures, in relative agreement with the AIOMFAC-modeled "dehydration branch" prediction. Minor differences in the AIOMFAC prediction vs. -measurement for diameter growth factors of mixed levoglucosan and AS in the RH range of 35-25 % here might be attributed to mixture viscosity effects at the higher levoglucosan contents, which may suppress the efflorescence of AS in the mixed systems on experimental timescale or it could simply be due to sufficient miscibility of dissolved AS in the aqueous levoglucosan solution (beyond that predicted by the model), such that a small step-change due to AS efflorescence could be beyond the experimental detection range. As a result, accounting for the effect of the organic components on the diameter growth factors of mixtures within aerosol particles is crucial to accurately modelling the equilibrium hygroscopic behavior.

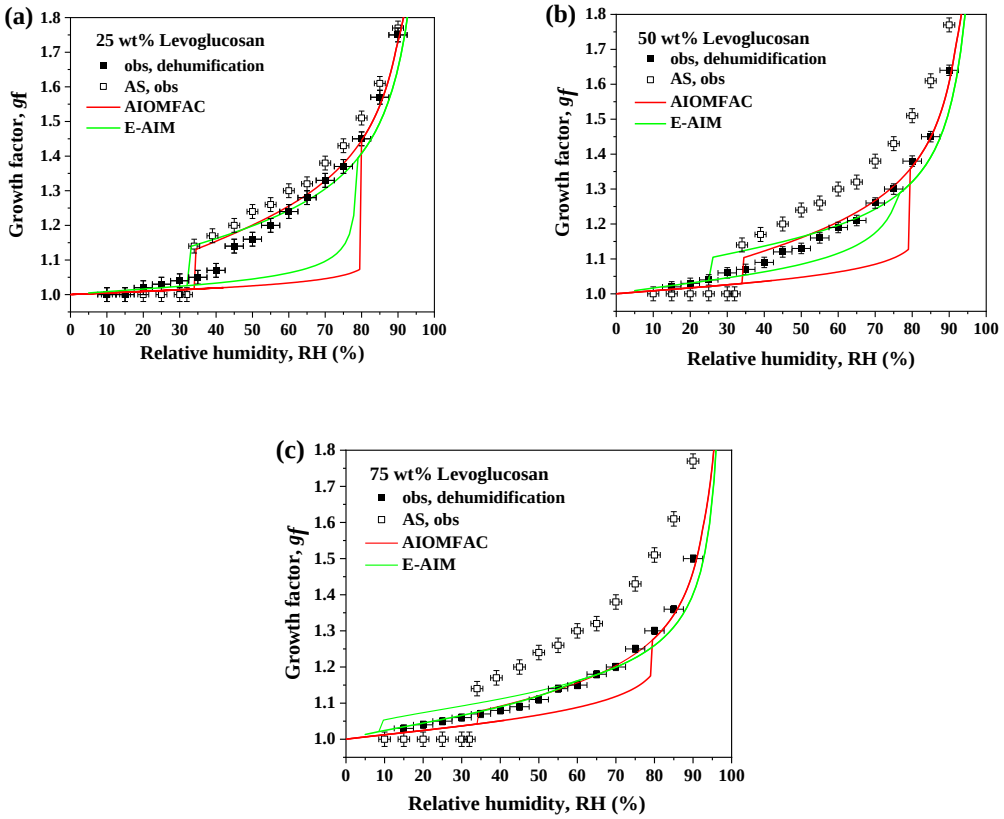

Figure 3. Hygroscopic growth, efflorescence of aerosol particles, and model predictions represent the diameter growth factor during dehydration experiments in the range from 90 % to 5 % RH at 298.15 K. (**a,b,c**). Hygroscopic growth curves of mixtures consisting of levoglucosan and ammonium sulfate (solid symbols) at three different dry state mass fraction for particles of an initial dry diameter of 100 nm at RH < 5 %) as compared to that of pure ammonium sulfate (open symbols, "AS, obs"). AIOMFAC-based model predictions for bulk systems are shown in red, E-AIM predictions are shown in green.

3.2.2 Mixed system: 4-hydroxybenzoic acid + ammonium sulfate

Mixtures of 4-hydroxybenzoic acid + AS with different organic mass fraction (25, 50, 75 wt %) exhibit a gradual water desorption before the AS fraction of the particle effloresces at a certain RH. With increasing 4-hydroxybenzoic acid mass fraction, no discontinuity step at the corresponding ERH in the dehydration curve of mixtures is observed. This suggests the presence of 4-hydroxybenzoic acid in the liquid state retards or offsets the efflorescence of AS in the mixtures. An interesting, yet contrasting phenomenon was observed for the hydration process of aerosol mixtures containing 4-hydroxybenzoic acid and AS by Lei et al. (2014). For the case of these mixtures during moistening, the deliquescence of ammonium sulfate in the mixed particles remains unaffected, within experimental resolution, by the presence of 4-hydroxybenzoic acid (Lei et al., 2014). Similar behavior has been observed for particles containing certain

organic acids of limited water-solubility mixed ammonium sulfate (Choi and Chan, 2002; Chan and Chan, 2003). For example, mixtures for succinic acid + ammonium sulfate showed no substantial influence on the deliquescence RH of ammonium sulfate in the hydration process (Choi and Chan, 2002). However, a clear RH shift of the deliquescence phase transition of ammonium sulfate or sodium chloride was determined for mixed particles containing organic acids of higher water-solubility and O: C ratio, such as citric acid and malonic acid (e.g. Choi and Chan, 2002). The DRH and ERH of pure organics and AS in the mixed organic-AS particles are summarized in Table 4, the measurements indicate that 4-hydroxybenzoic acid has a significant effect on the efflorescence of AS when present in sufficient amount. Also, there is a clear reduction in the diameter growth factors prior to crystallization for mixtures with increasing 4-hydroxybenzoic acid mass fraction.

The measurements of mixtures consisting of 4-hydroxybenzoic acid and AS are compared with model predictions based on different assumptions about the phase state of the organic component since the deviation from measurements might partly be explained by a transition in the physical state of the organic component. The E-AIM model prediction is referring to a system where the mixtures of 4-hydroxybenzoic acid is assumed to be in the liquid state at all RH levels, which the efflorescence of AS is considered. Neglecting the potential efflorescence of the organic component in the dehydration branch makes a systematic offset more obvious prior to the efflorescence of AS. A good E-AIM model-measurement agreement occurs below the predicted ERH of AS for mixed particles. The overestimation of HGFs before the efflorescence of AS is explained by the AIOMFAC model prediction with distinct assumptions about the organic phase state. A possible reason for the departure of model-measurement agreement at RH < 80 % is that there are two liquid-to-solid phase transitions, occurring in the mixed particles: a gradual one for the organic component and a step-like one for AS at lower RH. This phenomenon is shown in the grid square range in Fig. 4 and supported by comparison of the measured HGF data with AIOMFAC-based predictions for two assumptions about the organic phase state, especially in the case of mixtures with 50 and 75 wt % organic. We acknowledge that the model predictions of the HGF curves for the two organic phase state assumptions differ within experimental error for the case shown in Fig. 4a, indicating that alternative explanations, such as model/measurement uncertainty in the absence of a liquid-solid phase transition could

explain the observations. In the Fig. 4b, good agreement between measurements and the AIOMFAC model prediction with liquid organic assumption is found for RH > 65 %, while for RH ≤ 60 % the experimental data agree very well with the dashed red model curve for the case with consideration of a solid organic component. It suggests that crystallization followed by gradually increasing partitioning of organic from the solution to the solid organic phase occurs in the range from 70 to 60 % RH under conditions of dehumidification. Similarly, a liquid-to-solid phase transition occurs for the organic: AS mass ratio of 3:1 cases in the range from 80 to 50 % RH. Meanwhile, AS remains dissolved in a supersaturated aqueous solution phase. Moreover, the AIOMFAC-based equilibrium model predicts a liquid-liquid phase separation (LLPS) to occur at RH below ~ 90 % for the calculation cases with the assumption of the organic in the liquid state (for all three organic mass fractions in Fig. 4). This prediction leads to a liquid phase enriched in 4-hydroxybenzoic acid with some water and AS dissolved and a coexisting liquid phase enriched in AS and water. The onset of the LLPS during dehumidification leads to the kink in the red model curve near 90 % RH, since the slope of the HGF curve with RH changes in a non-smooth manner at the point of the LLPS phase transition. This change in slope is not noticeable from the experimental data alone, but the model-measurement comparison for the range above 80 % RH shows very good agreement. The two liquid phases will likely remain separated until nucleation of a crystalline 4-hydroxybenzoic acid phase occurs followed by gradual partitioning of the organic acid to the solid phase with decreasing RH (to ~50 % RH), at which point only a single liquid phase (an aqueous AS phase with a tiny amount of dissolved HA) will remain until efflorescence of AS occurs. Above ~90 % RH, a single, homogeneous liquid phase is predicted to exist. Interestingly, this AIOMFAC model-measurement comparison (Fig. 4, especially panels b and c) provides reasonable evidence that 4-hydroxybenzoic acid remains dissolved and therefore in a liquid phase state at high RH in the mixed particles upon dehumidification (it is present in both liquid phases below 90 % RH, but highly enriched in the AS-poor phase). In contrast, in the case of pure 4-hydroxybenzoic acid aerosol particles, particles exposed to initial RH of ≥ 90 % remain in the solid state (or crystallize at RH > 90 %) in the dehydration mode (Fig. 2c). What factors contribute to keeping the organic in the liquid solution? It is possible that the aerosols generated with those mixed solutions were allowing the 4-hydroxybenzoic acid to fully dissolve as the AS provides substantial particle phase

water content (within short time) into which the organic can be dissolved and may then further contribute to water uptake associated with the organic's hygroscopicity (unlike in the case of the pure 4-hydroxybenzoic acid particles). The 4-hydroxybenzoic acid remains dissolved in the mixture, possibly supersaturated with respect to the crystalline organic state (similarly to how AS stays supersaturated at RH below the DRH during drying). We consider this a reasonable explanation for the observed HGF data from the HTDMA in comparison to the different AIOMFAC-based curves.

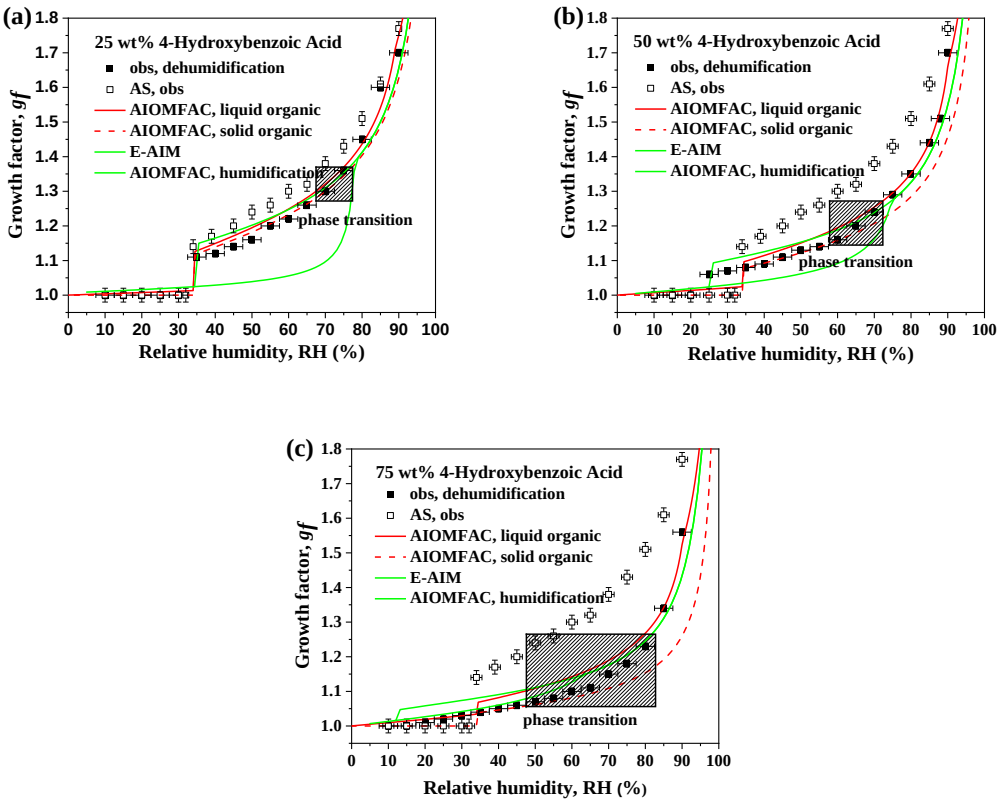

Figure 4. Hygroscopic growth factors, efflorescence of behavior, and model predications for dehydration experiments in the range from 90 % to 5 % RH at 298.15 K. (**a,b,c**) hygroscopic growth curves of mixtures consisting of 4-hydroxybenzoic acid and ammonium sulfate (solid symbols) at three different dry state mass fraction (initial dry diameter of 100 nm at RH < 5 %) as compared to that of pure ammonium sulfate (open symbols). AIOMFAC-based model predictions for bulk systems are shown in red, E-AIM-predictions are shown in green for the case of assuming that 4-hydroxybenzoic acid remains in the liquid state. Shaded rectangle: RH range of gradual crystallization of 4-hydroxybenzoic acid.

Table 4: Experimental studies of organic and ammonium sulfate (AS) deliquescence and efflorescence RH from this work and previous studies at 298K.

Signal compound/Mixture	Organic mass fraction (%)	Deliquescence relative humidity of AS or organic in the mixed particle	Efflorescence relative humidity of AS or organic in the mixed particle
Levoglucosan	-	80 %[a, b] 82.8 %[c]	< 4 %[a, b]
Levoglucosan+AS	25	80 %	45 %
	50	-	-
	75	-	-
4-hygroxybenzoic acid	-	> 97 %[a, b]	< 4 %[a, b]
4-Hydroxybenzoic acid+AS	25	80 %	35 %
	50	80 %	25 %
	75	80 %	-
Humic acid	-	-	-
Humic acid+AS	20	80 %	35 %
	50	80 %	35 %
	75	80 %	35 %

[a]the DRH and ERH of pure organic components. [b]Mochida and Kawamura. (2004), [c]Zamora et al. (2011)

3.2.3 Mixed system: humic acid + ammonium sulfate

Figure 5 shows that the experimental diameter growth factors of mixtures consisting of humic acid and AS with dry mass ratios of 1:3, 1:1 or 3:1 decreases with increasing mass fraction of humic acid at RH > 35 %. For example, at 35 % RH the measured HGF are 1.1, 1.05, 1.05 for the particles consisting of 25, 50, and 75 wt % humic acid. In comparison, the diameter growth factor of pure supersaturated AS particles is ~ 1.13 just prior to efflorescence of AS. Humic acid, unlike levoglucosan and 4-hydroxybenzoic acid aerosol particles, has no noticeable effect on the efflorescence point of AS in the mixed aerosol particles. Results of the ZSR model agrees well with measured hygroscopic growth for mixtures within the experimental error. The ZSR curves shown in Fig. 5 are based on the RH-dependent fitted hygroscopic growth

factors of humic acid with Eq. (5) and the AIOMFAC predicted diameter growth factors of AS in the dehydration mode. The success of the ZSR mixing rule for this system suggests that interactions of organic molecules with ammonium sulfate ions in aqueous solution will only marginally affect the hygroscopic growth factors of the mixtures containing humic acid and AS. Due to the lack of detailed information about the actual chemical structures of humic acid samples used, it was not possible to perform E-AIM and AIOMFAC model predictions for comparison with the measurement.

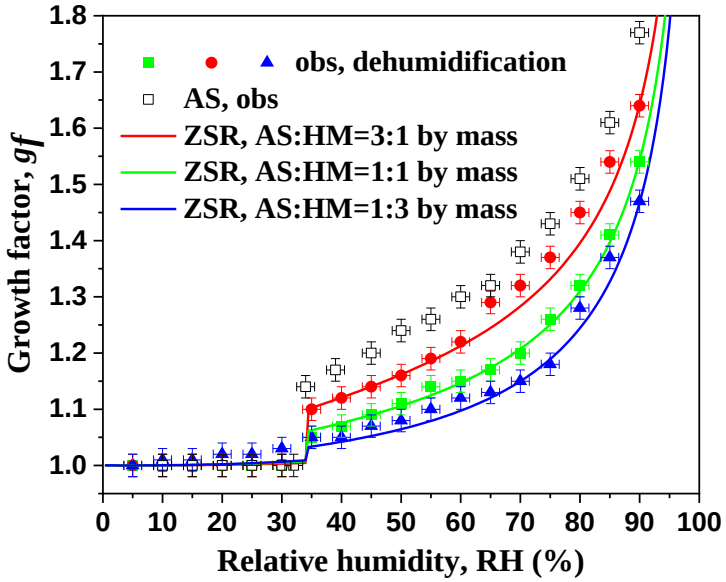

Figure 5. Hygroscopic growth factors, efflorescence of aerosol particles/constituents consisting of humic acid and ammonium sulfate at three different dry state mass fractions with initial dry diameter of 100 nm at RH < 5 % as compared to that of pure ammonium sulfate (open symbols). Colored curves: ZSR predictions of dimeter growth factors for dry particle compositions corresponding to the experimental data during dehumidification in the range from 90 % to 5 % RH at 298.15 K.

3.3 Mixtures of biomass burning organic surrogate components with ammonium sulfate

According to Decesari et al, (2006), sampling of aerosol particles, including the water-soluble organic carbon (WSOC) fraction, was conducted from 9 September to 14 November, 2002 in their field study, the sampling time was subdivided into different periods. Despite of significant changes in the chemical composition of tracer compounds from the dry to the wet period, the functional groups and general chemical classes of WSOC changed only to a small extent in the Amazon basin near Rondônia, Brazil. Model compounds represent semi-quantitatively (presence/abundance of

functional groups) and the chemical structure of WSOC can be used as surrogates in microphysical models involving organic aerosol particles over tropical areas affected by biomass burning scenarios (Andreae et al., 2002; Artaxo et al., 2002; Rissler et al., 2006; Decesari et al., 2006). Here, we focus on experimental observations and model calculations for relatively simple mixtures of inorganic-organic surrogate components reflecting mixtures of aerosol components found during different seasons during biomass burning events. However, we are fully aware of that fact that actual biomass burning aerosols are typically much more complex in terms of particle chemical composition. Aerosol particle properties from biomass burning events depend on the types of sources, external-internal population mixing state, water-solubilities, and phase state of the diversity of organic compounds and their mixing with inorganic constituents during different time periods in the field (e.g. Decesari et al., 2006).

3.3.1 Mixtures system: mix-bio-dry and mix-bio-wet aerosol particles

Figure 6a shows the small differences observed in the hygroscopicity parameter κ for mixtures of organic surrogate components and AS representing biomass burning particles during the dry and wet periods in the Amazon, respectively. Hygroscopicity parameter values for bio-mix-dry aerosol particles were determined to be between 0.16 and 0.18 with decreasing RH in the range from 90 to 40 % RH. The κ value representing the wet period in the Amazon is shown in Fig. 6b, derived from laboratory HTDMA measurements in the range from 90 % to 40 % RH. A similar trend of an increase in κ with a decrease in RH has also been observed by Cheung et al. (2015). Their observation is based on ambient particle measurement with a HTDMA in Hong Kong, therefore probing particles of more complex compositions in the field campaign. The variability of the hygroscopicity parameter in sub-saturated conditions reveals some limitations of a single-parameter hygroscopicity model for applications over a wide range of RH. At low, intermediate and high RH levels, differing degrees of solution non-ideality, potential for liquid-liquid phase separation, water-solubility limitations of organics in ambient organic-inorganic particles, and assumptions about constant/variable surface tension may all play a role (Mikhailov et al., 2009; Rastak et al., 2017; Ovadnevaite et al. 2017). In the case of κ of organic surrogates mixed with ammonium sulfate, the relevant κ value range is ~ 0.12 to 0.15 obtained from 90 to 40 % RH. The measured κ values of the mixtures are compared to field data of HTDMA and CCN measurements conducted at a remote rainforest site in the central Amazon

during the dry and wet seasons (Whitehead et al., 2016; Pöhlker et al., 2016), which are consistent with κ obtained at similar field sites (within the uncertainty of experiments). The likely reason for a relatively good agreement between the hygroscopicity of the laboratory mixtures and the field data is that the organic mass fractions of the mix-bio-dry and mix-bio-wet mixtures are chosen in our laboratory experiments to be similar to those of the latest field data from Amazon. For example, Pöhlker et al. (2016) obtained the effective hygroscopicity parameters κ between 0.3 ± 0.01 and 0.15 ± 0.01 based on the organic mass fraction range from 0.65 to 0.97 in the dry season by aerosol chemical speciation monitor (ACSM) and CCN measurements. The predicted κ values of the mixtures at various RH levels shown in Fig. 6 (black curves) are obtained by application of Eq. (4) with use of the RH-dependent fitted HGFs of the organic surrogates (Eq. 5), the predicted growth factor of AS by the AIOMFAC model (for the humidification case) and the volume fraction based mixing rule for a mixture's HGF (Eq. 6). For these calculations, a solution surface tension of 0.072 J m^{-2} was assumed. These predictions agree relatively well with the experimental κ_{dry} and κ_{wet} values obtained from the HTDMA over a wide range in RH referring to dehumidification conditions (no solid AS). Furthermore, the combined approach of Eqs. (4-6) allows for a prediction of the change in κ at high RH towards water vapor super-saturation. A small difference in κ between sub- and super-saturated conditions is observed for our mixed systems when comparing the HTDMA data and predictions at 90 % RH with the predictions near 100 % RH and the κ values from the CNN field measurements. The difference is more pronounced for the wet season case. Rastak et al. (2017) observed a marked difference in apparent hygroscopicity and related mixture κ of the organic aerosols (AS-free) occurring in the case of monoterpene-derived secondary organic aerosol (SOA) for sub- vs. super-saturated conditions. A smaller difference was reported for the isoprene-derived SOA (Pajunoja et al., 2015: Rastak et al., 2017), more like the difference observed here for the mixtures containing AS (and therefore having overall higher κ values than typical salt-free organic aerosols). Rastak et al. (2017) attribute the distinct difference in κ_{SOA} of the monoterpene SOA to the limited mutual solubility of certain SOA components in water, because a single liquid organic-phase of monoterpene oxidation products is present at RH below 95 %, but over a RH range above 95 %, liquid-liquid phase separation is observed by optical microscopy as well as predicted by the AIOMFAC-based equilibrium model. In the mix-bio-wet and mix-bio-dry cases

shown in Fig. 6, the likely reason for the change in characteristic mixture hygroscopicity is not necessarily due to a liquid-liquid phase separation at high RH. For example, the κ parameter obtained from field data is ~0.15±0.06 at 90 % RH, while its value reaches ~0.18±0.04 at RH > 100 % (just prior to CCN activation). A likely reason for the difference is that hygroscopic particles, especially those containing sparingly soluble organics like 4-hydroxybenzoic acid, take up water dramatically above 95 % RH when approaching 100 % RH (Hartz et al., 2006; Chan et al., 2008; Rastak et al., 2017), which is clear from model predictions, as demonstrated in Fig. 6 by application of Eq. (4). The predicted curve in the mixture's effective κ parameter may well capture the change in hygroscopicity under such high RH conditions. Consequently, for a precise representation of the hygroscopic growth behavior (e.g. HGF) at high RH (> 95 %) by the κ-Köhler model, the value of κ would need to be varied. While a variable κ value is contrary to the attempted simplicity of the single-parameter κ-Köhler model, it is at least advised to consider that κ values derived from HGF data at 80 or 90 % RH may not apply accurately for the calculation of CCN activation properties of such biomass burning aerosols.

To summarize, there is small difference in hygroscopicity parameters between sub-saturated measurement conditions at 90 % RH in the laboratory with HTDMA and supersaturated conditions using CCN measurements, in agreement with the findings of other studies. On a regional scale, in the dry and wet period, the hygroscopic behavior in some extent of the Amazon rainforest is influenced significantly by the biomass burning emissions, which enhances CCN activity and droplet number concentrations in warm clouds in that region and influences the radiation balance and cloud life time (Pöschl et al., 2010). Underestimation of organic surrogate component mass fractions in the mixed particles or organic : sulfate mass ratios may be responsible for the slight differences in the determined κ parameters of the laboratory and field measurements.

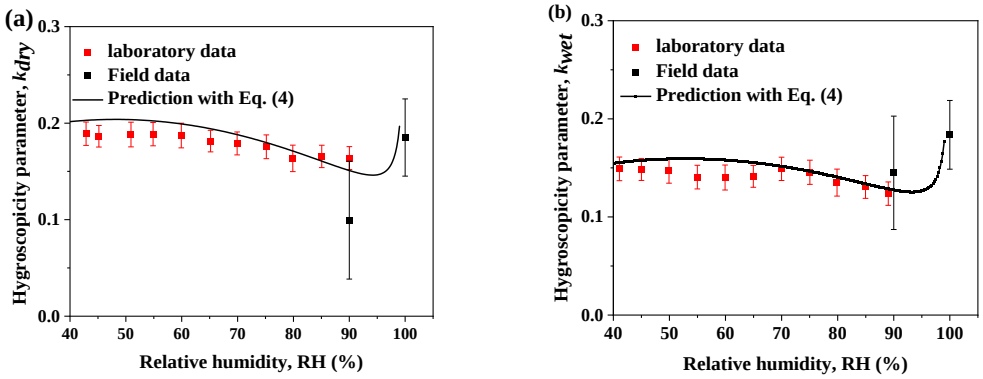

Figure 6. Hygroscopicity parameter, κ, representing mixed aerosol particles consisting of organic surrogate components and ammonium sulfate at different periods (initial dry diameter of 100 nm at RH < 5 %). The black curves in panels (a, b) show the κ prediction from Eq. (4) with HGF_{mix} calculated by Eq. (6) using component volume fractions and the HGF of the individual mixture components from a fit to the laboratory data (using Eq.5). The black symbols and error bars show field data from the Amazon during the dry and wet periods at conditions of water vapor sub-saturation (HTDMA measurement) and super-saturation (κ_{CNN}) (Whitehead et al., 2016; Pöhlker et al., 2016)."

5. Conclusion and Outlook

In this PhD project, nano-HTDMA apparatus is developed and applied to high accurate hygroscopicity measurements, especially for the sub-10 nm aerosol nanoparticles.

(1) In the first study, we presented our newly designed and self-assembled nano-HTDMA for measuring the hygroscopicity of nanoparticles in the sub-10 nm diameter size range. We also introduced comprehensive methods for system calibration and reported on the performance of the system, focusing on sizing accuracy and preventing predeliquescence in the deliquescence measurement mode. By comparing our findings with previous studies on ammonium sulfate nanoparticles (Biskos et al., 2006b), we show that our system is capable of providing high-quality data of the hygroscopic behavior of sub-10 nm nanoparticles. We then extended our measurements to sodium sulfate nanoparticles, for which size-dependent deliquescence and efflorescence have been clearly observed for nanoparticles down to 6 nm in size, and which demonstrate similar behavior to sodium chloride.

As we know, atmospheric aerosol particles consist of not only inorganic components but also a vast number of other organic components existing in the atmosphere. However, their physicochemical properties are still not fully understood, especially when it comes to the nanoscale and supersaturated concentration range. The nano-HTDMA system can be directly applicable for exploring the size dependence of aerosol nanoparticles. By combing the multisize measurements of hygroscopicity and the differential Köhler analyses (DKA; Cheng et al., 2015) in the nano size range, we will be able to characterize and parameterize the water activity and surface tension of different inorganic and organic systems. This will further help us to understand the formation and transformation of aerosol nanoparticles in the atmosphere and their interaction with water vapor.

(2) In the second study, we investigated the hygroscopic behavior of levoglucosan and D-glucose nanoparticles with diameters down to 6 nm using a nano-HTDMA. Due to the partial evaporation of sub-20 nm levoglucosan nanoparticles in the nano-HTDMA system, we measured hygroscopic growth factor of levoglucosan in the size range from 20 to 100 nm. There is a weak size dependence of hygroscopic growth factor of

levoglucosan in the size range from 20 to 100 nm, while a stronger size dependence of the hygroscopic growth factor of D-glucose has been clearly observed in the size range from 6 to 20 nm. No prompt phase transitions occur in both deliquescence and efflorescence modes for both levoglucosan and D-glucose nanoparticles in the RH range from 5 % to 90 % RH. By comparing with the E-AIM model and ideal solution theory, ideal solution theory predicts well the hygroscopic behavior of two specific organics with diameter higher than 15 nm (levoglucosan and D-glucose), while hygroscopic growth factor of sub-15 D-glucose are agreed with E-AIM model prediction, respectively.

Biomass burning is an important source of anthropogenic atmospheric aerosols. Aerosol particles in the biomass burning smoke enriched with hygroscopic behavior are suggested to act as efficient CCN. However, their physicochemical properties (e.g., water activity, surface tension) are still not fully understand, especially when it comes to nanoscale. It is well known that aerosol population can appear as externally mixed or internally mixed (homogeneously internally, core-shell internally) in the biomass burning. The mixing structure has an important effect on the hygroscopic behavior of aerosol particles, especially for sub-10 nm size range. In future, we will able to parameterize water activity and surface tension by combing measured results of nanoparticles in the different sizes with DKA method. Also, we will be able to investigate the effect of mixing state on the hygroscopic behavior of aerosol particles from biomass burning in the different sizes. This will further help us to understand their interaction with water vapor.

(3) In the third study, a number of field-based hygroscopicity studies about biomass burning aerosol focus on the growth factors of mixtures at high RH (e.g. 90 % RH). However, less attention has been paid to the growth behavior at low to moderate RH, limiting the database for accurate estimates of particles optical and radiative properties over those lower RH ranges. However, this is a RH range in which water uptake or release behavior demonstrates a considerable variability among different organic-inorganic systems. The occurrence or suppression of a liquid-solid phase transition affects the physicochemical particle properties in a relative narrow RH range, potentially leading to particles of different morphology and physical states, affecting effective particle size and density. In this work, measurements and thermodynamic equilibrium predictions for organic-inorganic aerosols related to components from

biomass burning emissions demonstrate a diversity of hygroscopic growth/shrinking behavior. For example, in the case of aerosol mixtures containing levoglucosan and ammonium sulfate, the presence of levoglucosan may cause the efflorescence of AS to occur at higher RH than in pure aqueous AS particles-or it may completely suppress AS efflorescence, as observed for mixtures with a high levoglucosan mass fraction. The growth curves predicted with an AIOMFAC-based thermodynamic equilibrium model reproduce the observations in most cases reasonably well and we demonstrate the usefulness of predictions with different assumptions about the physical state of the organic components for the interpretation of experimental data, such as in the case of mixtures of 4-hydroxybenzoic acid and AS. However, the accurate prediction of AS efflorescence or its suppression in mixed particles is difficult. The E-AIM-predicted growth curves reproduce the measured hygroscopic behavior relatively well for the consideration of the effect of 4-hydroxybenzoic acid on the hygroscopic behavior of mixtures with AS, which leads to suppression of the AS efflorescence. In the case of mixtures of humic acid and AS, continuous water desorption of aerosol particles shows no significant effect on the efflorescence of AS. Also, as expected, there is a clear reduction in the diameter growth factor of mixed systems, in comparison with that of pure AS particles. In addition, the small difference in hygroscopicity parameters of mix-bio-dry and mix-bio-wet systems between measured data in the laboratory using HTDMA and the field using CCN activity measurements is due to the similar O:C ratios of organic surrogate compounds and AS mass fractions used in the model mixtures when experimental κ data from sub- and supersaturated water vapor conditions are compared.

The range of measurement-model comparisons presented in this study indicate that providing accurate thermodynamic model predictions of the hygroscopic growth behavior of mixed organic-inorganic systems remains a challenging problem. At moderate and low RH, where aerosol solution phases become highly concentrated, step-like or gradual crystallization and related solid-liquid equilibria may occur with high sensitivity to the organic/inorganic mass ratio and the chemical nature of the mixture constituents. To further improve thermodynamic equilibrium models for the prediction of hygroscopicity and phase transitions, controlled laboratory experiments with single solutes and/or with mixed organic-inorganic systems of known phase state will be useful to constrain model parameters. Ideally, such measurements should cover the

high, intermediate and low RH ranges under humidification and dehumidification conditions.

A. List of Publications

Peer-Reviewed Journal Papers

1 **Lei, T.,** Ma, N., Hong, J., Tuch, T., Wang, X., Wang, Z., Pöhlker, M., Ge, M., Wang, W., Mikhailov, E., Hoffmann, T., Pöschl, U., Su, H., Wiedensohler, A., and Cheng, Y.: Nano-hygroscopicity tandem differential mobility analyzer (nano-HTDMA) for investigating hygroscopic properties of sub-10 nm aerosol nanoparticles, Atmos. Meas. Tech., 13, 5551–5567, https://doi.org/10.5194/amt-13-5551-2020, 2020.

2 Wang, X., Ma, N., **Lei, T**., Größ, J., Li, G., Liu, F., Meusel, H., Mikhailov, E., Wiedensohler, A., and Su, H.: Effective density and hygroscopicity of protein particles generated with spray-drying process, Journal of Aerosol Science, 137, 105441, 2019.

3 **Lei, T.,** Zuend, A., Cheng, Y., Su, H., Wang, W., and Ge, M.: Hygroscopicity of organic surrogate compounds from biomass burning and their effect on the efflorescence of ammonium sulfate in mixed aerosol particles, Atmos. Chem. Phys., 18, 1045-1064, 2018.

4 **Lei, T.,** Zuend, A., Wang, W. G., Zhang, Y. H., and Ge, M. F.: Hygroscopicity of organic compounds from biomass burning and their influence on the water uptake of mixed organic ammonium sulfate aerosols, Atmos. Chem. Phys., 14, 11165-11183, 2014.

5 Wang, W., **Lei, T.,** Zuend, A., Su, H., Cheng, Y., Shi, Y., Ge, M., and Liu, M.: Effect of mixing structure on the water uptake of mixtures of ammonium sulfate and phthalic acid particles, Atmos. Chem. Phys. Discuss., https://doi.org/10.5194/acp-2020-632, accepted, 2020. **(contribute equally)**.

B. List of Figures

C. List of Tables

D. References

Altaf, M. B., Zuend, A., and Freedman, M. A.: Role of nucleation mechanism on the size dependent morphology of organic aerosol, Chem. Commun., 52, 9220-9223, 2016.

Andreae, M. O., Afchine, A., Albrecht, R., Holanda, B. A., Artaxo, P., Barbosa, H. M. J., Borrmann, S., Cecchini, M. A., Costa, A., Dollner, M., Fütterer, D., Järvinen, E., Jurkat, T., Klimach, T., Konemann, T., Knote, C., Krämer, M., Krisna, T., Machado, L. A. T., Mertes, S., Minikin, A., Pöhlker, C., Pöhlker, M. L., Pöschl, U., Rosenfeld, D., Sauer, D., Schlager, H., Schnaiter, M., Schneider, J., Schulz, C., Spanu, A., Sperling, V. B., Voigt, C., Walser, A., Wang, J., Weinzierl, B., Wendisch, M., and Ziereis, H.: Aerosol characteristics and particle production in the upper troposphere over the Amazon Basin, Atmos. Chem. Phys., 18, 921-961, https://doi.org/10.5194/acp-18-921-2018, 2018.

Andreae, M. O. and Gelencser, A.: Black carbon or brown carbon? The nature of light-absorbing carbonaceous aerosols, Atmos. Chem. Phys., 6, 3131-3148, https://doi.org/10.5194/acp-6-3131-2006, 2006.

Andreae, M. O., Artaxo, P., Brandao, C., Carswell, F. E., Ciccioli, P., da Costa, A. L., Culf, A. D., Esteves, J. L., Gash, J. H. C., Grace, J., Kabat, P., Lelieveld, J., Malhi, Y., Manzi, A. O., Meixner, F. X., Nobre, A. D., Nobre, C., Ruivo, M., Silva-Dias, M. A., Stefani, P., Valentini, R., von Jouanne, J., and Waterloo, M. J.: Biogeochemical cycling of carbon, water, energy, trace gases, and aerosols in Amazonia: The LBA-EUSTACH experiments, J. Geophys. Res., 107, 8066, https://doi.org/10.1029/2001JD000524, 2002.

Apelblat, A.: The vapour pressures of saturated aqueous solutions of potassium bromide, ammonium sulfate, copper (II) sulfate, iron (II) sulfate, and manganese (II) dichloride, at temperatures from 283 K to 308 K, J. Chem. Thermodyn., 25, 1513–1520, 1993.

Arnold, S., Emmons, L., Monks, S., Law, K. S., Ridley, D., Turquety, S., Tilmes, S., Thomas, J. L., Bouarar, I., and Flemming, J.: Biomass burning influence on high-latitude tropospheric ozone and reactive nitrogen in summer 2008: a multi-model analysis based on POLMIP simulations, Atmos. Chem. Phys., 15, 6047–6068, https://doi.org/10.5194/acp-15-6047-2015, 2015.

Artaxo, P., Martins, J. V., Yamasoe, M. A., Procópio, A. S., Pauliquevis, T. M., Andreae, M. O., Guyon, P., Gatti, L. V., and Leal, A. M. C.: Physical and chemical properties of aerosols in the wet and dry seasons in Rondônia, Amazonia, J. Geophys. Res., 107, 8081, https://doi.org/10.1029/2001JD000666, 2002.

Atkins, P., De Paula, J., and Walters, V.: Physical Chemistry, W. H. Freeman, Oxford University Press. 2006.

Atkinson, D. B., Radney, J. G., Lum, J., Kolesar, K. R., Cziczo, D. J., Pekour, M. S., Zhang, Q., Setyan, A., Zelenyuk, A., and Cappa, C. D.: Aerosol optical hygroscopicity measurements during the 2010 CARES campaign, Atmos. Chem. Phys., 15, 4045–4061, https://doi.org/10.5194/acp-15-4045-2015, 2015.

Bertram, T.H. and J.A. Thornton,: Toward a general parameterization of N_2O_5 reactivity on aqueous particles: the competing effects of particle liquid water, nitrate and chloride. Atmos. Chem. Phys., 2009. 9(21): p. 8351-8363.

Bezantakos, S., Huang, L., Barmpounis, K., Martin, S. T., and Biskos, G.: Relative humidity non uniformities in hygroscopic tandem differential mobility analyzer measurements, J. Aerosol Sci., 101:1–9. doi:10.1016/j.jaerosci.2016.07.004.

Bhandari, B. and Bareyre, I.: Estimation of crystalline phase present in the glucose crystal–solution mixture by water activity measurement, LWT - Food Science and Technology, 36, 729-733, 2003.

Bhattarai, H., Saikawa, E., Wan, X., Zhu, H., Ram, K., Gao, S., Kang, S., Zhang, Q., Zhang, Y., Wu, G., Wang, X., Kawamura, K., Fu, P., and Cong, Z.: Levoglucosan as a tracer of biomass burning: Recent progress and perspectives, Atmos. Res., 220, 20–33, 2019.

Birmili, W., Stratmann, F., Wiedensohler, A., Covert, D., M. Russell, L., and Berg, O.:

Determination of differential mobility analyzer transfer functions using identical instruments in Series, Aerosol Sci. Technol., 27, 215– 223, 1997.

Birmili, W., Weinhold, K., Rasch, F., Sonntag, A., Sun, J., Merkel, M., Wiedensohler, A., Bastian, S., Schladitz, A., Löschau, G., Cyrys, J., Pitz, M., Gu, J., Kusch, T., Flentje, H., Quass, U., Kaminski, H., Kuhlbusch, T. A. J., Meinhardt, F., and Fiebig, M.: Long-term observations of tropospheric particle number size distributions and equivalent black carbon mass concentrations in the German Ultrafine Aerosol Network (GUAN), Earth Syst. Sci. Data, 8, 355–382, https://doi.org/10.5194/essd-8-355-2016, 2016.

Biskos, G., Malinowski, A., Russell, L. M., Buseck, P. R., and Martin, S. T.: Nanosize effect on the deliquescence and the efflorescence of sodium chloride particles, Aerosol Sci. Technol., 40, 97-106, 2006a.

Biskos, G., Paulsen, D., Russell, L. M., Buseck, P. R., and Martin, S. T.: Prompt deliquescence and efflorescence of aerosol nanoparticles, Atmos. Chem. Phys., 6, 4633–4642, https://doi.org/10.5194/acp-6-4633-2006, 2006b.

Biskos, G., Russell, L. M., Buseck, P. R., and Martin, S. T.: Nanosize effect on the hygroscopic growth factor of aerosol particles, Geophys. Res. Lett., 33, L07801, doi:10.1029/2005GL025199, 2007.

Bodsworth, A., Zobrist, B., and Bertram, A. K.: Inhibition of efflorescence in mixed organic-inorganic particles at temperatures less than 250 K, Phys. Chem. Chem. Phys., 12, 12259–12266, 2010.

Bohren, C. and Huffmann, D.: Absorption and scattering of light by small particles, Wiley-VCH, New York, USA, 2004.

Bones, D. L., Reid, J. P., Lienhard, D. M., and Krieger, U. K.: Comparing the mechanism of water condensation and evaporation in glassy aerosol, P. Natl. Acad. Sci. USA, 109, 11613–11618, 2012.

Boucher Olivier and David, R.: Clouds and Aerosols, Intergovernmental Panel on Climate Change, 2014, Climate Change 2013 – The Physical Science Basis: Working Group I Contribution to the Fifth Assessment Report of the Intergovernmental Panel on Climate Change, Cambridge University Press, Cambridge, https://doi.org/10.1017/CBO9781107415324, 2013.

Brooks, S. D., DeMott, P. J., and Kreidenweis, S. M.: Water uptake by particles containing humic materials and mixtures of humic materials with ammonium sulfate, Atmos. Environ., 38, 1859-1868, 2004.

Burgos, M. A., Andrews, E., Titos, G., Alados-Arboledas, L., Baltensperger, U., Day, D., Jefferson, A., Kalivitis, N., Mihalopoulos, N., Sherman, J., Sun, J., Weingartner, E., and Zieger, P.: A global view on the effect of water uptake on aerosol particle light scattering, Scientific Data, 6, 157, 2019.

Bzdek, B. R., Zordan, C. A., Luther, G. W., and Johnston, M. V.: Nanoparticle Chemical Composition During New Particle Formation, Aerosol Science and Technology, 45, 1041-1048, 2011.

Carrico, C. M., Petters, M. D., Kreidenweis, S. M., Collett, J. L., Engling, G., and Malm, W. C.: Aerosol hygroscopicity and cloud droplet activation of extracts of filters from biomass burning experiments, J. Geophys. Res., 113, D08206, https://doi.org/10.1029/2007JD009274, 2008.

Chan, M. N. and Chan, C. K.: Hygroscopic properties of two model humic-like substances and their mixtures with inorganics of atmospheric importance, Environ. Sci. Technol., 37, 5109–5115, 2003.

Chan, M. N., Choi, M. Y., Ng, N. L., and Chan, C. K.: Hygroscopicity of water-soluble organic compounds in atmospheric aerosols: Amino acids and biomass burning derived organic species, Environ. Sci. Technol., 37, 5109–5115, 2003.

Chan, M. N., Kreidenweis, S. M., and Chan, C. K.: Measurements of the Hygroscopic and Deliquescence Properties of Organic Compounds of Different Solubilities in Water and Their Relationship with Cloud Condensation Nuclei Activities, Environ. Sci. Technol., 42, 3602–3608, 2008.

Chan, M. N. C. and. Chan, C. K.: Mass transfer effects in hygroscopic measurements of aerosol particles, Atmos. Chem. Phys., 5, 2703–2712, https://doi.org/10.5194/acp-5-2703-2005, 2005.

Charlson, R. J., Schwartz, S. E., Hales, J. M., Cess, R. D., Coakley, J. A., Hansen, J. E., and Hoffmann, D. J.: Climate forcing by anthropogenic aerosols, Science, 255, 423-430, 1992.

Chen, Da-Ren, David Y.H. Pui, and Stanley L. Kaufman.: Electrospraying of conducting liquids for monodisperse aerosol generation in the 4 nm to 1.8 nm diameter range, J. Aerosol Sci., 26:963-977.

Cheng, Y. F., Wiedensohler, A., Eichler, H., Heintzenberg, J., Tesche, M., Ansmann, A., Wendisch, M., Su, H., Althausen, D., Herrmann, H., Gnauk, T., Brüggemann, E., Hu, M., and Zhang, Y. H.: Relative humidity dependence of aerosol optical properties and direct radiative forcing in the surface boundary layer at Xinken in Pearl River Delta of China: An observation based numerical study, Atmos. Environ., 42, 6373–6397, 2008.

Cheng, Y. F., Berghof, M., Garland, R. M., Wiedensohler, A., Wehner, B., Muller, T., Su, H., Zhang, Y. H., Achtert, P., Nowak, A., Pöschl, U., Zhu, T., Hu, M., and Zeng, L. M.: Influence of soot mixing state on aerosol light absorption and single scattering albedo during air mass aging at a polluted regional site in northeastern China, J. Geophys. Res., 114, D00G10, https://doi.org/10.1029/2008JD010883, 2009.

Cheng, Y. F., Su, H., Koop, T., Mikhailov, E., and Pöschl, U.: Size dependence of phase transitions in aerosol nanoparticles, Nat. Commun., 6, 5923, doi:10.1038/ncomms6923, 2015.

Cheng, Y. F., Su, H., Rose, D., Gunthe, S. S., Berghof, M.,Wehner, B., Achtert, P., Nowak, A., Takegawa, N., Kondo, Y., Shiraiwa, M., Gong, Y. G., Shao, M., Hu, M., Zhu, T., Zhang, Y. H., Carmichael, G. R., Wiedensohler, A., Andreae, M. O., and Pöschl, U.: Size-resolved measurement of the mixing state of soot in the megacity Beijing, China: diurnal cycle, aging and parameterization, Atmos. Chem. Phys., 12, 4477–4491, https://doi.org/10.5194/acp-12-4477-2012, 2012.

Cheng, Y. F., Zheng, G. J., Wei, C., Mu, Q., Zheng, B., Wang, Z. B., Gao, M., Zhang, Q., He, K. B., Carmichael, G., Pöschl, U., and Su, H.: Reactive nitrogen chemistry in aerosol water as a source of sulfate during haze events in China, Sci. Adv., 2, e1601530, https://doi.org/10.1126/sciadv.1601530, 2016.

Cheung, H. H. Y., Yeung, M. C., Li, Y. J., Lee, B. P., and Chan, C. K.: Relative Humidity-Dependent HTDMA Measurements of Ambient Aerosols at the HKUST Supersite in Hong Kong, China, Aerosol Sci. Tech., 49, 643–654, 2015.

Choi, M. Y. and Chan, C. K.: The effects of organic species on the hygroscopic behaviors of inorganic aerosols, Environ. Sci. Technol., 36, 2422–2428, 2002.

Chýlek, P. and Coakley, J. A.: Aerosols and climate, Science, 183, 75-77, 1974.

Ciarelli, G., Aksoyoglu, S., Crippa, M., Jimenez, J. L., Nemitz, E., Sellegri, K., Äijälä, M., Carbone, S., Mohr, C., O'Dowd, C., Poulain, L., Baltensperger, U., and Prévôt, A. S. H.: Evaluation of European air quality modelled by CAMx including the volatility basis set scheme, Atmos. Chem. Phys., 16, 10313-10332, 2016.

Ciobanu, V. G., Marcolli, C., Krieger, U. K., Zuend, A., and Peter, T.: Efflorescence of ammonium sulfate and coated ammonium sulfate particles: evidence for surface nucleation, J. Phys. Chem. A, 114, 9486–9495, 2010.

Clegg, S. L., Brimblecombe, P., and Wexler, A. S.: Thermodynamic Model of the System H^+-NH^+-SO_4^{2-}-NO_3^--H_2O at Tropospheric Temperatures, J. Phys. Chem. A, 102, 2137–2154, 1998.

Clegg, S. L. and Seinfeld, J. H.: Thermodynamic models of aqueous solutions containing inorganic electrolytes and dicarboxylic acids at 298.15 K. 2. Systems including dissociation equilibria, J. Phys. Chem. A, 110, 5718–5734, 2006.

Clegg, S. L., Seinfeld, J. H., and Brimblecombe, P.: Thermodynamic modelling of aqueous aerosols containing electrolytes and dissolved organic compounds, J. Aerosol Sci., 32, 713–738, doi:10.1016/s0021-8502(00)00105-1, 2001.

Clegg, S. L. and Wexler, A. S.: Densities and Apparent Molar Volumes of Atmospherically Important Electrolyte Solutions. 1. The Solutes H_2SO_4, HNO_3, HCl, Na_2SO_4, $NaNO_3$, NaCl, $(NH_4)(_2)SO_4$, NH_4NO_3, and NH_4Cl from 0 to 50 °C, Including Extrapolations to Very Low Temperature and to the Pure Liquid State, and $NaHSO_4$, NaOH, and NH_3 at 25 °C, J. Phys. Chem. A, 115, 3393–3460, 2011a.

Clegg, S. L. and Wexler, A. S.: Densities and apparent molar volumes of atmospherically important electrolyte solutions. 2. The systems $H(^+)$-$HSO_4(^-)$-$SO_4(^{2-})$-H_2O from 0 to 3 mol $kg(^{-1})$ as a function of temperature and $H(^+)$-$NH_4(^+)$-HSO_4(-)-$SO_4(^{2-})$-H_2O from 0 to 6 mol $kg(^{-1})$ at 25 °C using a Pitzer ion interaction model, and NH_4HSO_4-H_2O and $(NH_4)_3H(SO_4)_2$-H_2O over the entire concentration range, J. Phys. Chem. A, 115, 3461–3474, 2011b.

Comesaña, J. F., Correa, A., and Sereno, A. M.: Water activity at 35 °C in 'sugar' + water and 'sugar' + sodium chloride + water systems, Int. J. Food Sci. Tech., 36, 655-661, 2001.

DeCarlo, P. F., Slowik, J. G., Worsnop, D. R., Davidovits, P., and Jimenez, J. L.: Particle morphology and density characterization by combined mobility and aerodynamic diameter measurements. Part 1: Theory, Aerosol Sci. Technol., 38, 1185–1205, 2004.

Decesari, S., Fuzzi, S., Facchini, M. C., Mircea, M., Emblico, L., Cavalli, F., Maenhaut, W., Chi, X., Schkolnik, G., Falkovich, A., Rudich, Y., Claeys, M., Pashynska, V., Vas, G., Kourtchev, I., Vermeylen, R., Hoffer, A., Andreae, M. O., Tagliavini, E., Moretti, F., and Artaxo, P.: Characterization of the organic composition of aerosols from Rondonia, Brazil, during the LBA-SMOCC 2002 experiment and its representation through model compounds, Atmos. Chem. Phys., 6, 375–402, https://doi.org/10.5194/acp-6-375-2006, 2006.

Denjean, C., Formenti, P., Picquet-Varrault, B., Pangui, E., Zapf, P., Katrib, Y., Giorio, C., Tapparo, A., Monod, A., and Temime-Roussel, B.: Relating hygroscopicity and optical properties to chemical composition and structure of secondary organic aerosol particles generated from the ozonolysis of α-pinene, Atmos. Chem. Phys., 15, 3339–3358, https://doi.org/10.5194/acp-15-3339-2015, 2015.

Dick, W. D., Saxena, P., and McMurry, P. H.: Estimation of water uptake by organic compounds in submicron aerosols measured during the Southeastern Aerosol and Visibility Study, Journal of Geophysical Research-Atmospheres, 105, 1471-1479, 2000.

Dong, J. L., Xiao, H. S., Zhao, L. J., and Zhang, Y.-H.: Spatially resolved Raman investigation on phase separations of mixed Na_2SO_4/$MgSO_4$ droplets, J. Raman Spectrosc., 2009, 40 (3), 338–343.

Dunne, E. M., Gordon, H., Kürten, A., Almeida, J., Duplissy, J., Williamson, C., Ortega, I. K., Pringle, K. J., Adamov, A., Baltensperger, U., Barmet, P., Benduhn, F., Bianchi, F., Breitenlechner, M., Clarke, A., Curtius, J., Dommen, J., Donahue, N. M., Ehrhart, S., Flagan, R. C., Franchin, A., Guida, R., Hakala, J., Hansel, A., Heinritzi, M., Jokinen, T., Kangasluoma, J., Kirkby, J., Kulmala, M., Kupc, A., Lawler, M. J., Lehtipalo, K., Makhmutov, V., Mann, G., Mathot, S., Merikanto, J., Miettinen, P., Nenes, A., Onnela, A., Rap, A., Reddington, C. L. S., Riccobono,

F., Richards, N. A. D., Rissanen, M. P., Rondo, L., Sarnela, N., Schobesberger, S., Sengupta, K., Simon, M., Sipilä, M., Smith, J. N., Stozkhov, Y., Tomé, A., Tröstl, J., Wagner, P. E., Wimmer, D., Winkler, P. M., Worsnop, D. R., and Carslaw, K. S.: Global atmospheric particle formation from CERN CLOUD measurements, Science., 354, 1119-1124, 2016.

Duplissy, J., Gysel, M., Sjogren, S., Meyer, N., Good, N., Kammermann, L., Michaud, V., Weigel, R., Martins dos Santos, S., Gruening, C., Villani, P., Laj, P., Sellegri, K., Metzger, A., McFiggans, G. B., Wehrle, G., Richter, R., Dommen, J., Ristovski, Z., Baltensperger, U., and Weingartner, E.: Intercomparison study of six HTDMAs: results and recommendations, Atmos. Meas. Tech., 2, 363–378, https://doi.org/10.5194/amt-2-363-2009, 2009.

Dusek, U., Frank, G. P., Curtius, J., Drewnick, F., Schneider, J., Kürten, A., Rose, D., Andreae, M. O., Borrmann, S., and Pöschl, U.: Enhanced organic mass fraction and decreased hygroscopicity of cloud condensation nuclei (CCN) during new particle formation events, Geophys. Res. Lett., 37, 2010.

Dusek, U., Frank, G. P., Massling, A., Zeromskiene, K., Iinuma, Y., Schmid, O., Helas, G., Hennig, T., Wiedensohler, A., and Andreae, M. O.: Water uptake by biomass burning aerosol at sub- and supersaturated conditions: closure studies and implications for the role of organics, Atmos. Chem. Phys., 11, 9519–9532, https://doi.org/10.5194/acp-11-9519-2011, 2011.

Dutcher, C. S., Ge, X., Wexler, A. S. & Clegg, S. L. An Isotherm-Based Thermodynamic Model of Multicomponent Aqueous Solutions, Applicable Over the Entire Concentration Range. J. Phys. Chem. A 117, 3198-3213 (2013).

Ehn, M., Thornton, J. A., Kleist, E., Sipilä, M., Junninen, H., Pullinen, I., Springer, M., Rubach, F., Tillmann, R., Lee, B., Lopez-Hilfiker, F., Andres, S., Acir, I.-H., Rissanen, M., Jokinen, T., Schobesberger, S., Kangasluoma, J., Kontkanen, J., Nieminen, T., Kurtén, T., Nielsen, L. B., Jørgensen, S., Kjaergaard, H. G., Canagaratna, M., Maso, M. D., Berndt, T., Petäjä, T., Wahner, A., Kerminen, V.-M., Kulmala, M., Worsnop, D. R., Wildt, J., and Mentel, T. F.: A large source of low-volatility secondary organic aerosol, Nature., 506, 476-479, 2014.

Eichler, H., Cheng, Y. F., Birmili, W., Nowak, A., Wiedensohler, A., Brüggemann, E., Gnauk, T., Herrmann, H., Althausen, D., Ansmann, A., Engelmann, R., Tesche, M., Wendisch, M., Zhang, Y. H., Hu, M., Liu, S., and Zeng, L. M.: Hygroscopic

properties and extinction of aerosol particles at ambient relative humidity in South-Eastern China, Atmos. Environ., 42, 25, 6321–6334. doi:10.1016/j.atmosenv.2008.05.007, 2008.

Elias, V. O., Simoneit, B. R. T., Cordeiro, R. C., and Turcq, B.: Evaluating levoglucosan as an indicator of biomass burning in Carajás, amazônia: a comparison to the charcoal record22Associate editor: R. Summons, Geochim. Cosmochim. Acta., 65, 267-272, 2001.

Engelhart, G. J., Hennigan, C. J., Miracolo, M. A., Robinson, A. L., and Pandis, S. N.: Cloud condensation nuclei activity of fresh primary and aged biomass burning aerosol, Atmos. Chem. Phys., 12, 7285–7293, https://doi.org/10.5194/acp-12-7285-2012, 2012.

Estillore, A. D., Morris, H. S., Or, V. W., Lee, H. D., Alves, M. R., Marciano, M. A., Laskina, O., Qin, Z., Tivanski, A. V., and Grassian, V. H.: Linking hygroscopicity and the surface microstructure of model inorganic salts, simple and complex carbohydrates, and authentic sea spray aerosol particles, Phys. Chem. Chem. Phys., 2017,19, 21101-21111.

Fan, J. W., Rosenfeld, D., Zhang, Y. W., Giangrande, S. E., Li, Z. Q., Machado, L. A. T., Martin, S. T., Yang, Y., Wang, J., Artaxo, P., Barbosa, H. M. J., Braga, R. C., Comstock, J. M., Feng, Z., Gao, W. H., Gomes, H. B., Mei, F., Pöhlker, C., Pöhlker, M. L., Pöschl, U., and de Souza, R. A. F.: Substantial convection and precipitation enhancements by ultrafine aerosol particles, Science, 359, 411-418, 2018.

Favez, O., Alfaro, S. C., Sciare, J., Cachier, H., and Abdelwahab, M. M.: Ambient measurements of light-absorption by agricultural waste burning organic aerosols, J. Aerosol Sci., 40, 613–620, 2009.

Ferreira, O., Brignole, E. A., and Macedo, E. A.: Phase equilibria in sugar solutions using the A-UNIFAC model, Ind. Eng. Chem. Res., 42 (24), 6212–6222, 2003.

Fraser, M. P. and Lakshmanan, K.: Using Levoglucosan as a Molecular Marker for the Long-Range Transport of Biomass Combustion Aerosols, Environ. Sci. Technol., 34, 4560-4564, 2000.

Fredenslund, A., Jones, R. L., and Prausnitz, J. M.: Group-contribution estimation of activity-coefficients in nonideal liquid-mixtures, Aiche J., 21, 1086–1099, doi:10.1002/aic.690210607, 1975.

Fredenslund, A., Jones, R. L., and Prausnitz, J. M.: A group-contribution method is presented for the prediction of activity coefficients in nonelectrolyte liquid mixtures, Aiche J., 21, 1086–1099, 1975.Gilman, J. B., Lerner, B. M., Kuster, W. C., Goldan, P. D., Warneke, C., Veres, P. R., Roberts, J. M., de Gouw, J. A., Burling, I. R., and Yokelson, R. J.: Biomass burning emissions and potential air quality impacts of volatile organic compounds and other trace gases from fuels common in the US, Atmos. Chem. Phys., 15, 13915-13938, 2015.

Gao, Y. G, Chen, S. B., and Yu, L. E.: Efflorescence relative humidity for ammonium sulfate particles, J. Phys. Chem. A, 110, 7602– 7608, https://doi.org/10.1021/jp057574g, 2006.

Giamarelou, M., Smith, M., Papapanagiotou, E., Martin, S. T., and Biskos, G.: Hygroscopic properties of potassium-halide nanoparticles, Aerosol Sci. Technol., 52, 536–545, 2018.

Gilman, J. B., Lerner, B. M., Kuster,W. C., Goldan, P. D.,Warneke, C., Veres, P. R., Roberts, J. M., de Gouw, J. A., Burling, I.R., and Yokelson, R. J.: Biomass burning emissions and potential air quality impacts of volatile organic compounds and other trace gases from fuels common in the US, Atmos. Chem. Phys., 15, 13915–13938, https://doi.org/10.5194/acp-15-13915-2015, 2015.

Gupta, D., Eom, H. J., Cho, H. R., and Ro, C. U.: Hygroscopic behavior of NaCl–MgCl2 mixture particles as nascent sea-spray aerosol surrogates and observation of efflorescence during humidification, Atmos. Chem. Phys., 15, 11273-11290, 2015.

Gysel, M., Weingartner, E., and Baltensperger, U.: Hygroscopicity of aerosol particles at low temperatures. 2. Theoretical and experimental hygroscopic properties of laboratory generated aerosols, Environ. Sci. Technol., 36, 63–68, doi:10.1021/es010055g, 2002.

Hämeri, K., Laaksonen, A., Väkevä, M., and Suni, T.: Hygroscopic growth of ultrafine sodium chloride particles, J. Geophys. Res., 106, 20 749–20 757, 2001.

Hämeri, K., Väkevä, M., Hansson, H.-C., and Laaksonen, A.: Hygroscopic growth of ultrafine ammonium sulfate aerosol measured using an ultrafine tandem differential mobility analyzer, J. Geophys. Res., 105, 22 231–22 242, 2000.

Hansen, H. K., Rasmussen, P., Fredenslund, A., Schiller, M., and Gmehling, J.: Vapor-liquid equilibria by UNIFAC group contribution. 5. Revision and extension, Ind. Eng. Chem. Res., 30, 2352–2355, 1991.

Hartz, K. E. H., Tischuk, J. E., Chan, M. N., Chan, C. K., Donahue, N. M., and Pandis, S. N.: Cloud condensation nuclei activation of limited solubility organic aerosol, Atmos. Environ., 40, 605–617, 2006.

Hecobian, A., Zhang, X., Zheng, M., Frank, N., Edgerton, E. S., and Weber, R. J.: Water-Soluble Organic Aerosol material and the light-absorption characteristics of aqueous extracts measured over the Southeastern United States, Atmos. Chem. Phys., 10, 5965–5977, https://doi.org/10.5194/acp-10-5965-2010, 2010.

Hegg, D. A., Warren, S. G., Grenfell, T. C., Doherty, S. J., and Clarke, A. D.: Sources of light-absorbing aerosol in arctic snow and their seasonal variation, Atmos. Chem. Phys., 10, 10923–10938, https://doi.org/10.5194/acp-10-10923-2010, 2010.

Hennig, T., Massling, A., Brechtel, F. J., and Wiedensohler, A.: A tandem DMA for highly temperature-stabilized hygroscopic particle growth measurements between 90 % and 98% relative humidity, J. Aerosol Sci., 36, 1210–1223, 2005.

Hodas, N., Zuend, A., Mui, W., Flagan, R., and Seinfeld, J.: Influence of particle-phase state on the hygroscopic behavior of mixed organic–inorganic aerosols, Atmos. Chem. Phys., 15, 5027–5045, https://doi.org/10.5194/acp-15-5027-2015, 2015.

Hodas, N., Zuend, A., Schilling, K., Berkemeier, T., Shiraiwa, M., Flagan, R. C., and Seinfeld, J. H.: Discontinuities in hygroscopic growth below and above water saturation for laboratory surrogates of oligomers in organic atmospheric aerosols, Atmos. Chem. Phys., doi: 10.5194/acp-16-12767-2016, 2016.

Hong, J., Häkkinen, S. A. K., Paramonov, M., Äijälä, M., Hakala, J., Nieminen, T., Mikkilä, J., Prisle, N. L., Kulmala, M., Riipinen, I., Bilde, M., Kerminen, V. M., and Petäjä, T.: Hygroscopicity, CCN and volatility properties of submicron atmospheric aerosol in a boreal forest environment during the summer of 2010, Atmos. Chem. Phys., 14, 4733–4748, https://doi.org/10.5194/acp-14-4733-2014, 2014.

Hong, J., Kim, J., Nieminen, T., Duplissy, J., Ehn, M., Äijälä, M., Hao, L. Q., Nie, W., Sarnela, N., Prisle, N. L., Kulmala, M., Virtanen, A., Petäjä, T., and Kerminen, V. M.: Relating the hygroscopic properties of submicron aerosol to both gas- and

particle-phase chemical composition in a boreal forest environment, Atmos. Chem. Phys., 15, 11999–12009, https://doi.org/10.5194/acp-15-11999-2015, 2015.

Hu, D. W., Qiao, L. P., Chen, J.-M., Ye, X. N, Yang, X., Cheng, T. T., and Fang, W.: Hygroscopicity of inorganic aerosols: size and relative humidity effects on the growth factor, Aerosol Air Qual. Res., 10, 255−264. 2010.

Iskandar, F., Gradon, L., and Okuyama, K.: Control of the morphology of nanostructured particles prepared by the spray drying of a nanoparticle sol, J. Colloid Interface Sci., 265, 296–303. 2003.

Jacobson, M. Z.: Effects of biomass burning on climate, accounting for heat and moisture fluxes, black and brown carbon, and cloud absorption effects, J. Geophys. Res.-Atmos., 119, 8980–9002, 2014.

Jedelsk´y Jiri, L. ı. H. e. y., Pavel Hynˇcica, and Ivan and Cibulka: Partial molar volumes of organic solutes in water. IV. Benzoic and hydroxybenzoic acids at temperatures from T=298 K to T=498 K and pressures up to 30 MPa, J. Chem. Thermodyn., 32, 1299–1310, 2000.

Jing, B., Tong, S., Liu, Q., Li, K., Wang, W., Zhang, Y., and Ge, M.: Hygroscopic behavior of multicomponent organic aerosols and their internal mixtures with ammonium sulfate, Atmos. Chem. Phys., 16, 4101–4118, https://doi.org/10.5194/acp-16-4101-2016, 2016.

Kerminen, V.-M.: The effects of particle chemical character and atmospheric processes on particle hygroscopic properties, J. Aerosol Sci., 28, 121–132, 1997.

Keskinen, H., Virtanen, A., Joutsensaari, J., Tsagkogeorgas, G., Duplissy, J., Schobesberger, S., Gysel, M., Riccobono, F., Slowik, J. G., Bianchi, F., Yli-Juuti, T., Lehtipalo, K., Rondo, L., Breitenlechner, M., Kupc, A., Almeida, J., Amorim, A., Dunne, E. M., Downard, A. J., Ehrhart, S., Franchin, A., Kajos, M. K., Kirkby, J., Kürten, A., Nieminen, T., Makhmutov, V., Mathot, S., Miettinen, P., Onnela, A., Petäjä, T., Praplan, A., Santos, F. D., Schallhart, S., Sipilä, M., Stozhkov, Y., Tomé, A., Vaattovaara, P., Wimmer, D., Prevot, A., Dommen, J., Donahue, N. M., Flagan, R. C., Weingartner, E., Viisanen, Y., Riipinen, I., Hansel, A., Curtius, J., Kulmala, M., Worsnop, D. R., Baltensperger, U., Wex, H., Stratmann, F., and Laaksonen, A.: Evolution of particle composition in CLOUD nucleation experiments, Atmos. Chem. Phys., 13, 5587–5600, https://doi.org/10.5194/acp-

13-5587-2013, 2013.

Kim, J., Ahlm, L., Yli-Juuti, T., Lawler, M., Keskinen, H., Tröstl, J., Schobesberger, S., Duplissy, J., Amorim, A., Bianchi, F., Donahue, N. M., Flagan, R. C., Hakala, J., Heinritzi, M., Jokinen, T., Kürten, A., Laaksonen, A., Lehtipalo, K., Miettinen, P., Petäjä, T., Rissanen, M. P., Rondo, L., Sengupta, K., Simon, M., Tomé, A., Williamson, C., Wimmer, D., Winkler, P. M., Ehrhart, S., Ye, P., Kirkby, J., Curtius, J., Baltensperger, U., Kulmala, M., Lehtinen, K. E. J., Smith, J. N., Riipinen, I., and Virtanen, A.: Hygroscopicity of nanoparticles produced from homogeneous nucleation in the CLOUD experiments, Atmos. Chem. Phys., 16, 293–304, https://doi.org/10.5194/acp-16-293-2016, 2016.

Kinney, P. D., Pui, D. Y. H., Mullholland, G. W., and Bryner, N. P.: Use of the electrostatic classification method to size 0.1 μm SRM particles—a feasibility Study. J. Res. Natl. Stand. Technol. 96(2): 147– 176, 1991.

Kirkby, J., Curtius, J., Almeida, J., Dunne, E., Duplissy, J., Ehrhart, S., Franchin, A., Gagné, S., Ickes, L., Kürten, A., Kupc, A., Metzger, A., Riccobono, F., Rondo, L., Schobesberger, S., Tsagkogeorgas, G., Wimmer, D., Amorim, A., Bianchi, F., Breitenlechner, M., David, A., Dommen, J., Downard, A., Ehn, M., Flagan, R. C., Haider, S., Hansel, A., Hauser, D., Jud, W., Junninen, H., Kreissl, F., Kvashin, A., Laaksonen, A., Lehtipalo, K., Lima, J., Lovejoy, E. R., Makhmutov, V., Mathot, S., Mikkilä, J., Minginette, P., Mogo, S., Nieminen, T., Onnela, A., Pereira, P., Petäjä, T., Schnitzhofer, R., Seinfeld, J. H., Sipilä, M., Stozhkov, Y., Stratmann, F., Tomé, A., Vanhanen, J., Viisanen, Y., Vrtala, A., Wagner, P. E., Walther, H., Weingartner, E., Wex, H., Winkler, P. M., Carslaw, K. S., Worsnop, D. R., Baltensperger, U., and Kulmala, M.: Role of sulphuric acid, ammonia and galactic cosmic rays in atmospheric aerosol nucleation, Nature., 476, 429-433, 2011.

Kiss, G., Tombácz, E., and Hansson, H.-C.: Surface Tension Effects of Humic-Like Substances in the Aqueous Extract of Tropospheric Fine Aerosol, J. Atmos. Chem., 50, 279–294, 2005.

Knutson, E. O. and Whitby, K. T.: Aerosol classification by electric mobility: apparatus, theory, and applications, J. Aerosol Sci., 6, 443–451, 1975.

Koehler, K. A., Kreidenweis, S. M., DeMott, P. J., Prenni, A. J., Carrico, C. M., Ervens, B., and Feingold, G.: Water activity and activation diameters from hygroscopicity data - Part II: Application to organic species, Atmos. Chem. Phys., 6, 795-809,

2006.

Köhler, H.: The nucleus in and the growth of hygroscopic droplets, Trans. Faraday Soc., 32, 1152–1161, 1936.

Koop, T., Bookhold, J., Shiraiwa, M., and Poschl, U.: Glass transition and phase state of organic compounds: dependency on molecular properties and implications for secondary organic aerosols in the atmosphere, Phys. Chem. Chem. Phys., 13, 105 19238–19255, 2011.

Kreidenweis, S. M., Koehler, K., DeMott, P. J., Prenni, A. J., Carrico, C., and Ervens, B.: Water activity and activation diameters from hygroscopicity data - Part I: Theory and application to inorganic salts, Atmos. Chem. Phys., 5, 1357–1370, https://doi.org/10.5194/acp-5-1357-2005, 2005.

Kulmala, M., Kontkanen, J., Junninen, H., Lehtipalo, K., Manninen, H. E., Nieminen, T., Petäjä, T., Sipilä, M., Schobesberger, S., Rantala, P., Franchin, A., Jokinen, T., Järvinen, E., Äijälä, M., Kangasluoma, J., Hakala, J., Aalto, P. P., Paasonen, P., Mikkilä, J., Vanhanen, J., Aalto, J., Hakola, H., Makkonen, U., Ruuskanen, T., Mauldin, R. L., Duplissy, J., Vehkamäki, H., Bäck, J., Kortelainen, A., Riipinen, I., Kurtén, T., Johnston, M. V., Smith, J. N., Ehn, M., Mentel, T. F., Lehtinen, K. E. J., Laaksonen, A., Kerminen, V.-M., and Worsnop, D. R.: Direct Observations of Atmospheric Aerosol Nucleation, Science, 339, 943-946, 2013.

Laborde, M., Crippa, M., Tritscher, T., Juranyi, Z., Decarlo, P. F., Temime-Roussel, B., Marchand, N., Eckhardt, S., Stohl, A., Baltensperger, U., Prevot, A. S. H., Weingartner, E., and Gysel, M.: Black carbon physical properties and mixing state in the European megacity Paris, Atmos. Chem. Phys., 13, 5831–5856, https://doi.org/10.5194/acp-13-5831-2013, 2013.

Lack, D. A., Langridge, J. M., Bahreini, R., Cappa, C. D., Middlebrook, A. M., and Schwarz, J. P.: Brown carbon and internal mixing in biomass burning particles, P. Natl. Acad. Sci. USA, 115 109, 14802–14807, 2012.

Lawson, S. J., Keywood, M. D., Galbally, I. E., Gras, J. L., Cainey, J. M., Cope, M. E., Krummel, P. B., Fraser, P. J., Steele, L. P., Bentley, S. T., Meyer, C. P., Ristovski, Z., and Goldstein, A. H.: Biomass burning emissions of trace gases and particles in marine air at Cape Grim, Tasmania, Atmos. Chem. Phys., 15, 13393-13411, 2015.

Lee, Y. N.: Airborne measurement of inorganic ionic components of fine aerosol particles using the particle-into-liquid sampler coupled to ion chromatography technique during ACE-Asia and TRACE-P, J. Geophys. Res., 108, 8646, https://doi.org/10.1029/2002JD003265, 2003.

Lei, T., Zuend, A., Cheng, Y., Su, H., Wang, W., and Ge, M.: Hygroscopicity of organic surrogate compounds from biomass burning and their effect on the efflorescence of ammonium sulfate in mixed aerosol particles, Atmos. Chem. Phys., 18, 1045-1064, 2018.

Lei, T., Zuend, A., Wang, W. G., Zhang, Y. H., and Ge, M. F.: Hygroscopicity of organic compounds from biomass burning and their influence on the water uptake of mixed organic ammonium sulfate aerosols, Atmos. Chem. Phys., 14, 11165–11183, https://doi.org/10.5194/acp-14-11165-2014, 2014.

Lienhard, D. M., Bones, D. L., Zuend, A., Krieger, U. K., Reid, J. P., and Peter, T.: Measurements of thermodynamic and optical properties of selected aqueous organic and organic-inorganic mixtures of atmospheric relevance, J. Phys. Chem. A, 116, 9954–9968, 2012.

Lihavainen, H., Kerminen, V.-M., Komppula, M., Hatakka, J., Aaltonen, V., Kulmala, M., and Viisanen, Y.: Production of "potential" cloud condensation nuclei associated with atmospheric new-particle formation in northern Finland, J. Geophys. Res., 108, 4782, doi:10.1029/2003JD003887, 2003.

Liu, B. Y. H., Pui, D. Y. H., and Rubow, K. L. a. S., W.W.: ELECTROSTATIC EFFECTS IN AEROSOL SAMPLING AND FILTRATION, Arm. occup. Hyg., 29, 251-269, 1985.

Liu, J. M., Scheuer, E., Dibb, J., Ziemba, L. D., Thornhill, K. L., Anderson, B. E., Wisthaler, A., Mikoviny, T., Devi, J. J., Bergin, M., and Weber, R. J.: Brown carbon in the continental troposphere, Geophys. Res. Lett., 41, 2191–2195, 2014.

Liu, Q., Jing, B., Peng, C., Tong, S., Wang, W., and Ge, M.: Hygroscopicity of internally mixed multi-component aerosol particles of atmospheric relevance, Atmos. Environ., 125, 69-77, 2016.

Malm, W. C. and Kreidenweis, S. M.: The effects of models of aerosol hygroscopicity on the apportionment of extinction, Atmos. Environ., 31, 1965-1976, 1997.

Marcolli, C. and Peter, T.: Water activity in polyol/water systems: new UNIFAC parameterization, Atmos. Chem. Phys., 5, 1545-1555, 2005.

Marshall, F. H., Miles, R. E. H., Song, Y.-C., Ohm, P. B., Power, R. M., Reid, J. P., and Dutcher, C. S.: Diffusion and reactivity in ultraviscous aerosol and the correlation with particle viscosity, Chem. Sci, 7, 1298-1308, 2016.

Martin, M., Tritscher, T., Juranyi, Z., Heringa, M. F., Sierau, B., Weingartner, E., Chirico, R., Gysel, M., Prevot, A. S. H., Baltensperger, U., and Lohmann, U.: Hygroscopic properties of fresh and aged wood burning particles, J. Aerosol Sci., 56, 15–29, 2013.

Massling, A., Niedermeier, N., Hennig, T., Fors, E. O., Swietlicki, E., Ehn, M., Hämeri, K., Villani, P., Laj, P., Good, N., McFiggans, G., and Wiedensohler, A.: Results and recommendations from an intercomparison of six Hygroscopicity-TDMA systems, Atmos. Meas. Tech., 4, 485–497, https://doi.org/10.5194/amt-4-485-2011, 2011.

McFiggans, G., et al., The effect of physical and chemical aerosol properties on warm cloud droplet activation. Atmos. Chem. Phys., 2006. 6(9): p. 2593-2649.

Mikhailov, E. F., Vlasenko, S. S., and Ryshkevich, T. I.: Influence of chemical composition and microstructure on the hygroscopic growth of pyrogenic aerosol, Izv. Atmos. Ocean. Phy., 44, 416–431, 2008.

Mikhailov, E. F. and Vlasenko, S. S.: High humidity tandem differential mobility analyzer for accurate determination of aerosol hygroscopic growth, microstructure and activity coefficients over a wide range of relative humidity, Atmos. Meas. Tech., 13, 2035–2056, https://doi.org/10.5194/amt-13-2035-2020, 2020.

Mikhailov, E., Vlasenko, S., Niessner, R., and Pöschl, U.: Interaction of aerosol particles composed of protein and salts with water vapor: hygroscopic growth and microstructural rearrangement, Atmos. Chem. Phys., 4, 323–350, https://doi.org/10.5194/acp-4-323-2004, 2004.

Mikhailov, E., Vlasenko, S., Martin, S. T., Koop, T., and Pöschl, U.: Amorphous and crystalline aerosol particles interacting with water vapor: conceptual framework and experimental evidence for restructuring, phase transitions and kinetic limitations, Atmos. Chem. Phys., 9, 9491–9522, https://doi.org/10.5194/acp-9-9491-2009, 2009.

Mikhailov, E., Vlasenko, S., Rose, D., and Pöschl, U.: Mass-based hygroscopicity parameter interaction model and measurement of atmospheric aerosol water

uptake, Atmos. Chem. Phys., 13, 717–740, https://doi.org/10.5194/acp-13-717-2013, 2013.

Mikhailov, E. F., Vlasenko, S. S., and Ryshkevich, T. I.: Influence of chemical composition and microstructure on the hygroscopic growth of pyrogenic aerosol, Izv. Atmos. Ocean. Phy., 44, 416–431, 2008.

Mochida, M. and Kawamura, K.: Hygroscopic properties of levoglucosan and related organic compounds characteristic to biomass burning aerosol particles, J. Geophys. Res.-Atmos., 109, D21202, doi:10.1029/2004jd004962, 2004.

Moosmuller, H., Chakrabarty, R. K., and Arnott, W. P.: Aerosol light absorption and its measurement: A review, J. Quant. Spectrosc. Ra., 110, 844–878, 2009.

Mulholland, G. W., Donnelly, M. K., Hagwood, C. R., Kukuck, S. R., Hackley, V. A., and Pui, D. Y. H.: Measurement of 100 nm and 60 nm particle standards by differential mobility analysis, J. Res. Natl. Inst. Stand. Technol., 111, 257-312, 2006.

Ovadnevaite, J., Zuend, A., Laaksonen, A., Sanchez, K. J., Roberts, G., Ceburnis, D., Decesari, S., Rinaldi, M., Hodas, N., Facchini, M. C., Seinfeld, J. H., and O'Dowd, C.: Surface tension prevails over solute effect in organic-influenced cloud droplet activation, Nature, 546, 637–641, https://doi.org/10.1038/nature22806, 2017.

Paglione, M., Saarikoski, S., Carbone, S., Hillamo, R., Facchini, M. C., Finessi, E., Giulianelli, L., Carbone, C., Fuzzi, S., Moretti, F., Tagliavini, E., Swietlicki, E., Stenstrom, K. E., Prevot, A. S. H., Massoli, P., Canaragatna, M., Worsnop, D., and Decesari, S.: Primary and secondary biomass burning aerosols determined by proton nuclear magnetic resonance (H-1-NMR) spectroscopy during the 2008 EUCAARI campaign in the Po Valley (Italy), Atmos. Chem. Phys., 14, 5089–5110, https://doi.org/10.5194/acp-14-5089-2014, 2014.

Pajunoja, A, AT Lambe, J Hakala, N Rastak, MJ Cummings, JF Brogan, L Hao, M Paramonov, J Hong, NL Prisle, J Malila, S Romakkaniemi, KEJ Lehtinen, A Laaksonen, M Kulmala, P Massoli, TB Onasch, NM Donahue, I Riipinen, P Davidovits, DR Worsnop, T Petäjä, and A Virtanen (2015), Adsorptive uptake of water by semisolid secondary organic aerosols. Geophys. Res. Lett., 42, 3063–3068. doi: 10.1002/2015GL063142.

Peng, C., Chan, M. N., and Chan, C. K.: The hygroscopic properties of dicarboxylic and multifunctional acids: Measurements and UNIFAC predictions, Environ. Sci. Technol., 35, 4495–4501, 2001.

Petters, M. D. and. Kreidenweis, S. M.: A single parameter representation of hygroscopic growth and cloud condensation nucleus activity, Atmos. Chem. Phys., 7, 1961–1971, https://doi.org/10.5194/acp-7-1961-2007, 2007.

Pilinis, C., S.N. Pandis, and J.H. Seinfeld, Sensitivity of direct climate forcing by atmospheric aerosols to aerosol size and composition, J. Geophys. Res.-Atmos, 1995. 100(D9): p. 18739-18754.

Pöhlker, M. L., Pöhlker, C., Ditas, F., Klimach, T., Hrabe de Angelis, I., Araújo, A., Brito, J., Carbone, S., Cheng, Y., and Chi, X.: Long-term observations of cloud condensation nuclei in the Amazon rain forest–Part 1: Aerosol size distribution, hygroscopicity, and new model parametrizations for CCN prediction, Atmos. Chem. Phys., 16, 15709–15740, https://doi.org/10.5194/acp-16-15709-2016, 2016.

Pöschl, U., Martin, S. T., Sinha, B., Chen, Q., Gunthe, S. S., Huffman, J. A., Borrmann, S., Farmer, D. K., Garland, R. M., Helas, G., Jimenez, J. L., King, S. M., Manzi, A., Mikhailov, E., Pauliquevis, T., Petters, M. D., Prenni, A. J., Roldin, P., Rose, D., Schneider, J., Su, H., Zorn, S. R., Artaxo, P., and Andreae, M. O.: Rainforest Aerosols as Biogenic Nuclei of Clouds and Precipitation in the Amazon, Science, 329, 1513–1516, 2010.

Powelson, M. H., Espelien, B. M., Hawkins, L. N., Galloway, M. M., and De Haan, D. O.: Brown Carbon Formation by Aqueous-Phase Carbonyl Compound Reactions with Amines and Ammonium Sulfate, Environ. Sci. Technol., 48, 985–993, 2014.

Pratt, K. A. and Prather, K. A.: Aircraft measurements of vertical profiles of aerosol mixing states, J. Geophys. Res., 115, D11305, https://doi.org/10.1029/2009JD013150, 2010.

Pratt, K. A., Murphy, S. M., Subramanian, R., DeMott, P. J., Kok, G. L., Campos, T., Rogers, D. C., Prenni, A. J., Heymsfield, A. J., Seinfeld, J. H., and Prather, K. A.: Flight-based chemical characterization of biomass burning aerosols within two prescribed burn smoke plumes, Atmos. Chem. Phys., 11, 12549–12565, https://doi.org/10.5194/acp-11-12549-2011, 2011.

Pruppacher, H. R. and Klett, J. D: Microphysics of clouds and precipitation, Kluwer

Academic Publishers, 1997.

Psichoudaki, M. and Pandis, S. N.: Atmospheric aerosol water-soluble organic carbon measurement: a theoretical analysis, Environ. Sci. Technol., 47, 9791–9798, doi:10.1021/es402270y, 2013.

Rader, D. J. and McMurry, P. H.: Application of the tandem differential mobility analyzer to studies of droplet growth or evaporation, J. Aerosol Sci., 17, 771–787, 1986.

Raoux, S., Rettner, C. T., Jordan-Sweet, J. L., Kellock, A. J., Topuria, T., Rice, P. M., and Miller, D. C.: Direct observation of amorphous to crystalline phase transitions in nanoparticle arrays of phase change materials, J. Appl. Phys., 102, 094305 (2007).

Randles, C. A., Russell, L. M., and Ramaswamy, V.: Hygroscopic and optical properties of organic sea salt aerosol and consequences for climate forcing, Geophys. Res. Lett., 31, L16 108, doi:10.1029/2004GL020628, 2004.

Rastak, N., Pajunoja, A., Acosta Navarro, J. C., Ma, J., Song, M., Partridge, D. G., Kirkevåg, A., Leong, Y., Hu, W. W., Taylor, N. F., Lambe, A., Cerully, K., Bougiatioti, A., Liu, P., Krejci, R., Petäjä, T., Percival, C., Davidovits, P., Worsnop, D. R., Ekman, A. M. L., Nenes, A., Martin, S., Jimenez, J. L., Collins, D. R., Topping, D. O., Bertram, A. K., Zuend, A., Virtanen, A., and Riipinen, I.: Microphysical explanation of the RH-dependent water affinity of biogenic organic aerosol and its importance for climate, Geophys. Res. Lett., 44, 5167–5177, https://doi.org/10.1002/2017GL073056, 2017.

Reid, J. P., Dennis-Smither, B. J., Kwamena, N.-O. A., Miles, R. E. H., Hanford, K. L., and Homer, C. J.: The morphology of aerosol particles consisting of hydrophobic and hydrophilic phases: hydrocarbons, alcohols and fatty acids as the hydrophobic component, Phys. Chem. Chem. Phys., 13, 15559–15572, 2011.

Renbaum-Wolff, L., Song, M., Marcolli, C., Zhang, Y., Liu, P. F., Grayson, J. W., Geiger, F. M., Martin, S. T., and Bertram, A. K.: Observations and implications of liquid–liquid phase separation at high relative humidities in secondary organic material produced by α-pinene ozonolysis without inorganic salts, Atmos. Chem. Phys., 16, 7969-7979, 2016.

Rickards, A. M. J., Miles, R. E. H., Davies, J. F., Marshall, F. H., and Reid, J. P.: Measurements of the sensitivity of aerosol hygroscopicity and the κ parameter to

the O/C Ratio, J. Phys. Chem. A, 117, 14120-14131, 2013.

Rissler, J., Vestin, A., Swietlicki, E., Fisch, G., Zhou, J., Artaxo, P., and Andreae, M. O.: Size distribution and hygroscopic properties of aerosol particles from dry-season biomass burning in Amazonia, Atmos. Chem. Phys., 6, 471–491, https://doi.org/10.5194/acp-6-471-2006, 2006.

Rissler, J., Svenningsson, B., Fors, E. O., Bilde, M., and Swietlicki, E.: An evaluation and comparison of cloud condensation nucleus activity models: Predicting particle critical sat- uration from growth at subsaturation, J. Geophys. Res., 115, doi:10.1029/2010jd014391, 2010.

Rizzo, L. V., Correia, A. L., Artaxo, P., Procopio, A. S., and Andreae, M. O.: Spectral dependence of aerosol light absorption over the Amazon Basin, Atmos. Chem. Phys., 11, 8899–8912, https://doi.org/10.5194/acp-11-8899-2011, 2011.

Romakkaniemi, S., Hämeri, K., Väkevä, M., and Laaksonen, A.: Adsorption of water on 8−15 nm NaCl and $(NH_4)_2SO_4$ aerosols measured using an ultrafine tandem differential mobility analyzer, J. Phys. Chem. A, 105, 8183–8188, 2001.

Rose, D., Gunthe, S. S., Su, H., Garland, R. M., Yang, H., Berghof, M., Cheng, Y. F., Wehner, B., Achtert, P., Nowak, A., Wiedensohler, A., Takegawa, N., Kondo, Y., Hu, M., Zhang, Y., Andreae, M. O., and Poschl, U.: Cloud condensation nuclei in polluted air and biomass burning smoke near the mega-city Guangzhou, China - Part 2: Size-resolved aerosol chemical composition, diurnal cycles, and externally mixed weakly CCN-active soot particles, Atmos. Chem. Phys., 11, 2817–2836, https://doi.org/10.5194/acp-11-2817-2011, 2011.

Rubasinghege, G. and V.H. Grassian,: Role(s) of adsorbed water in the surface chemistry of environmental interfaces. Chem Commun (Camb), 2013. 49(30): p. 3071-94.

Russell, L. M. and Ming, Y.: Deliquescence of small particles, J. Chem. Phys., 116, 311–321, 2002.

Saarnio, K., Aurela, M., Timonen, H., Saarikoski, S., Teinila, K., Makela, T., Sofiev, M., Koskinen, J., Aalto, P. P., Kulmala, M., Kukkonen, J., and Hillamo, R.: Chemical composition of fine particles in fresh smoke plumes from boreal wild-land fires in Europe, Sci. Total Environ., 408, 2527–2542, 2010.

Sadezky, A., Muckenhuber, H., Grothe, H., Niessner, R., and Poschl, U.: Raman micro spectroscopy of soot and related carbonaceous materials: Spectral analysis and structural information, Carbon, 43, 1731-1742, 2005.

Sakurai, H., A. Fink, M., H. McMurry, P., Mauldin, R., F. Moore, K., N. Smith, J., and Eisele, F.: Hygroscopicity and volatility of 4–10 nm particles during summertime atmospheric nucleation events in urban Atlanta, J. Geophys. Res., 110, D22S04, doi:10.1029/2005JD005918, 2005.

Saleh, R., Hennigan, C. J., McMeeking, G. R., Chuang, W. K., Robinson, E. S., Coe, H., Donahue, N. M., and Robinson, A. L.: Absorptivity of brown carbon in fresh and photo-chemically aged biomass-burning emissions, Atmos. Chem. Phys., 13, 7683–7693, https://doi.org/10.5194/acp-13-7683-2013, 2013.

Saleh, R., Robinson, E. S., Tkacik, D. S., Ahern, A. T., Liu, S., Aiken, A. C., Sullivan, R. C., Presto, A. A., Dubey, M. K., Yokelson, R. J., Donahue, N. M., and Robinson, A. L.: Brownness of organics in aerosols from biomass burning linked to their black carbon content, Nat. Geosci., 7, 647-650, 2014.

Saxena, P., Hildemann, L. M., McMurry, P. H., and Seinfeld, J. H., Organics alter hygroscopic behavior of atmospheric particles. J. Geophys. Res.-Atmos, 1995. 100(D9): p. 18755-18770.

Seinfeld, J. and Pandis, S.: Atmospheric chemistry and physics. Wiley, Hoboken, NJ, 2006.

Shi, Y.J., M.F. Ge, and W.G. Wang, Hygroscopicity of internally mixed aerosol particles containing benzoic acid and inorganic salts. Atmos. Environ, 2012. 60: p. 9-17.

Shiraiwa, M., Ammann, M., Koop, T., and Pöschl, U.: Gas uptake and chemical aging of semisolid organic aerosol particles, PNAS, 108, 11003-11008, 2011.

Shiraiwa, M., Zuend, A., Bertram, A. K., and Seinfeld, J. H.: Gas-particle partitioning of atmospheric aerosols: interplay of physical state, non-ideal mixing and morphology, Phys. Chem. Chem. Phys., 15, 11441–11453, 2013.

Sihto, S. L., Mikkilä, J., Vanhanen, J., Ehn, M., Liao, L., Lehtipalo, K., Aalto, P. P., Duplissy, J., Petäjä, T., Kerminen, V. M., Boy, M., and Kulmala, M.: Seasonal variation of CCN concentrations and aerosol activation properties in boreal forest, Atmos. Chem. Phys., 11, 13269-13285, https://doi.org/10.5194/acp-11-13269-2011, 2011.

Simoneit, B. R. T., Schauer, J. J., Nolte, C. G., Oros, D. R., Elias, V. O., Fraser, M. P., Rogge, W. F., and Cass, G. R.: Levoglucosan, a tracer for cellulose in biomass burning and atmospheric particles, Atmos. Environ, 33, 173-182, 1999.

Sjogren, S., Gysel, M., Weingartner, E., Baltensperger, U., Cubison, M. J., Coe, H., Zardini, A. A., Marcolli, C., Krieger, U. K., and Peter, T.: Hygroscopic growth and water uptake kinetics of two-phase aerosol particles consisting of ammonium sulfate, adipic and humic acid mixtures, J. Aerosol Sci., 38, 157–171, 2007.

Smith, M. L., Bertram, A. K., and Martin, S. T.: Deliquescence, efflorescence, and phase miscibility of mixed particles of ammonium sulfate and isoprene-derived secondary organic material, Atmos. Chem. Phys., 12, 9613–9628, https://doi.org/10.5194/acp-12-9613-2012, 2012.

Song, M., Marcolli, C., Krieger, U. K., Zuend, A., and Peter, T.: Liquid-liquid phase separation and morphology of internally mixed dicarboxylic acids/ammonium sulfate/water particles, Atmos. Chem. Phys., 12, 2691–2712, https://doi.org/10.5194/acp-12-2691-2012, 2012.

Song, M., Marcolli, C., Krieger, U. K., Zuend, A., and Peter, T.: Liquid-liquid phase separation in aerosol particles: Dependence on O:C, organic functionalities, and compositional complexity, Geophys. Res. Lett., 39, L19801, https://doi.org/10.1029/2012GL052807, 2012.

Srinivas, B. and Sarin, M. M.: Light absorbing organic aerosols (brown carbon) over the tropical Indian Ocean: impact of biomass burning emissions, Environ. Res. Lett., 8, 044042, https://doi.org/10.1088/1748-9326/8/4/044042, 2013.

Srinivas, B. and Sarin, M. M.: Brown carbon in atmospheric outflow from the Indo-Gangetic Plain: Mass absorption efficiency and temporal variability, Atmos. Environ., 89, 835-843, 2014.

Stock, M., Cheng, Y. F., Birmili, W., Massling, A., Wehner, B., Müller, T., Leinert, S., Kalivitis, N., Mihalopoulos, N., and Wiedensohler, A.: Hygroscopic properties of atmospheric aerosol particles over the Eastern Mediterranean: implications for regional direct radiative forcing under clean and polluted conditions, Atmos. Chem. Phys., 11, 4251–4271, https://doi.org/10.5194/acp-11-4251-2011, 2011.

Suda, S. R. and Petters, M. D.: Accurate determination of aerosol activity coefficients at relative humidities up to 99 % using the hygroscopicity tandem differential mobility analyzer technique, Aerosol Sci. Technol., 47, 991–

1000, https://doi.org/10.1080/02786826.2013.807906, 2013.

Su, H., Rose, D., Cheng, Y. F., Gunthe, S. S., Massling, A., Stock, M., Wiedensohler, A., Andreae, M. O., and Pöschl, U.: Hygroscopicity distribution concept for measurement data analysis and modeling of aerosol particle mixing state with regard to hygroscopic growth and CCN activation, Atmos. Chem. Phys., 10, 7489–7503, https://doi.org/10.5194/acp-10-7489-2010, 2010.

Su, H., Cheng, Y., and Pöschl, U.: New Multiphase Chemical Processes Influencing Atmospheric Aerosols, Air Quality, and Climate in the Anthropocene, Acc. Chem. Res., e1601530-1602983, https://doi.org/10.1021/acs.accounts.0c00246, 2020.

Svenningsson, B., Rissler, J., Swietlicki, E., Mircea, M., Bilde, M., Facchini, M. C., Decesari, S., Fuzzi, S., Zhou, J., Monster, J., and Rosenorn, T.: Hygroscopic growth and critical supersaturations for mixed aerosol particles of inorganic and organic compounds of atmospheric relevance, Atmos. Chem. Phys., 6, 1937–1952, https://doi.org/10.5194/acp-6-1937-2006, 2006.

Tang, I. N.: Chemical and size effects of hygroscopic aerosols on light scattering coefficients, J. Geophys. Res., 101, 19 245– 19 250, 1996.

Tang, I. N. and Munkelwitz, H. R.: Composition and temperature dependence of the deliquescence properties of hygroscopic aerosols, Atmos. Environ. A-Gen., 27, 467–473, doi:10.1016/0960-1686(93)90204-C, 1993.

Tang, I. N. and Munkelwitz, H. R.: Water activities, densities, and refractive indices of aqueous sulfates and sodium nitrate droplets of atmospheric importance, J. Geophys. Res.-Atmos, 99, 18801– 18808, 1994.

Tang, I. N., Fung, K. H., Imre, D. G., and Munkelwitz, H. R.: Phase transformation and metastability of hygroscopic microparticles, Aerosol Sci. Technol., 23, 443–453, 1995.

Tang, M. J., Chan, C. K., Li, Y. J., Su, H., Ma, Q. X., Wu, Z. J., Zhang, G. H., Wang, Z., Ge, M. F., Hu, M., He, H., and Wang, X. M.: A review of experimental techniques for aerosol hygroscopicity studies, Atmos. Chem. Phys., 19, 12631–12686, https://doi.org/10.5194/acp-19-12631-2019, 2019.

Taylor, J. R. and Taylor, S. L. L. J. R.: Introduction To Error Analysis: The Study of Uncertainties in Physical Measurements, University Science Books, 1997.

Topping, D., McFiggans, G., and Coe, H.: A curved multi-component aerosol hygroscopicity model framework: Part 1–Inorganic compounds, Atmos. Chem. Phys., 5, 1205–1222, https://doi.org/10.5194/acp-5-1205-2005, 2005.

Tuckermann, R. a. C., H. K.: The surface tension of aqueous solutions of some atmospheric water-soluble organic compounds, Atmos. Environ., 38, 6135-6138, 2004.

Väkevä, M., Kulmala, M., Stratmann, F., and Hämeri, K.: Field measurements of hygroscopic properties and state of mixing of nucleation mode particles, Atmos. Chem. Phys., 2, 55–66, https://doi.org/10.5194/acp-2-55-2002, 2002.

Villani, P., Picard, D., Michaud, V., Laj, P., and Wiedensohler, A.: Design and validation of a volatility hygroscopic tandem differential mobility analyzer (VH-TDMA) to characterize the relationships between the thermal and hygroscopic properties of atmospheric aerosol particles, Aerosol Sci. Technol., 42, 729–741, 2008.

Wang, J., Cubison, M. J., Aiken, A. C., Jimenez, J. L., and Collins, D. R.: The importance of aerosol mixing state and size-resolved composition on CCN concentration and the variation of the importance with atmospheric aging of aerosols, Atmos. Chem. Phys., 10, 7267–7283, https://doi.org/10.5194/acp-10-7267-2010, 2010.

Wang, J., Krejci, R., Giangrande, S., Kuang, C., Barbosa, H. M. J., Brito, J., Carbone, S., Chi, X. G., Comstock, J., Ditas, F., Lavric, J., Manninen, H. E., Mei, F., Moran-Zuloaga, D., Pöhlker, C., Pöhlker, M. L., Saturno, J., Schmid, B., Souza, R. A. F., Springston, S. R., Tomlinson, J. M., Toto, T., Walter, D., Wimmer, D., Smith, J. N., Kulmala, M., Machado, L. A. T., Artaxo, P., Andreae, M. O., Petäjä, T., and Martin, S. T.: Amazon boundary layer aerosol concentration sustained by vertical transport during rainfall, Nature, 539, 416-419, 2016.

Wang, J., Shilling, J. E., Liu, J., Zelenyuk, A., Bell, D. M., Petters, M. D., Thalman, R., Mei, F., Zaveri, R. A., and Zheng, G.: Cloud droplet activation of secondary organic aerosol is mainly controlled by molecular weight, not water solubility, Atmos. Chem. Phys., 19, 941-954, 2019.

Wang, L., Khalizov, A. F., Zheng, J., Xu, W., Ma, Y., Lal, V., and Zhang, R. Y.: Atmospheric nanoparticles formed from heterogeneous reactions of organics, Nature Geosci., 3, 238–242, doi:10.1038/NGEO778, 2010.

Wang, X., Heald, C. L., Ridley, D. A., Schwarz, J. P., Spackman, J. R., Perring, A. E., Coe, H., Liu, D., and Clarke, A. D.: Exploiting simultaneous observational constraints on mass and absorption to estimate the global direct radiative forcing of black carbon and brown carbon, Atmos. Chem. Phys., 14, 10989–11010, https://doi.org/10.5194/acp-14-10989-2014, 2014.

Wang, X., Ma, N., Lei, T., Größ, J., Li, G., Liu, F. B., Meusel, H., Mikhailov, E., Wiedensohler, A., and Su, H.: Effective density and hygroscopicity of protein particles generated with spray-drying process, J. Aerosol Sci., 137, 105441, 2019.

Wang, X., Chen, C., Binder, K., Kuhn, U., Su, H., and Cheng Y.: Molecular dynamics simulation of the surface tension of aqueous sodium chloride: from dilute to highly supersaturated solutions and molten salt, Atmos. Chem. Phys., 18, 17077-17086, https://doi.org/10.5194/acp-18-17077-2018,2018.

Wang, X., Lei, H., Berger, R., Zhang, Y., Su, H., and Cheng, Y.: Hygroscopic properties of NaCl nanoparticles on the surface: a scanning force microscopy study, Phys. Chem. Phys., 22, 9967-9973, 2020.

Wang, Z., Cheng, Y., Ma, N., Mikhailov, E., Pöschl, U., and Su, H.: Dependence of the hygroscopicity parameter κ on particle size, humidity and solute concentration: implications for laboratory experiments, field measurements and model studies, Atmos. Chem. Phys. Discuss., 2017, 1-33, 2017.

Wang, Z., Su, H., Wang, X., Ma, N., Wiedensohler, A., Pöschl, U., and Cheng, Y.: Scanning supersaturation condensation particle counter applied as a nano-CCN counter for size-resolved analysis of the hygroscopicity and chemical composition of nanoparticles, Atmos. Meas. Tech., 8, 2161–2172, https://doi.org/10.5194/amt-8-2161-2015, 2015.

Wiedensohler, A., Cheng, Y. F., Nowak, A., Wehner, B., Achtert, P., Berghof, M., Birmili, W., Wu, Z. J., Hu, M., Zhu, T., Takegawa, N., Kita, K., Kondo, Y., Lou, S. R., Hofzumahaus, A., Holland, F., Wahner, A., Gunthe, S. S., Rose, D., Su, H., and Pöschl, U.: Rapid aerosol particle growth and increase of cloud condensation nucleus activity by secondary aerosol formation and condensation: A case study for regional air pollution in northeastern China, J. Geophys. Res.–Atmos., 114, doi:10.1029/2008JD010884, 2009.

Wiedensohler, A., Birmili, W., Nowak, A., Sonntag, A., Weinhold, K., Merkel, M., Wehner, B., Tuch, T., Pfeifer, S., Fiebig, M., Fjäraa, A. M., Asmi, E., Sellegri, K.,

Depuy, R., Venzac, H., Villani, P., Laj, P., Aalto, P., Ogren, J. A., Swietlicki, E., Williams, P., Roldin, P., Quincey, P., Hüglin, C., Fierz-Schmidhauser, R., Gysel, M., Weingartner, E., Riccobono, F., Santos, S., Grüning, C., Faloon, K., Beddows, D., Harrison, R., Monahan, C., Jennings, S. G., O'Dowd, C. D., Marinoni, A., Horn, H. G., Keck, L., Jiang, J., Scheckman, J., McMurry, P. H., Deng, Z., Zhao, C. S., Moerman, M., Henzing, B., de Leeuw, G., Löschau, G., and Bastian, S.: Mobility particle size spectrometers: harmonization of technical standards and data structure to facilitate high quality long-term observations of atmospheric particle number size distributions, Atmos. Meas. Tech., 5, 657–685, https://doi.org/10.5194/amt-5-657-2012, 2012.

Wiedensohler, A., Lütkemeier, E., Feldpausch, M., & Helsper, C. (1986). Investigation of the bipolar charge distribution at various gas conditions. J. Aerosol Sci., 17(3), 413–416. https://doi.org/10.1016/0021-8502(86)90118-7.

Wiedensohler, A., Wiesner, A., Weinhold, K., Birmili, W., Hermann, M., Merkel, M., Müller, T., Pfeifer, S., Schmidt, A., Tuch, T., Velarde, F., Quincey, P., Seeger, S., and Nowak, A.: Mobility particle size spectrometers: Calibration procedures and measurement uncertainties, Aerosol Sci. Technol., 52, 146–164, 2018.

Whitehead, J. D., Darbyshire, E., Brito, J., Barbosa, H. M., Crawford, I., Stern, R., Gallagher, M. W., Kaye, P. H., Allan, J. D., and Coe, H.: Biogenic cloud nuclei in the central Amazon during the transition from wet to dry season, Atmos. Chem. Phys., 16, 9727–9743, https://doi.org/10.5194/acp-16-9727-2016, 2016.

Wu, Z. J., Zheng, J., Shang, D. J., Du, Z. F., Wu, Y. S., Zeng, L. M., Wiedensohler, A., and Hu, M.: Particle hygroscopicity and its link to chemical composition in the urban atmosphere of Beijing, China, during summertime, Atmos. Chem. Phys., 16, 1123-1138, 2016.

Wu, Z. J., Nowak, A., Poulain, L., Herrmann, H., and Wiedensohler, A.: Hygroscopic behavior of atmospherically relevant water-soluble carboxylic salts and their influence on the water uptake of ammonium sulfate, Atmos. Chem. Phys., 11, 12617– 12626, https://doi.org/10.5194/acp-11-12617-2011, 2011.

Xu, B. and Schweiger, G.: In-situ Raman observation of phase transformation of Na2SO4 during the hydration/dehydration cycles on single levitated microparticle, J. Aerosol Sci., 30, S379-S380, 1999.

Yates III, L. M., Wandruszka, R.V.: Decontamination of polluted water bytreatment with a crude humic acid blend, Environ. Sci. Technol, 33, 2076-2080, 1999.

You, Y., Renbaum-Wolff, L., and Bertram, A. K.: Liquid–liquid phase separation in particles containing organics mixed with ammonium sulfate, ammonium bisulfate, ammonium nitrate or sodium chloride, Atmos. Chem. Phys., 13, 11723–11734, https://doi.org/10.5194/acp-13-11723-2013, 2013.

Zamora, I. R., Tabazadeh, A., Golden, D. M., and Jacobson, M. Z.: Hygroscopic growth of common organic aerosol solutes, including humic substances, as derived from water activity measurements, J. Geophys. Res., 116, D23207, https://doi.org/10.1029/2011JD016067, 2011.

Zardini, A. A., Sjogren, S., Marcolli, C., Krieger, U. K., Gysel, M., Weingartner, E., Baltensperger, U., and Peter, T.: A combined particle trap/HTDMA hygroscopicity study of mixed inorganic/organic aerosol particles, Atmos. Chem. Phys., 8, 5589–5601, https://doi.org/10.5194/acp-8-5589-2008, 2008.

Zawadowicz, M., Proud, S., Seppalainen, S., and Cziczo, D.: Hygroscopic and phase separation properties of ammonium sulfate/organics/water ternary solutions, Atmos. Chem. Phys., 15, 8975–8986, https://doi.org/10.5194/acp-15-8975-2015, 2015.

Zhao, L.-J., Zhang, Y.-H., Wei, Z.-F., Cheng, H., and Li, X.-H.: Magnesium sulfate aerosols studied by FTIR spectroscopy: hygroscopic properties, supersaturated structures, and implications for seawater aerosols, J. Phys. Chem. A, 110, 951-958, 2016

Zhang, R.: Getting to the Critical Nucleus of Aerosol Formation, Science, 328, 1366-1367, 2010.

Zhang, R., Khalizov, A., Wang, L., Hu, M., and Xu, W.: Nucleation and Growth of Nanoparticles in the Atmosphere, Chem. Re., 112, 1957-2011, 2012.

Zhang, R., Suh, I., Zhao, J., Zhang, D., Fortner, E. C., Tie, X., Molina, L. T., and Molina, M. J.: Atmospheric New Particle Formation Enhanced by Organic Acids, Science, 304, 1487-1490, 2004.

Zhang, S. L., Ma, N., Kecorius, S., Wang, P. C., Hu, M., Wang, Z. B., Größ, J., Wu, Z. J., and Wiedensohler, A.: Mixing state of atmospheric particles over the North China Plain, Atmos. Environ., 125, Part A, 152-164, 2016.

Zhang, Q., Jimenez, J. L., Canagaratna, M. R., Allan, J. D., Coe, H., Ulbrich, I., Alfarra, M. R., Takami, A., Middlebrook, A. M., Sun, Y. L., Dzepina, K., Dunlea, E., Docherty, K., DeCarlo, P. F., Salcedo, D., Onasch, T., Jayne, J. T., Miyoshi, T., Shimono, A., Hatakeyama, S., Takegawa, N., Kondo, Y., Schneider, J., Drewnick, F., Borrmann, S., Weimer, S., Demerjian, K., Williams, P., Bower, K., Bahreini, R., Cottrell, L., Griffin, R. J., Rautiainen, J., Sun, J. Y., Zhang, Y. M., and Worsnop, D. R.: Ubiquity and dominance of oxygenated species in organic aerosols in anthropogenically-influenced Northern Hemisphere midlatitudes, Geophys. Res. Lett., 34, L13801, https://doi.org/10.1029/2007GL029979, 2007.

Zheng, G. J., Duan, F. K., Su, H., Ma, Y. L., Cheng, Y., Zheng, B., Zhang, Q., Huang, T., Kimoto, T., Chang, D., Pöschl, U., Cheng, Y. F., and He, K. B.: Exploring the severe winter haze in Beijing: the impact of synoptic weather, regional transport and heterogeneous reactions, Atmos. Chem. Phys., 15, 2969–2983, https://doi.org/10.5194/acp-15-2969-2015, 2015.

Zheng, G., Su, H., Wang, S., Andreae, M. O., Pöschl, U., and Cheng, Y.: Multiphase buffer theory contrasts in atmospheric aerosol acidity, Science, 369, 1374-1377, 2020.

Zhong, M. and Jang, M.: Dynamic light absorption of biomass-burning organic carbon photochemically aged under natural sunlight, Atmos. Chem. Phys., 14, 1517–1525, https://doi.org/10.5194/acp-14-1517-2014, 2014.

Zieger, P., Fierz-Schmidhauser, R., Weingartner, E., and Baltensperger, U.: Effects of relative humidity on aerosol light scattering: results from different European sites, Atmos. Chem. Phys., 13, 10609–10631, https://doi.org/10.5194/acp-13-10609-2013, 2013.

Zuend, A. and Seinfeld, J. H.: Modeling the gas-particle partitioning of secondary organic aerosol: the importance of liquid-liquid phase separation, Atmos. Chem. Phys., 12, 3857–3882, https://doi.org/10.5194/acp-12-3857-2012, 2012.

Zuend, A., Marcolli, C., Luo, B. P., and Peter, T.: A thermodynamic model of mixed organic-inorganic aerosols to predict activity coefficients, Atmos. Chem. Phys., 8, 4559–4593, https://doi.org/10.5194/acp-8-4559-2008, 2008.

Zuend, A., Marcolli, C., Peter, T., and Seinfeld, J. H.: Computation of liquid-liquid equilibria and phase stabilities: implications for RH-dependent gas/particle

partitioning of organic-inorganic aerosols, Atmos. Chem. Phys., 10, 7795–7820, https://doi.org/10.5194/acp-10-7795-2010, 2010.

Zuend, A., Marcolli, C., Booth, A. M., Lienhard, D. M., Soonsin, V., Krieger, U. K., Topping, D. O., McFiggans, G., Peter, T., and Seinfeld, J. H.: New and extended parameterization of the thermodynamic model AIOMFAC: calculation of activity coefficients for organic-inorganic mixtures containing carboxyl, hydroxyl, carbonyl, ether, ester, alkenyl, alkyl, and aromatic functional groups, Atmos. Chem. Phys., 11, 9155–9206, https://doi.org/10.5194/acp-11-9155-2011, 2011.

E. Appendices

Appendix Wang et al. (2019)

Effective density and hygroscopicity of protein particles generated with spray-dring process

Authors: Xin Wang, Nan Ma, Ting Lei, Johannes Größ, Guo Li, Fobang Liu, hannah Meusel, Eugene Milkhailov, Alfred Wiedensohler, Hang Su

Publication date: 2019/8/14

Journal: Journal of Aerosol Science

I am the co-author of this work and my contribution to this work includes performing the experiments using a nano-HTDMA for measuring the hygroscopic properties of protein (bovine serum albumin) aerosol nanoparticles with diameter down to 40 nm, analyzing the data, giving comments on the manuscript.

Journal of Aerosol Science 137 (2019) 105441

Contents lists available at ScienceDirect

Journal of Aerosol Science

journal homepage: www.elsevier.com/locate/jaerosci

Effective density and hygroscopicity of protein particles generated with spray-drying process

Xin Wang[a], Nan Ma[b,a,*], Ting Lei[a], Johannes Größ[c], Guo Li[a], Fobang Liu[a], Hannah Meusel[a], Eugene Mikhailov[d], Alfred Wiedensohler[c], Hang Su[a]

[a] Multiphase Chemistry Department, Max Planck Institute for Chemistry, 55128, Mainz, Germany
[b] Institute for Environmental and Climate Research, Jinan Univeristy, 511443, Guangzhou, China
[c] Leibniz Institute for Tropospheric Research, 04318, Leipzig, Germany
[d] Atmospheric Physics Department, Institute of Physics, St. Petersburg State University, 198904, St. Petersburg, Russia

ARTICLE INFO

Keywords:
Protein particles
Morphology
Effective density
Hygroscopicity

ABSTRACT

Laboratory investigations of aerosol physico-chemical properties are usually initiated by spray-drying processes. Morphology of the generated particles may vary largely under different spray-drying conditions, which may further affect the characterization of particle properties. However, only limited data is available on the morphology of nebulized submicron particles, particularly for protein particles. To fill this gap, a centrifugal particle mass analyzer coupled with a scanning mobility particle sizer was used to analyze the effective density, an indicator of particle morphology, of nebulized protein particles (bovine serum albumin and ovalbumin) in a size range from 40 to 200 nm. Results indicate that the effective density of the protein particles generated via spray-drying processes is mainly determined by the competition between the removal of liquid water and the redistribution of the solute monomers in the sprayed droplets. Factors increasing the time needed for solute monomers redistribution (e.g. lower solution concentration and larger particle dry size) or decreasing the time needed for liquid water removal (e.g. higher drying rate) may result in a lower particle effective density, meaning a semi-solid structure or partially hollow morphology. This is also confirmed by the particle hygroscopicity measured with a nano-particle hygroscopic tandem differential mobility analyzer and a high humidity tandem differential mobility analyzer. Our results suggest that the factors affecting the morphology of particles may be complex and coupled with each other, highlighting the importance of monitoring particle effective densities in studies using aerosol particles generated via spray-drying processes.

1. Introduction

Characterization of the physico-chemical properties of aerosol particles is crucial for understanding their effects on climate and environment (Kulmala et al., 2004; Pöschl & Shiraiwa, 2015; Seinfeld & Pandis, 2016). Laboratory investigations usually start with spraying suspensions or solutions into droplets, followed by a drying process (Liu & Lee, 1975; Nandiyanto & Okuyama, 2011). Both the initial properties of the droplets and the drying process may influence the morphology of the generated particles (Iskandar, Gradon, & Okuyama, 2003), and further affect the determination of their properties and processes. However, only a few studies have

* Corresponding author. Institute for Environmental and Climate Research , Jinan University, 511443, Guangzhou, China.
E-mail addresses: nan.ma@jnu.edu.cn (N. Ma), h.su@mpic.de (H. Su).

https://doi.org/10.1016/j.jaerosci.2019.105441
Received 1 March 2019; Received in revised form 11 August 2019; Accepted 12 August 2019
Available online 14 August 2019
0021-8502/

investigated the influence of drying condition on particle morphology for submicron particles (Chang & Okuyama, 2002; Lee, Heng, Ng, Chan, & Tan, 2011; Okuyama, Abdullah, Wuled Lenggoro, & Iskandar, 2006; Okuyama & Lenggoro, 2003; Wang et al., 2010).

Proteins are very common macromolecular organic compounds in atmospheric aerosol. They can react with trace gases, act as surfactants, serve as ice nuclei, and cause adverse health effect (Meusel et al., 2017; Franze, Weller, Niessner, & Pöschl, 2003, 2005, 2001; Lang-Yona, Shuster-Meiseles, Mazar, Yarden, & Rudich, 2016; Miguel, Cass, Glovsky, & Weiss, 1999; Pummer et al., 2015; Zhang & Anastasio, 2003). The thermodynamic properties of both gas phase protein ions and aerosol phase protein particles have been investigated in many studies (e.g. Adler, Unger, & Lee, 2000; Butcher, Miksovska, Ridgeway, Park, & Fernandez-Lima, 2019; Hogan & de la Mora, 2011; Maißer et al., 2011; Meyer, Root, Zenobi, & Vidal-de-Miguel, 2016; Mikhailov, Vlasenko, Niessner, & Pöschl, 2004; Pummer et al., 2015; Vörös, 2004). Undenatured protein ions are relatively compact with a density around 1 g cm^{-3} (Hogan & de la Mora, 2011; Maißer et al., 2011). However, protein particles generated with spray-drying processes can be aggregated or dense, amorphous spheres depending on the spray-drying conditions. The open structure of aggregated protein particles may largely influence the assessment of their physico-chemical properties (Frahm, Pochopsky, Clarke, & Johnston, 2016). Therefore, a comprehensive evaluation of the dominant morphology of protein particles under different generation and drying conditions is needed.

Particle effective densities, defined as the ratio of particle mass to the volume of a sphere with a diameter equaling to the mobility diameter of the particle, can be used as a measure of particle morphology (Nandiyanto & Okuyama, 2011; Olfert, Symonds, & Collings, 2007). There have been several methods developed for determining particle effective density. For example, particle vacuum aerodynamic diameter measured with an aerosol mass spectrometer (AMS) and electrical mobility diameter measured with a mobility particle size spectrometer (MPSS, e.g. scanning mobility particle sizer, SMPS), were used to calculate the effective densities of secondary organic aerosol (Bahreini et al., 2005). A combination of an electrical low-pressure impactor (ELPI) and a MPSS was also used in several studies to investigate the effective densities of different types of aerosols (Kannosto et al., 2008; Keskinen et al., 2007; Virtanen, Ristimäki, & Keskinen, 2004, 2006). Particle effective density can be also obtained based on mobility and mass measurements (DeCarlo, Slowik, Worsnop, Davidovits, & Jimenez, 2004). Centrifugal particle mass analyzer (CPMA) and aerosol particle mass analyzer (APM) are frequently used techniques for the direct measurement of the mass of individual aerosol particles (Ehara, Hagwood, & Coakley, 1996; Johnson, Olfert, Yurteri, Cabot, & McAughey, 2015b; Kuwata, 2015), and were applied in the determination of particle effective densities. Lee, Widiyastuti, Tajima, Iskandar, and Okuyama (2009) measured the effective density of spherical aggregated and ordered porous particles using a differential mobility analyzer (DMA) and an APM. Similarly, a DMA-CPMA system was extensively applied in the measurement of the effective densities of diesel soot, coated soot, fractal-like agglomerates of carbon nanotubes, and cigarette smoke particles (Abegglen et al., 2015; Durdina et al., 2014; Ghazi & Olfert, 2013; Johnson et al., 2015a; Olfert et al., 2007; Wang, Bahk, Chen, & Pui, 2015). Based on similar principles, tandem ion mobility spectrometry–mass spectrometry (IMS-MS) was also used for measuring the effective densities of gas phase protein ions (Hogan & de la Mora, 2011).

In this study, two well-defined proteins, bovine serum albumin (BSA) and ovalbumin (OVA), were aerosolized via a spray-drying process. The effective density and hygroscopic growth factor of the generated protein particles were measured with a CPMA-SMPS and hygroscopic tandem differential mobility analyzer systems, respectively. The major factors influencing the effective density and morphology of protein particles, such as drying rate, solute concentration, particle diameter, and chemical substance were discussed.

2. Methods

2.1. Spray-drying of protein particles and effective density measurement

Two well-defined proteins, bovine serum albumin (BSA) and ovalbumin (OVA), were generated by nebulization of aqueous protein solutions. The solutions were prepared by dissolving appropriate amounts of BSA (fraction V, > 96%, Sigma-Aldrich) and OVA (fraction V, ≥ 98%, Sigma-Aldrich) in high purity water (Milli-Q integral 3 water system, 18.2 MΩ cm, Merck Millipore). The Molecular weight (M), bulk density (ρ_{bulk}) and gas phase density (ρ_{ions}) of BSA and OVA are listed in Table 1.

Fig. 1 shows the schematic diagram of the system used in this study. An atomizer (Model 3076, TSI) was operated with nitrogen carrier gas with a flow rate of 3 L min^{-1}. After nebulization, an aerosol sample flow with flow rates ranging from 0.3 to 1.5 L min^{-1} was fed into a silica gel diffusion dryer (self-manufactured, see Appendix A Fig. S1b). The relative humidity (RH) of the aerosol sample was gradually reduced in the dryer by radical diffusion of water vapor from the aerosol to the densely packed silica gel surrounded. The reduction of RH, quantified as aerosol drying rate, highly depends on the aerosol flow rate in the diffusion dryer

Table 1
Molecular weight (M), bulk density (ρ_{bulk}) and gas phase density (ρ_{ions}) of BSA and OVA at 295 ± 1 K (Haynes, 2014; Maißer et al., 2011; Muramatsu & Minton, 1988; Neurath & Bull, 1936; Nisbet, Saundry, Moir, Fothergill, & Fothergill, 1981).

	BSA	OVA
M (kDa)	66.4	42.7
ρ_{bulk} (g cm^{-3})	1.32	1.27
ρ_{ions} (g cm^{-3})	0.96	1.01

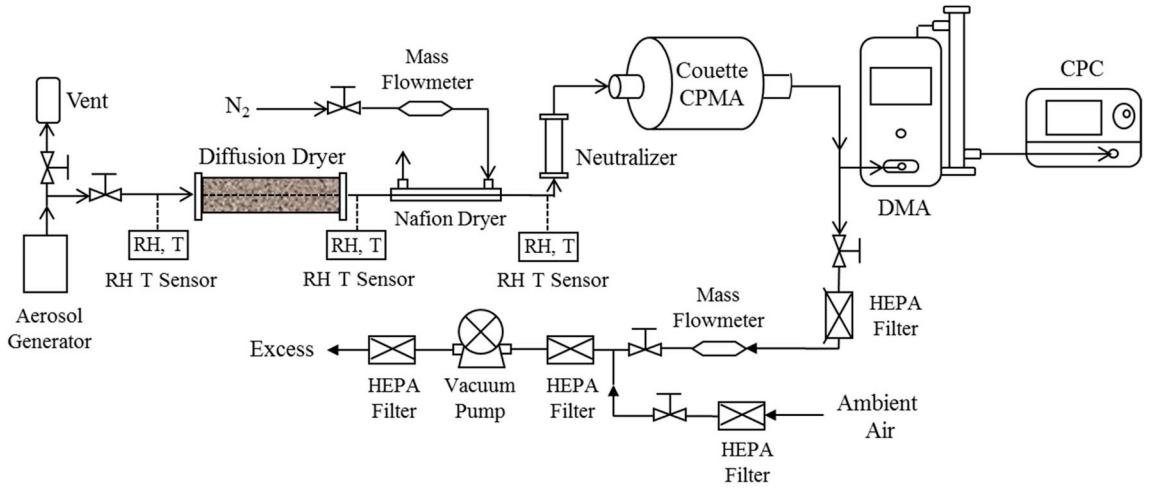

Fig. 1. Schematic overview of the CPMA-SMPS system.

(hereinafter referred to as aerosol drying flow rate). A list of the investigated aerosol drying flow rates and corresponding drying rates is shown in Table 2. The calculation of drying rates can be found in Supplement material. Downstream of the diffusion dryer, the aerosol flow was further dried with a Nafion conditioner (self-manufactured, semi-permeable membrane in stain steel jacket, 70 cm length and 0.771 cm I.D.) to a RH of 3 ± 1%. This RH is much lower than the reported efflorescence relative humidity (ERH) of BSA particles (35% for 98 nm particles; Mikhailov et al., 2004). The RH of the aerosol flow was monitored with high accuracy RH sensors (Vaisala HMT330) at the inlet and outlet of the diffusion dryer and the Nafion conditioner. The accuracy of the RH sensors is within 1% below 90% RH and 1.7% above 90% RH. All the experiments were performed at room temperature and pressure (295 ± 1 K, ~960 hPa).

A combination of a CPMA and a SMPS was used to determine the effective densities of the generated particles, as shown in Fig. 1. Aerosol particles were neutralized by a Kr-85 bipolar diffusion neutralizer (Model 3077, TSI) and classified by the CPMA according to their mass (Olfert & Collings, 2005). Downstream a SMPS was used to measure the number size distribution of the mass-classified particles. A second Kr-85 bipolar diffusion neutralizer (Model 3077, TSI) was used to neutralize the particles before it enters the SMPS. The aerosol flow rates for both CPMA and SMPS were set to 0.3 L min^{-1}. Various particle mass was chose to cover a diameter range from about 40 nm to 200 nm. The effective density (ρ_{eff}) of protein particles can be obtained from their electrical mobility diameter (D_m) and mass (m_p) respectively measured with the SMPS and CPMA (DeCarlo et al., 2004):

$$\rho_{eff} = \frac{6m_p}{\pi D_m^3} \tag{1}$$

In our experiment, the number size distributions of the protein particles measured with the SMPS are not infinitely narrow (Fig. S3), which is mainly due to two reasons. Firstly, the morphology of protein particles generated at a certain drying condition are not exactly the same, resulting in varying mobility diameters of the particles with the same mass. Secondly, the transfer functions of both CPMA and DMA have certain width. Even if all the particles have the same effective density, the measured number size distribution of the mass-selected particles will still show a certain width. Fig. 2 shows an example of the measured number size distribution (BSA particles generated with 0.1% solution and aerosol drying flow rate of 0.6 L min^{-1}). Multiple modes can be seen due to the existence of particles carrying multiple charges in CMPA or/and DMA. In Fig. 2, mode 1 consists of particles carrying one elementary charge in both CPMA and DMA. This mode is used to calculate particle effective densities. The other three modes (2–4) consist of particles

Table 2
The calculated drying rates in the silica gel diffusion dryer corresponding to the four investigated aerosol drying flow rates.

Experiment	Diffusion dryer conditions				Calculated drying rates[a]	
	Aerosol drying flow rate (L min^{-1})	RH (%)		ΔRH (%)	RH'$_{ERH=35\%}$ (RH s^{-1})	RH'$_{RH=5\%}$ (RH s^{-1})
		Inlet	Outlet			
1	0.3	99.0 ± 1.7	2.6 ± 1.0	96.4 ± 2.0	−4.7	−0.7
2	0.6	99.0 ± 1.7	4.5 ± 1.0	94.5 ± 2.0	−8.0	−1.1
3	1.0	99.0 ± 1.7	12.6 ± 1.0	86.4 ± 2.0	−8.8	−1.3
4	1.5	99.0 ± 1.7	15.7 ± 1.0	83.3 ± 2.0	−11.8	−1.8

[a] The drying rates were calculated at RH of 35% and 5% (35% RH is the efflorescence RH of BSA particles; Mikhailov et al., 2004). Details of the calculation can be found in Supplement material.

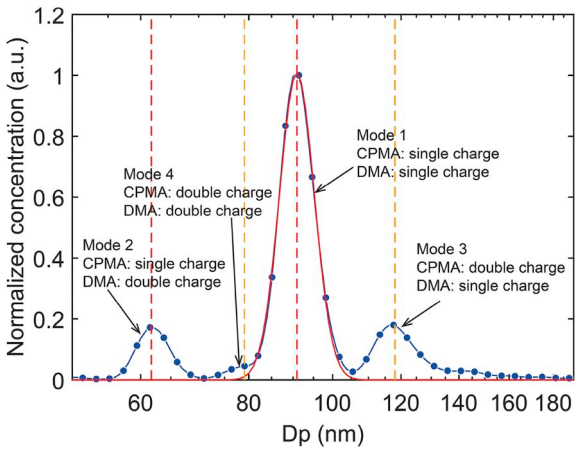

Fig. 2. A typical number size distribution of the generated protein particles measured with our CPMA-SMPS system. Red solid line shows the lognormal-fit of the main mode. (For interpretation of the references to colour in this figure legend, the reader is referred to the Web version of this article.)

carrying two elementary charges in either CPMA or DMA, or both. To avoid the influence of multiply charged particles and CPMA and DMA transfer functions on the determination of the mean diameter of the mass-selected particles, log-normal fit was applied to the main mode (mode 1) of the measured number size distribution. The geometric mean diameter of the log-normal distribution (red dashed and solid line in Fig. 2) was used for the calculation of ρ_{eff} with Eq. (1). In most cases, the influence of modes 2–4 on the lognormal-fit of mode 1 is negligible.

The uncertainty of the measured particle effective density ($\varepsilon_{\rho_{eff}}$) can be estimated based on the measurement uncertainty of CPMA and SMPS:

$$\varepsilon_{\rho_{eff}} = \sqrt{\varepsilon_{m_p}^2 + \left(3\varepsilon_{D_m}\right)^2} \tag{2}$$

where, ε_{m_p} and ε_{D_m} are the relative uncertainties of the measured m_p and D_m, respectively. For our system, $\varepsilon_{\rho_{eff}}$ was calculated to be 7.8%. The system was also tested with polystyrene latex (PSL) and ammonium sulfate particles. For PSL, the relative differences between the measured effective densities and its bulk density are respectively 3%, 4% and 3% for 150 nm, 200 nm and 350 nm particles, which are within the estimated $\varepsilon_{\rho_{eff}}$. For ammonium sulfate particles, the measured effective density is lower than its bulk density (1.77 g cm^{-3}). The differences are within 12% for sizes ranging from 40 nm to 130 nm (details in Table S1). This is consistent with previous studies reporting that ammonium sulfate particles are not ideal spheres and may contain water and voids (Leskinen et al., 2012; Mikhailov, Vlasenko, Martin, Koop, & Pöschl, 2009). As a reference, McMurry, Wang, Park, and Ehara (2002) observed a bias within 5% for 100 and 300 nm particles. Leskinen et al. (2014) reported a bias of 15% for 79 nm ammonium sulfate particles with their APM-MPSS system.

2.2. Determination of hygroscopic growth factors of protein particles

To better characterize the morphology of the protein particles generated via a spray-drying process, particle hygroscopic growth factor was measured with a nano-particle hygroscopic tandem differential mobility analyzer (Nano-HTDMA, Leibniz Institute for Tropospheric Research) and a high humidity tandem differential mobility analyzer (HH-TDMA, Leibniz Institute for Tropospheric Research). Particle hygroscopic growth factors (f_g) were determined at RHs from 5% to 99%. A detailed description of the HH-TDMA system is available in Hennig, Massling, Brechtel, and Wiedensohler (2005).

The Nano-HTDMA consists of two Hauke-type DMAs connected in series, two humidifiers (self-made, 70 cm length and 0.771 cm I.D.), and a condensation particle counter (CPC, Model 3772, TSI) with a sample flow of 1 L min^{-1} (Liu et al., 1978; Swietlicki et al., 2008). Briefly, dry polydisperse aerosol particles pass through a Kr-85 bipolar diffusion neutralizer (Model 3077, TSI) and enter the first nano-DMA (Self-made, Hauke type, center rod length 11 cm; Birmili, Stratmann, & Wiedensohler, 1999). The output monodisperse particles are then exposed to a humid environment through the humidifiers, after which the number size distributions of the particles are measured with the second DMA (self-made, Hauke type, center rod length 28 cm) and the CPC. The residence time of the particles in the humidifiers and the second DMA is around 4.6 s which is enough for protein particles to reach equilibrium at the predefined RH. The TDMA-*inv* algorithm is applied to the Nano-HTMDA and HH-TDMA data to retrieve the probability distribution functions of growth factor (f_g-PDF; Gysel, McFiggans, & Coe, 2009). The mean f_g is obtained by fitting the f_g-PDFs with lognormal distribution, based on six to eight scans at the predefined RH. The relative uncertainty of the measured f_g (ε_{f_g}) can be calculated as

$$\varepsilon_{f_g} = \sqrt{\left(\left(f_g \frac{\sqrt{2}\,\varepsilon_{Dp}}{D_p}\right)^2 + \left(\varepsilon_{RH}\frac{dG}{dRH}\right)^2\right)} \tag{3}$$

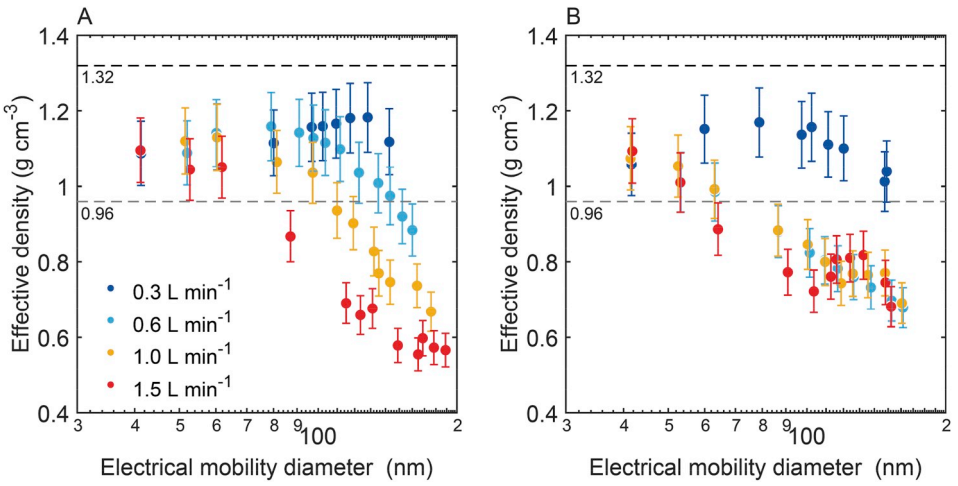

Fig. 3. The effective densities of BSA particles generated from (A) 0.1% and (B) 0.001% BSA solution at aerosol drying flow rates of 0.3 L min^{-1} (dark blue), 0.6 L min^{-1} (light blue), 1 L min^{-1} (yellow), and 1.5 L min^{-1} (red). Error bars show the uncertainty of the measured effective densities (details in Sect. 2.1). The bulk density (ρ_{bulk}) and gas phase density (ρ_{ions}) of BSA are marked as black and gray dashed lines, respectively. (For interpretation of the references to colour in this figure legend, the reader is referred to the Web version of this article.)

where ε_{Dp}, ε_{RH}, and D_p are respectively the uncertainty of particle mobility diameter, the uncertainty of relative humidity, and particle diameter (Mochida & Kawamura, 2004). Depending on RH, f_g, and D_p, the ε_{f_g} ranges from 2.8% to 6.8%.

3. Results and discussion

3.1. Observed effective densities of spray-drying generated BSA and OVA particles

As introduced in Sect. 2.1, the effective densities of BSA and OVA particles generated via a spray-drying process were measured with a CPMA-SMPS system. To investigate the factors influencing the morphology and effective density of BSA and OVA particles with diameter from 40 to 200 nm, two solution concentrations (0.1% and 0.001%, w/w) and four aerosol drying flow rates (0.3, 0.6, 1.0, and 1.5 L min^{-1}) were applied.

Fig. 3A and B illustrate the measured effective densities of BSA particles generated from 0.1% to 0.001% solutions, respectively. The measured particle effective density varies with particle size, solution concentration, and aerosol drying flow rate. It should be noted that all the measured values are lower than BSA bulk density (1.32 g cm^{-3}, marked as black dashed line in Fig. 3). Due to the irregular surfaces, protein particles may have an average diameter larger than the theoretical minimum even if they are approximately compact spheres (Erickson, 2009). The effective densities of relatively compact BSA particles (e.g. those generated with aerosol drying flow rate of 0.3 L min^{-1}) are higher than the density of gas phase BSA ions (0.96 g cm^{-3}, marked as gray dashed line in Fig. 3; Maißer et al., 2011), since gas phase protein molecule has its native conformation and is not necessarily aspherical.

For BSA particles generated from 0.1% solution, the effective densities decrease with increasing particle size (Fig. 3A). And the decreasing rates highly depend on the aerosol drying flow rates. The most significant downward trend is found at the highest aerosol drying flow rate applied, 1.5 L min^{-1}; while the downward trend is not observed at 0.3 L min^{-1}. 40 nm particles generated with the four aerosol drying flow rates show very similar effective densities (about 1.1 g cm^{-3}); while for 140 nm particles, the effective densities are respectively measured as 1.12, 0.97, 0.75 and 0.58 g cm^{-3} at aerosol drying flow rates of 0.3, 0.6, 1.0 and 1.5 L min^{-1}. Fig. 3B shows the measured effective densities of BSA particles generated from 0.001% solution. Similar as the results for 0.1% solution, decreasing effective densities with increasing particle size also can be found. However, the measured effective densities at aerosol drying flow rates of 0.6, 1.0 and 1.5 L min^{-1} show very similar size dependence. The downward trend for 0.3 L min^{-1} is weak but still visible for particle size over 100 nm.

Proteins have remarkably diverse properties including conformation, size, charge and solubility, which can affect their physicochemical behavior in solid and liquid phase (Scopelliti et al., 2010). Therefore, we have also measured the effective densities of another protein, OVA. OVA has a lower molecular mass (42.7 kDa) and exhibits a slower adsorption process at air–water interface than BSA (Kudryashova, Meinders, Visser, van Hoek, & de Jongh, 2003; Wierenga, Meinders, Egmond, Voragen, & de Jongh, 2003). Fig. 4 shows the measured effective densities of the OVA particles generated from 0.1% and 0.001% solutions via a spray-drying process. As shown in Fig. 4A, the effective densities of OVA particles generated from 0.1% solution are nearly independent of particle size in the measured size range. The differences among the measurements for the four aerosol drying flow rates are also insignificant. All measured values are higher than OVA gas phase density (1.01 g cm^{-3}; Maißer et al., 2011) and close to its bulk density (1.27 g cm^{-3}), demonstrating that the generated OVA particles have an approximately compact spherical shape. For particles generated from 0.001% OVA solution (Fig. 4B), the measured effective densities decrease from about 1.1 g cm^{-3} at 50 nm to about 0.7 g cm^{-3} at 200 nm for all the four drying flow rates, indicating the formation of uncompact particles at larger sizes. It is interesting

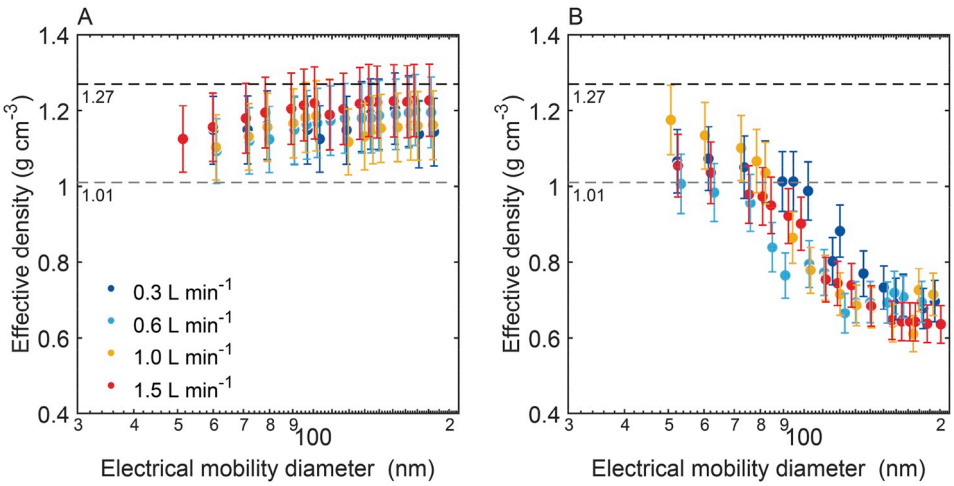

Fig. 4. The effective densities of OVA particles generated from (A) 0.1% and (B) 0.001% OVA solution at aerosol drying flow rates of 0.3 L min^{-1} (dark blue), 0.6 L min^{-1} (light blue), 1 L min^{-1} (yellow) and 1.5 L min^{-1} (red). Error bars show the uncertainty of the measured effective densities (details in Sect. 2.1). The bulk density (ρ_{bulk}) and gas phase density (ρ_{ions}) of OVA are marked as black and gray dashed lines, respectively. (For interpretation of the references to colour in this figure legend, the reader is referred to the Web version of this article.)

to note that the effective densities of OVA particles is insensitive on the aerosol drying flow rate, which is different from BSA particles.

We also noted that the width of the distribution of the measured effective densities may be different at different particle diameters and drying conditions. The σ_g of the lognormal fits of the measured number size distributions increases with increasing particle size (Fig. S4), indicating that the effective densities of larger particles span over a wider range. This is because compact particles (small particles, as shown in Figs. 3 and 4) have similar morphology and therefore nearly uniform effective densities. But for particles with semi-solid structure or partially hollow morphology (large particles in most cases, as shown in Figs. 3 and 4), the morphology may be largely different among particles, resulting in a broader distribution of effective densities. The σ_g also changes with drying conditions. For example, although the effective densities of large (> 150 nm) OVA particles generated with 0.001% solution are quite similar (Fig. 4B), the σ_g of particles generated with 0.3 and 0.6 L min^{-1} aerosol drying flow rates are obviously higher than those generated with 1.0 and 1.5 L min^{-1} (Fig. S4B). This result suggests that even with the same mean effective density, the uniformity of the effective densities (i.e. the uniformity of morphology) of generated protein particles can be different at different drying conditions.

3.2. Factors influencing the effective densities of spray-drying generated protein particles

The drying of the atomized droplets includes two processes: water evaporation and rearrangement of the solute monomers. Key concepts to interpret the observed variation in the effective densities of protein particles (Sect. 3.1) include: 1) particle morphology is developed by the diffusive movement of solute monomers; 2) the diffusive movement of solute monomers is facilitated by the liquid water in the particle (Wang et al., 2010). During a sufficiently fast drying, water evaporation is much faster than the diffusive movement of solute monomers. There is not enough time for solute monomers to move from near surface to the particle center to form a compact morphology, resulting in a low effective density of the dried particle. During a sufficiently slow drying, the diffusive movement of solute monomers is faster than water evaporation. The solute monomers therefore have enough time to redistribute and form a compact dry particle with a high effective density. It should be noted that “fast” and “slow” mentioned above do not refer in particular to the drying rates. Whether there is enough time for the solute monomers to well redistribute depends on particle size, solute concentration, and the chemical substance of the solute. In this section, factors influencing the effective densities of protein particles generated via spray-drying processes will be discussed in detail.

3.2.1. Dependence of particle effective density on drying rate

Previous studies found that the drying rate can affect the microstructure and morphology of particles generated via spray-drying processes (Mifflin, Smith, & Martin, 2009; Vehring, Foss, & Lechuga-Ballesteros, 2007). In our study, aerosol drying rates are directly controlled by the aerosol drying flow rates (Table 2). The influence of drying rates on particle effective densities is observed. As shown in Fig. 3A, the effective densities of BSA particles generated with different aerosol drying flow rates (means different drying rates) largely differ from each other, with the highest effective densities at the lowest drying rate ($RH'_{ERH} = -4.7$ RH s^{-1}) and the lowest effective densities at the highest drying rate ($RH'_{ERH} = -11.8$ RH s^{-1}). Theoretically, compact dry particles can be produced if the drying of the nebulized droplets is slow enough since there is sufficient time for the solute monomers to redistribute by diffusion throughout the evaporating droplet. In contrast, if the drying of the droplet is fast, solute monomers may accumulate near the drying front of the droplet (Huang, 2011). The measurements of BSA shown in Fig. 3A give good examples covering solute redistributing time from “sufficient” to “extremely insufficient”.

However, for spray-drying generated OVA particles, the four drying rates applied in our experiments do not cover the two extreme

cases. As shown in Fig. 4, OVA particles generated with the four drying rates always show similar effective densities. The measured effective densities of OVA particles generated from 0.1% solution are quite close to OVA bulk density; while decrease trends with increasing particle size can be seen for particles generated from 0.001% solution. This result indicates that for 0.1% solution, OVA monomers have sufficient time to redistribute in the particle even at the highest drying rate ($RH'_{ERH} = -11.8$ RH s^{-1}). But for 0.001% solution, the time for OVA monomers to redistribute is extremely insufficient even at the lowest drying rate applied ($RH'_{ERH} = -4.7$ RH s^{-1}). It is also worth noticing that, for a given solute substance and solution concentration, there is a lower limit of the effective density of dried particles which depends only on particle size. Increasing only the drying rate will not produce particles with effective density lower than this limit.

3.2.2. Dependence of particle effective density on particle size

The effective densities of protein particles generated via spray-drying processes also depend on particle size. Although influenced by particle morphology, the electrical mobility diameter of a dried particle reflects approximately the amount of solute monomers it contains. Larger particles contain larger amount of solute monomers and more liquid water before dried. Thus longer time may be needed for the redistribution of the solute monomers in the evaporating droplets.

The characteristic time of the diffusive movements of solute monomers scales as L^2/D, where L is the length scale (i.e. particle size) and D is the diffusion coefficient of solute monomers (Wang et al., 2010). Since the characteristic time is proportional to L^2, it increases dramatically with increasing particle size. For particles with sufficiently large L, the characteristic time of diffusive movements of solute monomers is much longer than the time needed for the evaporation of liquid water. Therefore, at a given drying rate, larger particles tend to have a semi-solid structure or partially hollow morphology, and thus lower effective densities as shown in Figs. 3 and 4.

3.2.3. Dependence of particle effective density on solution concentration

Protein particles with a certain electrical mobility diameter can be generated from solutions with different solute concentrations. With the same drying rate, the effective densities of the dried particles at a certain diameter can be largely different under different solution concentrations. As shown in Fig. 3, except aerosol drying flow rate of 1.5 L min^{-1}, BSA particles generated from 0.1% solution have always higher effective densities than those generated with 0.001% solution. The difference is even larger for OVA particles.

Under a lower solution concentration, larger droplets are required to produce dry particles with desired diameter. The solution concentration therefore determines the amount of liquid water in the droplets, and thus the average distance between solute monomers before entering the dryer (Erickson, 2009). Although the evaporation of liquid water needs a longer time for larger droplets, following the L^2-Law (Sect. 3.2.2), the characteristic time of diffusive movements of solute monomers is much longer. Particles with lower effective densities are therefore produced.

3.2.4. Discussion

The effective densities of protein particles generated via spray-drying processes are found to depend on drying rate, particle size, and solution concentration. As discussed above, particle size and solution concentration determine the amount of solute monomers and liquid water in droplets; drying rate determines the time needed for removing all liquid water from the droplets. The competition between the removal of liquid water and the redistribution of the solute monomers in the droplets determines the final morphology and effective density of the dried particles. In addition, the morphology of dried particles may also depend on solute chemical substance. As an example, under the four drying rates and the two solution concentrations applied in our study, the effective densities of OVA particles are more sensitive on solution concentration and less sensitive on drying rate, while an opposite behavior is observed for BSA particles. Besides the difference in diffusion coefficients of BSA and OVA, such a difference may be also attributed to different surface activities of the two proteins. Theoretically, proteins with high surface activity can result in preferential adsorption of solute monomers on the droplet surface (Vehring, 2008), which causes a diffusional flux toward the surface and subsequently results in early shell formation. Razumovsky and Damodaran (1999) reported a higher surface activity of BSA than OVA, which is very likely to stem from the different secondary structure contents of the two proteins. Because surface activity of globular proteins is found to be intimately related to their molecular flexibility which is determined by the secondary structure content and the spatial organization of the secondary structure elements in the tertiary structure of the protein (Razumovsky & Damodaran, 1999).

It is difficult to simply correlate the effective densities of protein particles with only one of the factors discussed above, since their influences are coupled with each other. In other words, under certain conditions, particle effective densities can be very sensitive on both drying rate and solution concentration. A change in any of them may result in a change of particle morphology from one extreme (compact particle with high effective density) to the other (particle with void or hallow morphology, with low effective density). This suggests that when generating BSA and OVA particles (and probably also other protein particles) with spray-drying method, one needs to be very careful with both the drying rate and solution concentration. Because an improper combination of generation parameters may result in unexpected particle morphology and effective densities.

It is also worth noticing that higher drying rates or lower solution concentrations may not always result in lower effective densities of the dried protein particles. And protein particles with an effective density equaling to its bulk density can not be obtained by just decreasing drying rate or increasing solution concentration. There seems to be lower and higher boundaries of the effective densities of spray-drying generated protein particles which depend only on solute substance and dry particle size. The possible range of the effective densities is getting narrower with decreasing particle size. For sufficiently small particles (smaller than ~40 nm), a constant effective density is observed independent of drying rate and solution concentration. Therefore, one needs to be more careful

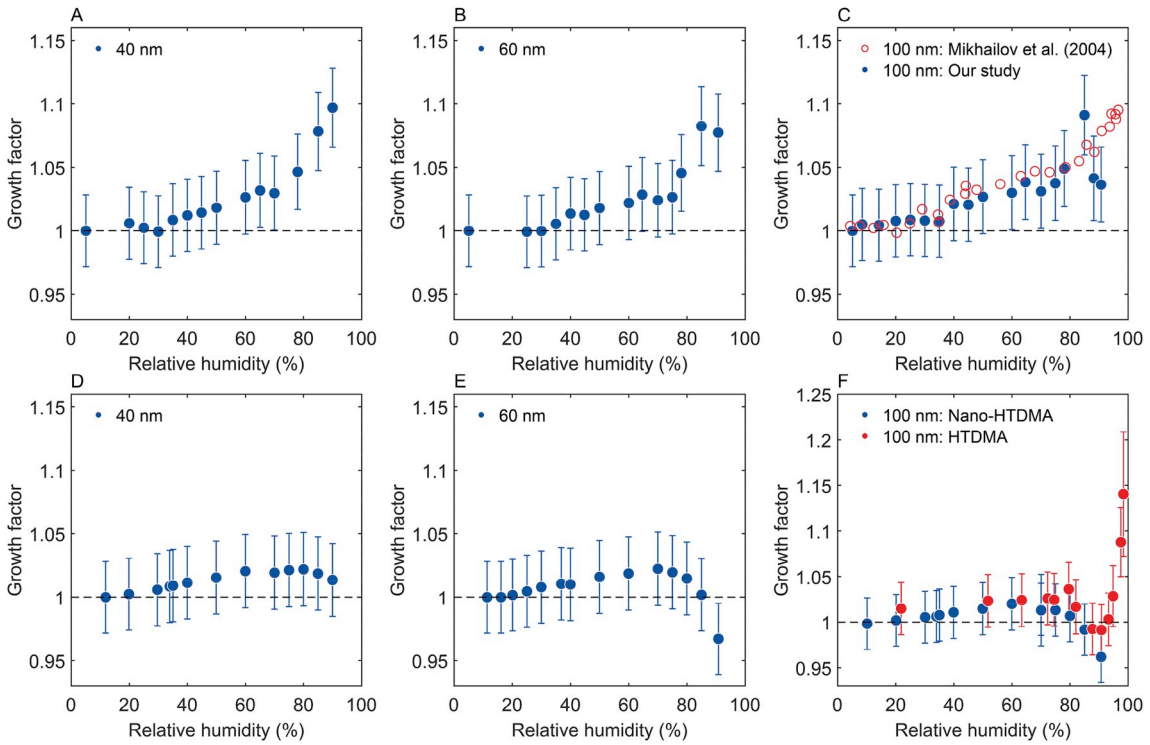

Fig. 5. Hygroscopic growth factors of 40, 60 and 100 nm BSA particles generated from 0.1% solution (A–C) and 0.001% solution (D–F) under RH of 5–92% at 293 K. The red open circles in Fig. 5C show the results from Mikhailov et al. (2004). The red dots in Fig. 5F show measurements of HHTDMA under RH from 22% to 99%. Error bars show the measurement uncertainty of the hygroscopic growth factors (details in Sect. 2.2). (For interpretation of the references to colour in this figure legend, the reader is referred to the Web version of this article.)

when generating larger (> 100 nm) protein particles.

In this study, we have only investigated the influences of four factors (i.e. drying rate, concentration of solution, particle diameter, and chemical substance) on the morphology and effective densities of spray-drying generated protein particles. There may be more factors having strong influence, for example, pH and ionic strength of the solution used for particle generation. The conformation of proteins in solution strongly depends on solution pH. It is therefore also interesting and needed to investigate how solution pH may influence the morphology and effective densities of spray-drying generated protein particles.

3.3. Influence of morphology on the hygroscopic growth of protein particles

Previous studies found that particle morphology can influence its hygroscopicity (Mikhailov et al., 2004, 2009). The hygroscopic growth factors of BSA particles generated via a spray-drying process were measured in this study with a Nano-HTDMA and a HH-TDMA (Sect. 2.2). Only an aerosol drying flow rate of 1 L min^{-1} was applied because 1) decreases of effective densities are observed at this drying rate for both 0.001% and 0.1% BSA solutions, and 2) this aerosol drying flow rate fits well with our Nano-HTDMA and HHTDMA system.

The hygroscopic growth factors of 40, 60 and 100 nm BSA particles generated from 0.1% solution were measured with the Nano-HTDMA system, and the results are shown in Fig. 5A–C. Only a slight growth (growth factor of 1–1.03) is observed in RH range of 35–75%, which can be explained mainly by particle surface adsorption of water vapor. Bulk absorption of water vapor may also play a role (Keskinen et al., 2011; Popovicheva et al., 2008). For 60 and 100 nm BSA particles, decreases of growth factors at RH of about 85% accompanied by pronounced broadening of the size distribution of the grown particles are observed. Mikhailov et al. (2009) extended the definition of deliquescence as the transformation of a (semi-)solid substance into a liquid aqueous solution. It is very likely that these observed decreases of particle hygroscopic growth factors at 85% RH are caused by particle microstructural re-arrangement during its deliquescence transition (Sjogren et al., 2007). As shown in Sect. 3.1, 60 and 100 nm BSA particles generated from 0.1% solution and dried with an aerosol drying flow rate of 1 L min^{-1} have low effective densities, i.e., a semi-solid structure or (partially) hollow morphology. For RH $< 80\%$, particle absorbs water vapor by mainly surface adsorption and minor bulk absorption but retains (partially) its hollow morphology. At around 85% RH, its loose structure starts to collapse, and the particle starts to transform from a semi-solid state into a more compact highly viscous or gel-like matrix. Therefore, a decrease in particle diameter can be observed. For 40 nm BSA particles, decrease of growth factor is not observed throughout the investigated RH range. This also agrees with the effective density measurement that 40 nm BSA particles are relatively compact. Mikhailov et al. (2004) performed measurements of hygroscopic growth factors of 98 nm BSA particles generated from 0.1% BSA solution with spray-drying method and reported continuously increasing hygroscopic growth factors up to 95% RH. Their measurement result is also given in Fig. 5C as red

open circles. Compared with our measurement, the growth factors in Mikhailov et al. (2004) are slightly higher at RH lower than 80%, and no decrease is observed at RH of 85%. This difference in hygroscopic growth factors is very likely to stem from the different spray-drying conditions applied in the two experiments. The residence times of particles in humidification conditioner may be different in the two HTDMA systems, which can be also a factor resulting in the different results.

Fig. 5D–F illustrate the hygroscopic growth factors of BSA particles generated from 0.001% solution. Gradual decreases of particle hygroscopic growth factors with increasing RH accompanied by broadening of the particle size distributions are observed at RH above 80%. Such decreases of growth factors are also observed for BSA particles generated with 0.1% solution. However, the decreases for BSA particles generated with 0.001% solution are more pronounced and start at lower RHs. This result indicates that the BSA particles generated with 0.001% solution are closer to semi-solid structure or hollow morphology, which consists well with the effective density measurements shown in Sect. 3.1.

To obtain the hygroscopic growth behavior of BSA particles at RH above 90%, a HHTDMA system was applied in our study. Hygroscopic growth factors of 100 nm BSA particles generated from 0.001% solution was measured at RH from 20% to 98% under highly temperature-stabilized condition. The results are shown as red solid dots in Fig. 5F. At RH between 20% and 90%, only a small difference is observed between the growth factors measured with the Nano-HTDMA and the HHTDMA. Such a minor difference may stem from instrumental factors (Biskos, Paulsen, Russell, Buseck, & Martin, 2006). After its minima at about 90% RH, particle hygroscopic growth factor increases significantly again, and reaches 1.09 at RH of about 97%, which is quite close to the value measured by Mikhailov et al. (2004). The most plausible explanation for such a behavior can be that the BSA particles transform from a semi-solid state into a highly viscous or gel-like matrix at around 90% RH. With a compact structure, the lowest growth factor of the particles is observed at 90% RH. Above 90% RH, increase of RH leads to water absorption and thereby diameter growth. However, the absorption of water may be still limited by diffusion or structural rearrangements. At RH above 95%, the viscous or gel-like matrix becomes so dilute (or fully dissolved) that it ceased to inhibit particle hygroscopic growth. Instead, it shows a characteristic of liquid aqueous solution droplets (Mikhailov et al., 2009).

4. Conclusions

To investigate the morphology of protein particles generated via spray-drying processes, particle effective densities and hygroscopic growth factors were measured with a CPMA-SMPS and HTDMA systems, respectively. The major factors influencing the morphology (effective density) of spray-drying generated protein particles are found to be drying rate, concentration of solution, particle diameter, and chemical substance. Main conclusions include:

- Drying rate determines the time needed for removing liquid water from the droplets. In the case of fast drying under a high drying rate, the solute monomers in the droplet do not have enough time to well redistribute, leading to a low effective density of the dried protein particles.
- Solution concentration determines the size of the droplets needed for producing dry particles with a certain diameter. The protein monomers need shorter time to redistribute in smaller droplets during a drying process. Therefore, protein particles generated from high-concentration solution tend to have a compact morphology, and thus a high effective density.
- Larger dry protein particles contain larger amount of solute monomers, thus longer time is needed for the redistribution of the solute monomers in the evaporating droplets. In other words, at a given drying rate, larger particles tend to have a semi-solid structure or partially hollow morphology, and thus a lower effective density.
- The morphology of dried particles may also depend on solute chemical substance, since different proteins may have different diffusion coefficients and surface activities.
- There seems to be lower and higher boundaries of the effective densities which depend only on dry particle size. The possible range of the effective densities gets narrower with decreasing particle size. For sufficiently small particles (smaller than 40 nm), a constant effective density is observed independent of drying rate and solution concentration.
- The morphology of protein particles can significantly influence their hygroscopicity. For BSA particles with a semi-solid structure (low effective density), decreasing hygroscopic growth factor with increasing RH is observed at RH around 80%, indicating the transform of particle morphology from a semi-solid state into a more compact highly viscous or gel-like matrix.

It is difficult to find a simple correlation between the effective densities of protein particles and one of the factors studied, since their influences are complex and coupled with each other. Therefore, when generating protein particles with spray-drying method, the effects of drying rate and solution concentration should be considered. An improper combination of generation parameters may result in unexpected particle morphology and effective densities. Additionally, the aforementioned factors may play different roles for different chemical substances. There may be also other factors (e.g. pH of solution used for particle generation) influencing the morphology and effective densities of spray-drying generated particles. Further well-designed investigations of other atmospheric aerosol substances and the influence of other factors are required.

Acknowledgments

This work has been supported by National Key Research and Development Program of China (2017YFC0210104), National Natural Science Foundation of China (91644218), Guangdong Innovative and Entrepreneurial Research Team Program (2016ZT06N263), Russian Foundation for Basic Research (grant 16-05-00717), and China Scholarship Council (CSC).

Appendix A. Supplementary material

Supplementary data to this article can be found online at https://doi.org/10.1016/j.jaerosci.2019.105441.

References

Abegglen, M., Durdina, L., Brem, B. T., Wang, J., Rindlisbacher, T., Corbin, J. C., et al. (2015). Effective density and mass–mobility exponents of particulate matter in aircraft turbine exhaust: Dependence on engine thrust and particle size. *Journal of Aerosol Science, 88*, 135–147.

Adler, M., Unger, M., & Lee, G. (2000). Surface composition of spray-dried particles of bovine serum albumin/trehalose/surfactant. *Pharmaceutical Research, 17*, 863–870.

Bahreini, R., Keywood, M. D., Ng, N. L., Varutbangkul, V., Gao, S., Flagan, R. C., et al. (2005). Measurements of secondary organic aerosol from oxidation of cycloalkenes, terpenes, and m-xylene using an Aerodyne aerosol mass spectrometer. *Environmental Science & Technology, 39*, 5674–5688.

Birmili, W., Stratmann, F., & Wiedensohler, A. (1999). Design of a Dma-based size spectrometer for a large particle size range and stable operation. *Journal of Aerosol Science, 30*, 549–553.

Biskos, G., Paulsen, D., Russell, L. M., Buseck, P. R., & Martin, S. T. (2006). Prompt deliquescence and efflorescence of aerosol nanoparticles. *Atmospheric Chemistry and Physics, 6*, 4633–4642.

Butcher, D., Miksovska, J., Ridgeway, M. E., Park, M. A., & Fernandez-Lima, F. (2019). The effects of solution additives and gas-phase modifiers on the molecular environment and conformational space of common heme proteins. *Rapid Communications in Mass Spectrometry, 33*(5), 399–404.

Chang, H., & Okuyama, K. (2002). Optical properties of dense and porous spheroids consisting of primary silica nanoparticles. *Journal of Aerosol Science, 33*, 1701–1720.

DeCarlo, P. F., Slowik, J. G., Worsnop, D. R., Davidovits, P., & Jimenez, J. L. (2004). Particle morphology and density characterization by combined mobility and aerodynamic diameter measurements. Part 1: Theory. *Aerosol Science and Technology, 38*, 1185–1205.

Durdina, L., Brem, B. T., Abegglen, M., Lobo, P., Rindlisbacher, T., Thomson, K. A., et al. (2014). Determination of PM mass emissions from an aircraft turbine engine using particle effective density. *Atmospheric Environment, 99*, 500–507.

Ehara, K., Hagwood, C., & Coakley, K. J. (1996). Novel method to classify aerosol particles according to their mass-to-charge ratio—aerosol particle mass analyser. *Journal of Aerosol Science, 27*, 217–234.

Erickson, H. P. (2009). Size and shape of protein molecules at the nanometer level determined by sedimentation, gel filtration, and electron microscopy. *Biological Procedures Online, 11*, 32–51.

Frahm, G. E., Pochopsky, A. W. T., Clarke, T. M., & Johnston, M. J. W. (2016). Evaluation of microflow digital imaging particle analysis for sub-visible particles formulated with an opaque vaccine adjuvant. *PLoS One, 11*, e0150229.

Franze, T., Weller, M. G., Niessner, R., & Pöschl, U. (2003). Enzyme immunoassays for the investigation of protein nitration by air pollutants. *Analyst, 128*, 824–831.

Franze, T., Weller, M. G., Niessner, R., & Pöschl, U. (2005). Protein nitration by polluted air. *Environmental Science & Technology, 39*, 1673–1678.

Franze, T., Zerrath, A., Weller, M., Niessner, R., & Pöschl, U. (2001). Analysis of biopolymers in road dust and atmospheric aerosol samples. *Journal of Aerosol Science, 32*.

Ghazi, R., & Olfert, J. S. (2013). Coating mass dependence of soot aggregate restructuring due to coatings of oleic acid and dioctyl sebacate. *Aerosol Science and Technology, 47*, 192–200.

Gysel, M., McFiggans, G. B., & Coe, H. (2009). Inversion of tandem differential mobility analyser (TDMA) measurements. *Journal of Aerosol Science, 40*, 134–151.

Haynes, W. M. (2014). *CRC handbook of chemistry and physics.* CRC press.

Hennig, T., Massling, A., Brechtel, F. J., & Wiedensohler, A. (2005). A Tandem DMA for highly temperature-stabilized hygroscopic particle growth measurements between 90% and 98% relative humidity. *Journal of Aerosol Science, 36*, 1210–1223.

Hogan, C. J., & de la Mora, J. F. (2011). Ion mobility measurements of nondenatured 12–150 kDa proteins and protein multimers by tandem differential mobility analysis–mass spectrometry (DMA-MS). *Journal of the American Society for Mass Spectrometry, 22*(1), 158–172.

Huang, D. (2011). Modeling of particle formation during spray drying. *European drying conference, October 26–28, Palma Balearic Island, Spain*.

Iskandar, F., Gradon, L., & Okuyama, K. (2003). Control of the morphology of nanostructured particles prepared by the spray drying of a nanoparticle sol. *Journal of Colloid and Interface Science, 265*, 296–303.

Johnson, T. J., Olfert, J. S., Cabot, R., Treacy, C., Yurteri, C. U., Dickens, C., et al. (2015a). Transient measurement of the effective particle density of cigarette smoke. *Journal of Aerosol Science, 87*, 63–74.

Johnson, T. J., Olfert, J. S., Yurteri, C. U., Cabot, R., & McAughey, J. (2015b). Hygroscopic effects on the mobility and mass of cigarette smoke particles. *Journal of Aerosol Science, 86*, 69–78.

Kannosto, J., Virtanen, A., Lemmetty, M., Mäkelä, J. M., Keskinen, J., Junninen, H., et al. (2008). Mode resolved density of atmospheric aerosol particles. *Atmospheric Chemistry and Physics, 8*, 5327–5337.

Keskinen, H., Mäkelä, J., Aromaa, M., Ristimäki, J., Kanerva, T., Levänen, E., et al. (2007). Effect of silver addition on the formation and deposition of titania nanoparticles produced by liquid flame spray. *Journal of Nanoparticle Research, 9*, 569–588.

Keskinen, H., Romakkaniemi, S., Jaatinen, A., Miettinen, P., Saukko, E., Jorma, J., et al. (2011). On-line characterization of morphology and water adsorption on fumed silica nanoparticles. *Aerosol Science and Technology, 45*, 1441–1447.

Kudryashova, E. V., Meinders, M. B. J., Visser, A. J. W. G., van Hoek, A., & de Jongh, H. H. J. (2003). Structure and dynamics of egg white ovalbumin adsorbed at the air/water interface. *European Biophysics Journal, 32*, 553–562.

Kulmala, M., Suni, T., Lehtinen, K. E. J., Dal Maso, M., Boy, M., Reissell, A., et al. (2004). A new feedback mechanism linking forests, aerosols, and climate. *Atmospheric Chemistry and Physics, 4*, 557–562.

Kuwata, M. (2015). Particle classification by the tandem differential mobility analyzer–particle mass analyzer system. *Aerosol Science and Technology, 49*, 508–520.

Lang-Yona, N., Shuster-Meiseles, T., Mazar, Y., Yarden, O., & Rudich, Y. (2016). Impact of urban air pollution on the allergenicity of Aspergillus fumigatus conidia: Outdoor exposure study supported by laboratory experiments. *The Science of the Total Environment, 541*, 365–371.

Lee, S. H., Heng, D., Ng, W. K., Chan, H.-K., & Tan, R. B. H. (2011). Nano spray drying: A novel method for preparing protein nanoparticles for protein therapy. *International Journal of Pharmaceutics, 403*, 192–200.

Lee, S. Y., Widiyastuti, W., Tajima, N., Iskandar, F., & Okuyama, K. (2009). Measurement of the effective density of both spherical aggregated and ordered porous aerosol particles using mobility- and mass-analyzers. *Aerosol Science and Technology, 43*, 136–144.

Leskinen, J., Ihalainen, M., Torvela, T., Kortelainen, M., Lamberg, H., Tiitta, P., et al. (2014). Effective density and morphology of particles emitted from small-scale combustion of various wood fuels. *Environmental Science & Technology, 48*, 13298–13306.

Leskinen, J., Joutsensaari, J., Lyyränen, J., Koivisto, J., Ruusunen, J., Järvelä, M., et al. (2012). Comparison of nanoparticle measurement instruments for occupational health applications. *Journal of Nanoparticle Research, 14*, 1–16.

Liu, B. Y. H., & Lee, K. W. (1975). An aerosol generator of high stability. *American Industrial Hygiene Association Journal, 36*, 861–865.

Liu, B. Y. H., Pui, D. Y. H., Whitby, K. T., Kittelson, D. B., Kousaka, Y., & McKenzie, R. L. (1978). The aerosol mobility chromatograph: A new detector for sulfuric acid aerosols. *Atmospheric Environment, 12*, 99–104 (1967).

Maißer, A., Premnath, V., Ghosh, A., Nguyen, T. A., Attoui, M., & Hogan, C. J. (2011). Determination of gas phase protein ion densities via ion mobility analysis with charge reduction. *Physical Chemistry Chemical Physics, 13*(48), 21630–21641.

McMurry, P. H., Wang, X., Park, K., & Ehara, K. (2002). The relationship between mass and mobility for atmospheric particles: A new technique for measuring particle density. *Aerosol Science and Technology, 36*, 227–238.

Meusel, H., Elshorbany, Y., Kuhn, U., Bartels-Rausch, T., Reinmuth-Selzle, K., Kampf, C. J., et al. (2017). Light-induced protein nitration and degradation with HONO emission. *Atmos. Chem. Phys. 17*, 11819–11833. https://doi.org/10.5194/acp-17-11819-2017.
Meyer, N. A., Root, K., Zenobi, R., & Vidal-de-Miguel, G. (2016). Gas-phase dopant-induced conformational changes monitored with transversal modulation ion mobility spectrometry. *Analytical Chemistry, 88*(4), 2033–2040.
Mifflin, A. L., Smith, M. L., & Martin, S. T. (2009). Morphology hypothesized to influence aerosol particle deliquescence. *Physical Chemistry Chemical Physics, 11*, 10095–10107.
Miguel, A. G., Cass, G. R., Glovsky, M. M., & Weiss, J. (1999). Allergens in paved road dust and airborne particles. *Environmental Science & Technology, 33*, 4159–4168.
Mikhailov, E., Vlasenko, S., Martin, S., Koop, T., & Pöschl, U. (2009). Amorphous and crystalline aerosol particles interacting with water vapor: Conceptual framework and experimental evidence for restructuring, phase transitions and kinetic limitations. *Atmospheric Chemistry and Physics, 9*, 9491–9522.
Mikhailov, E., Vlasenko, S., Niessner, R., & Pöschl, U. (2004). Interaction of aerosol particles composed of protein and saltswith water vapor: Hygroscopic growth and microstructural rearrangement. *Atmospheric Chemistry and Physics, 4*, 323–350.
Mochida, M., & Kawamura, K. (2004). Hygroscopic properties of levoglucosan and related organic compounds characteristic to biomass burning aerosol particles. *Journal of Geophysical Research: Atmosphere, 109*(D21).
Muramatsu, N., & Minton, A. P. (1988). Tracer diffusion of globular proteins in concentrated protein solutions. *Proceedings of the National Academy of Sciences, 85*, 2984–2988.
Nandiyanto, A. B. D., & Okuyama, K. (2011). Progress in developing spray-drying methods for the production of controlled morphology particles: From the nanometer to submicrometer size ranges. *Advanced Powder Technology, 22*, 1–19.
Neurath, H., & Bull, H. B. (1936). The denaturation and hydration of proteins. *Journal of Biological Chemistry, 115*, 519–528.
Nisbet, A. D., Saundry, R. H., Moir, A. J. G., Fothergill, L. A., & Fothergill, J. E. (1981). The complete amino-acid sequence of hen ovalbumin. *European Journal of Biochemistry, 115*, 335–345.
Okuyama, K., Abdullah, M., Wuled Lenggoro, I., & Iskandar, F. (2006). Preparation of functional nanostructured particles by spray drying. *Advanced Powder Technology, 17*, 587–611.
Okuyama, K., & Lenggoro, I. W. (2003). Preparation of nanoparticles via spray route. *Chemical Engineering Science, 58*, 537–547.
Olfert, J. S., & Collings, N. (2005). New method for particle mass classification—the Couette centrifugal particle mass analyzer. *Journal of Aerosol Science, 36*, 1338–1352.
Olfert, J. S., Symonds, J. P. R., & Collings, N. (2007). The effective density and fractal dimension of particles emitted from a light-duty diesel vehicle with a diesel oxidation catalyst. *Journal of Aerosol Science, 38*, 69–82.
Popovicheva, O., Persiantseva, N. M., Shonija, N. K., DeMott, P., Koehler, K., Petters, M., et al. (2008). Water interaction with hydrophobic and hydrophilic soot particles. *Physical Chemistry Chemical Physics, 10*, 2332–2344.
Pöschl, U., & Shiraiwa, M. (2015). Multiphase chemistry at the atmosphere–biosphere interface influencing climate and public health in the anthropocene. *Chemical Reviews, 115*, 4440–4475.
Pummer, B., Budke, C., Augustin-Bauditz, S., Niedermeier, D., Felgitsch, L., Kampf, C., et al. (2015). Ice nucleation by water-soluble macromolecules. *Atmospheric Chemistry and Physics, 15*, 4077–4091.
Razumovsky, L., & Damodaran, S. (1999). Surface activity− compressibility relationship of proteins at the air− water interface. *Langmuir, 15*(4), 1392–1399.
Scopelliti, P. E., Borgonovo, A., Indrieri, M., Giorgetti, L., Bongiorno, G., Carbone, R., et al. (2010). The effect of surface nanometre-scale morphology on protein adsorption. *PLoS One, 5*, e11862.
Seinfeld, J. H., & Pandis, S. N. (2016). *Atmospheric chemistry and physics: From air pollution to climate change.* John Wiley & Sons.
Sjogren, S., Gysel, M., Weingartner, E., Baltensperger, U., Cubison, M. J., Coe, H., et al. (2007). Hygroscopic growth and water uptake kinetics of two-phase aerosol particles consisting of ammonium sulfate, adipic and humic acid mixtures. *Journal of Aerosol Science, 38*, 157–171.
Swietlicki, E., Hansson, H. C., HÄMeri, K., Svenningsson, B., Massling, A., McFiggans, G., et al. (2008). Hygroscopic properties of submicrometer atmospheric aerosol particles measured with H-TDMA instruments in various environments—a review. *Tellus B, 60*, 432–469.
Vehring, R. (2008). Pharmaceutical particle engineering via spray drying. *Pharmaceutical Research, 25*, 999–1022.
Vehring, R., Foss, W. R., & Lechuga-Ballesteros, D. (2007). Particle formation in spray drying. *Journal of Aerosol Science, 38*, 728–746.
Virtanen, A., Ristimäki, J., & Keskinen, J. (2004). Method for measuring effective density and fractal dimension of aerosol agglomerates. *Aerosol Science and Technology, 38*, 437–446.
Virtanen, A., Rönkkö, T., Kannosto, J., Ristimäki, J., Mäkelä, J., Keskinen, J., et al. (2006). Winter and summer time size distributions and densities of traffic-related aerosol particles at a busy highway in Helsinki. *Atmospheric Chemistry and Physics, 6*, 2411–2421.
Vörös, J. (2004). The density and refractive index of adsorbing protein layers. *Biophysical Journal, 87*, 553–561.
Wang, J., Bahk, Y. K., Chen, S.-C., & Pui, D. Y. H. (2015). Characteristics of airborne fractal-like agglomerates of carbon nanotubes. *Carbon, 93*, 441–450.
Wang, Z., King, S., Freney, E., Rosenoern, T., Smith, M., Chen, Q., et al. (2010). The dynamic shape factor of sodium chloride nanoparticles as regulated by drying rate. *Aerosol Science and Technology, 44*, 939–953.
Wierenga, P. A., Meinders, M. B. J., Egmond, M. R., Voragen, F. A. G. J., & de Jongh, H. H. J. (2003). Protein exposed hydrophobicity reduces the kinetic barrier for adsorption of ovalbumin to the Air−Water interface. *Langmuir, 19*, 8964–8970.
Zhang, Q., & Anastasio, C. (2003). Free and combined amino compounds in atmospheric fine particles (PM 2.5) and fog waters from Northern California. *Atmospheric Environment, 37*, 2247–2258.

Supporting information (SI) of "Effective density and hygroscopicity of protein particles generated with spray-drying process"

1. Drying rate at efflorescence relative humidity (ERH)

The drying rates at ERH were quantified on the basis of a diffusion calculation for the four different aerosol drying flow rates (Sect. 2 in the main text). Figure S1 shows the geometry of the apparatus with respect to the calculation of drying rates at ERH. For our experimental conditions, the Reynolds number of aerosol flow in the diffusion dryer were 26, 51, 85, and 128 for 0.3, 0.6, 1.0 and 1.5 L min^{-1} respectively, indicating a laminar flow in the dryer. A dry silica gel jacket was used to surround the inner core of humid aerosol particles flowing along the central longitudinal axis. Thus, as illustrated by Fick's Law (Association, 1999), the dominant mechanism for water vapor movement in the radial coordinate is diffusion in this case.

A quantitative model of these processes can be developed for the cylindrical geometry of the diffusion dryer. The diffusion equations describing the general mass balance for water combined with Fick's Law as a function of axial and radial position (z, r), are as follows (Wang et al., 2010):

$$v_z \frac{\partial RH}{\partial z} = \frac{D}{r}\frac{\partial}{\partial r}\left(r\frac{\partial RH}{\partial r}\right) \quad \text{(S1)}$$

The experimental setup imposes several boundary conditions for Eq. S1 as follows (Li et al., 2016):

$$-D\left.\frac{\partial RH}{\partial r}\right|_{wall} = RH\frac{\bar{v}}{4}\frac{\gamma}{1-\left(\frac{\gamma}{2}\right)} \quad \text{(S2)}$$

$$-\left.\frac{\partial RH}{\partial r^*}\right|_{r^*=1} = N_{Shw}RH \quad \text{(S3)}$$

$$r^* = \frac{r}{R} \quad \text{(S4)}$$

where v_z denotes the advective flow velocity at longitudinal coordinate z, RH denotes the relative humidity, D denotes the diffusion coefficient of water vapor in air, $\bar{v}$ denotes the mean molecular speed, ã denotes the uptake coefficient of water vapor by silica gel, N_{Shw} denotes the Sherwood number, and R is the radius of the diffusion dryer. For each given aerosol drying flow rate, a differential equation can be solved for a RH profile and the functional relationship between transmittance of the water vapor in the diffusion dryer. The RH profiles are illustrated in Fig. S2, with each line representing a radially averaged RH with respect to an aerosol drying flow rate. In this study, an average drying rate RH'_{ERH} at which particles crystallize in the diffusion dryer, can be calculated as follows (Wang et al., 2010):

$$RH'_{ERH} = \left(\frac{dRH}{dt}\right)_{ERH} = \frac{v_z\int_0^R r\left(\frac{\partial RH}{\partial x}\right)_{ERH,r}dr}{\int_0^R r dr} \quad \text{(S5)}$$

where $(\partial RH/\partial z)_{ERH,r}$ is evaluated at the position r that satisfies $RH_{(r,\,z)} =$ ERH as illustrated in Fig. S2.

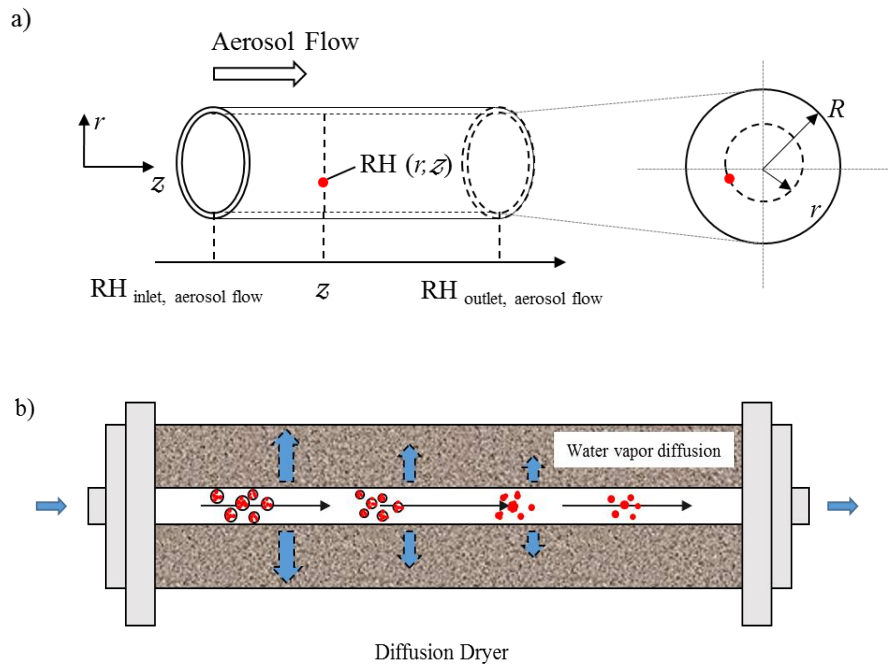

Figure S1. Illustration of the drying of the aerosol flow by radial water vapor diffusion on the wall of silica gel.

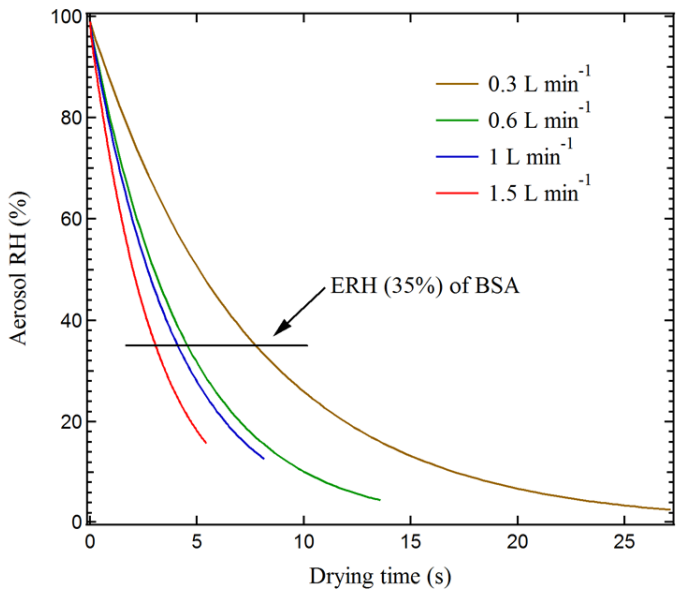

Figure S2. Calculated RH in the aerosol flow against the drying time for aerosol drying flow rates of 0.3 L min^{-1} (yellow), 0.6 L min^{-1} (green), 1.0 L min^{-1} (blue), and 1.5 L min^{-1} (red). The drying time can be related to the longitudinal position in the diffusion dryer by using the linear flow velocity converted from the aerosol drying flow rate. The horizontal line pointed by the arrow indicates the ERH of BSA particles (i.e. 35%), while the ERH of OVA particles is still absent. The slope of the curve at this point is the drying rate (RH S^{-1}) for aerosol particles at its efflorescence RH.

2. Validation of the CPMA-SMPS system with ammonium sulfate particles

The CPMA-SMPS system was tested with ammonium sulfate particles, which were generated via a spray-drying process with four aerosol drying flow rates. For each drying rate, the effective densities of dried particles with 12 diameters ranging from about 40 to 130 nm was measured. The result of the measurement is summarized in Table S1.

Table S1. Average effective densities of spray-drying generated ammonium sulfate particles (from 0.1% (w/w) ammonium sulfate solution) for aerosol drying flow rates of 0.3 to 1.5 L min^{-1}.

Aerosol flow rate	0.3 L min^{-1}			0.6 L min^{-1}			1 L min^{-1}			1.5 L min^{-1}		
Experiment	Electrical mobility diameter (nm)	Effective density (g cm^{-3})	accuracy (%)	Electrical mobility diameter (nm)	Effective density (g cm^{-3})	accuracy (%)	Electrical mobility diameter (nm)	Effective density (g cm^{-3})	accuracy (%)	Electrical mobility diameter (nm)	Effective density (g cm^{-3})	accuracy (%)
1	42	1.58	10.76	38	1.57	11.33	47	1.58	10.76	38	1.57	11.27
2	54	1.59	10.22	53	1.60	9.66	54	1.57	11.35	52	1.59	10.22
3	73	1.57	11.24	70	1.59	10.11	71	1.57	11.24	70	1.58	10.90
4	83	1.60	9.91	83	1.6	9.34	82	1.56	11.60	83	1.57	11.04
5	86	1.62	8.48	87	1.62	8.60	87	1.61	9.16	85	1.61	9.16
6	91	1.62	8.75	90	1.67	5.93	92	1.62	8.75	90	1.65	7.06
7	100	1.64	7.37	99	1.63	7.82	98	1.63	7.94	97	1.65	6.81
8	106	1.64	7.30	104	1.62	8.64	105	1.63	7.87	106	1.66	6.17
9	118	1.63	7.76	116	1.64	7.20	115	1.63	7.76	114	1.67	5.50
10	122	1.64	7.55	122	1.66	6.42	121	1.64	7.55	120	1.69	4.72
11	127	1.64	7.28	125	1.64	7.28	127	1.63	7.68	127	1.65	6.72
12	133	1.63	7.79	134	1.63	8.03	133	1.63	7.79	132	1.66	6.09

Note that the standard deviation (N = 8 for each experiment) in the measured electrical mobility diameter and effective density is within ± 0.19 nm and 0.007 g cm^{-3}, respectively, which is not listed in this table.

3. Measured number size distributions of mass-selected particles

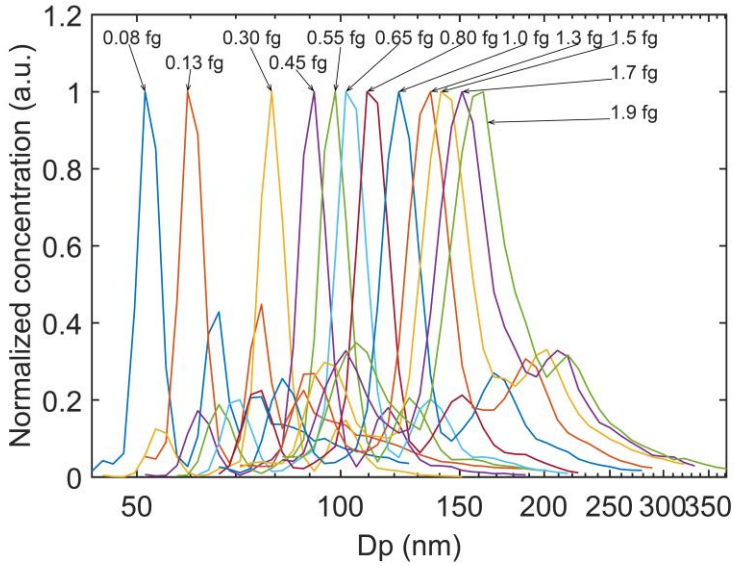

Fig. S3: Measured number size distributions of BSA particles pathing through CPMA. The BSA particles are generated with 0.1% solution and 0.6 L min^{-1} aerosol drying flow rate.

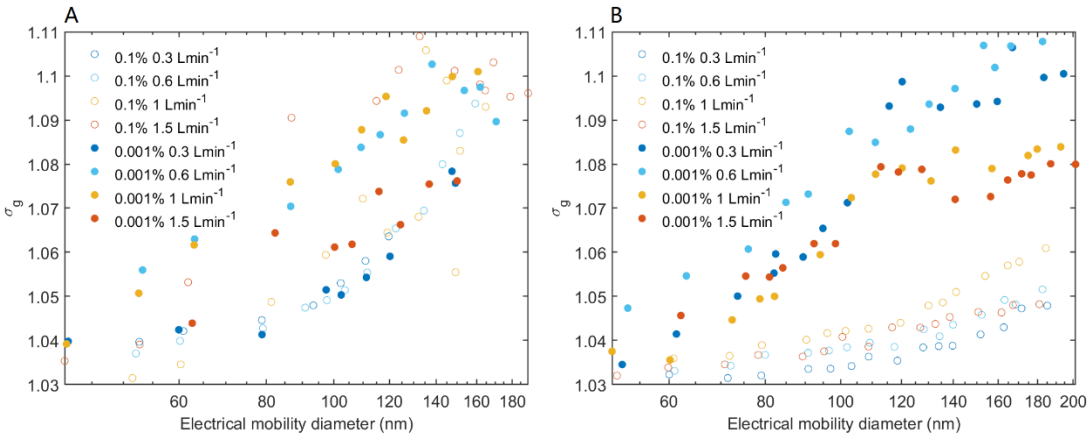

Fig. S4: σ_g of the lognormal fits of the main mode of the measured number size distributions for (A) BSA and (B) OVA particles generated at different drying conditions